High resolution MR imaging of the arrhythmogenic cardiac substrate

Marylène Delcey

université de BORDEAUX

THESE PRESENTEE

POUR OBTENIR LE GRADE DE

DOCTEUR DE L'UNIVERSITÉ DE BORDEAUX

ECOLE DOCTORALE SCIENCES DE LA VIE ET DE LA SANTE

SPECIALITE: BIOIMAGERIE

PAR Marylène DELCEY

High resolution MR imaging of the arrhythmogenic cardiac substrate

Sous la direction de: Dr. Quesson Bruno

Soutenue le 12/03/2021

Membres du jury :

Dr. STUBER Matthias, Professeur, Directeur CIBM, Lausanne	Rapporteur
Dr. BEUF Olivier, Directeur de recherche CNRS, CREATIS-INSA, Lyon	Rapporteur
Dr. BERNARD Monique, Directeur de recherche CNRS,CRMBM, Marseille	Examinateur
Dr. QUESSON Bruno, Directeur de recherche CNRS, CRCTB, Bordeaux	Examinateur

Titre: Imagerie par Résonance Magnétique (IRM) haute résolution du coeur pour la caractérisation du substrat arythmogène

---

Résumé: L'imagerie par résonance magnétique (IRM) cardiaque est la modalité clinique de référence pour caractériser le substrat anatomique à l'origine de pathologies cardiaques. En plus de sa haute valeur diagnostic liée à la multiplicité des contrastes qu'elle peut générer, l'IRM cardiaque présente un intérêt potentiel pour le suivi en temps réel des thérapies mini- ou non-invasives en imagerie interventionnelle. Cependant, la résolution spatiale actuelle des images en clinique reste limitée au mieux à 1 mm, ce qui est insuffisant pour fournir un diagnostic précis et estimer l'étendue de la lésion créée par radiofréquence (RF). En particulier, l'exploration de l'oreillette reste difficile du fait de la faible épaisseur du tissu atrial (2 à 5mm). Le rapport signal sur bruit (RSB) limité des antennes utilisées en clinique ainsi que la présence de mouvements respiratoires et cardiaques constituent les principaux verrous technologiques à lever pour augmenter la valeur diagnostic de l'IRM cardiaque.

Une première étude s'est concentrée sur l'augmentation du RSB en IRM et l'amélioration de la sélectivité spatiale au niveau du cœur. Un prototype d'antenne de surface en réception seule a été conçu et interfacé avec le scanner. Les expériences menées ont démontré qu'un gain de 30 en RSB pouvait être obtenu en utilisant une telle antenne de surface, permettant l'acquisition d'images à une résolution spatiale de 200 µm dans le plan, à champ clinique, sur échantillons ex vivo comme sur cœur battant.

Une deuxième étude s'est attachée au développement d'un algorithme pour la compensation du mouvement basé sur l'exploitation de micro-antennes intégrées à un cathéter. Une séquence d'acquisition qui combine une mesure 3D rapide ($\sim$ 27 ms) et précise (incertitude inférieure à 1 mm) de la position des micro-antennes entrelacée avec une acquisition radiale du k-space a été implémentée. Le tri rétrospectif des données brutes en fonction des positions des micro-antennes a permis de reconstruire des images de bonne qualité à partir de k-space fortement sous-échantillonnés à l'aide d'algorithmes non linéaires (compressed sensing, variation totale, nuFFT). Après validation sur un phantom mobile, décrivant un mouvement de translation linéaire et circulaire avec des paramètres réalistes (60-90 bpm, amplitude de 2cm), une évaluation in vivo a été réalisée sur cochon et mouton. Ceci a permis d'illustrer l'efficacité de la méthode et de la comparer à la méthode conventionnelle de synchronisation cardiaque et respiratoire.

Une étude préliminaire combinant l'imagerie avec l'antenne de surface locale et l'algorithme de compensation de mouvement a ensuite été menée. Les résultats obtenus in vivo montrent le potentiel d'une telle technique pour obtenir des images hautes résolution de la paroi ventriculaire (300 µm dans le plan), affranchies de tout mouvement.

Ces technologies étant destinées à une utilisation future chez l'homme, les aspects inhérents à l'insertion d'une antenne intravasculaire chez le patient ont été étudiés. Les dommages thermiques étant le principal risque associé aux dispositifs implantés, une méthode de thermométrie IRM alternant un module de déposition d'énergie ajustable avec l'acquisition d'images EPI a été implémentée pour quantifier l'évolution de la température dans les tissus environnant un fil implanté. Les expériences menées sur gel et cerveau humain ont démontré la possibilité de mesurer la température avec une précision de 0.2°C. Une telle précision est considérée suffisante pour évaluer la sécurité des dispositifs implantés.

Ce travail de thèse présente les premières étapes techniques vers une IRM cardiaque haute résolution sans mouvement. Les applications sont une meilleure définition du substrat pour un diagnostic amélioré et une meilleure caractérisation des lésions pendant les procédures d'intervention guidées par IRM.

Mots clés : coeur, antennes, compensation mouvement, thermométrie, imagerie par résonance magnétique

Title: High resolution MR imaging of the arrhythmogenic cardiac substrate

---

Abstract: Cardiovascular magnetic resonance (CMR) is the clinical imaging modality of reference for characterizing anatomical substrate of pathological hearts. In addition to its high diagnostic value resulting from versatile contrasts it can generate, CMR has also a potential interest in interventional imaging for guiding in real-time minimally or non-invasive therapies. However, current spatial resolution of MRI images in clinical scanners remains limited to 1 mm at best, which provides insufficient value for diagnosis and for precise visualization of atrial walls (2 to 5 mm thickness) or for characterizing thermal lesions during interventional procedures. Limited signal-to-noise ratio provided by large receiver coils, together with cardiac and respiratory motions are limiting factors that justify technical developments to increase the value of cardiac MRI. This thesis work aimed at proposing innovative solutions to alleviate the aforementioned challenges, through a combined development of dedicated hardware and software.

In order to increase the signal-to-noise ratio of MRI and improve spatial selectivity onto the heart, a receive-only surface coil prototype was designed and interfaced with the scanner. We demonstrate that with such a small coil, a gain in SNR of approximately 30 can be achieved and that good quality images with a spatial resolution of 200 µm in-plane can be obtained at clinical field both on ex vivo samples of fixed hearts and on beating hearts.

In a second part of the work, motion compensation techniques were investigated exploiting MR-compatible micro-coils embodied on a catheter. A home-made acquisition sequence was implemented, combining rapid (~ 27 ms) and precise (less than 1 mm uncertainty) 3D measurements of the coil position interleaved with acquisition of several radial k-space lines. Retrospective sorting of raw-data as a function of micro-coil positions allowed reconstruction of good quality images from highly under sampled k-spaces using nonlinear algorithms (compress sensing, total variation, nuFFT). Validation was first assessed on a mobile calibration phantom depicting linear and rotating trajectories with realistic parameters (60-90 bpm, 2 cm amplitude). Then, in vivo evaluation was performed in sheep and in pig to illustrate efficiency of the method and compare it to conventional synchronization with ECG and respiratory sensors.

In an attempt to combine high-resolution imaging with motion compensation technique, a preliminary study was conducted that combines imaging with our local surface coil and

catheter-based motion compensation using our implemented acquisition sequence and associated reconstruction algorithm. Results obtained in vivo shows the potential of such a technique for providing motion-free high resolved images of the ventricle wall at 300 µm in-plane spatial resolution.

These technologies being later intended for human use, safety aspects inherent to insertion of a MRI receiver coil inside the body were also investigated. Since thermal damage is the main risk associated with inserted devices, a MRI-thermometry technique that interleaves acquisition of several gradient echo EPI slices every second and an energy deposition module with adjustable parameters was implemented to quantify temperature evolution in tissue surrounding an implanted wire. Experiments in gel and in human brain demonstrated feasibility to measure temperature change with 0.2°C certainty. Such a precision was considered sufficient to evaluate device safety. The method could therefore be used to establish individualized safety levels for RF exposure in the presence of implanted device (such as an intravascular coil).

This thesis work presents the first technical steps toward high-resolution motion free CMR. Applications are better substrate definition for enhanced diagnosis and improved lesion characterization during MR-guided interventional procedures.

Keywords: heart, therapeutic ultrasounds, magnetic resonance imaging

Unité de recherche

LIRYC - L'Institut de Rythmologie et Modélisation Cardiaque.

Centre de Recherche Cardio-Thoracique de Bordeaux - INSERM U1045

Avenue du Haut Lévêque, 33600 Pessac

Résumés en français

Introduction

La plupart des techniques actuelles d'Imagerie par Résonance Magnétique (IRM) cardiaque en clinique (essentiellement 1.5 T et 3T) offrent des résolutions spatiales de l'ordre du millimètre. La caractérisation anatomique précise des tissus fins comme ceux de la paroi de l'oreillette (1 à 3 mm) reste donc difficile à mettre en œuvre. Pour s'affranchir de cette limitation, notre équipe ambitionne d'atteindre une résolution de 300 μm ou mieux, ce qui nécessite d'importants développements en instrumentation, techniques d'acquisition et de reconstruction d'image. Plusieurs groupes de recherche ont proposé des conceptions d'antennes intravasculaires pour imager plus finement des altérations de l'endocarde (lésions, infarctus) qui pourrait contribuer à l'initiation et l'entretien des arythmies cardiaques. En effet, une antenne intravasculaire amenée à proximité de la région à imager permet d'exploiter la sélectivité spatiale du détecteur pour limiter le champ de vue à la zone d'intérêt tout en bénéficiant également d'une sensibilité accrue permettant d'augmenter le rapport signal sur bruit.

L'utilisation de cathéters intra cavitaires est une pratique clinique courante en électrophysiologie pour diagnostiquer et traiter les arythmies cardiaques. Cependant, l'utilisation de l'IRM comme modalité peropératoire reste encore peu développée, notamment à cause des contraintes d'environnement magnétique et des risques associés à l'insertion d'un dispositif médical actif pouvant interférer avec l'IRM et conduire à des dommages tissulaires irréversibles pour le patient.

L'objectif de cette thèse est donc de développer l'imagerie haute résolution pour mieux caractériser le remodelage structurel du cœur par IRM.

Par ailleurs, le mouvement cardiaque est un challenge important pour réduire la présence d'artefacts dans les images reconstruites. Ce challenge est d'autant plus grand en imagerie haute résolution où la correction du mouvement doit être d'autant plus précise que la résolution spatiale est fine.

Pour lever ces verrous technologiques et obtenir des images très résolues et d'une grande qualité, nous avons développé une antenne locale de surface et implémenté une technique

d'acquisition particulière associée à des algorithmes de compensation de mouvement. Différentes méthodes de reconstruction d'image ont également été implémentées et testées à partir de données sous-échantillonnées, afin d'accélérer la durée d'acquisition des images. Ce projet impliquant le développement d'un dispositif médical devant à terme être inséré par voie endovasculaire, nous avons également proposé une méthode d'imagerie pour l'évaluation de la sécurité basée sur une technique de thermométrie rapide et volumique. Le manuscrit de thèse est subdivisé en trois chapitres.

Chapitre 2: Développement d'une antenne IRM pour l'imagerie haute résolution à champ clinique

Ne disposant pas de cathéter intégrant des capacités d'imagerie par IRM, nous avons développé un premier prototype d'antenne de surface en réception de 2 cm de diamètre. Pour répondre en partie à la problématique de sécurité liée à l'introduction d'un câble conducteur transportant un courant continu jusqu'au détecteur, nous avons intégré un système de découplage actif de l'antenne par voie optique, synchronisée avec l'émission RF des séquences IRM via un boitier d'interface. Ce dispositif a été comparé avec la technique conventionnelle basée sur un découplage par commande électrique.

Le gain en rapport signal-sur-bruit obtenu par ces deux antennes ainsi que leurs sélectivités spatiales ont été quantifiés sur Fantôme calibré. Cette approche exploitant un détecteur local permet de gagner un facteur 50 par rapport aux antennes extracorporelles, ce qui permet en théorie d'améliorer la résolution spatiale des images jusqu'à 300 μm. Aucun impact significatif du système de découplage n'a été observé, permettant de valider l'approche de découplage par voie optique.

Des expériences ex vivo sur cœurs isolés battant de cochon ont ensuite permis de confirmer la faisabilité d'obtenir des images de bonne qualité à une résolution de 200 μm. Des tests préliminaires sont ensuite été effectués in vivo à thorax ouvert sur un animal, afin de valider cette technique en présence de mouvements (cf chapitre suivant). Cette antenne a également été testée dans le cadre de la thermométrie IRM et permet soit d'améliorer la précision de la technique actuelle (environ facteur 5, à résolution identique), soit d'exploiter la grande sensibilité du détecteur pour améliorer la résolution spatiale de cartes de température (700 μm).

Dans la perspective du transfert vers le patient, un travail important sur le design et le choix

des composants doit être mené pour rendre intégrer le dispositif d'imagerie sur un cathéter flexible, avec une sonde déployable dans les cavités cardiaques.

Chapitre 3: Compensation du mouvement

Dans ce second chapitre, des méthodes de compensation de mouvements ont été implémentées, avec comme objectif de caractériser et compenser en 3D les déplacements locaux avec une précision analogue à celle de l'imagerie (300 μm). Les techniques conventionnelles exploitant des capteurs externes (électrodes ECG, ceintures respiratoires) ou IRM (échos de navigation positionnés sur le foie) sont jugées insuffisamment précises puisqu'elles ne reflètent qu'un mouvement relatif de l'organe et pas un mouvement local en 3D de la région à imager. De plus, le signal ECG enregistré est souvent déformé par les effets magnétohydrodynamiques et une commutation élevée des gradients des séquences IRM, ce qui complique la synchronisation de l'acquisition sur les oreillettes, en particulier en présence d'arythmie.

Nous avons choisi ici d'exploiter des micro-antennes intégrées à un cathéter compatible IRM dont nous disposions. Une séquence IRM particulière a été implémentée et intègre un module de suivi 3D du cathéter entrelacé avec la lecture de données dans le plan de fourier (acquisition radiale) d'une acquisition en écho de gradient rapide. Le schéma d'échantillonnage radial à angle d'or (GA) présente une robustesse intrinsèque au mouvement et est adapté au tri retrospectif des données. En combinant le suivi et l'acquisition radiale, nous avons également développé une méthode de reconstruction d'image qui acquiert en continu des données de l'espace réciproque et les trie en plusieurs ensembles de données sous-échantillonnées en fonction des positions en 3D du capteur.

Afin de combiner robustesse au mouvement et accélération du temps d'acquisition, tout en maintenant une qualité d'image acceptable, nous avons exploité des techniques de reconstruction d'image itératives basées sur un des algorithmes d'optimisation sur les données préalablement triées.

La méthode a été testée ex vivo et in vivo sur cœurs de mouton et de cochon, et a montré que l'incertitude sur la position était de l'ordre de 200 μm. Une étude préliminaire a ensuite été menée en combinant cette méthode d'imagerie avec le capteur présenté au chapitre précédent sur un thorax ouvert. L'antenne de surface a été placée au contact de l'endocarde du ventricule gauche et une image haute résolution (300 µm dans le plan) compensée en mouvement a pu

être obtenue. Des expériences supplémentaires doivent cependant être menées pour valider notre méthode, notamment pour imager l'oreillette. Les méthodes de reconstruction doivent également être optimisées davantage pour permettre une plus grande accélération du temps d'acquisition.

Chapitre 4: Evaluation de la sécurité des dispositifs implantés par thermométrie IRM

Ce dernier chapitre est consacré à l'évaluation de la sécurité liée à l'insertion d'un dispositif chez le patient. En effet, les ondes électromagnétiques émises lors d'une acquisition IRM peuvent se coupler avec le dispositif et générer des courants électriques dans ce dernier. Ce phénomène, appelé effet antenne, peut conduire à un échauffement excessif (pouvant conduire à des brulures irréversibles) avec des conséquences délétères pour le patient.

Pour évaluer les risques d'échauffement, plusieurs méthodes ont été proposées dans la littérature, la plupart exploitant des approches indirectes (cartographie du champ B1 émis, limitation de l'énergie émise par la séquence d'acquisition, simulations) ou invasives (capteurs de température ou de courant intégré au dispositif), alors que le paramètre pertinent pour la sécurité du patient est la mesure de l'échauffement tissulaire.

Notre équipe possède une expertise reconnue sur la thermométrie IRM et nous avons donc proposé une méthode pour mesurer les échauffements par IRM temps réel. Bien que des méthodes de quantification de l'échauffement par IRM aient déjà été proposées, elles ne permettent pas d'obtenir une bonne précision (incertitude inférieure à 1°C), une résolution temporelle suffisante (idéalement 1 mm ou mieux) et une couverture spatiale suffisante (imagerie volumétrique) pour caractériser précisément l'échauffement tissulaire autour du dispositif.

Nous avons adapté une méthode déjà développée par notre équipe (≪single-shot≫ Gradient Echo Echo Planar Imaging - EPI, 75 ms/coupe) en incorporant un module de déposition d'énergie (émission de plusieurs impulsions radiofréquences) entrelacé avec l'acquisition de plusieurs coupes IRM de manière répétitive. Les paramètres de ce module peuvent être réglés par l'utilisateur (énergie, durée et nombre d'impulsions) pour reproduire l'énergie émise par n'importe quelle autre séquence IRM. Cette séquence étant multi-coupes, elle rend possible la visualisation de la distribution spatiale de la température autour du dispositif implanté. La précision de la méthode a été mesurée à 0.2°C sur fantôme et sur le cerveau d'un volontaire

sain à 1.5T. Des mesures simultanées obtenues au contact d'un dispositif test inséré dans un gel ont permis de quantifier l'échauffement induit en fonction de l'énergie déposée par la séquence. Cette méthode a permis de quantifier les échauffements induits autour d'un câble de pacemaker inséré dans un gel, simulant la présence d'une sonde cassée et laissée à demeure (cas clinique).

Cette approche pourrait donc permettre de définir les niveaux maximaux d'exposition RF personnalisés (échauffement tissulaire < 2°C) en présence d'un dispositif implanté en début d'examen IRM, et donc d'améliorer la sécurité des examens IRM pour les patients porteurs de dispositifs implantés.

Conclusion et perspectives

L'imagerie haute résolution cardiaque à champ clinique (1.5T) représente un grand défi car elle se heurte à deux difficultés majeures : le manque de signal inhérent aux technologies d'antenne actuelles et le mouvement complexe et rapide du cœur. Au terme de cette thèse, nous avons ouvert de nouvelles perspectives pour améliorer significativement la résolution de l'IRM cardiaque sur une machine IRM de type clinique. A l'issu de nos développements, nous avons démontré la faisabilité d'imager avec une résolution spatiale de 200 μm dans le plan sur cœur battant. Ces travaux préliminaires devront être poursuivis pour développer un cathéter disposant d'une sonde d'imagerie déployable dans la cavité cardiaque. Cet obstacle semble accessible, notamment par l'utilisation des nouvelles technologies innovantes en impression 3D de composants et en flexibilité des matériaux. Les travaux sur l'instrumentation développés dans le cadre de cette thèses serviront de base pour concevoir un dispositif médical diagnostic (et éventuellement intégrant des capacités thérapeutiques) répondant aux besoins cliniques, en proposant des solutions techniques permettant de satisfaire aux contraintes de sécurité. Dans une deuxième étape, nous avons cherché une solution permettant l'accès à un descripteur 3D, local et rapide du mouvement. Notre choix s'est porté sur l'exploitation du signal de micro antennes intégrées à un cathéter existant et a montré une précision suffisante. L'information de position a été exploitée par un algorithme de compensation de mouvement et nous avons démontré la possibilité d'obtenir des images de bonne qualité en présence de mouvement. Un grand travail d'optimisation reste cependant a effectuer pour améliorer les méthodes de reconstructions itératives et permettre une acquisition plus rapide des images. Par ailleurs, le développement d'un réseau d'antenne permettant l'intégration de méthode d'imagerie parallèle

doit être menée en parallèle pour ouvrir de nouvelles perspectives d'acquisition/reconstruction. Dans cette étude, nous n'avons cependant pas évalué la possibilité d'obtenir des images avec différents contrastes, ce qui devra également être abordé par la suite. La combinaison de ces trois études a finalement permis de développer des outils et méthodes pour répondre aux challenges de l'imagerie cardiaque intravasculaire que sont le besoin de signal, le mouvement et la sécurité.

Remerciements

J'ai souvent pensé au jour où j'écrirais cette page. Ce moment représentait pour moi la concrétisation du manuscrit et avec lui le terme de mon expérience de thèse. Dans les moments plus difficiles, c'est en pensant aux prénoms inscrits ici que je retrouvais de l'énergie puisqu'il n'y a rien de plus réjouissant et motivant que le sentiment de reconnaissance.

Ces travaux de thèse ont été réalisés dans le cadre d'une collaboration entre l'IHU Liryc et l'entreprise Siemens Healthineers. En premier lieu, je souhaite exprimer toute ma gratitude envers l'ensemble des acteurs de ces deux entités qui m'ont octroyé leur confiance et permis d'évoluer dans un cadre propice, privilégié même je dois dire, pour mener à bien mes travaux de recherche. Je remercie ainsi chaleureusement l'entreprise Siemens Healthineers de m'avoir accompagnée et soutenue financièrement tout au long de ma thèse CIFRE. Grâce à son appui, j'ai pu bénéficier de conditions matérielles idéales et ai eu l'opportunité de présenter mes résultats dans des congrès nationaux comme internationaux. Un grand merci également à l'IHU Liryc, entité d'excellence à l'interface entre recherche et clinique, riche de sa diversité de profils, de m'avoir accueillie en son sein et de m'avoir offert un environnement chaleureux, stimulant et favorable aux échanges scientifiques.

Je souhaite exprimer toute ma reconnaissance envers mon directeur de thèse, Bruno Quesson, sans qui ce travail de recherche n'aurait pas pu voir le jour. Ses idées originales ont permis l'élaboration d'un sujet de thèse audacieux, aux multiples challenges et ancré dans les enjeux biomédicaux actuels. Sa rigueur et sa franchise ont permis des échanges constructifs pour mener à bien mon doctorat. Je tiens sincèrement à le remercier pour ses remarques avisées et son entêtement dans la recherche de perfection qui m'ont permis de muscler mon esprit critique. Merci de m'avoir fait découvrir ce monde fascinant de l'IRM et de m'avoir donné l'occasion, à plusieurs reprises de présenter mes travaux devant la communauté internationale.

Je tiens à remercier mes deux co-bureaux, Pierre Bour et Valéry Ozenne qui m'ont vue évoluer dans mes recherches, ont suivi mes doutes et interrogations. Je pense vous avoir intrigués

lorsque je m'aventurais sur des chemins plus incertains et alambiqués mais vous avez su garder l'œil bienveillant quant à mes tâtonnements du début et à force d'y croire, cela a fonctionné. Vous avez été pour moi de véritables bibliographies vivantes, complémentaires de surcroît : l'un maniant à la perfection l'art des séquences, l'autre la manière des reconstructions. J'ai beaucoup appris à vos côtés et en cela je tiens à vous témoigner ma gratitude pour avoir toujours su répondre présent dans l'expérimentation comme dans la programmation.

Je souhaite témoigner ma reconnaissance aux filles, amies, du "bureau d'en face", Dounia El Hamrani et Julie Magat. Dounia, nous avions ce canal de communication privilégié inter-couloir qui faisait qu'en un regard, un murmure de chanson et la liaison était établit, ce canal va me manquer. Vous avez été pour moi de véritables modèles de chercheuses acharnées et douées. Dans ce contexte difficile de pandémie qui a marquée l'année 2020, la rédaction de thèse a été une sacrée épreuve et si je l'ai surmontée, c'est aussi grâce à vos encouragements, votre humour et votre bienveillance quotidienne. Merci de m'avoir imprégnée de votre passion débordante pour l'IRM et de votre pugnacité à toutes épreuves face aux tumultes de la recherche.

Après le "bureau d'en face", ma pensée va à ma co-équipière de thèse, Cindy Michel, avec qui nous avons partagé bien plus que le mur entre nos deux bureaux. A l'instar du film "un peu beaucoup aveuglément", c'est à travers cette cloison que nous avons parfois communiqué lorsque chacune, tard le soir nous restions rivées à nos écrans et qu'il suffisait d'un petit bruit de la part de l'autre pour sentir sa présence de l'autre côté. Je tiens à la remercier pour ses mots justes, ses phrases originales, ses expressions souvent "lunaires" (ce mot il t'est associé maintenant dans ma tête), son humour décapant et sa simple présence qui rendait mes journées de fin de thèse beaucoup plus agréables.

Ma gratitude va aussi à Lisa Gottlieb, arrivée un mois avant moi à l'IHU, il n'a pas fallu longtemps pour que nous nous apprécions et voilà maintenant 4 ans que nous partageons nos coups de sang, nos coups de cœur (littéraires et musicaux), nos joies et nos petites tristesses. La passion et les convictions qui t'animent te donne ce caractère et ce charme qu'il fait bon de côtoyer.

Bien évidemment une pensée affectueuse pour les membres de mon équipe, l'équipe imagerie: Maxime, Aurélien, Jérôme, Quentin, Manon, Kylian et Mathieu. Maxime, je me souviendrai toujours de ce cathéter avec lequel, sans le vouloir bien évidemment, nous avions manqué de rejouer la "Belle et le Clochard". Un grand merci à Aurélien Bustin et Aurélien Trottier (du RMSB) de m'avoir partagé leur expertise en reconstruction itérative. Aurélien Trottier, tu as été d'une grande aide dans la découverte de l'environnement BART, Aurélien Bustin je te remercie pour les discussions et ton aide avec la méthode "Patch-based".

Je tiens à remercier Fanny Vaillant et Emma Abell qui m'ont toujours fascinée dans leur aisance à faire "battre des cœurs". Leur grande expertise dans le cœur battant a permis d'incroyables expériences, souvent tardives mais porteuses puisqu'elles nous ont valu un "suma cum laude" à l'ISMRM.

Au cours de ce doctorat, j'ai eu la chance de croiser la route d'Isabelle Saniour, post-doc à l'IR4M (devenu maintenant Biomaps). Entre nous (les concepteurs d'antennes comprendront ce jeu de mot...), ça a tout de suite matché ! Je lui adresse mes plus chaleureux remerciements pour l'aide précieuse qu'elle m'a apportée lors du développement d'antenne et sans qui le découplage optique n'aurait pas pu être raconté ici, dans cette thèse. Je partage avec Isabelle également la fierté du "suma cum laude". Au-delà de sa grande expertise scientifique c'est pour son extrême gentillesse et sa patience que je lui suis reconnaissante. Nos nombreux échanges scientifiques ont été le lieu d'une amitié grandissante au fil des années et je suis heureuse des liens que nous avons tissés. Bien évidemment, notre "team coils" ne serait pas au complet sans Lena Nohava et Sajad Hossein Nezhadian avec qui les virées Parisiennes ont été de sacrées aventures. Je n'oublierai jamais notre expédition à "Niort" qui s'est avéré être finalement... New York.

Je tiens à remercier la Professeure Marie Poirier-Quinot pour la collaboration qu'elle a permis entre nos deux laboratoires IHU Liryc et biomaps. Son humour et son dynamisme ont pimenté et enjolivé les échanges. Je lui suis reconnaissante d'avoir partagé, avec Isabelle, son savoir sur l'art des antennes et de m'avoir accueillie une semaine en février 2019 pour réaliser le découplage optique.

Je dois également à Jacques Felblinger, directeur du Laboratoire IADI et Sara Aissani, ancienn-ement post-Doc dans ce laboratoire ma découverte des antennes IRM. Merci à eux de m'avoir ouvert leur porte une semaine en 2017 et de m'avoir initiée à la conception d'antennes.

Je souhaite remercier vivement Loïc Durand et Ruben Yoyotte, les protagonistes du service informatiques à l'IHU Liryc pour leur disponibilité et réactivité. Toujours prêts à rendre service au moindre problème de licence, de serveur... voire d'adaptateur USB/ethernet! Plus que leur temps, c'est leur bonne humeur sans faille qu'ils donnent ! Je n'oublie pas les personnes de l'IHU avec qui j'ai eu le plaisir d'échanger : merci à Olivier Bernus, Rick Walton, Laura Bear, Jason Bayer, Sylvain Caubet (et ses fantastiques set-up), Jairo Padilla, Nestor Pallarès, Peter Langfield, Yingjing Feng, Virginie Loyer (pour ton aide très précieuse lors des expérimentations), Alice Récalde, Philippe Pasdois, Anne-France Cotentin, Agnès Chenu, Amanda Belle-isle qui ne manque jamais de fantaisie et conversation, sans oublier Delphine Ge qui a toujours su répondre présente dès que je la sollicitais.

Un grand merci également à mes rapporteurs de thèse : Matthias Stuber et Olivier Beuf qui ont accepté avec enthousiasme d'examiner mes travaux de thèse. Leurs appréciations m'ont beaucoup touchée. Merci également à Monique Bernard d'avoir présidé le jury de thèse et à Marie Poirier-Quinot de s'être déplacée, dans ce contexte particulier de crise sanitaire, pour assister à la soutenance.

Je souhaite exprimer toute ma gratitude envers Matthieu Lepetit-coiffe et Christian Bert qui m'ont accordé leur confiance et m'ont encadrée au sein de Siemens, merci pour votre disponibilité et encouragements à tous les deux. Merci également à Wadie Ben Hassen de m'avoir accompagnée durant les deux premières années de ma thèse et à Solenn Toupin, clinical scientist Siemens Bordeaux d'avoir su si bien prendre le relais et de m'avoir suivie pendant ma dernière année. Je remercie également Alexis Vaussy, que je connais depuis l'école d'ingénieur et qui a su me mettre sur le bon chemin de cette thèse, un soir de remise de diplôme. Enfin, je tiens à exprimer ma reconnaissance à Cédric Pasquier pour avoir pris le temps d'échanger avec moi lorsque j'étais en fin de thèse et pour ses précieux conseils en sécurité IRM.

Cette thèse, je la partage avec mes amis qui tout au long de l'aventure m'ont apporté leur soutien et leur bonne humeur. A toi Norine, qui de marraine en école d'ingénieurs est devenue ma meilleure amie (sorte de marraine de vie ?). Merci pour tes multiples colis surprise qui ont su à chaque fois me redonner le sourire et tes nombreuses marques d'affection qui m'ont aidée à traverser les moments difficiles! Delphine, comme tu le dis si bien, notre rencontre n'a tenu qu'à un fil (de textile..., pensées d'ailleurs pour cette entremetteuse de machine à laver) et nous voilà maintenant avec 5 ans de péripéties derrière nous et bien d'autres à venir. Rodolphe, mon petit Torontois maintenant, mes meilleurs souvenir d'école d'ingé ils sont avec toi ! Pierre, tu as marqué mon année 2016 et plus que l'open space en stage c'est ton open mind que tu as partagé avec moi, merci pour tous ces fous rires. Merci à Adrien et Marie qui ont su m'accueillir dans cette très belle ville qu'est Bordeaux. Une pensée à Marion et Louise, mes deux canailles canadiennes qui m'ont ouvert leur Montréal chéri.

Enfin ces dernières lignes de remerciements, je les adresse à ma maman, Françoise, qui depuis toutes ces années s'est dévouée pour me donner les moyens de réussir dans mes études comme dans ma vie et ce, malgré les difficultés. A deux nous avons su surmonter beaucoup d'épreuves et c'est de là que je puise cette énergie, cette force de vie. Merci pour tout l'amour et la douceur que tu m'as prodigués, merci pour toutes ces fois où tu as su me redonner du courage.

Contents

ABBREVIATIONS

General

2D	Two Dimensional
3D	Three Dimensional
RF	Radiofrequency

Heart

ECG	Electrocardiogram
EP	Electro-Physiology
CVDs	Cardiovascular Diseases
LA	Left Atrium
LV	Left Ventricle
RA	Right Atrium
RV	Right Ventricle

MR-imaging

EPI	Echo Planar Imaging
FOV	Field Of View
GRAPPA	Generalized Autocalibrating Partially Parallel Acquisitions
MRI	Magnetic Resonance Imaging
MRTI	Magnetic Resonance Temperature Imaging
PRFS	Proton Resonance Frequency Shift
GE-EPI	Single shot Gradient Echo Echo-Planar Imaging sequence
TE	Echo Time
TR	Repetition Time
FA	Flip Angle

Safety

SAR	Specific Absorption Rate
B_{1+rms}	$B_{1+\ root}$ mean square

Chapter 1

General Introduction

1.1. The heart

1.1.1. Anatomy

The heart is composed of four distinct chambers with muscular walls of different thicknesses (Figure 1-1). The left atrium (LA) and right atrium (RA) are small, thin-walled chambers (thickness ranging from 1 to 3 mm [1] located just above the left ventricle (LV) and right ventricle (RV), respectively. The ventricles are larger thick-walled chambers (thickness ranging from 8 to 12 mm) The RA collects the venous blood that is pumped into the RV and then transferred to the lungs through the pulmonary arteries. The returning blood from the lungs enters the LA before being pumped to the LV and then expelled in the aorta to supply the body with oxygen-rich blood. Between LA-RA and LA-LV chambers, two valves (tricuspid and mitral valves) act as mechanical barriers activated by difference of pressure between atria and ventricles during the contraction. Two other valves are

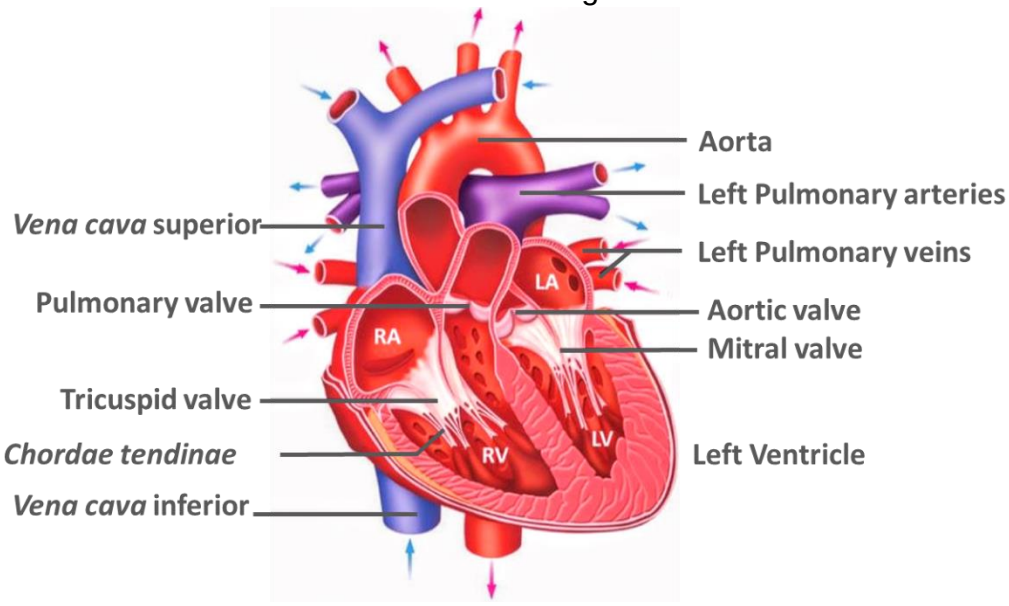

Figure 1-1: Heart Anatomy

located at the beginning of the aorta (aortic valve) and pulmonary artery (pulmonary valve) to ensure correct blood transfer toward the arteries and lungs, respectively.

1.1.2. Cardiac electrophysiology

The cardiac mechanical activity is controlled by an electrical conduction system that coordinates the contraction of the various chambers of the heart. The normal activation sequence of the myocardium is described in Figure 1-2. The electrical activity is recorded with an electrocardiogram (ECG) and each wave of the ECG corresponds to a certain event in the cardiac cycle. The conduction is initiated by an autonomous electrical stimulus generated by the sinoatrial node (SA), which spreads a depolarization wave over the atrium to the atrioventricular node (AVN). This event corresponds to the P-wave on the ECG. The electrical impulse then continues down into the ventricles via the conduction pathway the His bundle. The His bundle divides into right and left pathways, called bundle branches, to stimulate the right and left ventricles (QRS-complex) through the Purkinje network

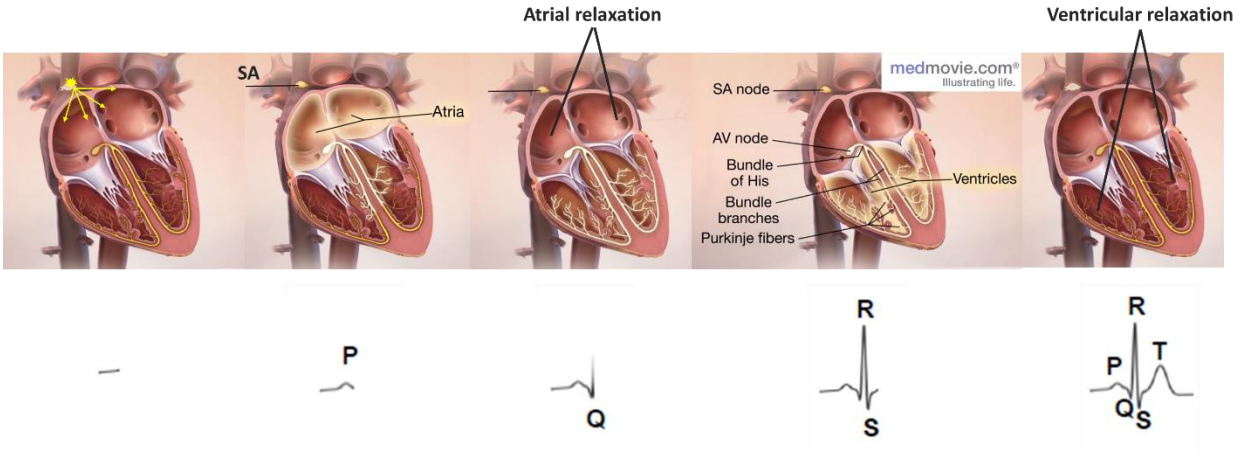

Figure 1-2: Electrical activity of the healthy heart. Each wave of the ECG corresponds to a certain event of the cardiac electrical cycle. (Modified from https://medmovie.com and [27])

1.1.3. Motion

The contraction of the heart consists of several major components that occur almost simultaneously: a shortening of both the left and right ventricles (LV and RV) in the long axis direction, a circumferential shortening of the ventricles and wall thickening, and a “wringing”

motion of the LV, which consists of a clockwise rotation at its base and a simultaneous counterclockwise rotation at its apex [2].

A healthy heart beats in a range of frequencies from 50 to 100 times per minutes. The maximum velocity of the left ventricle during a cycle was estimated to be 140 ± 40 mm/s (longitudinal velocity) and a 51 ± 18 mm/s (radial velocity)[2] . This is normally the fastest motion that MRI has to account for. The mean maximum of cardiac motion was found to be 10.2 ± 2.7 mm (min = 5.5 mm, max = 16.9 mm), estimated from EAM data of 27 patients undergoing clinical LV mapping) [3].

The respiratory motion frequency ranges from 12 to 15 breathing per minutes. This motion directly affects thoracic and abdominal motion. Breathing induces predominantly a translation of the heart in the head-feet with a mean maximum amplitude estimated to 8.8 ± 2.3 mm (min = 4.3, max = 14.8 mm) [3].

1.2. Cardiac arrhythmia

In healthy subjects, the electrical conduction pathway is well organized and regular. However, several heart diseases can modify the propagation of the electrical impulse, altering the capacity of the heart to pump blood to the rest of the body.

Cardiovascular disease (CVD) is the first cause of mortality in the world and is responsible for 16% of the world's total deaths. Since 2000, the largest increase in deaths has been for this disease, rising by more than 2 million to 8.9 million deaths in 2019. Each year CVD causes 3.9 million deaths in Europe and over 1.8 million deaths in the European Union (EU) [4]. In 2016, 17.9 million people died from cardiovascular disease, i.e. 31% of deaths worldwide (180,000 deaths in France (French society of cardiology)), ahead of cancer (8.2 million) and diabetes (1.5 million). By 2030, cardiovascular disease could account for more than 23 million deaths worldwide [5]. The American Heart Association predicted that by 2030, upwards of 40 percent of the U.S population would suffer from some form of CVD. With the ageing of the population, the economic burden related to these diseases increases and weighs more and more on the economic constraints of public health systems. In 2017, overall CVD was estimated to cost the EU economy €210 billion a year [4].

Amongst cardiovascular diseases, **cardiac electrical diseases** represent a significant burden for patients (high mortality, reduced quality of life) and for the health system. **Atrial fibrillation** (AF) accounts for 20% of CVDs [6].

1.2.1. Atrial Fibrillation

AF is the most common sustained arrhythmia in humans [7], causing increasing number of complications and deaths. Overall, 20-30% of all strokes are caused by AF [8]. The ischemic strokes seen in association with the arrhythmia are more often disabling or fatal. In addition, AF is associated with a 3-fold higher risk of heart failure, 2 to 3 times higher likelihood of hospitalization and twice the mortality risk and is projected to affect up to 16 million people by 2050 [9]. In France, it is estimated that around 300,000 people are affected by AF (Federation Française de Cardiologie).

1.2.2. Ventricular tachycardia

Ventricular tachycardia (VT) and ventricular fibrillation cause most cases of sudden cardiac death with an estimated rate of 300,000 deaths each year in the United States. This accounts for approximately half of the deaths related to cardiac causes [10]. VT is a heart rhythm disorder (arrhythmia) caused by abnormal electrical signals in the ventricles. While a healthy heart normally beats about 60 to 100 times a minute at rest, in ventricular tachycardia, the heartbeats faster than normal, usually 100 or more beats a minute. VT occurs most commonly in patients with a history of myocardial infarction.

1.2.3. Structural correlate of AF and VT

AF was long thought to be a merely functional disorder that was not characterized by anatomical changes [11]. However, evolution of mapping and imaging techniques have led to the identification of atrial sites involved in initiation of AF, such as
in pulmonary veins in (90% of cases) [12]. This triggered the interest in understanding the pathogenesis of AF and led to more studies to elucidate the underlying substrate and the progressive histologic changes that occur.

Whatever the initial cause and triggers, AF induces alterations in atrial electrical properties. This process, called electrical remodeling comprises alterations in ion channel function yielding to changes in action potential duration and conduction velocity. However, beyond electrical remodeling, recent studies have evidenced the existence of alteration in atria structure. In AF, cardiomyocytes undergo dramatic structural changes including cellular hypertrophy, disintegration of the contractile apparatus [13]. In addition, atrial myocytes show signs of degeneration and apoptosis. All these studies suggested the existence of a second factor in the pathogenesis of AF that is **structural remodeling** [13]–[15]. **Figure *1-3***: Masson's trichome staining of atrial tissue samples, 2µm thick, show that the amount of fibrosis (blue) increases with AF burden in patients (Hansen et al., 2017, modified from Platonov et al 2011 [12]) shows example of the structural alteration (fibrosis extent) of atrial tissues collected in patients without history of AF, with paroxysmal AF and with permanent AF.

These alterations may both favor the occurrence of "triggers" for AF that initiate the arrhythmia and enhance the formation of a "**substrate for AF**" that promotes its perpetuation [16]. In its persistent form, AF is thought to be triggered by focal sources of automatic discharge and maintained by reentrant activities organizing within the atrial tissue, the so-called rotors, sustaining high-frequency activity [17]. These focal sources may be unique or multiples. Recently, the localized driver hypothesis of AF has gained momentum and it has been shown that focal and rotational arrhythmogenic sources locating in the left atrial (LA) body outside the pulmonary veins (PV) were also playing an important role in the perpetuation of persistent AF [18]. Additional studies have suggested that atrial tissue fibrosis is a major determinant of the progression of AF [19], [20]. Atrial fibrosis may lead to disruption of normal electric conduction and establishment of reentry circuits and thereby contribute to an increased susceptibility to and maintenance of AF. The extent of fibrosis and extracellular matrix expansion determined histologically has been shown to correlate with persistence of AF. Platonov et al. [14] provided histologic evidence of a robust association between extent of structural changes in left atrial walls and major atrial conduction pathways with AF history. Patients with paroxysmal AF had 2 to 3 times greater fibrosis than patients without AF history. [14]

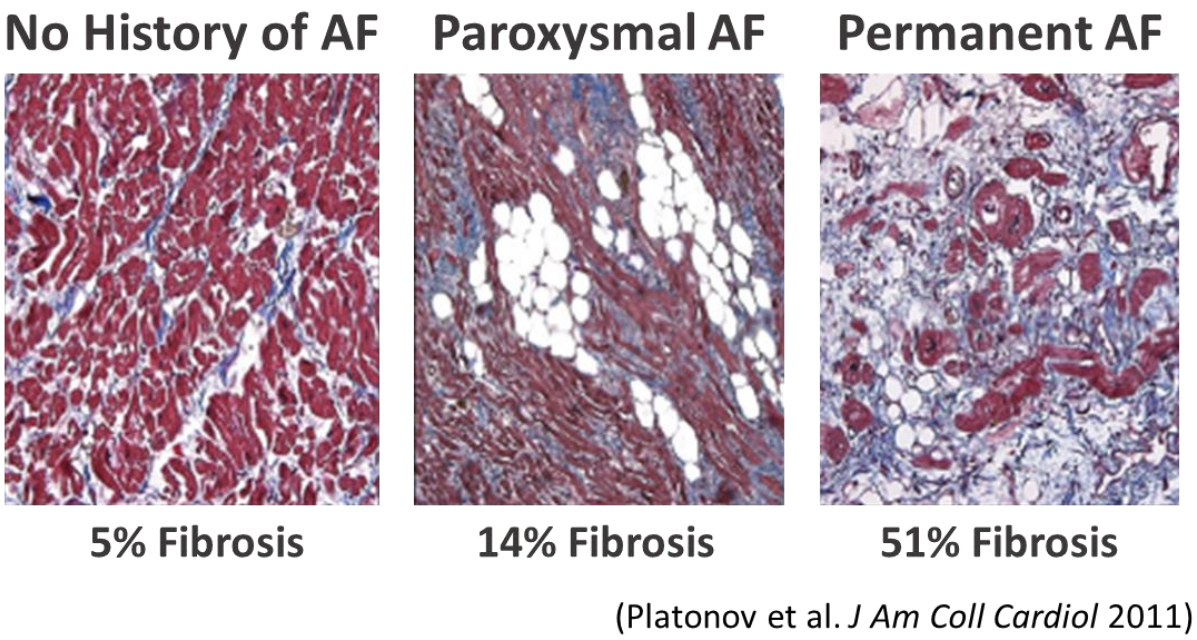

Figure 1-3: Masson's trichome staining of atrial tissue samples, 2µm thick, show that the amount of fibrosis (blue) increases with AF burden in patients (Hansen et al., 2017, modified from Platonov et al 2011 [12])

Regarding VT, scar-related sustained monomorphic VT is a common arrhythmia after myocardial infarction. Main mechanism of VT has been demonstrated to be reentry circuits existing mainly in or adjacent to scar border zones (BZ) [21]. Indeed, several studies supported the concept that reentry occurred via isolated bundles of surviving myocytes within the infarct and the larger sub-endocardial muscle mass [22]. Dense fibrosis with minimal surviving bundles sets up the environment for unidirectional block and directs the arrhythmic circuit. Viable myocytes bundles along the infarct BZ and within the infarct core are also involved and form the slow conduction central circuit zones necessary for VT maintenance. With an initiating factor, the reentry cycle therefore starts, passes through slow conduction channels and completes the circuit around the dense scar. Additional studies suggested that the degree of scar transmurality and proximity to the scar core were indicators of arrhythmogenic substrates in patients with VT and that central pathway sites tended to exist within relatively dense and transmural scar. Critical sites for maintenance of VT have been confined to areas of the scar with > 75% transmurality and in core-BZ transition sites [23].

Despite the conflicting results found in the literature, several studies agree that both dense scars and infarct BZ contribute to substrate for scar-related VTs. Example of ex-vivo, high-resolution VT reentry isthmus is given in Figure 1-4. It is characterized by a small volume of normal myocardium bound by scar tissue at the infarct BZ or over the infarct.

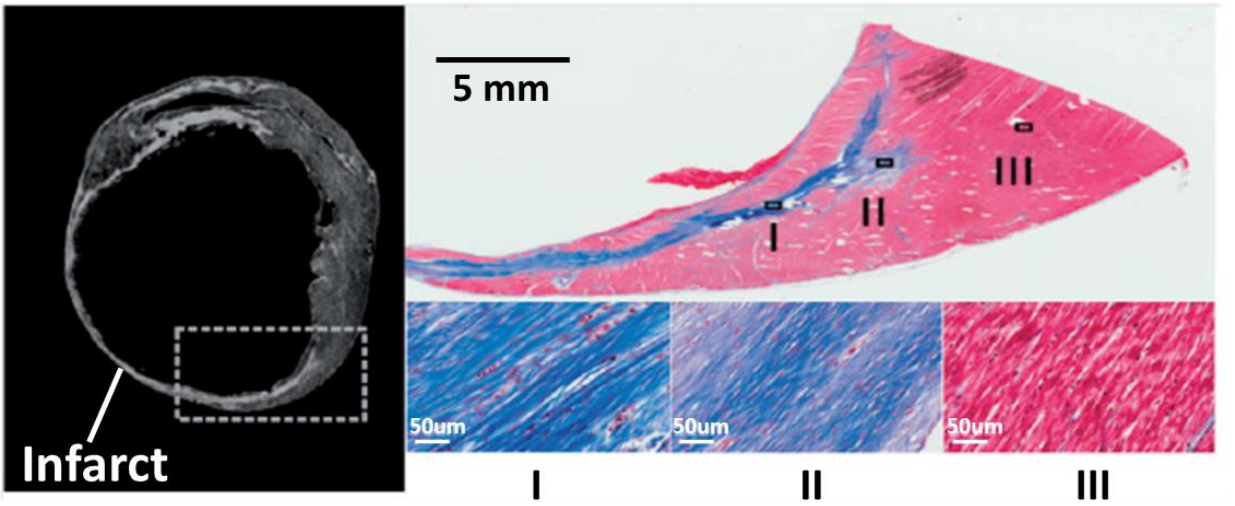

(Mukherjee et al. *Europace* 2018 reproduced from Pashakhanloo et al. *J Cardiovasc Magn Reson* 2017)

Figure 1-4: *Ex vivo* MRI and histology in a section of infarcted wall using Trichome staining [Pashakhanloo et al., 2017]. Left- A slice of LGE image delineating the aera of hyper-enhanced infarct with a thin rim of normal myocardium at the endocardial border. Top right- Masson's trichome stainin histology of the region framed in left panel. Bottom-right- 40 x magnification of the regions I, II and II selected in the infarct area on the top right panel. Blue represents collagenous scar whilst pink represents normal myocardial tissue in non-infarcted regions.

While fundamental mechanisms underlying AF have long been debated, it is now admitted electrical, contractile and structural remodeling are each important synergistic contributors to the AF substrate and that fibrosis is a hallmark of arrhythmogenic structural remodeling. Concerning VT, it has been evidenced that structural changes due to myocardial infarcts become the substrate for reentrant VT. Therefore, a thorough understanding of atrial and ventricular structure and function could lead to improvements in the ability to predict the risk of developing arrhythmia and the response to treatments in patients with this arrhythmia. However, assessment of structure and function of the atria as well as the ventricle is often limited by a lack of suitable methods for making these measurements,

especially due to the insufficient spatial resolution required to image myocardium wall in vivo.

1.2.4. Treatment of arrhythmia

Treatments for arrhythmia include medicines to control the heart rate and reduce the risk of stroke, and procedures such as cardioversion to restore normal heart rhythm. In patients presenting with prior myocardial infarction, a first approach consists in administration of antiarrhythmic drugs associated with the implantation of a cardioverter-defibrillator (ICD). Despite a high success rate of effective electrical cardioversion (70% to 90%), less than half of the patients remained in sinus rhythm after one year. The high recurrence rate and associated morbidity and mortality of AF and VT as well as the ineffectiveness and side effects of anti-arrhythmic drugs have resulted in efforts to develop new management strategies.

Radiofrequency (RF) catheter ablation has emerged as a promising management strategy and can reduce recurrences of VT and delay the incidence of implantable cardioverter defibrillator therapy in patients with both ischemic cardiomyopathy and non- ischemic cardiomyopathy [23]. AF is also amenable to catheter ablation [22]. Indeed, since the seminal observation of pulmonary vein triggers of clinical AF, ablation has rapidly become the first-line therapy for the management of symptomatic AF. Approximately 110,000 ablations are performed in the US and Europe per year [24]. This therapy is most often performed for maintenance of sinus rhythm in patients with symptomatic, drug-refractory paroxysmal or persistent AF or as an initial rhythm control strategy in lieu of anti-arrhythmic drug therapy in patients with paroxysmal AF.

Curing AF or VT through catheter ablation (CA) is based on the elimination of the initiating triggers and/or the maintaining substrate [25]. Once the trigger site is identified, an ablation catheter is positioned at this location and RF energy is applied at the tip of the catheter to induce a necrosis of this targeted cardiac tissue (Figure 1-5). Critical sites are thus electrically isolated or cauterized to restore a normal conduction. This surgical procedure is performed in electrophysiology (EP) laboratory where both diagnosis and ablation are

achieved. Catheters are usually inserted through the femoral vein, under X-ray guidance, and navigated until the heart.

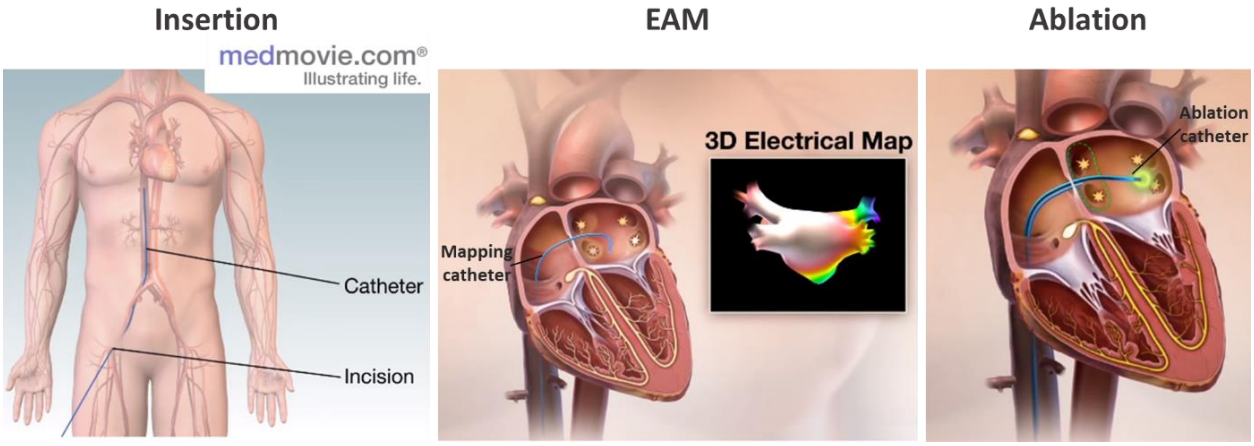

Figure 1-5: Cardiac catheterization. The catheter is inserted through the femoral vein via a small incision made in the patient's upper thigh and carefully guide through the blood vessels until it is inside the heart. Prior to ablation procedure, the standard approach uses electro-anatomical mapping (EAM). This procedure uses electrically sensitive catheter to map the electrical activity in the chamber of the heart and map it on a 3D model of the heart's chambers. The map informs the surgeon which sites to ablate. These sites are destroyed using an ablation catheter that delivers energy to scar the problematic areas. (Modified from https://medmovie.com)

Prior to ablation, a standard approach uses electro-anatomical mapping (EAM) and electrogram-defined surrogates of abnormal myocardium to target the regions potentially capable of sustaining re-entry. During EAM, a catheter-based mapping is performed where intra-cardiac electrograms and catheter tip location are recorded for various point location in the LV. A 3D shell representing the LV surface, color coded with electrogram characteristics is then 3D rendered on a dedicated navigation platform and used for the guidance of the ablation procedure. EAM allows identification of the core scar area and heterogeneous tissues [3].

1.2.5. Challenges of catheter ablation: toward interventional MRI

The increased efficacy of catheter ablation over anti-arrhythmic drug therapy to maintain sinus rhythm has been demonstrated in several studies [26]. Unfortunately, a significant recurrence rate of arrhythmia is observed: up to 30% of the patients for AF and 37% for VT require a repeat ablation [27].

Successful ablation requires the correct identification of underlying critical arrhythmogenic substrates on a patient-by-patient basis. Additional difficulty comes from the fact that some types of scar may be more arrhythmogenic than others: for example, as aforementioned, the critical isthmus of the VT circuit is often located within the scar or scar border zones (BZ) which remains complex to identify. In addition, recent clinical studies have suggested that AF can be driven from localized sources outside the pulmonary veins, which are heterogeneous and patient specific.

In the commonly used technique of EAM, substrates are identified indirectly, by collecting local voltage amplitudes as a surrogate of the state of nearby myocardium. There are several limitations, however, which may account for the modest long-term success rates of ablation targeting EAM-defined arrhythmia substrate in the setting of complex arrhythmias. [23]. This method indeed offers a limited information on the tissue viability due to its lack of sensitivity for scar substrates deep to the surface being mapped. Bipolar voltage mapping typically has a limited field of view and may miss the intramural or epicardial substrate. In patients with non-ischemic cardiomyopathy, the substrate is often deep to the surface and difficult to identify with surface voltage mapping. Hence, if clinical mapping techniques have aided in the search of AF drivers or VT substrates, it however has necessarily been limited in clinical use by low-electrode spatial resolution as well as surface only recordings, which may miss or misinterpret the complex 3D geometry of scar [22], [23].

Conversely, **cardiovascular magnetic resonance** (CMR) has the ability to characterize cardiac anatomy and function and therefore can help visualize myocardial scar, the most common substrate for reentrant arrhythmias. MRI can therefore play a major role in the optimization of ablation procedure by integrating pre-procedural scar segmentation into EAM system. Recently, several centers have integrated anatomical scar data from MRI into the EAM navigation system during catheter ablation to complement the functional electrophysiological assessment and facilitate ablation procedure for VT. However, the fusion of voltage map and MRI data invariably result in registration errors [23]. Cardiac and respiratory motion are additional difficulty that could lead to discrepancies between structural data and electrical substrate [3].

Real-time MRI guided electrophysiology offers potential to overcome the limitations of image integration while offering the possibility of visualizing infarcted, ischemic and arrhythmogenic tissue. Over the past two decades, interventional MRI has gained momentum for cardiac interventions and has yielded to development of MR-conditional devices and imaging techniques such as active catheter tracking and robust tools for real-time lesion assessment [28]–[30]. With emergence of interventional MRI, **diagnostic cardiac catheterization** has become valuable to target focal pathology and offer data about structure and pathophysiology of the underlying cardiac lesion.

1.3. Current CMR techniques for tissue characterization

Cardiovascular magnetic resonance has developed over several decades from an ancillary research tool to a clinically imaging modality of reference for in vivo tissue characterization. This section briefly introduces the current techniques used in clinic to assess the myocardial viability. The latter is a non-exhaustive list and does not pretend to cover all the available techniques.

1.3.1. Late gadolinium enhancement

In cardiovascular MRI, late gadolinium enhancement (LGE) has become the cornerstone for quantification and visualization of the extent of scar tissue. It is widely used in clinical routine to detect and quantify infarcted ventricular myocardium as well as localized myocardial scarring in a variety of cardiomyopathies [20]. However, current clinical cardiac DE-MRI has only been able to achieve ~1 mm^3 resolution even with state-of-the-art 3-T systems [9]. This limited spatial resolution prevents the precise characterization of fibrosis in thin structures, such as the atrial wall. The left atrial wall thickness ranges from 0.4 to 3.0 mm in patients with AF (mean thickness 1.7 ± 0.3 mm) [1], which therefore require a spatial submillimeter resolution at least to be accurately imaged. With the common clinical 2D DE-MR resolution of 1.4 x 1.9 x 6-8 mm [31], the entire thickness of the atrial wall may therefore be seen by only 1 to 2 pixels. Also, adjacent structure enhancement (such as the valve structure and aortic wall enhancement) on LGE imaging must be distinguished from left atrial myocardial enhancement. Regarding VT, the critical sites involved in VT circuits such as conducting channels are difficult to detect by the current resolution of CMR.

Moreover, it has been supported that obstructive patchy or interstitial arrhythmogenic fibrotic strands could be as small as 200 µm across, which would inevitably have its high signal averaged with surrounding myocyte (partial volume effect), missing the information [9].

The recent growing interest in imaging left atrial fibrosis has led to the development of novel three-dimensional (3D) whole-heart high-resolution LGE (HR-LGE) sequences, which allows small scars that were invisible with conventional LGE to be detectable. The smaller voxels of HR-LGE offer a better characterization of the scar complexity, especially the conducting channels [32]. Spatial resolution reported in literature are 1.4 mm isotropic at 3T [33] and 1.5 x 1.5 x 2.5 mm at 1.5T [18]. Some studies reported the initial feasibility of atrial LGE [34], [35]. However, in both studies, voxel size was 1.3 x 1.3 x 5 mm^3 [Peters et al, 2007] and 1.25 x 1.25 x 2.5 $mm^{3,}$ which is the same order of magnitude than the atrial wall thickness. Of note, HR-LGE offers an improved spatial resolution at the expense of an extended acquisition time (10 min in average), which does not make it compatible with most clinical workflows.

1.3.2. T1 and T2 mapping

Parametric mapping techniques provide a non-invasive tool for quantifying tissue alterations in myocardial diseases. T1 mapping allows for a direct myocardial signal quantification according to myocardium's longitudinal relaxation time. To date, myocardial T1 mapping has been used merely for tissue quantification of the left ventricular myocardium. Recently, Luetkens et al [36] investigated the pre-procedural value of native T1 mapping for the prediction of poor response to ablation therapy. Spatial resolution was 2.0 x 2.0 x 8.0 mm^3. They reported that T1 relaxation time was significantly increased in patients with recurrence of AF compared to patients without recurrence. They therefore showed that pre-procedural T1 mapping seemed to be a valuable tool for prediction of poor response to catheter ablation therapy. However, the limited spatial resolution may have led to inaccuracy in the CMR quantitative value, due to partial volume effect.

Other commonly used technique is based on T2 mapping. T2 mapping has emerged to directly quantify local myocardial inflammation and edema and can help for differentiating acute myocarditis from recent-onset heart failure. The spatial resolution is confined to ~2

mm in plane spatial resolution and 6 mm slice thickness [37], which precludes from thin structures exploration such as atrium wall.

Despite advances in LGE CMR technology and T1/T2 mapping over the past decade, myocardium imaging raises several technical limitations, including motion blurring, flow artifacts and limited image resolution as well as variations in the scar threshold based on selected inversion time. As compared to conventional LGE, ventricular HR-LGE imaging appears as a valuable tool that could significantly impact decision making in clinical routine. However, the long HR-LGE scan duration limits its wide clinical adoption. Additional difficulty comes from the cardiac and respiratory motions that may create artifact and blurring on the resulting image. To compensate for motion, majority of CMR imaging relies on cardiac and respiratory gating. Counterparts of such a technique is long and unpredictable scan times, particularly in patients suffering from arrhythmia.

1.4. Objectives of the PhD

Whether MRI can accurately identify the specific regions of tissue that participate in the VT reentrant circuits or constitute the AF drivers remains an open question.

This thesis work aimed at significantly increase the spatial resolution at clinical field (1.5 T) of cardiac MR imaging in order to provide relevant information on the cardiac substrate related to arrhythmia. Challenges are **low signal to noise ratio** associated with reduced voxel size and **complex motion-induced** by the heart contraction and respiratory together with presence of **irregular motion** during arrhythmia.

This thesis therefore proposes important advances to remove the current locks of the technology allowing to envision a high-resolution, motion corrected cardiac imaging. For that purpose, three mains axis were developed:

- In Chapter 2, we implemented a local surface coil to improve the selectivity and sensitivity. We sought to address the safety issue of the active decoupling circuit by integrating an active optical decoupling to the original circuit. This technical

implementation was evaluated ex vivo and on a beating heart. The feasibility of high-resolution at clinical field is demonstrated.

- In Chapter 3, the issue of motion was investigated. A motion compensation technique was implemented that exploits the signal of micro-coils embodied on a MR-compatible catheter. Ex vivo and in vivo evaluation were conducted. In a last experiment, we proposed to combine the developed local coil and the motion compensation technique to perform high-resolution, motion-corrected image of the left endocardial ventricle via an open-chest approach. Preliminary results are presented.

- In Chapter 4, safety aspects (potential coil wire heating due to absorption of RF emitted by the body coil during MRI acquisition sequence) inherent to the insertion of a MRI receiver coil inside the patient's body was investigated. An MR-thermometry method was developed to quantify the temperature evolution near an implanted wire. Precision of the method was evaluated in gel and in vivo on human brain.

Context of the PhD

This thesis was granted by the company Siemens Healthcare via a CIFRE contract with "L'Institut de RYthmologie et Modélisation Cardiaque" (LYRIC) in Pessac. This institute is one of the six "Institut Hospitalo-Universitaire" in France, and it is dedicated to heart diseases.

Available means and methods at the beginning of the PhD:

- Two MRI scanners (1.5T, AERA and AVANTO, MAGNETOM, Siemens Erlangen, Germany)
- Research agreement providing access to source code for sequence implementation.

- Calculation server connected to the MRI for high demand reconstruction and image processing (parallel computing on graphic cards) with Matlab licenses (including Gadgetron environment [38]).
- MRI-compatible ablation catheters (Imricor Medical Systems, Burnsville, Minnesota, USA)
- Real-time thermometry pipeline implemented in the Gadgetron framework.
- All necessary equipment for large animal experimentation (sheeps) with in-house animal facilities, anesthesia equipment, experienced technicians and Vet for MRI guided cardiac interventions

1.5. References

[1] A. F. Thomsen, ‘Left Atrial Wall Thickness and Pulmonary Vein Size are Increased in Patients with Atrial Fibrillation Compared to Healthy Controls - A Multidetector Computed Tomography Study’, Int J Clin Cardiol, vol. 4, no. 2, Jun. 2017.

[2] R. B. van Heeswijk, G. Bonanno, S. Coppo, A. Coristine, T. Kober, and M. Stuber, ‘Motion Compensation Strategies in Magnetic Resonance Imaging’, Crit Rev Biomed Eng, vol. 40, no. 2, pp. 99–119, 2012.

[3] S. Roujol, E. Anter, M. E. Josephson, and R. Nezafat, ‘Characterization of Respiratory and Cardiac Motion from Electro-Anatomical Mapping Data for Improved Fusion of MRI to Left Ventricular Electrograms’, PLoS ONE, vol. 8, no. 11, p. e78852, Nov. 2013.

[4] ‘CVD Statistics 2017’. http://www.ehnheart.org/cvd-statistics/cvd-statistics-2017.html (accessed Nov. 19, 2019).

[5] E. J. Benjamin et al., ‘Heart Disease and Stroke Statistics—2019 Update: A Report From the American Heart Association’, Circulation, vol. 139, no. 10, Mar. 2019.

[6] ‘Global Scourge of Cardiovascular Disease | Elsevier Enhanced Reader’. https://reader.elsevier.com/reader/sd/pii/S0735109717373163 (accessed Jan. 13, 2021).

[7] M. Hocini, P. Jais, F. Sacher, P. Bordachar, J. Clementy, and M. Haissaguerre, ‘Fibrillation auriculaire’, Réalités Cardiologiques, no. 217, p. 4, May 2006.

[8] P. Kirchhof et al., ‘2016 ESC Guidelines for the management of atrial fibrillation developed in collaboration with EACTS’, Eur Heart J, vol. 37, no. 38, pp. 2893–2962, Oct. 2016.

[9] B. J. Hansen, J. Zhao, and V. V. Fedorov, ‘Fibrosis and Atrial Fibrillation: Computerized and Optical Mapping’, JACC: Clinical Electrophysiology, vol. 3, no. 6, pp. 531–546, Jun. 2017.

[10] C. Foth, M. K. Gangwani, and A. H. Alvey, Ventricular Tachycardia, StatPearls [Internet]. 2020 (accessed Jan. 12, 2021).

[11] D. Corradi, S. Callegari, R. Maestri, S. Benussi, and O. Alfieri, ‘Structural remodeling in atrial fibrillation’, Nat Rev Cardiol, vol. 5, no. 12, pp. 782–796, Dec. 2008.

[12] M. Haïssaguerre et al., ‘Spontaneous Initiation of Atrial Fibrillation by Ectopic Beats Originating in the Pulmonary Veins’, N Engl J Med, vol. 339, no. 10, pp. 659–666, Sep. 1998.

[13] S. Kostin, ‘Structural correlate of atrial fibrillation in human patients’, Cardiovascular Research, vol. 54, no. 2, pp. 361–379, May 2002.

[14] P. G. Platonov, L. B. Mitrofanova, V. Orshanskaya, and S. Y. Ho, ‘Structural Abnormalities in Atrial Walls Are Associated With Presence and Persistency of Atrial Fibrillation But Not With Age’, Journal of the American College of Cardiology, vol. 58, no. 21, pp. 2225–2232, Nov. 2011.

[15] G. J. Volpe et al., ‘Left Ventricular Scar and Prognosis in Chronic Chagas Cardiomyopathy’, Journal of the American College of Cardiology, vol. 72, no. 21, pp. 2567–2576, Nov. 2018.

[16] U. Schotten, S. Verheule, P. Kirchhof, and A. Goette, ‘Pathophysiological Mechanisms of Atrial Fibrillation: A Translational Appraisal’, Physiological Reviews, vol. 91, no. 1, pp. 265–325, Jan. 2011.

[17] H. Cochet et al., ‘Relationship Between Fibrosis Detected on Late Gadolinium-Enhanced Cardiac Magnetic Resonance and Re-Entrant Activity Assessed With Electrocardiographic Imaging in Human Persistent Atrial Fibrillation’, JACC: Clinical Electrophysiology, vol. 4, no. 1, pp. 17–29, Jan. 2018.

[18] J. Chen et al., ‘Extent and spatial distribution of left atrial arrhythmogenic sites, late gadolinium enhancement at magnetic resonance imaging, and low-voltage areas in patients with persistent atrial fibrillation: comparison of imaging vs. electrical parameters of fibrosis and arrhythmogenesis’, EP Europace, vol. 21, no. 10, pp. 1484–1493, Oct. 2019.

[19] B. Burstein and S. Nattel, ‘Atrial Fibrosis: Mechanisms and Clinical Relevance in Atrial Fibrillation’, Journal of the American College of Cardiology, vol. 51, no. 8, pp. 802–809, Feb. 2008.

[20] S. S. Kuppahally et al., ‘Left Atrial Strain and Strain Rate in Patients With Paroxysmal and Persistent Atrial Fibrillation: Relationship to Left Atrial Structural Remodeling Detected by Delayed-Enhancement MRI’, Circ Cardiovasc Imaging, vol. 3, no. 3, pp. 231–239, May 2010.

[21] K. Sonoda et al., ‘Scar characteristics derived from two- and three-dimensional reconstructions of cardiac contrast-enhanced magnetic resonance images: Relationship to

ventricular tachycardia inducibility and ablation success', Journal of Arrhythmia, vol. 33, no. 5, pp. 447–454, Oct. 2017.

[22] E. Gucuk Ipek and S. Nazarian, 'Cardiac magnetic resonance for prediction of arrhythmogenic areas', Trends in Cardiovascular Medicine, vol. 25, no. 7, pp. 635–642, Oct. 2015.

[23] R. K. Mukherjee, J. Whitaker, S. E. Williams, R. Razavi, and M. D. O'Neill, 'Magnetic resonance imaging guidance for the optimization of ventricular tachycardia ablation', Europace, vol. 20, no. 11, pp. 1721–1732, Nov. 2018.

[24] D. E. Krummen and S. M. Narayan, 'Ablating Persistent Atrial Fibrillation Successfully', Curr Cardiol Rep, vol. 14, no. 5, pp. 563–570, Oct. 2012.

[25] M. Haïssaguerre et al., 'Localized Sources Maintaining Atrial Fibrillation Organized by Prior Ablation', Circulation, vol. 113, no. 5, pp. 616–625, Feb. 2006.

[26] A. E. Darby, 'Recurrent Atrial Fibrillation After Catheter Ablation: Considerations For Repeat Ablation And Strategies To Optimize Success', Journal of Atrial Fibrillation, vol. 9, no. 1, 2016.

[27] S. Toupin, 'Cardiac MR Thermometry for the monitoring of radiofrequency ablation', HAL Id: tel-01511066, Apr 2017.

[28] A. E. Campbell-Washburn et al., 'Real-time MRI guidance of cardiac interventions: Real-Time Cardiac MRI Interventions', J. Magn. Reson. Imaging, vol. 46, no. 4, pp. 935–950, Oct. 2017.

[29] T. Rogers and R. J. Lederman, 'Interventional Cardiovascular MRI', in Cardiovascular Magnetic Resonance Imaging, R. Y. Kwong, M. Jerosch-Herold, and B. Heydari, Eds. New York, NY: Springer New York, 2019.

[30] J. Garot, N. Pointeaud, and S. Toupin, 'Interventional Cardiovascular Magnetic Resonance: Initial Clinical Experience for Right Heart Catheterization', MAGNETOM Flash SCMR Edition, p. 5, 2020.

[31] C. M. Kramer, J. Barkhausen, C. Bucciarelli-Ducci, S. D. Flamm, R. J. Kim, and E. Nagel, 'Standardized cardiovascular magnetic resonance imaging (CMR) protocols: 2020 update', J Cardiovasc Magn Reson, vol. 22, no. 1, p. 17, Dec. 2020.

[32] D. C. Peters et al., 'Left ventricular infarct size, peri-infarct zone, and papillary scar measurements: A comparison of high-resolution 3D and conventional 2D late gadolinium enhancement cardiac MR', J. Magn. Reson. Imaging, vol. 30, no. 4, pp. 794–800, Oct. 2009.

[33] D. Andreu et al., ‘Cardiac magnetic resonance–aided scar dechanneling: Influence on acute and long-term outcomes’, Heart Rhythm, vol. 14, no. 8, pp. 1121–1128, Aug. 2017.

[34] D. C. Peters et al., ‘Detection of Pulmonary Vein and Left Atrial Scar after Catheter Ablation with Three-dimensional Navigator-gated Delayed Enhancement MR Imaging: Initial Experience 1’, Radiology, vol. 243, no. 3, pp. 690–695, Jun. 2007.

[35] R. S. Oakes et al., ‘Detection and Quantification of Left Atrial Structural Remodeling With Delayed-Enhancement Magnetic Resonance Imaging in Patients With Atrial Fibrillation’, Circulation, vol. 119, no. 13, pp. 1758–1767, Apr. 2009.

[36] J. A. Luetkens et al., ‘Cardiac magnetic resonance using late gadolinium enhancement and atrial T1 mapping predicts poor outcome in patients with atrial fibrillation after catheter ablation therapy’, Sci Rep, vol. 8, no. 1, p. 13618, Dec. 2018.

[37] M. Ugander et al., ‘Myocardial Edema as Detected by Pre-Contrast T1 and T2 CMR Delineates Area at Risk Associated With Acute Myocardial Infarction’, JACC: Cardiovascular Imaging, vol. 5, no. 6, pp. 596–603, Jun. 2012.

[38] M. S. Hansen and T. S. Sørensen, ‘Gadgetron: An open source framework for medical image reconstruction: Gadgetron’, Magnetic Resonance in Medicine, vol. 69, no. 6, pp. 1768–1776, Jun. 2013.

Chapter 2

Development of a MRI coil for high-resolution imaging at clinical field

2.1. Introduction

High spatial-resolution imaging of heart anatomy and physiology is required to increase the value of diagnostic MRI and to guide or monitor therapeutic processes. In patients presenting with persistent atrial fibrillation (AF), precise description of the extent and location of fibrosis in the atria would allow early diagnosis of the pathology and help at triaging AF therapeutic directions, such as determining which sites to ablate or weighting the benefits of ablation versus pharmacological treatment [1]. As the wall thickness of atrium ranges from 1 to 3 mm [2], depiction of fine structures within the wall requires a much higher spatial resolution than the one currently achieved in clinical cardiac MRI (often limited to more than one millimeter spatial resolution within an acceptable time window). Ideally, a spatial resolution of 300 µm isotropic or better would be desirable for proper identification of the arrhythmogenic substrate. One major determinant in performing high spatial resolution scans is the intrinsic Signal-to-Noise ratio (SNR) of the Radio frequency (RF) receiver coils. SNR is proportional to the volume of the voxel. Therefore, if we want to increase the spatial resolution (i.e., to decrease the dimensions of the voxel) from 1 mm^3 to 0.3 mm^3 (i.e., dividing the dimensions of the voxel by a factor 3), we lose a factor of 27 (3^3) in signal. This loss in signal has to be compensated via a gain in coil sensitivity. RF coils are the front end of the magnetic. RF coils are the front end of the instrumental chain of a magnetic resonance imaging. Despite the huge technical progresses in RF coils, based on the phased array technology with increase of channels [3], [4] together with MR scanners featuring multiple receive channels, spatial resolution of clinical cardiac MR images currently remains around 1 mm or larger. It is of utmost importance to increase the sensitivity of the RF coil in order to increase the SNR and exploit this gain to reduce the voxel size.

Current external MRI coils placed on the surface of the torso are limited in sensitivity due to their physical distance from the heart itself. Also, the use of large coil elements that image more than the heart may negatively affect SNR of the resulting images of the myocardium. The development of specialized radio-frequency coils for imaging a specific anatomic region can somewhat overcome the practical obstacles of limited SNR and risks of image aliasing associated with imaging of small field of view with high spatial resolution. The earliest and most often pursued solution to improve the RF coil detection sensitivity is to reduce the coil size, i.e., to use small surface coils [5] that would be placed in proximity to the target tissue. As the sensitive volume is adapted to the region of interest, this allows optimization of the filling factor of the receiver coil, thereby improving SNR of the resulting images. Furthermore, the high selectivity provided by the local coil is an advantage: since it is not sensitive to the objects at far field, image wrap-around is not a problem (the signal drops drastically with distance to the coil) allowing acquiring images with small field of view (FOV) and thus reduce MR image acquisition time. Indeed, the acquisition time is linearly dependent on the k-space matrix, therefore on the FOV/spatial resolution ratio. Hence, in order to maintain an acceptable acquisition time, it is preferable to reduce the FOV (by a factor of 3 in the above example). For these reasons, intravascular RF receiver coils have been developed and widely considered preferred for targeted cardiac imaging [6]–[10].

However, for clinical use, safety aspects inherent to the insertion of a MRI receiver coil inside the body have to be investigated and specific technical solutions have to be implemented to guarantee patients' safety. One of the major risks is the conductive wires linking the coil to the connecting plug of the MR system. In fact, the conducting cables can act as an antenna [11], [12] and capture the electromagnetic waves of the radiofrequency pulses of the MRI sequence, resulting in heat production [13] (see Chapter 4). This heating is particularly pronounced when the length of the electrically conducting structures approaches the B_0-dependent resonant length [14]. Furthermore, the propagation of direct current (DC) to actively detune the coil during the RF-transmission (Tx) phase introduces additional risks of inducing cardiac arrest. In order to prevent from harmful interactions between the intravascular coil and the MR environment and thus protect patients from RF-related side effects, optical fibers were used to transmit the direct current instead of coaxial cables for the active decoupling [15].

As intravascular coils show a real benefit in terms of image quality for heart exploration, it was further desired in this PhD to converge toward a practical implementation of an intracardiac MRI RF coil offering high sensitivity (gain in SNR) and spatial selectivity (reduced FOV to fit with the region of interest), while being sufficiently mechanically robust and electrically safe. The use of mini-invasive coils is not problematic in this context since state-of-the heart therapies commonly require the use of endo-cavitary catheters (electrical mapping, ablation) for the treatment of arrhythmia.

To this end, a first receive-only coil prototype was designed following geometric and size requirements to fit with the heart anatomy and vasculature dimensions. Furthermore, as RF coils are not stand-alone devices, they must be interfaced with the MRI system. This involved the design of a specific tuning/matching and detuning circuitry together with a dedicated box to interface the system receiver. In order to alleviate the aforementioned safety issues, a key step of the probe construction was to replace the conventional galvanic connections used for the transmission of the DC current necessary for the decoupling phase by optical connections. This was realized in collaboration with Dr. Isabelle Saniour who implemented an optical decoupling technique during her PhD. Adaptations of her work was made to fit with our coil matching/tuning network. In a second stage, characterization of the probe on a RF workbench was performed. The probe was then evaluated in the presence of a sample loading to test its behavior in terms of frequency shift, tuning and matching capabilities as well as decoupling performances. Comparison of SNR gain relative to conventional coils between active and optical detuning techniques was performed before the first test ex-vivo. Finally, in order to test behavior and performances of our coil in presence of motion, experiments on ex-vivo working heart from pig were conducted using the designed probe. In a last study, the SNR gain offered by the intravascular coil was invested in MR-thermometry to evaluate the potential of such a coil at improving temperature accuracy.

2.2. Objectives and Challenges

This chapter focuses on the following objectives and challenges:

- **Need**: An imaging System capable of providing detailed, qualitative and quantitative data regarding the status of myocardium at the time of surgical intervention could favorably improve patient outcomes by enabling premature detection of structural myocardial abnormalities. It would also serve to provide precise guidance for various forms of localized therapy such as thermal ablation where high resolution temperature maps are needed.
- **Problem**: External surface coils do not achieve a sufficient Signal to Noise Ratio (SNR) for structures far from the surface of the body.
- **Solution**: Designing a local coil to enhance the signal while reducing the noise. Since it is not sensitive to the objects at far field, image wrap-around is no more a problem in high-resolution, small field-of-view images. Also, the lack of sensitivity to sources far from the coil results in lower noise amplitude [16], [17]. The local surface coil intrinsically combines a high selectivity with a high sensitivity that allows a smaller voxel size and a faster acquisition time (due to the reduced FOV). Hence, an intracardiac RF coil inserted close to the region of interest could drastically increase the SNR and thus enabling images with high resolution (desired resolution : 300 µm in-plane or better)
- **Challenges** of this project are multiple. First, achieving the highest signal with the highest spatial resolution, i.e. the smallest voxel. However, these two factors are mutually exclusive and, in addition, extend the acquisition time. In addition, the small size of insertion permitted by the vasculature structure constrains the technical developments to a certain dimension and the geometry of the antenna must be adapted according to it. Also, a major associated challenge with in vivo application is the cardiac and respiratory motions. In addition, several causes for image artifacts associated with flow have to be considered: first-order and higher order motion of flowing blood, coil motion relative to the myocardium wall and pulsatility induced motion of the vascular wall itself. These can severely impact the image quality creating ghost artifact as well as blurring.

Since no expertise on coil hardware and coil interfacing was pre-existing at the IHU LIRYC institute at that time, significant work has been achieved during the 1st year of PhD to review the state-of-the-art intravascular coil and coil theory. Within this same year, first prototypes were implemented. During the second year of the PhD, collaboration with BioMaps laboratory (Inserm UMR1281) and especially with Dr. Isabelle Saniour and Dr. Marie Poirier-Quinot brought expertise on optical detuning as well as coil theory. I closely worked with Isabelle Saniour to design the coil circuitries and integrate the optical detuning solution to the original circuity.

Personal contributions:

- Participation in the study design
- Designing the original galvanic-detuned coil circuit
- Supervising the coil interfacing with the MR scanner (in collaboration with Dr. Stark)
- Participation in the integration of the optical decoupling circuit and laser command system (work supervised by Dr. Saniour)
- Conducting Ex vivo and working heart experimentations (acquisitions and processing of the data)
- Production of the figures

2.3. Intravascular coil history: emergence and development

Papers of Atalar [18] and Cavalcante et Larose [19] provided support to write this part. The state of the art was realized for a 1.5 T field strength as this is our field of interest here.

The concept of intracavitary probe, also called catheter coils was first investigated in 1984 by Dr. Howard Kantor [6] in order to increase the signal to noise ratio (SNR) in ^{31}P Nuclear Magnetic Resonance (NMR) spectra. As it is well known indeed, the ^{31}P signal is very weak compared to the signal of proton and it is therefore difficult to obtain relevant clinical results. Regarding the anatomic region of interest which in their case was the heart, Kantor et al designed a transmit/receive two-turn elliptical coil (7.5 x 24 mm, copper wire insulated with polystyrene) that they placed in contact with the right ventricle of a dog and **obtained a**

gain in SNR of 9. Their pioneering approach triggered the interest of several research groups in catheter coils and resulted in many other publications. Shortly after, Schnall et al designed an intracavity inflatable surface coil for high sensitivity and high resolution imaging of the male prostate and associated areas [20]. Their invention consisted of an insertable receiver coil embodied on an inflatable patient interface balloon including an inner and an outer balloons between which the coil was enclosed.

Depending on the anatomic region of interest (blood vessels, prostate, colon, heart…) different coil designs were introduced. First, potential therapeutic implications associated with in vivo characterization of atherosclerotic plaque have motivated the pursuance of various concepts for high resolution imaging of the arterial walls. Reports of catheter coils designed to image the arterial lumen emerged as early as 1992, at times proposing creative and alternative approaches such as advancing the coil in an adjacent vein in order to circumvent the difficulty of accessing the artery. Almost simultaneously, three research groups led by Dr. Hurst, Dr. Martin and Dr. Kandarpa explored the feasibility of catheter-based receiver coils for high-resolution imaging of blood vessels. While Hurst et al and Martin et al used opposed solenoid coil, Kandarpa et al. [21] exploited a small rectangular loop fitting a 8Fr (2.67 mm) catheter. Reflecting their superior in-plane signal homogeneity and penetration depth, initial assessments of intravascular imaging coils favored opposed solenoid designs [16], [22]. A limiting factor of such a design nevertheless is that the coil sensitivity nulls occur at locations approximately at the center of each solenoid. In opposite, the **single-loop, multi-turn coil** proposed by Kandarpa et al. provided better SNR and a slightly better longitudinal coverage for multi-slice imaging compared with the opposed solenoid coils. Ex-vivo images (10 slices) of freshly excised rabbit heart were acquired with **200 µm in-plane** resolution, 1.5 mm slice thickness in 17 min. Imaging device remained, however, rather rigid and was not evaluated under in vivo condition. Using an **opposed solenoid design**, successful phantom experiments revealed the feasibility of submillimeter in-plane resolution. Hurst et al. [22] acquired images in situ (cadaver) with **78 x 78 µm in-plane** voxel size and 2 mm slice thickness in less than 10-min. For a target defined by an annulus in a plane perpendicular to B_0, the opposed solenoid design provided the best in-plane homogeneity in the region between the solenoid when compared to the birdcage and multipole designs. However, this design did not provide sufficient SNR performance in this region of optimal homogeneity. In vivo tests conducted by this same team were not conclusive due to important motion artifacts that precluded good depiction of the wall

structure. Martin et al. [16] showed the opposed-solenoid configuration exhibited better performance relatively to the quality factor (Q) value and appeared to be less subjected to coil resistance than the opposed-loop design. Ex-vivo human femoral artery acquisition was achieved with a **156 µm in-plane** resolution and 3 mm slice thickness. Opposed-solenoid were used in the study of Martin et Henkelman [23] to obtain high-resolution images in vivo (swine aorta). However, motion of the coil in the pulsatile blood stream was identified as a major obstacle to obtain sufficient image quality. To overcome this issue, they implemented a “bullet tip” to stabilize the coil in the center of the vessel and to limit the ghost artifacts. They could obtain images with **312 µm in-plane** resolution with 3 mm slice thickness in less than 6 min and gated the images with ECG while saturating the spins upstream from the imaging plane to improve image quality. However, rigidity and large mass of the resultant device made it impractical in a patient setting. In an attempt to improve the longitudinal coverage of the catheter coil and to overcome the mechanical rigidity associated with the opposed-solenoid and single loop designs, Atalar et al. [17] presented an alternative catheter coil design which consisted on **an elongated loop**. This design combined the advantage of enlarged longitudinal coverage, smaller size together with greater flexibility while limiting the change in inductance when the coil flexes. While the coil itself was 4 Fr in size (diameter: 1.33 mm), the maximum diameter of the design (around the region where the capacitors are placed) was 9 Fr (diameter: 3 mm). Decoupling was achieved by placing a shunt PIN diode on the coaxial cable. Using their coil, they reported **a SNR of 20** or more in the close vicinity of their receive-only elongated loop design and acquire in vivo image with a spatial resolution of **98 µm x 98 µm x 3 mm^3** of a rabbit aorta. In opposite to the loop and solenoid design that require the tuning/matching network to be close to the coil, Ocali et Atalar [24] provided convincing theoretical evidence that a modified design, based on a **loopless coil** with tuning and matching circuits located outside the vessel, could possibly be miniaturized to the order of 1.5 French (0.5 mm) in diameter while still providing adequate SNR. Intravascular loopless antennae utilize much thinner and more flexible coaxial cable [25]. The inner conductors of these antennae are extended by about a quarter wavelength to form a “whip” suitable for imaging small vessels. The relatively short length of the intravascular MR whip, however, results in relatively small longitudinal coverage. Another solution to render the coil more flexible while benefiting of a loop design relies on expandable coils where the current loop coils is mounted on a balloon [9], [10], [26], [27] or mounted on pre-shaped filament [9].

When discussing the performance of every catheter coil design, one of the most critical parameters that one has to take into account is their mechanical properties and dimensions.

2.4. Theory

Radiofrequency coils are an essential MRI hardware component as they are responsible for the excitation and the reception of the MR signal. As such, they directly impact the spatial and temporal resolution, sensitivity and uniformity in MRI [28]. Their shape, size and position have a critical importance for the SNR of the acquired images [18]. In general RF coils are optimized to obtain the higher SNR. For optimum performance, the RF coils should be adapted to the target biomedical application and the sensitive volume of the coil should equal the desired field of view (FOV) of the region of interest to optimize the filling factor and thereby increase the selectivity while improving the sensitivity. As a result, numerous RF coils with various geometry and dimension have been introduced. Also, RF coils are differentiated by their operating modes. Here, we only focus on the design of receive-only coils.

2.4.1. The surface coil as a receive-only probe

In their simple form, surface coils consist of a loop of wire, creating an inhomogeneous magnetic field that decreases quickly when increasing distance from the coil plane. This allows imaging a restricted region of interest within a large sample. Furthermore, as the field of view is reduced, less noise from the sample is coupled to the coil, resulting in higher SNR.

The signal detected by the surface receive coil is highly dependent on its dimensions and its geometry. Considering a single circular surface loop of diameter r, carrying a current I, the magnetic field induced by the coil at a distance d from its axis and normalized by the current I can be expressed according to Biot-Savart equation:

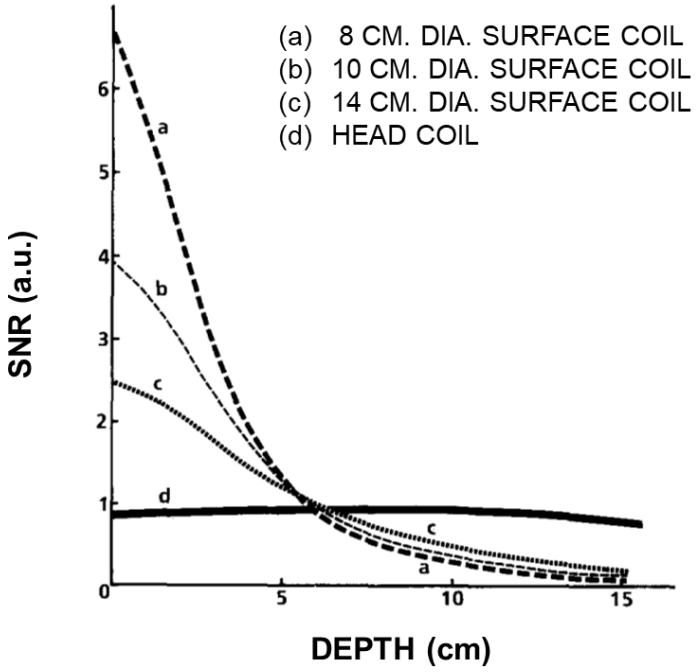

Figure 2-1: Signal-to-noise ratio versus depth in a head-sized phantom imaged with surface coils of three different diameters and the head coil. Figure from Hayes et Axel 1985.

$$\frac{|\overrightarrow{B_1}|}{I} = \frac{\mu 0}{2} \frac{r^2}{[r^2 + d^2]^{3/2}} \quad (2\text{-}1)$$

with μ_0 the permeability of free space. This equation showed that, in the vicinity of the coil (d << r), the induction coefficient $|\overrightarrow{B_1}|/I$ is inversely proportional to the radius of the surface loop coil. Thus, using the principle of reciprocity, the NRM signal intensity increases when the radius of the circular loop decreases. Hayes et Axel [29] showed that for a region 2 cm below the surface, the 8 cm diameter surface coil SNR is 4.7 times better than that of the head coil, which allow to reduce the volume of the voxel by the same factor while still retaining the same SNR as provided by the head coil (Figure 2-1).

In contrast to head or body coils, the SNR for surface coils depends little on the losses in the total tissue sample but greatly on coil geometry. Note also that the noise contribution from the object and from the sensor decrease when decreasing the coil diameter. Hence, for this type of coil, the SNR is as high as the radius of the coil is small. On the other hand,

as the diameter decreases the penetration depth also decreases, which yields to a compromise between the desired sensitivity and the depth of exploration.

2.4.2. SNR in detail

The signal and noise detected in nuclear magnetic resonance (NMR) experiments can be quantified using the reciprocity principle that states that the receive sensitivity of a coil is proportional to its transmit field, e.g. that the electromagnetic force (emf) induced in an RF coil by a rotating magnetic dipole **m** at a given point in space is proportional to the magnetic field $\mathbf{B_1}$ produced at the same point by a current I circulating in the coil [30]. The emf induced by m is given by:

$$\mathrm{emf} = -\frac{\partial}{\partial \mathrm{t}} \frac{\mathbf{B_1}.\mathbf{m}}{\mathrm{I}} \tag{2-2}$$

This emf is responsible for the current to flow in the RF loop coil. This causes a voltage at the open terminals of the loop and constitutes the NMR signal, which is resolved into voxels. For a sample volume V, with the sample magnetization flipped into the xy-plane by a 90° RF pulse, the emf induced in the coil is given by:

$$\mathrm{emf} = -\int_{\mathrm{sample}} \frac{\partial}{\partial \mathrm{t}} \frac{\mathbf{B_1}.\mathbf{M_0}}{\mathrm{I}}\, \mathrm{dV} \tag{2-3}$$

$\mathbf{B_1}$ and $\mathbf{M_0}$ are both rotating in the xy-plane at the Larmor frequency ω_0 ($\omega_0 = 2\pi.\mathrm{f}_0$). Assuming that the B_1 field is homogeneous over the sample volume (which is reasonable for typical voxel sizes of several cubic millimeters), and neglecting phase, it can be shown that equation yields

$$\mathrm{emf} = \omega_0 \frac{\mathrm{B}_{1,\mathrm{xy}}}{\mathrm{I}} \mathrm{M}_0 \mathrm{V} \cos(\omega_0 \mathrm{t}) \tag{2-4}$$

A rigorous mathematical description of the application of the reciprocity Principle for calculation of the NMR signal strength was given in Hoult at Richards [31]. This signal is

altered by noise from several sources including the resistance of the receiver coil, dielectric losses, and inductive losses arising within the sample to be imaged. The noise can be thought of as arising from an equivalent coil resistance R_{eq}, composed of the equivalent series resistance due to the resistance of the coil (R_c), dielectric losses (R_e), and inductive losses (R_m). The proportion of each of these contributions to overall noise depends strongly on the fabrication properties of the coil and the degree of coupling between the coil and a lossy medium [16]. The voltage associated with noise is given by the following equation:

$$V = \sqrt{4K_B\,T\Delta f R_{eq}} \tag{2-5}$$

With Δf the receiver bandwidth and K_B the Boltzmann constant. TR_{eq} is the equivalent temperature-weighted sum of resistances according to the respective dissipation rates and local temperatures in the different media.

The signal to noise ratio (SNR) is defined as the ratio of the emf induced in the coil over the noise voltage, as shown in the following equation:

$$SNR = \frac{emf}{V} = \frac{B_{1,xy}}{I}.\frac{\omega_0\,M_0 V\cos(\omega_0 t)}{\sqrt{4K_B\,T\Delta f R_{eq}}} \tag{2-6}$$

Combining equation (2-1) and (2-6), this suggests that the SNR at the surface of the coil (d = 0) increases rapidly as the coil radius r is decreased and that the radius r is the scale factor which determines how rapidly the SNR rolls off with distance to the sample. Besides the **coil's loop size** and the **electrical properties**, main factors influencing the SNR are the following [28]:

- **The penetration depth**: is defined as the depth at which the coils sensitivity drops to 37% of that at the center of the coil. The loop-coil has a very local sensitivity depending on the penetration depth. It is usually admitted, as a rule of thumb, that the penetration depth of a loop coil is approximately equal to its diameter.

- **The effective temperature**: which is responsible for the losses of all the components,

- **The performance of the preamplifier** to amplify the emf.

- **The quality factor**: which is a measure to compare coil loops in their efficiency to detect the MR signal. The Q-factor is a dimensionless indicator for the loss mechanisms in the coil. It could either be measured considering the following equation:

$$Q = \frac{\omega_0 L}{R_c} \qquad (2\text{-}7)$$

where L is the inductance of the coil, or be measured in terms of the width of the resonance peak at -3dB :

$$Q = \frac{f_0}{\Delta f} \qquad (2\text{-}8)$$

with Δf corresponding to the -3dB bandwidth of the resonance peak.

- **The filling factor**: which is the ratio of magnetic field energy stored inside the sample volume versus the total magnetic energy stored by the loop. To maximize this factor and thereby the SNR, the coil must be chosen (or designed) to fit the closest as possible with the targeted region to be imaged. As the field of view is reduced, less noise from the sample is coupled to the coil, resulting in higher SNR. The filling factor of a surface coil being high and the probe being small, its sensitivity is very high when one is interested in a small sample [32].

2.4.3. Basic Principles

2.4.3.1. RLC Circuit

The coil itself is an inductor with inductance L forming a basic loop. Furthermore, the loop wire has inherent resistive losses R. The source of energy loss or heating in probe components are essentially the conductor resistance and the dissipation of energy in the capacitor's dielectric or any substrate supporting the circuit. Therefore, the energy is not only stored in the coil but also dissipated through ohmic losses [33]. The source of energy loss or heating in probe components is essentially dependent on the conductor [32]. Adding

a capacitor C to the R,L circuit creates a resonant circuit that can be tuned to the appropriate frequency using appropriate value of C. The coil is then connected to a transmission line must match its characteristic impedance to maximize energy transfer and ensure optimal SNR.

2.4.3.2. Tuning and matching

Tuning a coil means adjusting the capacitance (and sometimes the inductance) so that the frequency of the electrical resonance of the coil circuit matches the Larmor frequency. The resonance of a sensor results in a frequency selectivity and therefore, filters out some of the noise associated with the detection of the NMR signal. At the electrical resonance thus a small external perturbation, here the emf generated by the transient motion of the nuclear magnetization, induces a large response from the coil. Usually, the capacitor C_t ensures the tuning function and changing this value adjusts the resonance frequency of the receiver coil (on the S11 magnitude chart).

Matching the coil means maximizing the signal power transmission. Connections between the RF probe and the MR scanner is usually ensured by coaxial cables having a characteristic impedance of 50 Ohms. It is thus important to transfer the maximum available power to the RF probe during RF transmission. To this end, the coil and cable should have the same impedance Z_0 (typically 50 Ohms). This condition is called “power matching” and a mismatch in impedance induces a less efficient receive chain. [33]. Capacitor Cm is used for matching the coil to the 50 Ohms impedance of the receiver circuit.

In practice, there are usually two common ways to tune and match the network: **capacitive** and **inductive** techniques. Although inductive matching presents several advantages, particularly the reduction of load effects when the sensor is placed near the object to be imaged together with independency of the tuning and matching adaptation with the resonant loop, the capacitors used in capacitive coupling is more advantageous to minimize dielectric losses and make sensors decoupling more efficient [34]. According to this observation, our choice was in favor of a **capacitive tuning** and matching network. Moreover, this configuration allows a more compact circuit which is desired in our case.

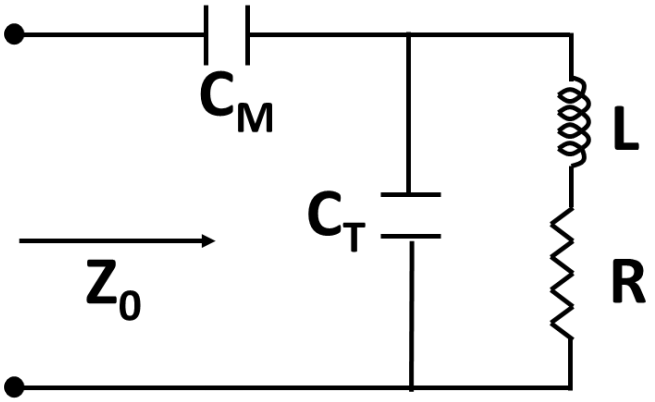

Figure 2-2: Parallel tuned/series matched circuit. The coil inductance L is tuned at the operating frequency ω_0 by the capacitance CT. The high resistance of the coil resonator is matched to 50 Ω by the matching capacitor C_M.

In the basic capacitive tuning and matching network, two capacitors are used (Figure 2-2). One in parallel with the RF probe and the other in series with the RF coaxial cable. Two configurations exist: one with parallel tuned/series matched and the other with series tuned/parallel matched circuits. As exposed in Mispelter et al [32], the losses in the parallel tuned/series matched circuit are about half the losses in the series tuned/parallel matched circuit. Therefore, without special care or particular needs, the parallel tuned/series matched circuit is preferred.

In this configuration, theoretical values of capacitors are given by this system of equations:

$$C_T = \frac{\omega_0 . L . Z_0 - \sqrt{R . Z_0 (\omega_0^2 . L^2 - R . Z_0 + R}}{\omega_0 . Z_0 (\omega_0^2 . L^2 + R^2)} \qquad (2\text{-}9)$$

$$C_M = \frac{2.\omega_0^2.L.C_T - \omega_0^4.L^2.C_T^2 - \omega_0^2.R^2.C_T^2}{\omega_0^2(R^2.C_T^2 - L + \omega_0^2.L.C_T)}$$

where ω_0 is the operating frequency, L the coil inductance, Z_0 the characteristic impedance equal to 50 Ω and R the resistance which reflects the losses in the loop. Equation (2-9) shows the interdependency of the capacitor values. Therefore, in practice, modifying one will induce variation in the other and vice versa.

2.4.3.3. Decoupling

During the RF excitation phase, assumed to be provided by a uniform body transmit coil, the receiver coil must be decoupled from the transmission coil to prevent both distortion of the transmitted magnetic field (B1+) and local hot spots generation (points of excessive RF power deposition) inside the body due to the associated electric field concentration. More precisely, during transmission, if no detuning is performed, the current induced in the receiver coil will create a magnetic field that will add or subtract to the primary exciting RF field created by the transmit coil. This will result in a inhomogeneous excitation in the vicinity of the receiver coil, affecting the local flip angle profile [32]. Moreover, during the receiving phase, part of the electromagnetic energy received by the receiver coil will be dissipated in the resistance of the large resonator and noise currents flowing in the transmitting coil will induce noise currents in the receiver coil, affecting thus the resulting image [35].

In addition to the aforementioned side effects, coupling between the two coils could also lead to undesirable transfer of energy into the Rx chain during the transmission. Indeed, as the transmit power is orders of magnitude greater than the received signal, the preamplifier of the Rx coil needs thus to be protected from damage due to the high power of the RF transmission. These can be avoided by electronically damping the resonance of the receiver coil during RF excitation. The detuning circuit performs this task by limiting the RF induced currents to negligible levels by switching on high impedance elements in the coil loop [36]. This way, RF induced currents are limited to negligible levels or even canceled out.

There are mainly two categories of decoupling circuits: **passive** decoupling and **active** decoupling.

Passive decoupling could theoretically be achieved geometrically, however, to reduce the interaction to a tolerable level by this method, the mutual orientation of the two coils should be adjusted with a high degree of accuracy which is impossible in practice. Hence, in most of cases, a geometric decoupling should be accompanied by another effective means that cancels out or at least minimizes the induced currents in each coil [32]. Back to back diodes may be used to produce a circuit element that conducts at voltage above a certain threshold. When the RF field is transmitted, the induced current alternatively switches one of the diodes within the circuit, activating the detuning circuit or not. Edelstein et al [35] proposed and efficient circuit that employs passive crossed diodes. An auxiliary inductance (L_2 in the following example, Figure 2-3-Left) is connected by the switching diodes in parallel to one of the surface coil tuning capacitors (here C_2), constituting a resonant blocking circuit (also called detuning trap or pole insertion). The trap detuned the detection coil when activated by a PIN diode, i.e. when the diode's forward-bias threshold was exceeded by the transmit trigger voltage. The diodes act as a switch connecting the resonant trap to the coil, thus inserting a high impedance parallel L_2-C_2 circuit in series in the loop and preventing significant current flow in the receiver loop. The transmitted field will be unaffected by currents in the receiver coil if the impedance of the receiver blocking circuit is substantially greater than the impedance of the closed receiver loop.

Active decoupling still makes use of diode properties and becomes particularly efficient when using PIN diode. In this configuration, diodes are biased by an external circuit that delivers DC synchronized with the pulse sequence. The DC is provided by the MR scanner. Edelstein et al proposed an active detuning trap in which the diodes can be PIN diodes actively driven by a current sent down the input cable. The connections of the switching diode to the diode driver device require a choke inductance. This inductance provides a path to the DC power while presenting a high impedance to the RF current at the operating frequency to block RF path in the active decoupling circuit. During reception (Rx), the diode is biased off, and the MRI signal is conducted from the antenna to the scanner.

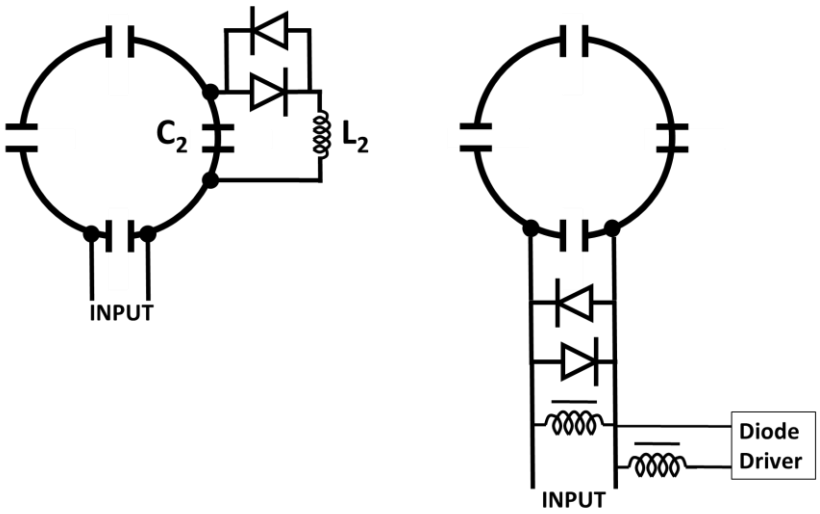

Figure 2-3: Passive (left) and Active (right) decoupling configurations. Modified from Edelstein et al., 1986

Advantage of the passive decoupling is its intrinsic wireless property, which avoids introduction of cables inside the patient and the associated safety challenges (see Chapter 4). However, passive detuning may be not sufficiently effective because, depending on RF pulses used, the induced current is not always sufficient to activate the PIN diode which can again affect the uniformity and contrast in the resulting image. Moreover, the high conduction losses in fast switching diodes may induce for intravascular coil considerable heat inside patient's body [37]. Hence, in the most configurations, active detuning is thus preferred since more reliable and faster.

2.4.3.4. Coaxial cables: safety concerns

Conventionally, the DC bias current is provided by the MR system and transmitted using a coaxial cable. However, for clinical use, conducting coaxial cables linking the coil (deeply introduced into the patient) to the connecting plug of the MR system may induce safety issues (cf Safety chapter). In this situation indeed, the electrical field accompanying the RF magnetic field B_1 induces current in the conducting cables at the same frequency, resulting in local hotspots at the cable-tissue interface. This issue limits the use of intravascular probes.

Coaxial cables or transmission lines are used to transport the RF energy. They are composed of two conductors laid concentrically along the same axis (Figure 2-4-Left). The core (center) is a copper wire which allows the transport of the signal. This copper wire is surrounded by a dielectric insulator, which is in turn surrounded by the outer conductor, producing an electrically shielded transmission circuit. The whole cable is then wrapped in a protective plastic sheathing. The dominant mode of propagation within a transmission line is the transverse electromagnetic mode.

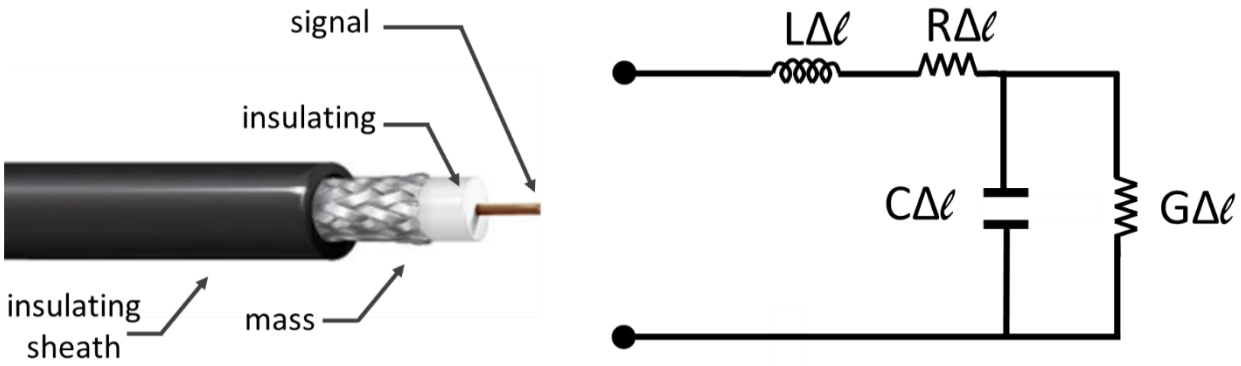

Figure 2-4: Composition of a coaxial cable (left) and its corresponding electrical representation. Modified from [34]

Figure 2-4-Right represents a segment of a transmission line where the inductance L per unit of length of a transmission line is the inductance of the loop formed by the current flowing in one of the conductors (of unit length) and the capacitance C is the capacitance per unit length between the two conductors. The losses in the transmission lines are determined by the series resistance R of the conductors and by the conductance G of the dielectric medium[32].

Efficient transfer of energy is done when the transmission line functions in the so-called differential mode. In this mode, the currents in the two wires flow in opposite directions and the electromagnetic field created outside the line is negligible. However, an undesired mode may also be excited, the so-called common mode. In this mode, the currents in both conductors flow in the same direction. The transmission line becomes thus “asymmetrical” and the common mode is the transmission mode of parasites. One of the reasons this common mode exists is a poor grounding. In this mode, the coaxial cable can act as an

antenna in which standing wave propagates. The generated current exhibits maxima at distances corresponding to an odd number of quarter wavelength as shown in the following schemes [34]:

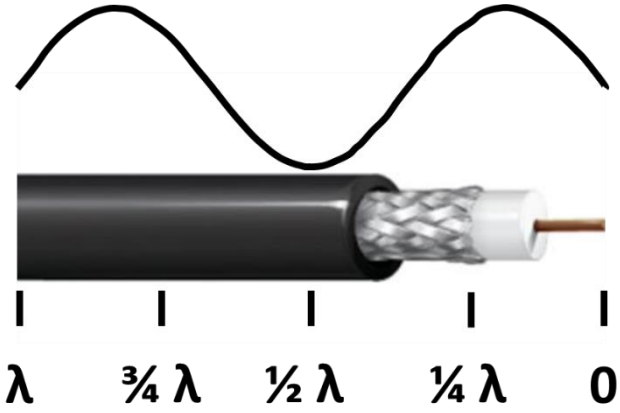

Figure 2-5: Standing wave propagating in a coaxial cable in common mode and positions of the maxima.

An electromagnetic field is generated that radiated outside the cable, leading to losses, probe coil detuning and RF interference. It may also lead to patients burning in clinical MRI. This phenomenon is well documented and several authors have clearly highlighted the considerable temperature increase at the tip of the coaxial cable, where the electric field is the most intense [11], [14], [38]. Different approaches have already been proposed to reduce these RF-induced currents such as adding coaxial choke [14] or baluns matching circuits and traps [39].

2.5. Conception, development and interfacing of intra-cardiac MRI coils

The technical developments, which are described in the following in order to manufacture the surface loop coil, were carried out in collaboration with the research group of Biomaps (Dr. Marie Poirier-Quinot and Dr. Isabelle Saniour). Preliminary researches were conducted upstream the collaboration in order to select the most suitable coil design that would fit with the geometry of the atria. Collaboration started in September 2018 with the goal of improving the design of the loop coil, printing it and implement the optical decoupling to address safety issues raised by the catheter coil. Such developments were based on the already published work of Saniour et al., [15]. We worked together to adapt her research

works to the circuit I had previously designed. Dr. Saniour was of great help with the printing and development of the interfacing laser box for optical decoupling.

Design criteria

When designing a coil, as previously discussed, one have to think about the anatomic target and application our coil is intended to. Shape and size will depend on this first step. For an intravascular coil to perform well at imaging the cardiac cavity, it should have several properties [16]:

- a high sensitivity at the close vicinity of the coil
- a minimized sensitivity fall off radial to the coil, which makes it highly selective allowing thus a reduced FOV
- an homogeneous response to objects radially equidistant to it
- an homogeneous response to objects axially equidistant to it
- an insensitivity to the orientation around B_0 axis

These criteria were carefully validated in the following and represent a large part of the realized work.

2.5.1. Design

A conductive circular loop seemed the most appropriate design to image cardiac arrhythmogenic substrate within the atrium [7], [8]. Diameter of the coil was chosen regarding two parameters: the dimension of the typical Left Atrium (LA) chamber of patients and the desired penetration depth at which the local loop-coil sensitivity should be the highest (covering the typical left atrial wall thickness ranging from 3-5 mm). Moreover, dimension of the cryoablation ballons (23 and 28 mm, Artic Front, Medtronic) and Lasso mapping catheters (12-35 mm, BiosenseWebster) used for the treatment of AF [40] served as a reference to get an idea of the order of the possible diameters. Considering these elements, we chose a diameter of 2 cm.

The 2 cm-diameter (inner diameter) receive-only circular loop coil was designed using a 35 µm-thick copper trace on a FR4 (*Flame Resistant 4*) substrate (relative permittivity $\varepsilon_r = 4$,

thickness t = 0.8 mm). The width e of the circular coil inductance trace was 3 mm which gives an outer diameter r_{ext} of 23 mm. The thickness ℓ of the copper trace was chosen in accordance with the skin depth δ of the copper (magnetic permeability: $\mu = 1.25 \times 10^{-6}$ H/m, conductivity: $\sigma = 5.96 \times 10^{7}$ S/m) at the resonant frequency (f = 63.6 MHz; AERA magnet, Siemens). At this frequency, the current distribution in the conductor is not uniform. In fact, it is concentrated on the surface of the conductor, over a limited thickness called “effective area”. This induced a resistance (called AC resistance in opposite to DC resistance) greater than that determined in direct current (DC) regime, affecting the quality factor of the coil and increasing the Joule effect. To limit this problem, the thickness of the conductor has to be greater than the skin depth δ [34]:

$$\delta = \frac{1}{\sqrt{\pi f \mu \sigma}} = \sqrt{\frac{2}{\omega_0 \mu \sigma}} = \sqrt{\frac{2\rho}{\omega_0 \mu}} \qquad (2\text{-}10)$$

with ω_0 the pulsation of the sinusoidal excitation at the Larmor frequency in rad/s and ρ the resistivity of the copper (1.70×10^{-8} Ωm). The skin depth of the copper, at this frequency, is 8.2 µm

2.5.2. Tuning and matching of the coil

Given the geometry and the dimension of the circular surface coil, theoretical value of the inductance was computed according to the following equations corresponding to the geometry given in Figure 2-6 [32]:

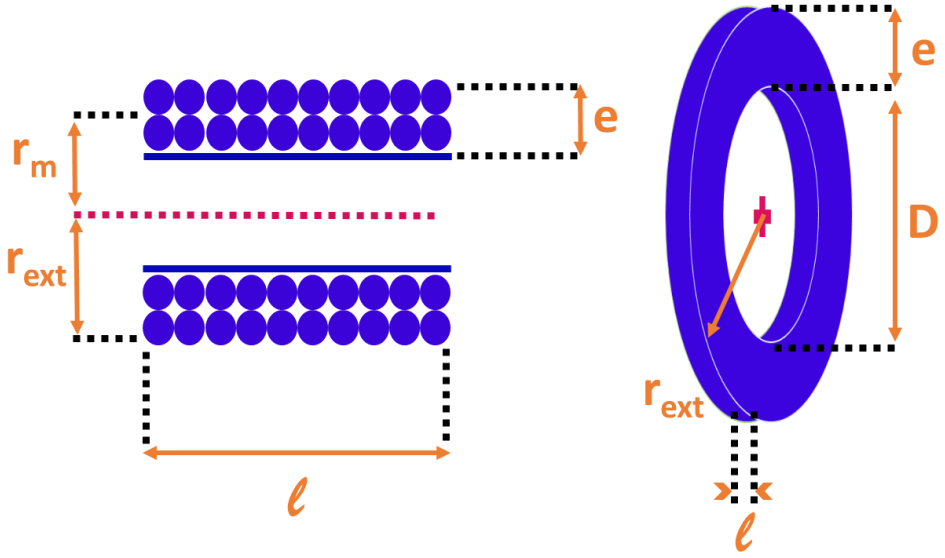

Figure 2-6: Geometry used for the self-inductance computation. Modified from Mispelter Book (Appendix A,p.695)

$$L = 0.4\pi^2 n^2 \frac{r_m^2}{l + e + r_{ext}} AB$$

$$A = \frac{10l + 12e + 2r_{ext}}{10l + 10e + 1.4r_{ext}} \qquad (2\text{-}11)$$

$$B = 0.5\log_{10}\left[100 + \frac{14r_{ext}}{2l + 3e}\right]$$

with n the total number of turns (n=1 in our case). The resulting value is in nH and the dimensions are given in mm. This formula assumes that the dimensions are much smaller than a wavelength, which is the case ($\lambda_{1.5T,air}$ = 4.8 m). Theoretical value of inductance was found to be L_{the} = 43.5 nH. In addition, experimental value of the inductance was measured on a Vector Network Analyzer (VNA) by adding a known capacitor at the terminal of the circular loop wire and was found to be 41 nH.

Theoretical value allowed us a first estimation of the capacitors' values required for the tuning and matching. A local, parallel tuned/series matched circuit was implemented to

tune the coil at the operating frequency ω_0. The loop was adapted using a capacitive coupling, as introduced in the section 2.4.3.2. This method is the most common: it is based on the addition of a capacitor C_m to obtain the desired input impedance (50 Ω in our case) in order to limit the power reflection. Tuning was realized using a combination of two capacitors C_{t1} and C_{t2}. The capacitors (100B, American Technical Ceramics (ATC), New York, USA) were chosen to be small (2.79 x 2.79 x 2.59 mm, L x W x T) and non-magnetic (ceramic-based with non-magnetic barrier termination). Additionally, these capacitors have a high quality factors Q in the range of 1000 at 63.6 MHz. The receiver coil was designed to operate with an AERA 1.5 T MR System (Siemens, Erlangen Germany, f_0 = 63.6 MHz). Values of each component (capacitors and inductance) were computed using the following equations in Figure 2-7.

As we want C_{t1} in series with L be an inductance, this condition fixes the minimum value of C_{t1}. L_d is the inductor used together with C_{t1} to form a blocking resonant circuit when detuning is activated (i.e., when PIN diode is activated), see 2.4.3.3. According to [34], the resistance R (Figure 2-2) is relatively low (around 0.7 Ω). Therefore, for simplicity, R is not represented in the above schemes.

L_{the} = 43.5 nH	F_a = 2 MHz	F_a = 20 MHz	F_a = 43 MHz	F_a = 62 MHz
C_{t1} (pF)	145658	1457	315	152
C_{t2} (pF)	144	160	265	2899
L_d (nH)	0.04	4	20	41

Table 2-1: Theoretical values of Ct1, Ct2 and Ld computed from the above equations.

Given C_{t1}, C_{t2} can be determined as well as L_d. Regarding these equations and the theoretical value of inductance, we found theoretical values of C_{t1} = 315 pF, C_{t2} = 265 pF and L_d = 20 nH to be a good set of values, avoiding high values of capacitances (orange values in Table 2-1).

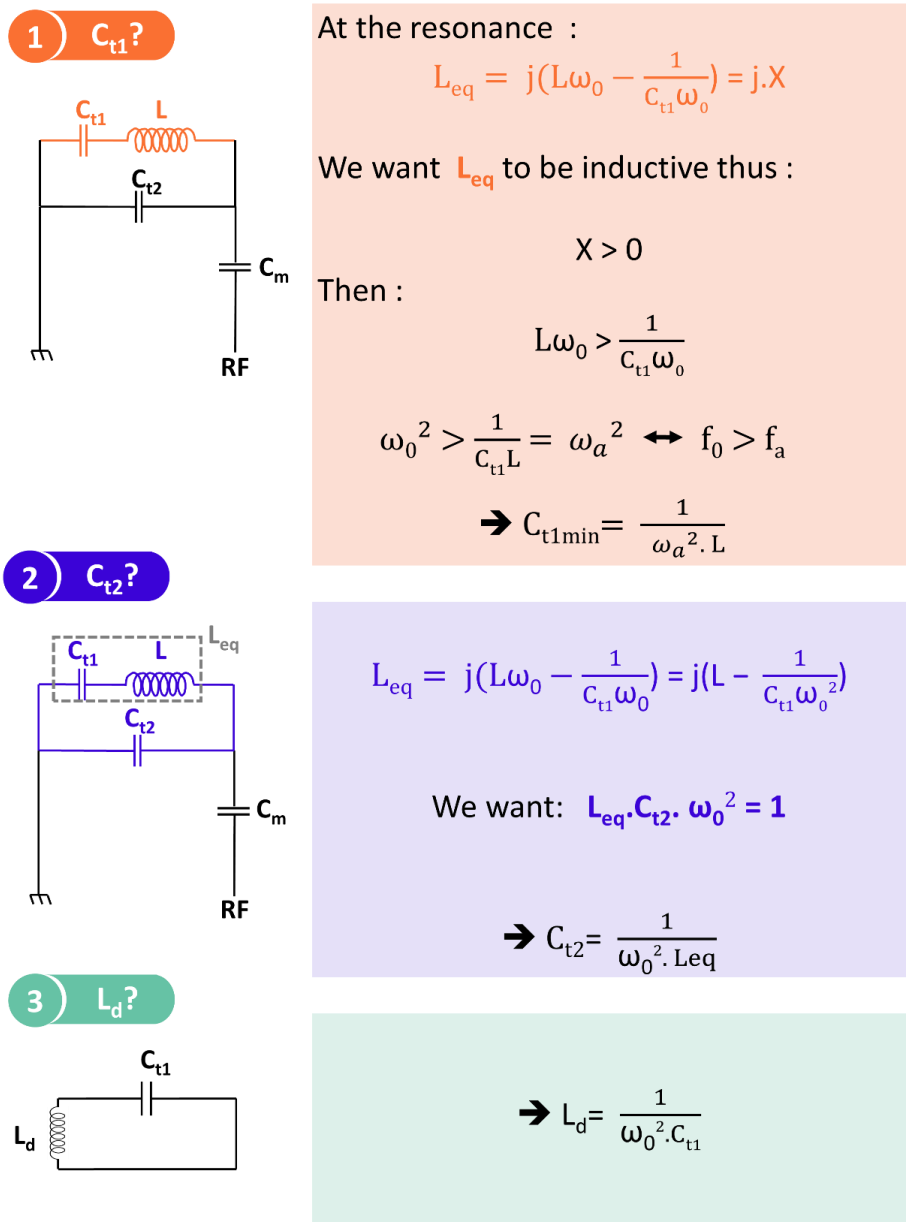

Figure 2-7: Schematic of the electrical circuits and corresponding equations used to compute the theoretical values of the capacitors.

The matching capacitor was experimentally chosen to maximize the quality factor. A coaxial cable (36 AWG, mouser), 1.8 m length with a characteristic impedance Z_c = 50 Ω was used to link the coil circuit to the interface network and performances of the resulting coil was tested in terms on both quality factor and SNR.

2.5.3. Classical active decoupling with galvanic connections

An active decoupling circuit was implemented using a PIN diode added to the resonant circuit. The switching diode was connected to the diode driver using a choke inductance which role is to block RF path in the active decoupling circuit. The impedance value of the choke, at the operating frequency, is dependent on the impedance value of the circuit where the inductor is inserted. In our case, the impedance value of the circuit being 50 Ω, a value of inductance of about 1 µH is recommended [32]. According to this, we chose a value of 1.2 µH for the choke inductance.

Capacitor values based on the theoretical values were adjusted to ensure an optimal tuning of the coil to 63.6 MHz and its adaptation to 50 Ω. Furthermore, the PIN diode welded in parallel with one of the tuning capacitors slightly disturbed the input impedance of the coil, requiring fine adaptation of the tuning and matching capacitors. Tuning and matching values were 333 pF for C_{t1}, 289 pF for C_{t2} and 12 pF for C_m. These values are close to the theoretical values. Indeed, the capacitors welded on the loop have a tolerance of 5% compared to their nominal value. In our case, the tuned capacitor C_{t1} of the tuning network was used together with L_d to form a blocking resonant circuit when the diode is activated

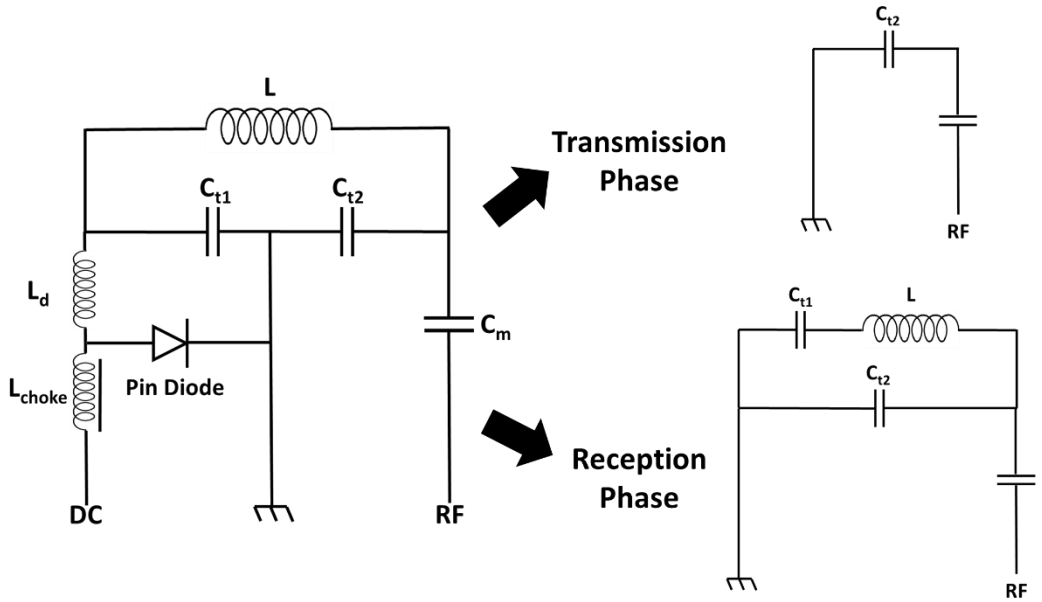

Figure 2-8: Equivalent circuit for the Transmission and Reception phases. During the transmission phase, the PIN diode is switched on, the inductor Ld together with Ct1 constitute a resonant blocking circuit and detune the coil. During reception, the diode is biased off, and the MRI signal is conducted from the antenna to the scanner.

via the DC bias current provided by the MR system. The value of L_d was 18 nH which is close to the theoretical value. During the transmission, a direct current of the order of 100 mA current (max +12 V) is emitted by the Siemens 1.5 T MR system to detune the coil. In opposite, during the reception, the scanner imposes by default a negative voltage (around -30 V, and an approximately -300 mA) to ensure functionality of the receiver coil. In the case of conventional decoupling, these signals are used to activate (with current of 100 mA) or block (with the negative voltage of -30 V) the PIN diode added to the resonant loop. Equivalent electrical circuits of the loop coil are provided in Figure 2-8 for both transmission and reception phase.

The coil was implemented (Figure 2-9) with the geometry and dimensions of the copper traces and substrate corresponding to those given in the paragraph 2.5.1.

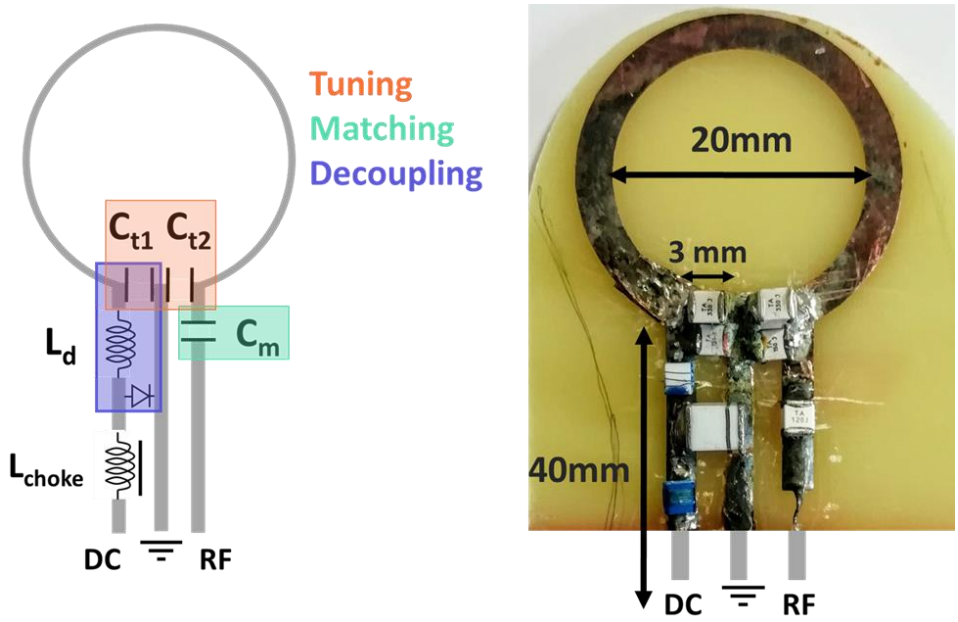

Figure 2-9 : Galvanic Decoupling. **Left-** Electrical scheme of the optical decoupling. **Right-** Photo of the galvanic-detuned coil circuit.

2.5.4. Optical decoupling

2.5.4.1. Implementation

In order to address safety issues, an optical decoupling circuit, devoid of any galvanic connections to drive the DC current to the PIN diode was implemented. These

developments were based on the published work of Dr. Saniour and were realized in collaboration with Biomaps.

Regarding the technical implementation, modification of the conventional active decoupling circuit consisted in adding a photodiode to transmit the DC current to the PIN diode and a shunt resistance to force the rapid discharge of the photodiode, as described in [15]. The photodiode simply acts as a current source controlled and supplied by an external optical device. Figure 2-10 shows the electrical representation together with the technical implementation.

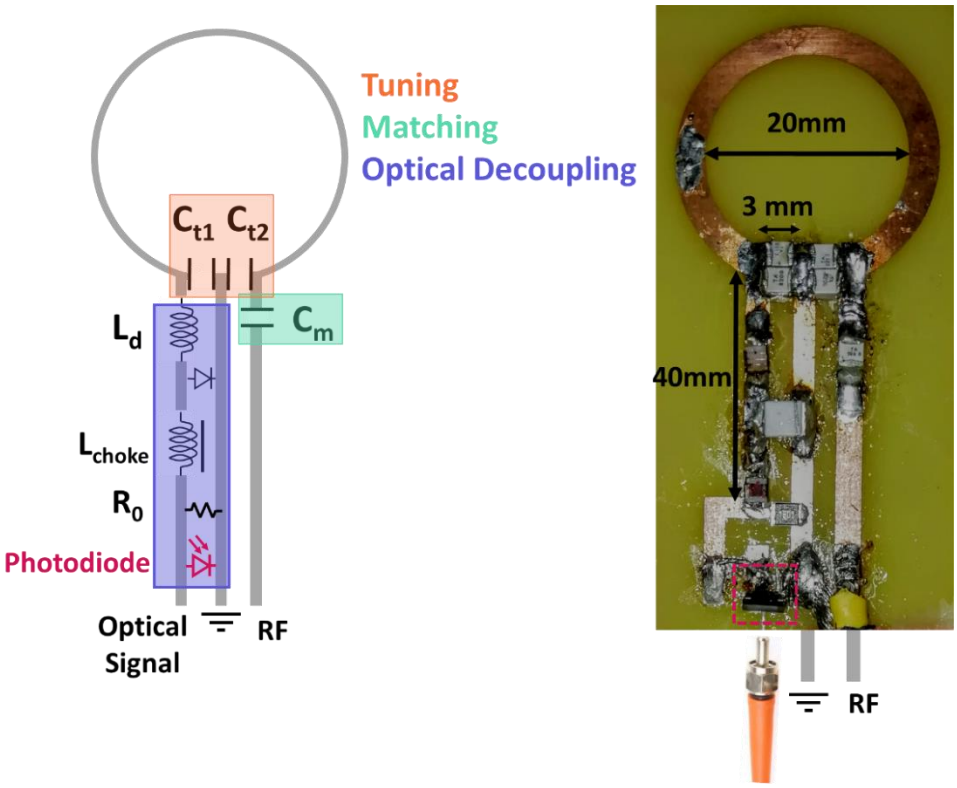

Figure 2-10: Optical Decoupling. **Left-** Electrical scheme of the optical decoupling. **Right-** Photo of the optical decoupling circuit. The photodiode is indicated by the pink frame.

Original implementation comprised two photodiodes but in our configuration, only one photodiode was sufficient to ensure the requested voltage for a PIN diode to operate in direct mode. A silicon S12158-01CT photodiode (Hamamatsu Photonics, Japan) was used, with a 2.77 x 2.77 mm photosensitive area.

This photodiode was chosen in accordance with the following requirements [34]:

- The amplitude of the current generated by the photodiode must be sufficient to ensure activation of the PIN diode.
- The photodiode has to be 'low-magnetic' in order to be MR compatible
- Geometry and size of the photodiode should be small enough to fit with the dimension of the receiver only loop and to be further embodied in a catheter sheath.
- The response time of the photodiode should be low to ensure the optical-to-electric conversion be fast enough. Indeed, the application times of the RF pulses in clinical MRI sequences are in the order of milliseconds at minimum. The circuit of optical decoupling that contains the photodiode must therefore switch quickly before these application times, in other words, having a commutation time of a few microseconds to more.

Tuning and matching values were 302pF for C_{t1}, 302 pF for C_{t2} and 13 pF for C_m. L_d was 18 nH. Similarly to the galvanic detuning circuit, a choke inductor of 1.2 µH was added between the loop and the photodiode to block any alternating current from interacting with the detuning circuit during NMR reception phase. This choke inductor also prevents the photodiode impedance from changing the blocking circuit resonance frequency. When switching from detuning to tuning phase, the response of the coil is slow. Indeed parasitic capacitance of illuminated photodiodes enables photoelectrons to accumulate. Once light is off, these residual charges slowly flow out through the PIN diode which is still weakly biased (under the threshold voltage) (Saleh et al 2007). Hence, a shunt resistance R_0 of 1.8 kΩ was added in parallel to force a rapid discharge of the photodiodes [15]. This value was experimentally determined by Isabelle Saniour during her PhD and is a tradeoff between the adequate value of resistance to ensure the minimum commutation time to tuning mode and reciprocally to detuning mode.

2.5.4.2. Optical converting unit

In order to detune the coil, the photodiode added to the coil has to be illuminated by using a 30 mW fibred modulated laser diode (Laser Components ®, Germany, λ = 650 nm). An optical fiber (Radiospare, 0.2 mm core diameter, SMA connector) was used to transmit the optical signal from the laser diode to the center of the photosensitive area of the

photodiode. In order to convert directly the outgoing DC current provided by the MR scanner system to an optical signal, an optical converting circuit (also named laser command circuit) was designed. The optical conversion begins when the MR system provides a bias DC current (+100 mA) or a negative voltage to detune the coil by turning on the laser diode or tune the coil back by turning it off. The required voltage to turn on or off the laser is 0 V and 5 V respectively. However, the MR sent a voltage of -30 V in reception phase and + 15 V in transmission phase (data sheet of the constructor). Therefore, an inverting operational amplifier (TL081) with resistors $R_1 = 33$ kΩ and $R_2 = 6.7$ kΩ was used to adapt the output voltages of the DC trigger to the modulation threshold of the laser diode. Figure 2-11 illustrates the scheme of the inverting operational amplifier and a photo of the optical converting unit integrating the inverting amplifier, the laser diode and the battery for both the amplifier and the laser diode.

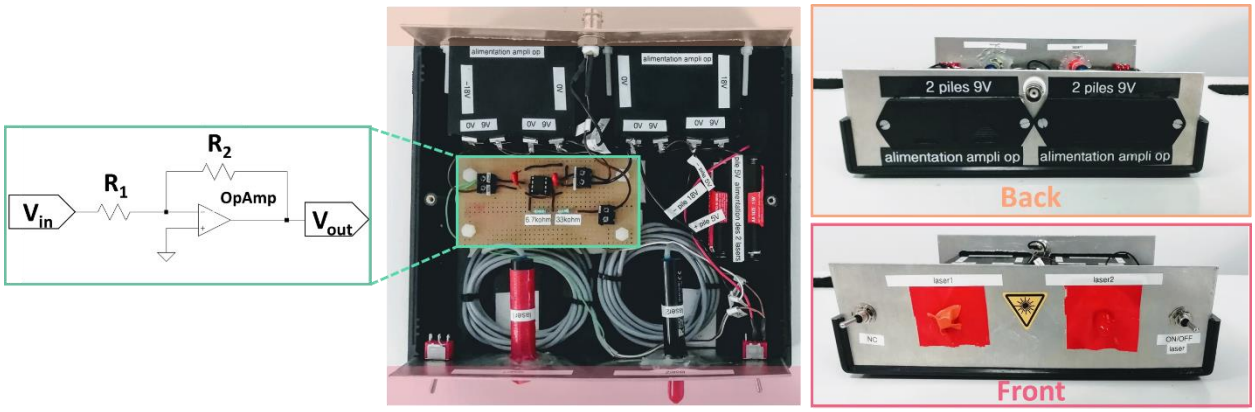

Figure 2-11: Photograph of the optical converting unit. Blue frame indicates the inverting operational amplifier and its associated electrical scheme.

Figure 2-12 represents the conversion chain of the direct current sent by the MR scanner to an optical signal. This optical signal is transmitted via an optical fiber and directly injected in the photosensitive area of the photodiode.

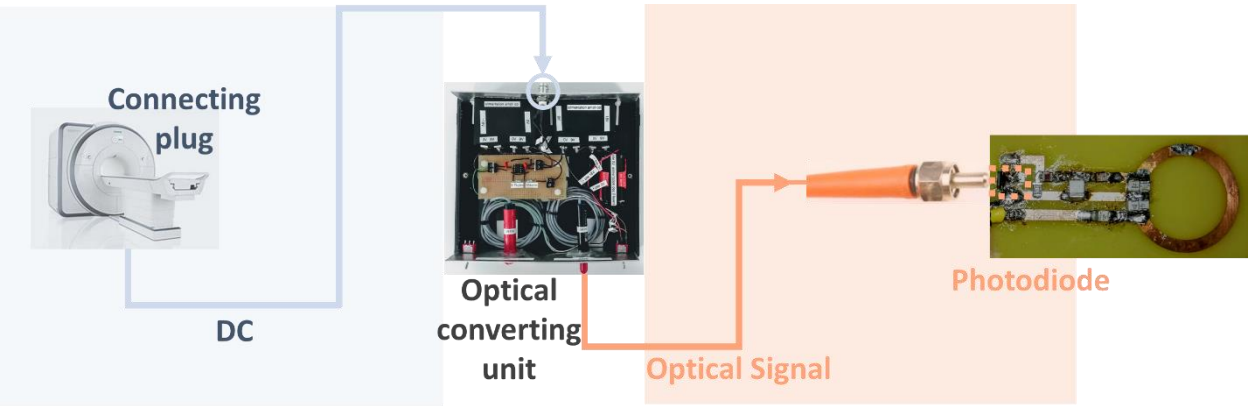

Figure 2-12: Conversion chain of the direct current. The DC sent by the MR table fed the input of the optical detuning unit (blue). The optical converting unit converts the DC into an optical signal that is transmitted via an optical fiber to the photodiode of the optical detuning circuit of the loop coil.

2.5.5. Interfacing the receiver coil with the MR scanner

A dedicated interface box (named 8_Ch_Box) was designed in collaboration with Dr. Helmut Stark who ensures support on RF coils and MRI hardware for Siemens. It consists of 8 BNC connectors (receive mode) in order for us to develop different types of coil that could be combined and an output for DC supply in order to feed both the galvanic and optical decoupling circuit. The add-on system was designed to interface with a 1.5 T MRI system (MAGNETOM Aera, Siemens Healthcare, Erlangen Germany) using the system's local transmit coil interface ('Total Imaging Matrix', or TIM adaptor), located on the patient bed, as the primary interface. To suppress dangerous currents on the cable to the receiver coil, and thus to ensure patient safety, cable trap was placed on the receiver cable. A coil file was added to the scanner to allow recognition of this interface by the MRI. On the scanner imaging interface, each Rx channel could then be selected individually (RX1-RX8) and the elements that were not selected had detuning current for the PIN diode all the time during the sequence.

Figure 2-13: Interface box to connect the coils to the MR table. The box includes a detuning trigger (extra BNC socket) that provides the DC signal during the transmission phase. Each coil can be connected to one of the 8 RX channels and individually selected on the scanner imaging interface.

2.6. Characterization of the RF coils on the RF Workbench

Characterization of the resonant loops was performed using a Vector Network Analyzer (VNA, DG8SAQ USB-Controlled VNWA 3, SDR-Kits®, United Kingdom) on phantom. The phantom consisted of a bottle filled with a solution of 3.75g $NiSO_4$ x $6H_2O$ + 5g NaCl per 1000g distilled H_20.

From an electrical point of view, the probe, in its simplest form, behaves as a one-port network. The impedance presented at the input should be matched to a real 50 Ω value, at a particular frequency. Using VNA, the amplitude and phase information of the electrical network as a function of frequency can be measured. The reflection coefficient modulus $|S_{11}|$ as a function of the frequency and Q factor were measured for each coil prototype when not loaded or loaded with a quality assurance phantom. The quality factor was

measured by dividing the resonance frequency by the bandwidth at -3dB (2-8). For every experiment, the Rx part of the coil was connected to the Tx Out sma plug of the VNA.

2.6.1. Galvanic-detuned coil

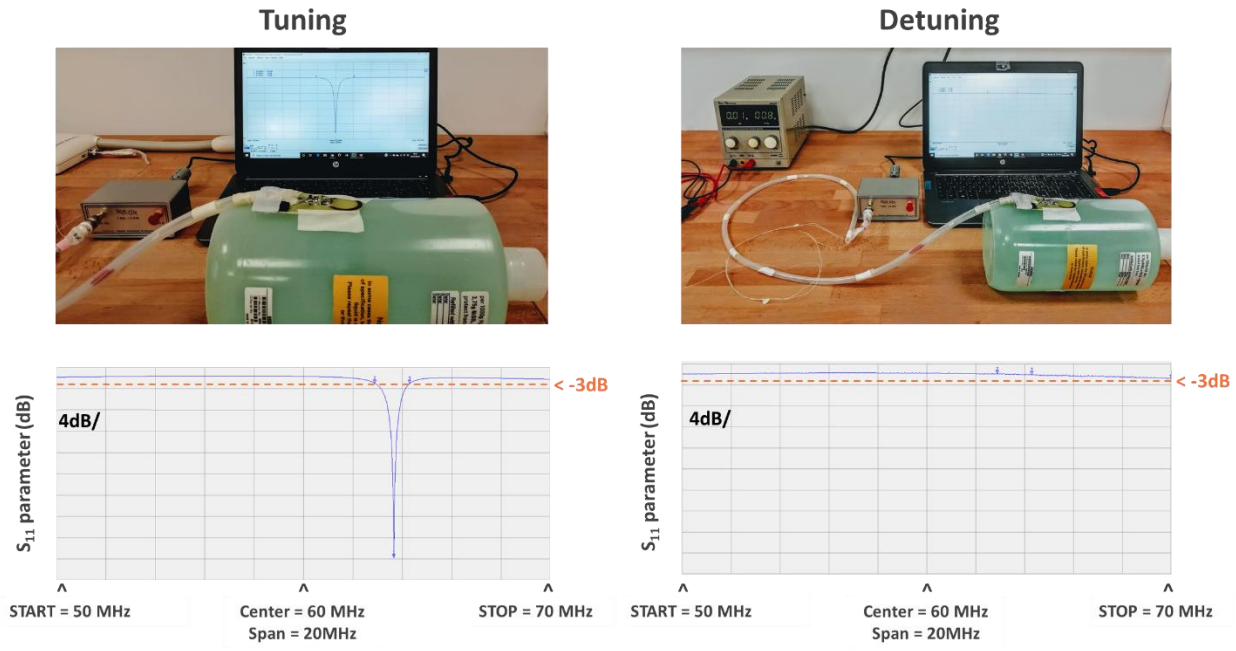

Figure 2-14: Photograph of the RF workbench used to characterize the tuning and matching of the galvanic-detuned coil as well as the efficiency of the decoupling circuit when coil is loaded by the phantom. Screenshots of the VNA measurements ($|S_{11}|$ parameter in dB) demonstrate a sharp peak at 63.59 MHz when coil is tuned and no peak when coil is detuned.

The resonance frequency of the coil was 63.59 MHz. The quality factor of the tuned coil when not loaded was 49 and 45 when loaded with the phantom. No difference was observed when coil was connected to the interface box or not. On tuned mode, when the coil was loaded, the reflection coefficient $|S_{11}|$ was -37.6 dB. This value confirmed that the probe was correctly tuned and matched. In order to test the detuning performance, a 100 mA DC current and 0.8 V voltage was generated by a voltage generator and transmitted via a coaxial cable to the detuning part of the coil, as indicated in Figure 2-14. On detuned mode, $|S_{11}|$ was 0.9 dB, illustrating the efficiency of the detuning circuit.

2.6.2. Optical-detuned coil

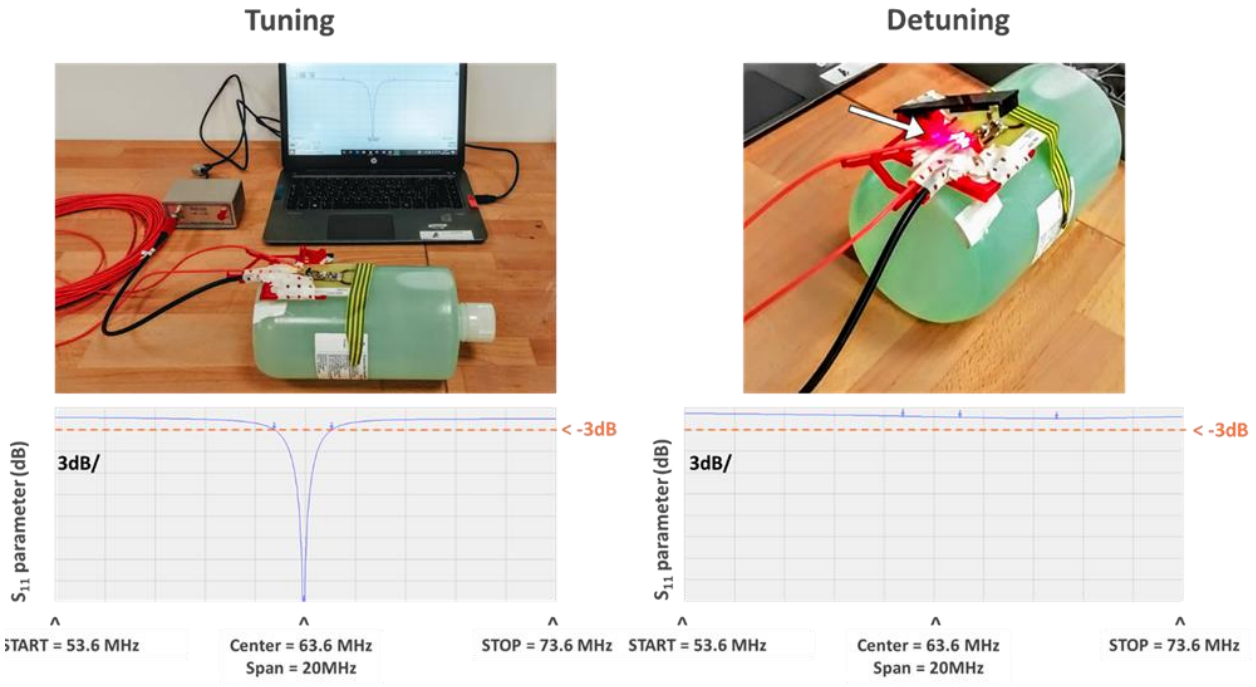

Figure 2-15: Photograph of the RF workbench used to characterize the tuning and matching of the optical-detuned coil as well as the efficiency of the decoupling circuit when coil is loaded by the phantom. Screenshots of the VNA measurements ($|S_{11}|$ parameter in dB) are given for both tuning and detuning modes. Detuning of the coil was ensured by turning ON the laser, as indicated on the picture (white arrow).

The resonance frequency of the coil was 63.53 MHz. The quality factor of the tuned coil when not loaded was 44 and 35 when loaded with the phantom. On tuned mode, when the coil was loaded, the reflection coefficient $|S_{11}|$ was -35.2 dB. Optical detuning was tested by turning on the laser. One photodiode was found to be sufficient to ensure optimal decoupling of the coil. On detuned mode, at 63.6 MHz, the reflection coefficient of the coil was -1.1 dB. This result demonstrates that the current provided by only one photodiode was sufficient to properly detune the coil. Photograph of the setup and screenshots of the reflection measurement with the VNA are provided in Figure 2-15.

2.6.3. Evaluating efficiency of the optical detuning unit

In order to test the efficiency of the laser command circuit, a pick-up coil was connected to a frequency synthesizer generating a 63.6 MHz sinusoid. The pick-up coil was used to

make the optical-detuned coil resonates at 63.6 MHz. A voltage generator was calibrated to provide a square signal between -10 V and +2 V at 1Hz. These values were used to simulate the DC bias provided by the MR scanner. The optical detuning circuit of the coil was supplied by the optical fiber transmitting the optical signal obtained at the output of the laser command circuit. The Rx part of the optical-detuned coil was connected to the first channel of the oscilloscope. The second channel was connected to the voltage generator to visualize the square signal. After setting all the parameters and connecting the different part of the experimental bench, we could see that during the transmission phase (when the square DC voltage is at +2 V) the laser was turned on, providing an optical signal therefore decoupling the coil. No oscillation was visible. During the reception phase (when DC voltage is -10V), the laser was turned off and the coil oscillates at 63.6MHz, confirming the reception mode of the coil. The scheme and the corresponding photograph of the experimental workbench are provided in Figure 2-16. A screenshot of the oscilloscope (Figure 2-16c) demonstrates the efficiency of the laser command box.

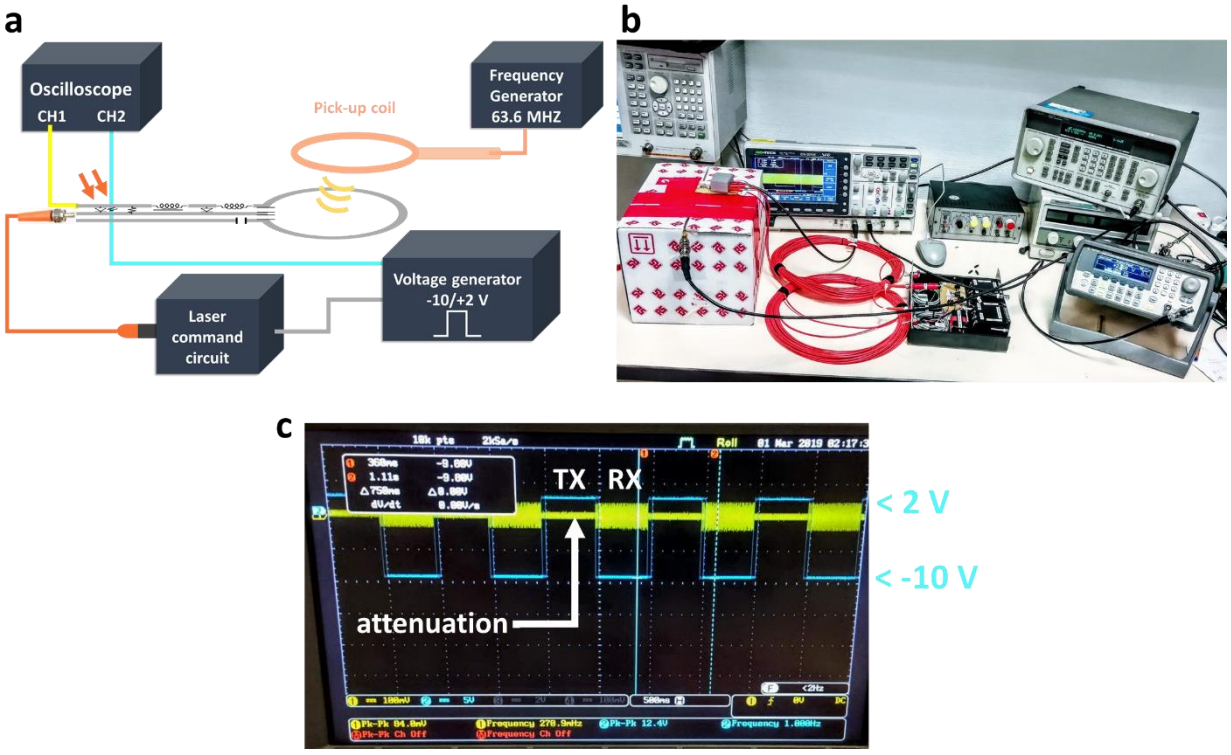

Figure 2-16: Evaluating efficiency of the laser command circuit. a) Schematic representation of the workbench. b) Photograph of the workbench. c) Screenshot of the oscilloscope recording. Channel 1 (yellow) corresponds to the signal generated by the optical-detuned coil and Channel 2 (blue) corresponds to the voltage generator signal.

2.7. Evaluating performances of the loop coils in MRI environment

The two coils were then tested in MRI environment to evaluate their decoupling performances. Signal profile and SNR map for each coil was obtained and compared to conventional chest and spine external coils as well a loop coils from the MR constructor with a diameter of 11, 7 and 4 cm. Further tests were performed to ensure that SNR profile of the custom loop coils was independent of their position relative to Spine and Body antennas of the MR scanner.

2.7.1. Evaluating the two decoupling strategies

Phantom experiments were performed on a 1.5 T MRI (Aera, MAGNETOM, Siemens, Erlangen Germany). Coils were placed on top of the phantom as illustrated in section 2.6.1. For each experiment, marks were made on the phantom to ensure coils were placed at the same location.

Efficiency of both detuning strategy was assessed when coils were physically forced to be detuned and when coils were connected to the interface box with the body coil used as a transceiver. Decoupling between the loop coils and different constructor coils was further evaluated.

2.7.1.1. Evaluating detuning efficiency when detuning is forced

During the MR acquisition, coils were either always tuned (no connection with the MR table) or always detuned. Detuning of the galvanic-detuned coil was ensured with a voltage generator providing a voltage of 0.8V and a current of 100 mA. Detuning of the optical-detuned coil was ensured by permanently turning on the laser. Corresponding image of the phantom without any loop coils was also acquired to provide a reference.

A 2D-balanced steady state free precession sequence was performed with the following imaging parameters: FOV = 300 x 300 mm; Matrix size = 256 x 256 pixels, TR/TE = 7.3/3.7 ms; FA = 20°; bandwidth = 179 Hz/pixels; slice thickness = 6 mm; resulting voxel size was 1.2 x 1.2 x 6 mm^3. A total of 10 transversal images were acquired along the length z of the loops. The body coil was used as a transceiver.

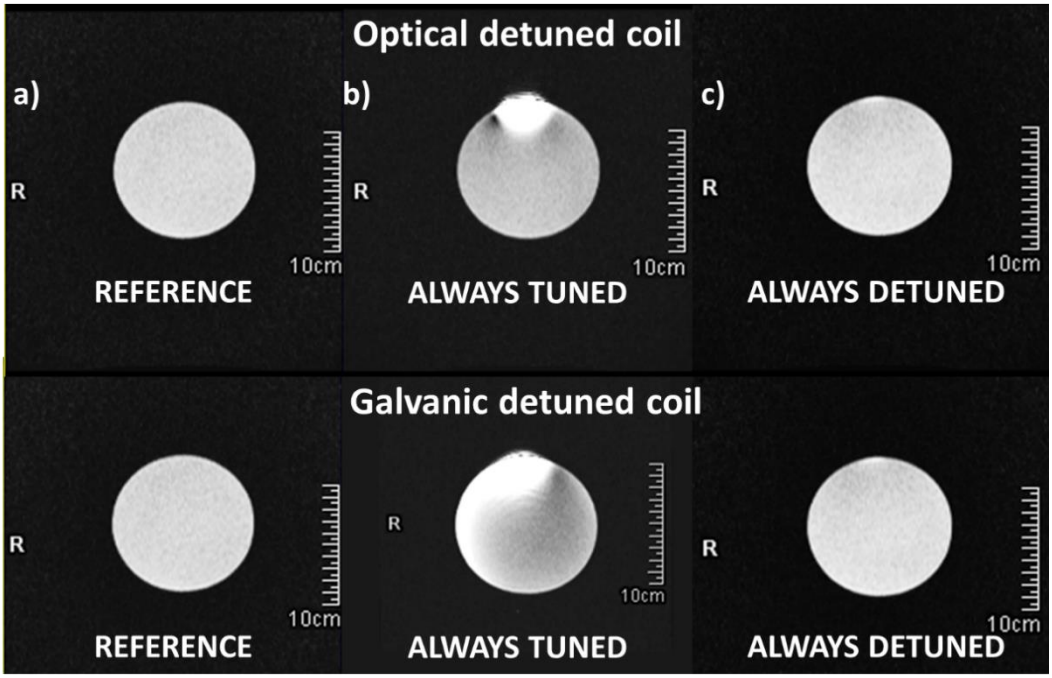

Figure 2-17: Evaluation of the decoupling efficiency for both strategies (Top: optic / Bottom: galvanic). The body coil was used as a transceiver. a) Reference image. b) Coils are always tuned during the MR acquisition. c) Coils are always detuned (forced to be detuned) during the MR acquisition.

Figure 2-17a shows the resulting images when no coil is present (reference image). When coils are always tuned (Figure 2-17b), the image intensity is strongly altered by the cross-coil coupling and a large bright spot can be visualized at the location of the coil. Permanent detuning of both coils (Figure 2-17c) drastically reduced the spot, demonstrating the efficiency of both decoupling strategies. However, a residual tiny bright spot remained at the location of the coil. This may be explained by the fact that compared to MR commercial coils that are encapsulated in a plastic box, our coils were put directly in contact with the phantom without being insulated or without keeping a distance related to the phantom surface. This has certainly resulted in more interactions with the phantom sample. Indeed, as indicated in [32], in general, a small gap (of the order of one tenth the coil diameter) should be kept between the sample and the coil. This way, the parasitic capacitance between the sample and the loop is reduced in favor of a better SNR and reduction of undesired electrical effect.

2.7.1.2. Evaluating decoupling efficiency when coils are plugged into MR table

Experiments were further conducted when both coils were connected to the interface box in order to assess the ability of the box to correctly pilot the decoupling during image acquisition. The galvanic-detuned coil was connected to the detuning trigger (supplying the DC) of the 8_Ch_Box while decoupling of the optical-detuned coil was ensured by connecting the detuning trigger of the 8_Ch_Box to the optical converting unit (as described in 2.5.4.2) for the laser command.

The decoupling efficiency was assessed for three different imaging protocols:

- **2D Gradient Echo (GRE) sequence**: FOV = 200 x 200 mm; Matrix size = 192 x 192 pixels; TR / TE = 125 / 7.4 ms; FA = 71°; bandwidth = 130 Hz/pixels; slice thickness 2.5 mm, Average (Nex) = 4. The resulting voxel size was 1 x 1 x 2.5 mm3. were acquired for a total. Acquisition time was 4 min 48 s.

- **2D balanced Steady State Free Precession (TrueFisp) sequence**: FOV = 200 x 200 mm; Matrix size = 192 x 192 pixels; TR/TE = 8.4 / 4 ms; FA = 93°; bandwidth = 200 Hz/pixels; slice thickness 2.5 mm, Average (Nex) = 4. The resulting voxel size was 1 x 1 x 2.5 mm3. Acquisition time was 21 s.

- **2D Turbo Spin Echo (TSE) sequence**: FOV = 200x200 mm; Matrix size = 192x192 pixels; TR/TE = 3000 / 13 ms; FA = 180°; Turbo Factor = 4; bandwidth = 100 Hz/pixels; slice thickness 2.5 mm, Average (Nex) = 4. The resulting voxel size was 1 x 1 x 2.5 mm^3. Acquisition time was 9 min 41 s.

The body coil was used as a transceiver for all three protocols. Corresponding images of the phantom without any loop coil, were also acquired to provide a basic reference. The SNR calculation was realized using MATLAB language (Mathworks, Milwaukee, USA). The SNR was determined by the mean of the signal intensity in the entire MR image divided by the mean standard deviation of a region of noise chosen outside the image of the phantom (in the air).

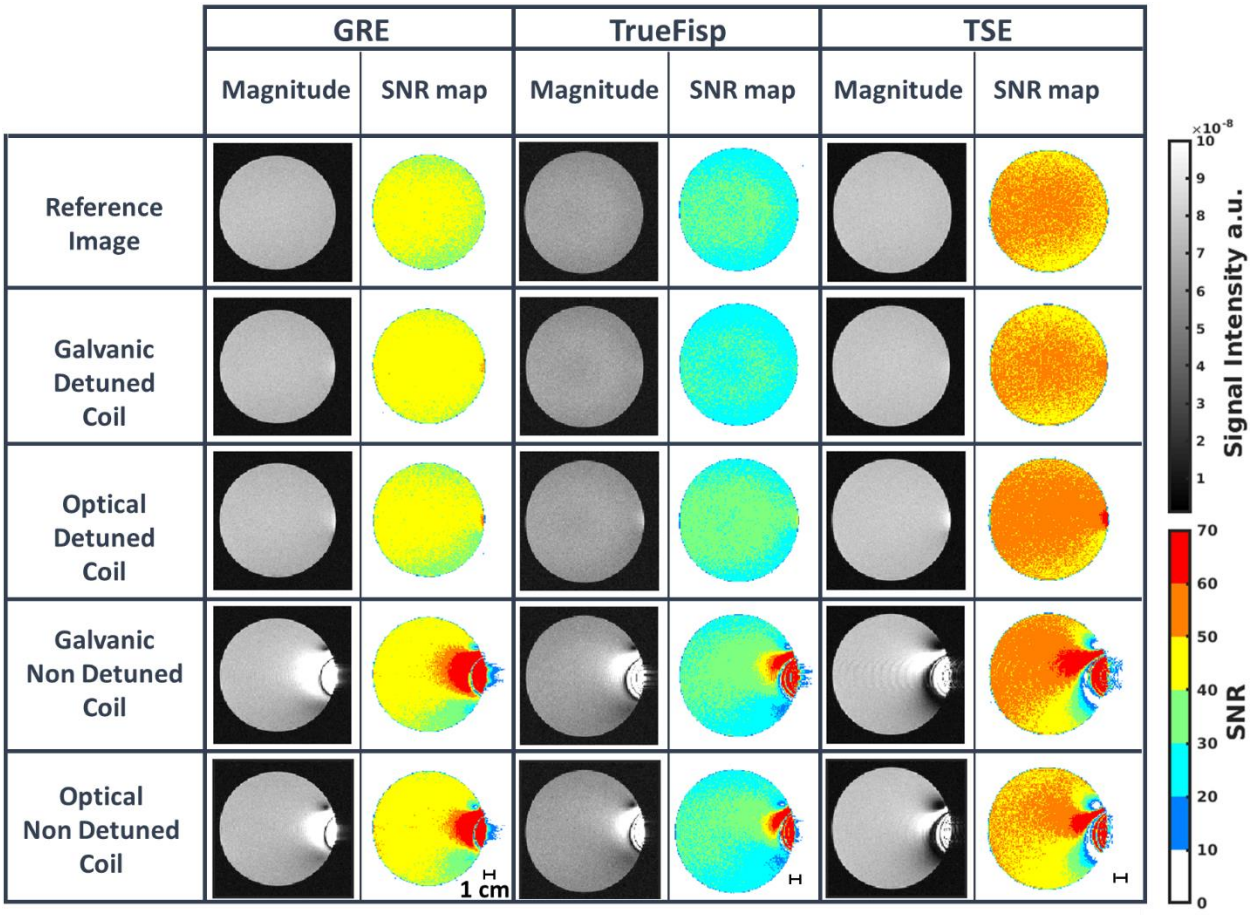

Figure 2-18: Transversal images and SNR mapping of the phantom using GRE, TrueFisp and TSE sequence with the body coils used as a transceiver. During acquisition, detuning of the coils was ensured by the interface box (Galvanic Detuned Coil and Optical Detuned Coil). Same experiments were performed when coils were always tuned (i.e., disconnect from the interface box)

Transversal images together with their associated SNR maps are displayed in Figure 2-18. Signal intensity images and SNR maps corresponding to the non-detuned coils clearly show the non-uniform signal distribution close to the coil caused by the RF B_1 field, demonstrating the coil detuning is mandatory. In addition, the signal intensity profile shows a distinct pattern with different regions of hyper or hypo contrast depending on the sequence used. For each sequence, the signal intensity profile images and SNR maps acquired with the detuned coils are uniform and very comparable to the basic reference image.

2.7.1.3. Decoupling between the loop coils and the routinely used coils in clinic

Efficiency of the decoupling between our loop coils and the coils routinely used in clinic for cardiac MRI was assessed.

A 2D GRE was performed with the following parameters: FOV = 200x200 mm; Matrix size = 192 x 192 pixels; TR/TE = 1784 / 5 ms; FA = 15°; bandwidth = 300 Hz/pixels; slice thickness 2.5 mm. The resulting voxel size was 1 x 1 x 2.5 mm3. Acquisition time was 1 min 47 s. The body coil was used in transmission and 18 chest elements plus 4 spine elements were used to receive. A total of 30 images were acquired (10 per orientation: Transversal, Coronal and Sagittal), each spaced of 0.125 mm (total of 30 images).

Figure 2-19 shows, for each orientation, the central image of the stack chosen to be in the middle of the coil sensitivity as pictured on the top of the figure. The signal intensity profile of the detuned coils is similar to the signal intensity profile of the reference image independently of the orientation and SNR maps of both detuned coils are uniform and very comparable to the reference image.

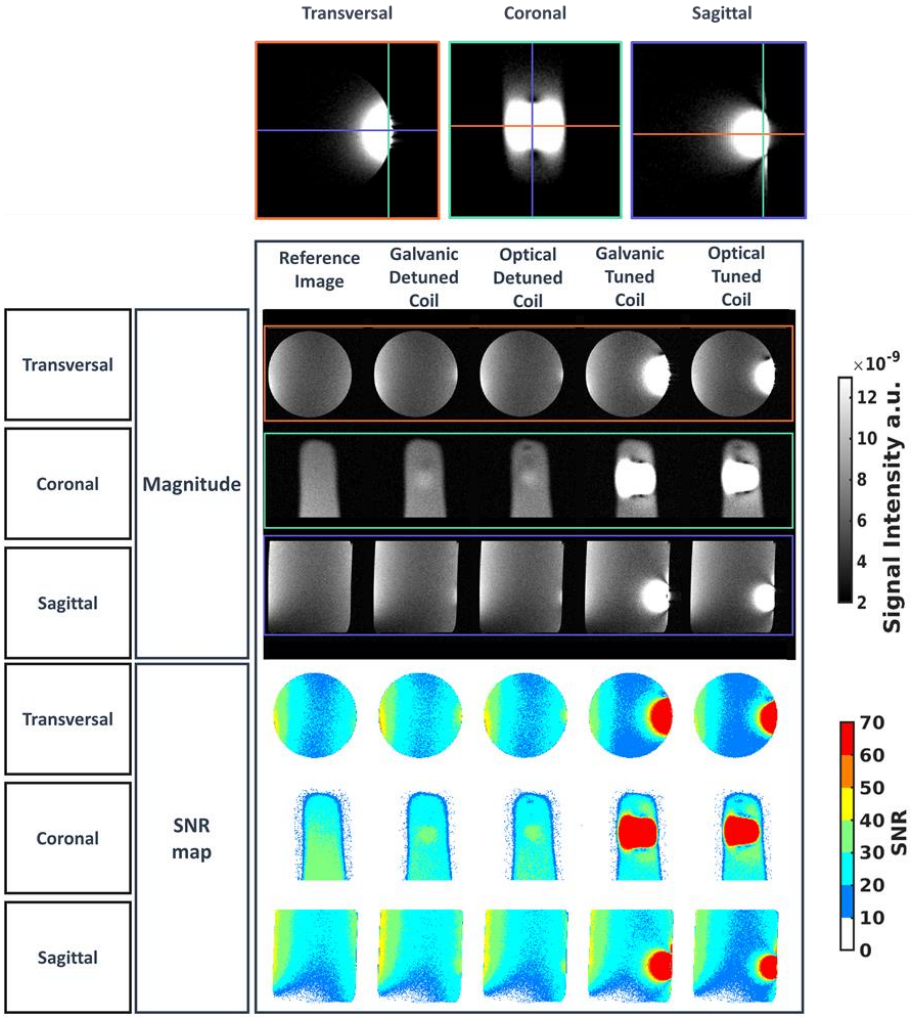

Figure 2-19: Signal intensity images and SNR maps in the three anatomical planes using GRE sequence with Chest coil combined to Spine coil.

In order to study the SNR uniformity along the coil length Z, the mean SNR was measured in a square region of interest (ROI) of about 64 mm^2 as shown in the Figure 2-20.

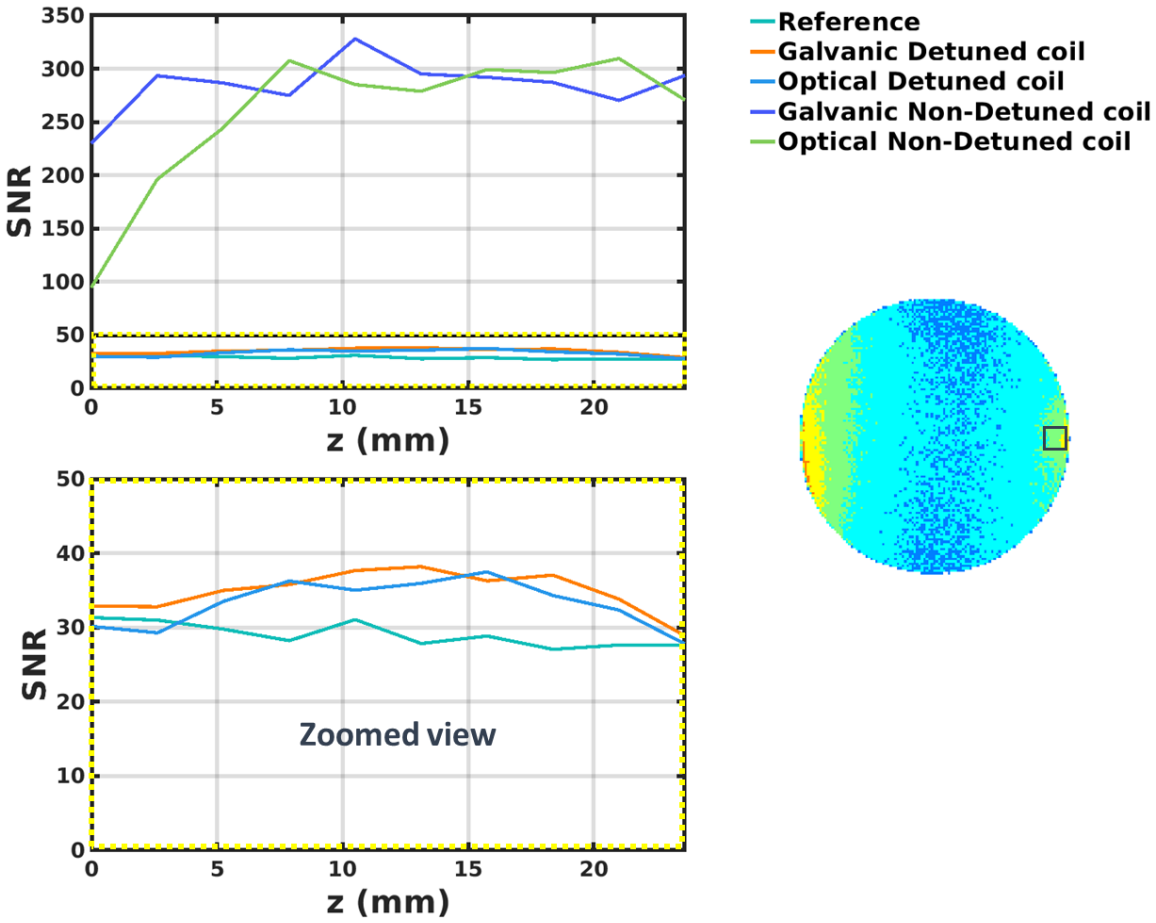

Figure 2-20: SNR profiles along the Z axis in the vicinity of the loop coil. **Top left-** plots of all the SNR profiles. **Bottom-left-** zoomed-view of the graph represented by a yellow frame in the graph above. **Right-** Transversal SNR map of the galvanic-detuned coil with the ROI indicated by the black square.

Position of the ROI was identical for each image slice and was chosen relative to the position of the residual bright spot remaining in images acquired while using detuned coils. The performance of each decoupling strategy was assessed by comparing the mean SNR of the ROI within each transversal image of the stack when coils were tuned or detuned, relative to the mean SNR of the ROI without any loop coil. Plots show that the SNR difference between the non-detuned coils and the detuned coils exceeds 280 and that the SNR difference between the detuned coils and the reference image is approximately 10 (maximal difference of 10.3 and 8.6 for the galvanic detuned coil and optical detuned coil, respectively).

2.7.1.4. Decoupling efficiency: conclusion

These results emphasize that:

- Interface box efficiently controls the coils active tuning/detuning

- The optical detuning is as efficient as a classical galvanic detuning whatever the sequence used (comparable signal intensity profile and uniform SNR map)

- Both galvanic and optical decoupling methods are efficient when using a set of different coil as receivers demonstrating the possibility to integrate our coils within the workflow of an MRI procedure without interference on image quality when these coils are physically connected to the scanner but not used for the reception.

2.7.2. Evaluating the coils selectivity and sensitivity

The 3D coil sensitivity profiles and associated SNR maps were assessed in phantoms. The same 2D-GRE performed in the 2.7.1.3 was applied, this time, using the body coil as the RF transmitter and the loop coils as receivers. Corresponding images of the phantom were acquired using the chest coil array for comparison purpose. The chest coil array was placed at approximately 4 cm away from the phantom to mimic clinical conditions where chest coil is placed on the patient's thorax, at a distance of approximately 4-5 cm away from the heart. Loop coils were successively placed in contact with the phantom, at the same location. The magnitude images were used to generate profiles and SNR maps in the three anatomical planes.

Figure 2-21 shows the signal intensity profiles acquired with both the galvanic-detuned and optical-detuned coils compared to the signal intensity obtained with the conventional chest coil only. As expected from the theory [32] of single-loop design, an ellipsoidal shape can be visualized for both loop coils with a high sensitivity very close to the loop. The sensitivity region covers approximately 4 x 3 x 2.5 cm^3 for both the galvanic-detuned and optical-detuned coils. This region was computed by including the signal intensity values comprised between the maximum intensity value obtained with the loop coils (>1.10^{-7} a.u.) and the maximal intensity value obtained with the chest coil (~2.10^{-8} a.u.) along the same profile.

This result demonstrates the higher spatial selectivity of both the loop coils compared to the chest coil.

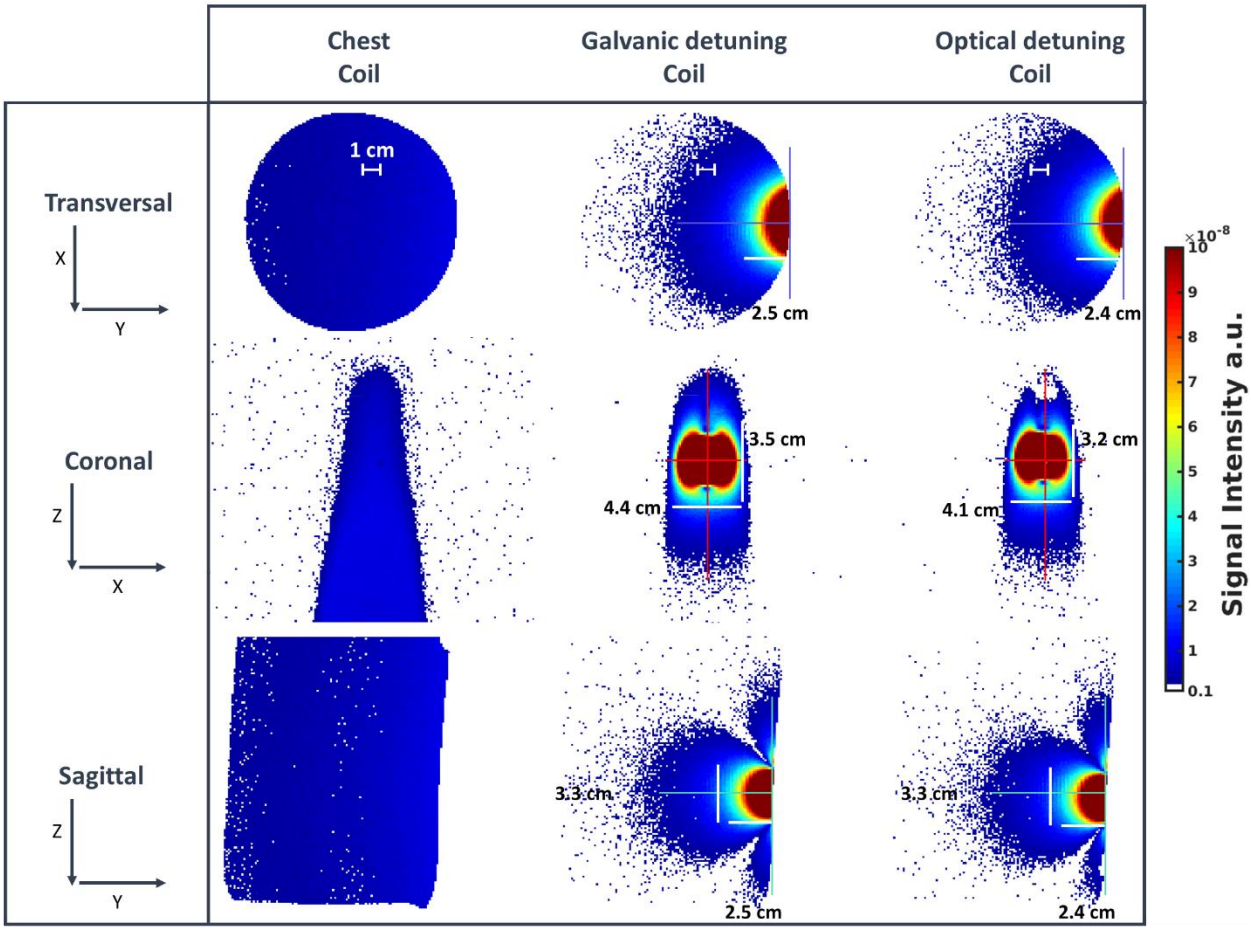

Figure 2-21: Signal intensity profiles in the three anatomical planes using 2D GRE sequence with the Chest coil, the Galvanic-detuned coil and the Optical detuned coil. Perpendicular lines overlaid on the images indicate the position of the loop center. Dimensions of the loop coils sensitivity are indicated and correspond to intensity value comprised between the maximum intensity obtained with the loop coils and the maximal intensity value obtained with the chest coil along a same profile.

Figure 2-22 represents the signal intensity profile along the Y direction for both the loop coils and chest coil.

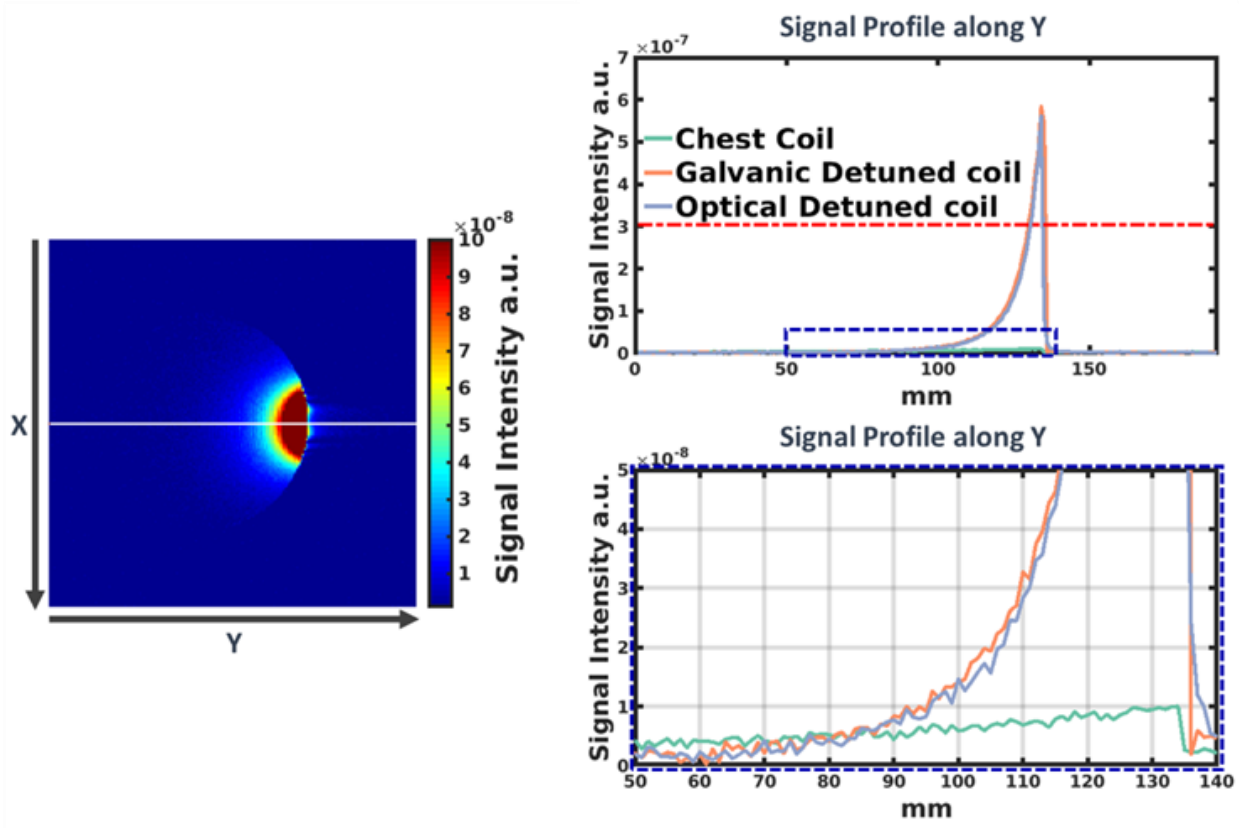

Figure 2-22: Signal intensity profiles along Y direction for both the loop coils and the conventional chest coil. **Left-** Signal intensity image in transversal orientation of the galvanic-detuned coil. Overlaid white line indicates the profile selected for spatial distribution of the signal analysis. **Top right-** Plots of the signal intensity profiles of the Chest Coil, the Galvanic-detuned coil and the Optical-detuned coil. Red dotted line delineates the threshold where 50% of the maximal sensitivity is obtained for the Galvanic-detuned coil. **Bottom right-** zoomed view of the graph indicated by the blued frame on the graph above.

Image on the left is a transversal slice and was chosen to be located at the position where the sensitivity is the highest. The white line represents the position where the profile was evaluated and resulting plots are drawn on the right with the bottom figure being a zoomed view of the figure above. The red dotted line delineates the threshold where 50% of the maximal sensitivity is obtained for the galvanic-detuned coil. This result emphasizes that:

- The maximal achievable signal when using the optical-detuned coil is comparable to the one achieved with the galvanic detuned coil (peak intensity = **96%** of the peak intensity attained with the galvanic detuned coil) proving the efficiency of the optical coil at providing similar performance in terms of sensitivity.

- The sensitivity of the loop coils is markedly higher to a distance of about **1.7 times** their diameter compared to the chest coil.

- The sensitivity drops rapidly with distance to the coil and falls off under 50% of the maximal intensity over only a **5 mm distance** for both coil.

Corresponding SNR maps of the signal sensitivity images demonstrates the very high, local sensitivity of the loop coils with SNR up to 100 over an approximately 4 x 3 x 2 cm area (Figure 2-23). Close to the surface of the loop (at approximately 3 mm from the center of the loop), the SNR achieved by the coils (both prototypes) is **up to 1000**, which represents a **32-fold improvement** in sensitivity compared to the chest coil, over the same region.

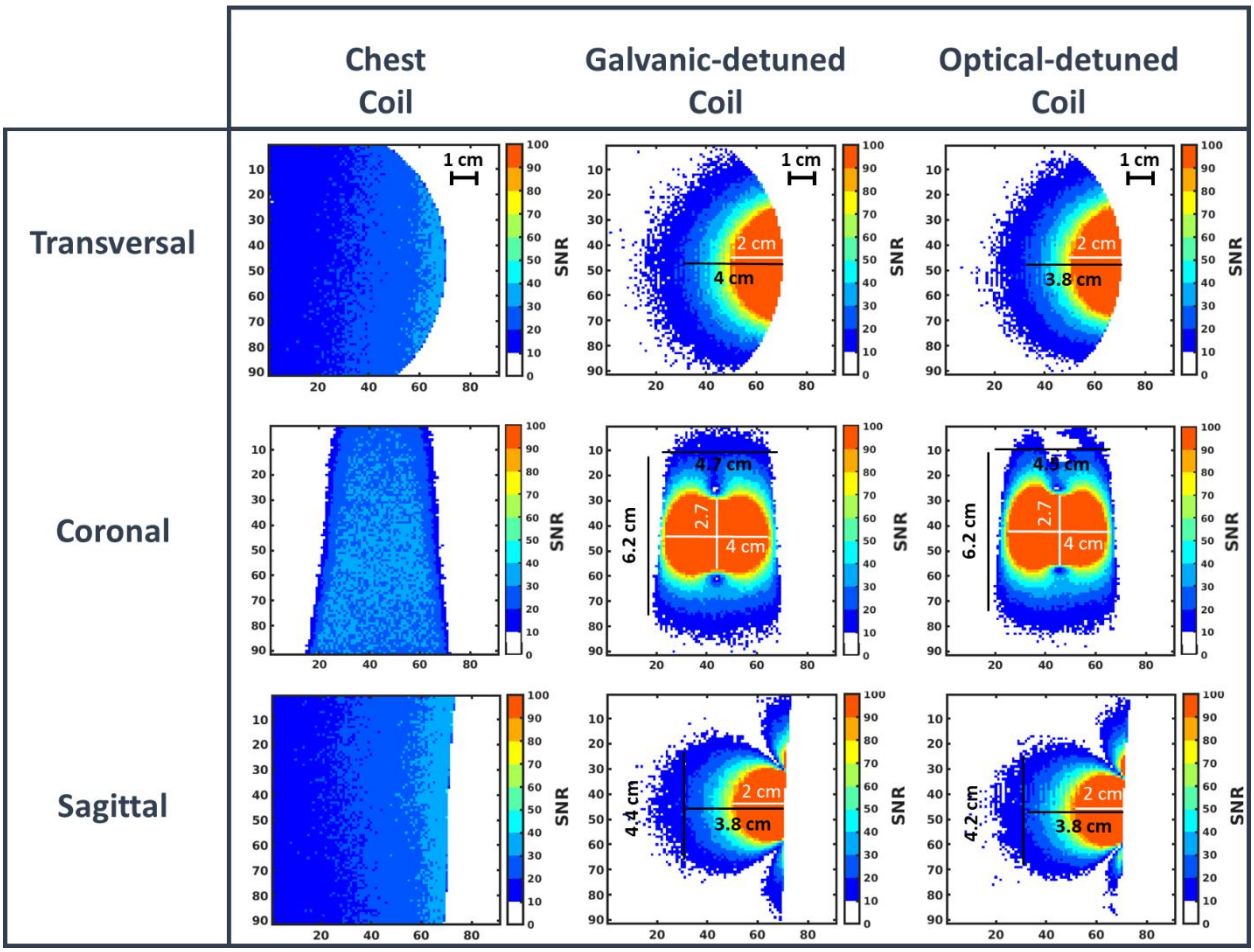

Figure 2-23: SNR maps of the acquired 2D GRE images with the Chest coil, the Galvanic-detuned coil and the Optical-detuned coil. Dimensions indicated in white correspond to the region with SNR ≥ 100 while dimensions indicated in black correspond to the region at equivalent SNR (20-30) between the loop coils and the Chest coil.

The SNR gain attainable using successively the galvanic-detuned and the optical-detuned local coils compared to the chest coil is shown in Figure 2-24. A 20-fold improvement in sensitivity is performed over a 2.5-cm x 2.2-cm x 0.5-cm region for both the galvanic-detuned coil and the optical-detuned coil and a **SNR gain up to 35** is achieved at the very close proximity of the coils (over approximately a 2 cm x 1.5-cm x 0.2-cm region). Considering the current spatial resolution of 1-mm isotropic attainable using the chest coil in clinical cardiac MRI, it would be possible to reduce the voxel size of up to $\sqrt[3]{SNR_{gain}}$ in each dimension (dX, dY, dZ) while keeping a sufficient SNR. Given the maximal gain of 35, it is possible to consider an isotropic voxel of around 300 µm in dimension ($1/\sqrt[3]{35}$).

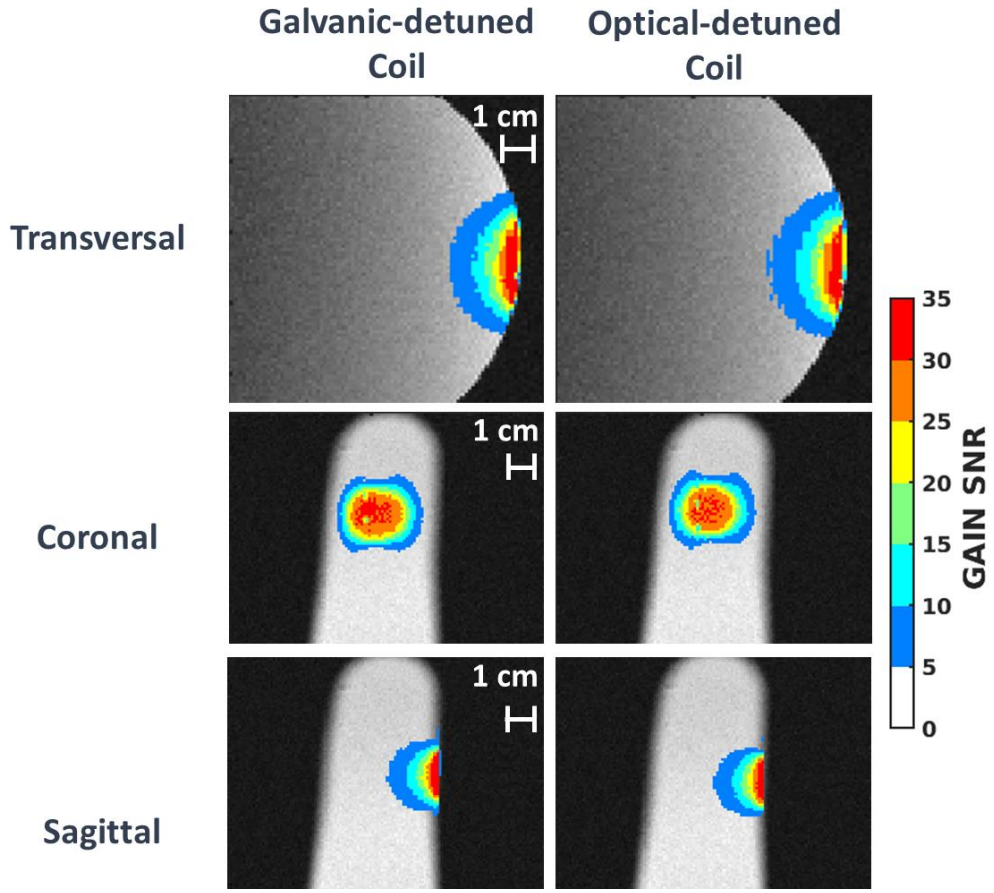

Figure 2-24: SNR gain attainable with the Galvanic-detuned coil and the Optical-detuned compared to the Chest coil at the same location. SNR gain is overlaid on the corresponding magnitude image acquired with the Chest Coil.

These results emphasize that:

- A **high selectivity** with a sufficient SNR (ranging from 30 to 1000) is obtained using our loop coils over a 6-cm x 5-cm x 4-cm region, making possible to acquire highly resolved images with a reduced FOV.

- A **SNR gain up to 35** is achieved using our local coils in the close vicinity of the coils (over a depth of 3-mm) and both coils show **a 20-fold improvement in sensitivity** over a region of 2.5-cm x 2.2-cm x 0.5-cm in dimension. Moreover, the highest sensitive region is larger than a standard RF ablation burn (0.5-to-1-cm in diameter and 1-to-3-mm deep), making high-resolution MR thermometry to monitor RF ablation procedure feasible.
- Acquiring images with a **voxel size of 300 µm** appears feasible with these coils

- Coils can be used simultaneously with conventional chest coils

2.7.3. Dependence of SNR on coil position

Influence of the coil orientation relative to the main magnetic field was evaluated to ensure coil could be used with equal sensitivity performances whatever its position. The galvanic-detuned coil was fixed at the surface of the phantom, which was oriented along the head-foot axis, thus collinear to the static field. The system {Phantom + Coil} was rotated around the Z-axis with an iterative step of 45°. Transversal images were acquired using the 2D GRE sequence described in 2.7.1.3 with the galvanic-detuned coils. A schematic representation of the set-up and experiment is given in Figure 2-25 together with corresponding SNR maps and contour plots.
Similar performances in terms of sensitivity are obtained independently of the coil orientation, demonstrating that the coil can be used to detect MR signals in all orientations relative to the main field without modified performance and that no interaction (geometrical coupling) with the other surrounding coil (Spine array and Body coil) is occurring.

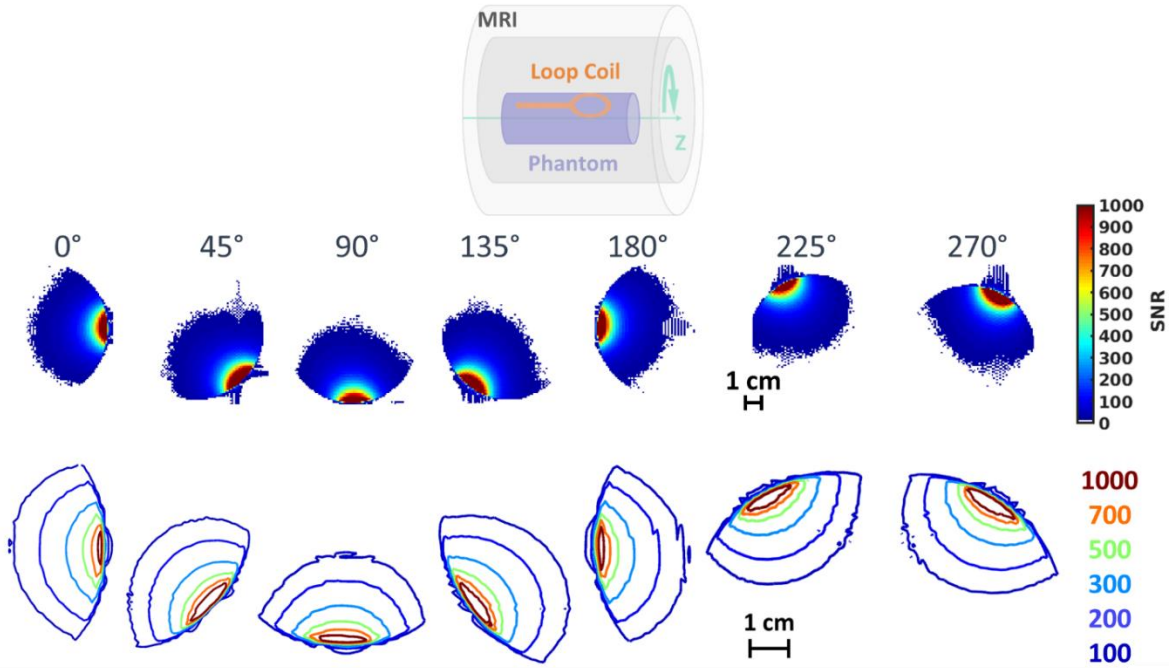

Figure 2-25: SNR dependence on coil position. **Top-** Scheme of the setup used for the experiment. The galvanic-detuned coil is initially placed at the top of the Phantom bottle (0°) and iteratively rotated around Z-axis with a 45° step. **Middle-** Signal intensity images are displayed for each orientation (0° - 270°). **Bottom-** Corresponding SNR maps.

2.8. Application to ex vivo and in-vitro imaging

Objectives of the following ex-vivo and in-vitro experiments were to evaluate the minimum FOV that would be possible to perform given a specific sequence parameters set (and gradient strength available on the MR scanner, here 45 mT/m at 200 T/m/s) together with assessing the highest spatial resolution achievable in the region of interest within a reasonable acquisition time.

Experiments were performed on a 1.5 T MR System (Aera, MAGNETOM, Siemens, Erlangen Germany, f_0 = 63.6 MHz).

2.8.1. Phantom experiment

The benefits of our developed coils for high-resolution imaging were first tested on a resolution phantom. 3D Images were obtained with a small FOV compared to the one usually required by the external chest coil. The phantom was a rectangular-shaped, 3D-printed plastic piece with holes and bars of different diameters and thicknesses.

Photograph of the phantom is given in Figure 2-26. In order to accurately characterize the dimensions of each hole and bars, a µCT scanner image was acquired at 40 µm isotropic resolution.

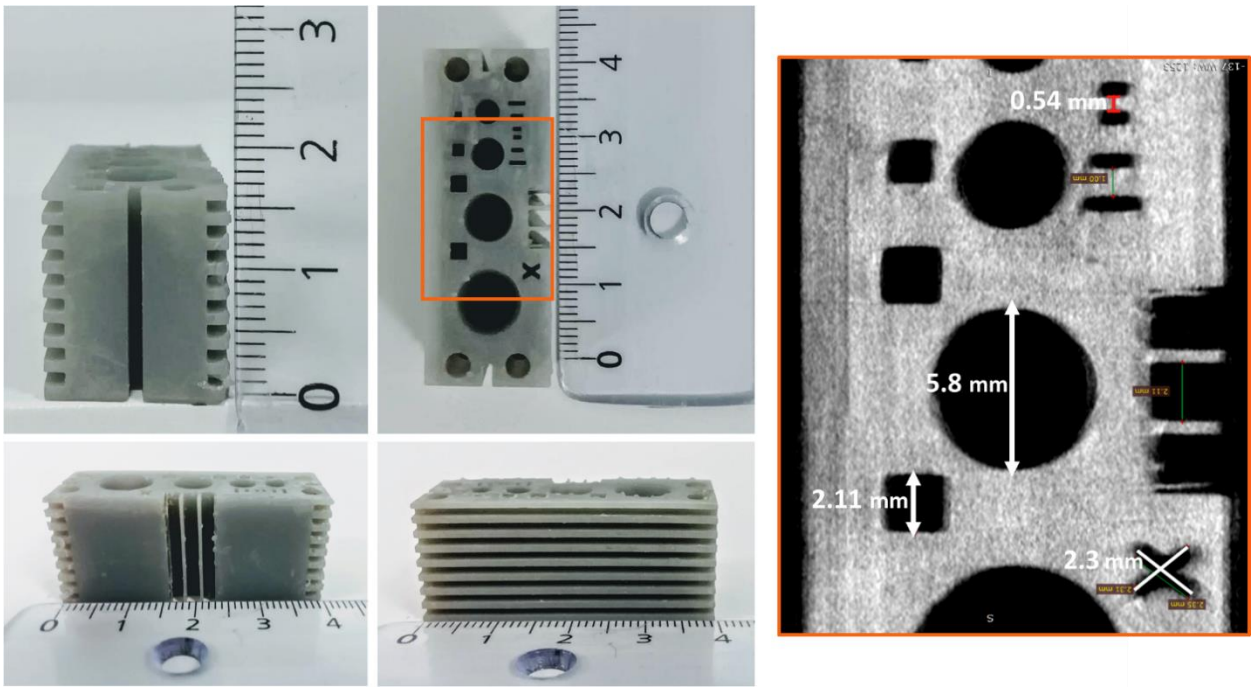

Figure 2-26: Photograph of the phantom used for ex-vivo experiment (**right**) and µCT scanner image with 40 µm isotropic spatial resolution (**left**) corresponding to the region of the phantom indicated in orange in the photo.

A 3D GRE was used to image the phantom with the following parameters: FOV = 80 x 50 x 22.88 mm^3; Matrix size = 336 x 210 x 104 pixels; slice thickness = 0.22 mm; TR/TE = 23 / 13 ms; FA = 6°; bandwidth = 170 Hz/pixels. The resulting voxel size was **200 µm isotropic**. Acquisition time was 11 min 36 s. The galvanic-detuned coil was used as a receiver and the body coil as a transceiver. Same acquisition was realized with **a 500 µm isotropic** spatial resolution with the following adjusted parameters: Matrix size = 176 x 110 x 50 pixels; Acquisition time = 5 min 16.

Figure 2-27 displays he corresponding images. The coil provides sufficient SNR to image at 200 µm isotropic resolution with a small field of view. Clear delineation of the two bars indicated with a white arrow was made possible with a 200 µm isotropic resolution compared to the images acquired at 500 µm isotropic where, unless visible, it was difficult to precisely quantify distance between both bars and demarcate them.

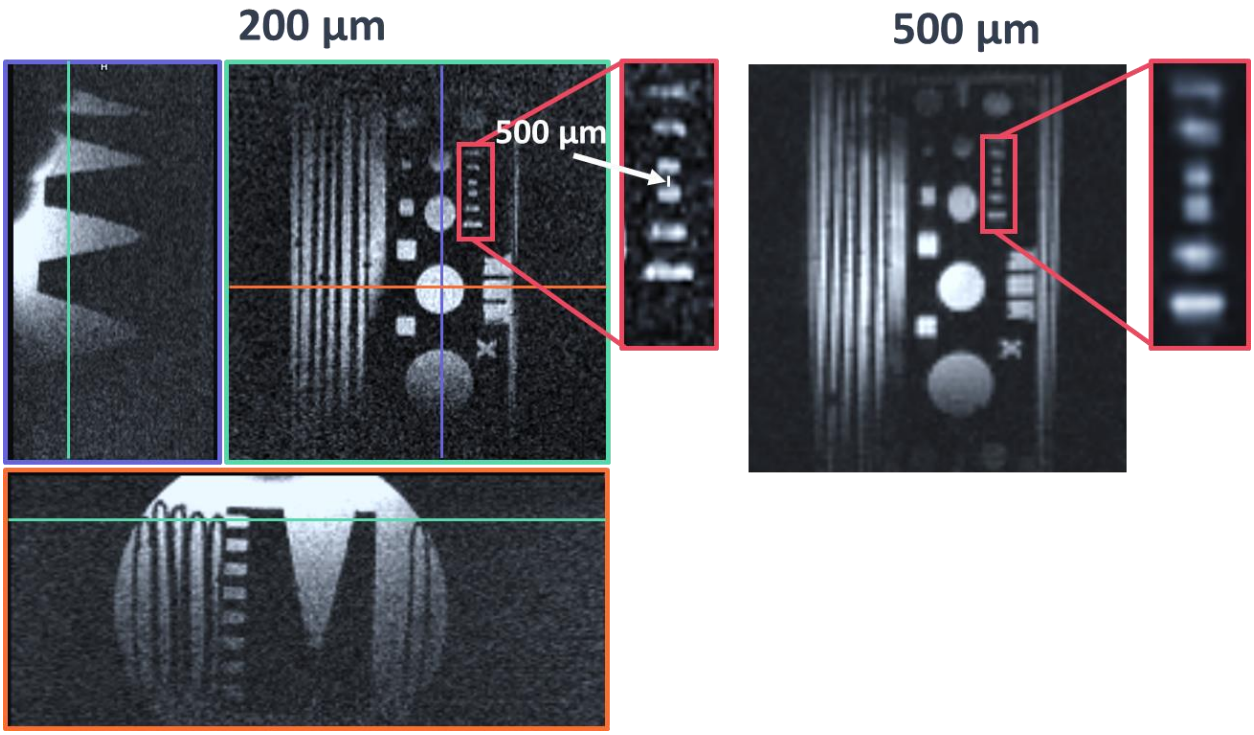

Figure 2-27: 3D GRE acquisitions of the phantom with the galvanic-detuned coil with a 200 µm isotropic (**left**) and a 500 µm isotropic (**right**) spatial resolution. Pink frame displays a zoomed-view of the phantom details (horizontal bars).

2.8.2. In-vitro experiments

The performance of the galvanic-detuned coil was also investigated in a series of ex vivo samples.

2.8.2.1. Atria sample

First, a freshly surgically excised left atrium from sheep was imaged. The atrium was immersed in a cardioplegic solution in order to preserve the tissue property along the acquisition time. The coil was placed in contact with the sample which was contained in a plastic tube. A 3D-GRE 300 µm isotropic in resolution was performed with the following parameters: FOV = 82 x 49 x 31 mm^3; Matrix size = 240 x 148 x 104 pixels; TR/TE = 18.7 / 11 ms; FA = 15°; bandwidth = 170 Hz/pixels. Taking advantage of the small FOV, total acquisition time was 4 min 48 s which is relatively short for such a high-resolution acquisition.

Figure 2-28 depicts the resulting image highlighting vasculature details within the atrium wall among which one of them having a section of 400 µm.

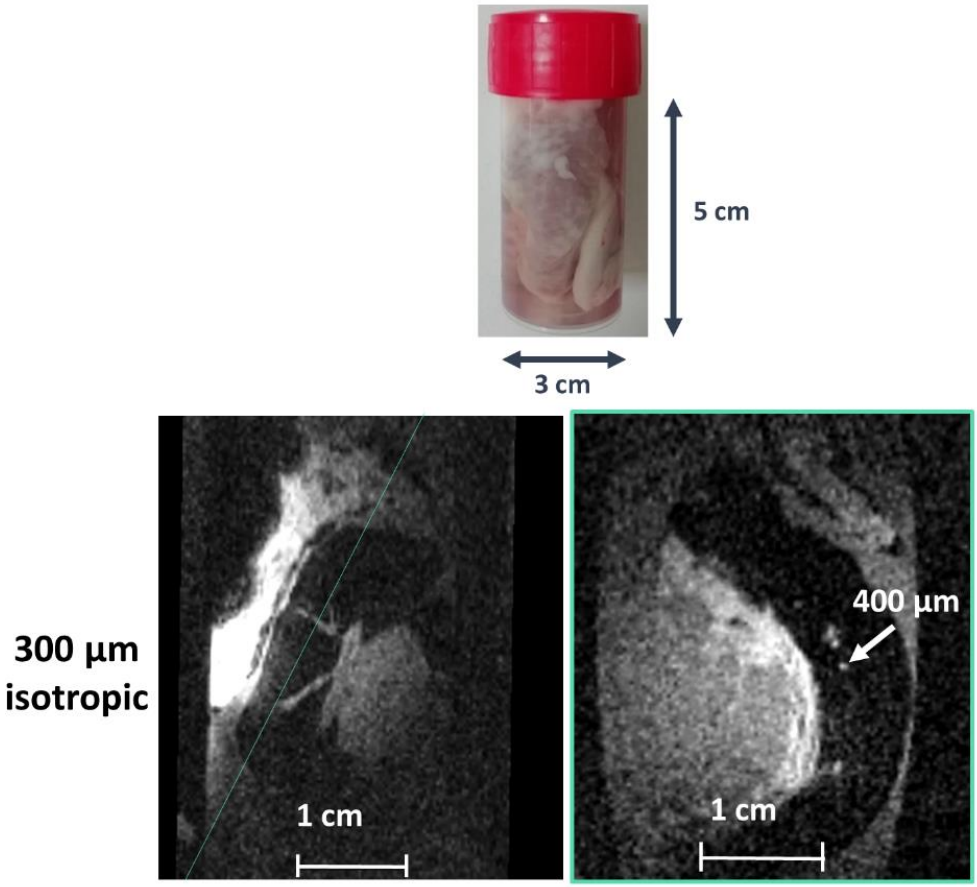

Figure 2-28: In-vitro experiment on freshly excised left atrium from sheep. Top- Photograph of the atrium sample with its corresponding dimensions. Bottom- 3D GRE images acquired with the galvanic detuned coil with a 300 µm spatial resolution. White arrow shows vasculature details within the atrium wall.

2.8.2.2. Septum sample

The second sample consisted in a formalin-fixed septum from sheep. A 3D-GRE, 200 µm isotropic spatial resolution, T2* weighted was performed with the following parameters: FOV = 80 x 50 x 23 mm^3; Matrix size = 336 x 210 x 104 pixels; TR/TE = 40 / 22 ms; FA = 33°; bandwidth = 172 Hz/pixels. Acquisition time = 16 min. Resulting images are shown for the three orientation planes in Figure 2-29. Structural details of the order of 200 to 300 µm are markedly visible, highlighting performances of our coil at providing sufficient SNR to achieve such a high degree of refinement.

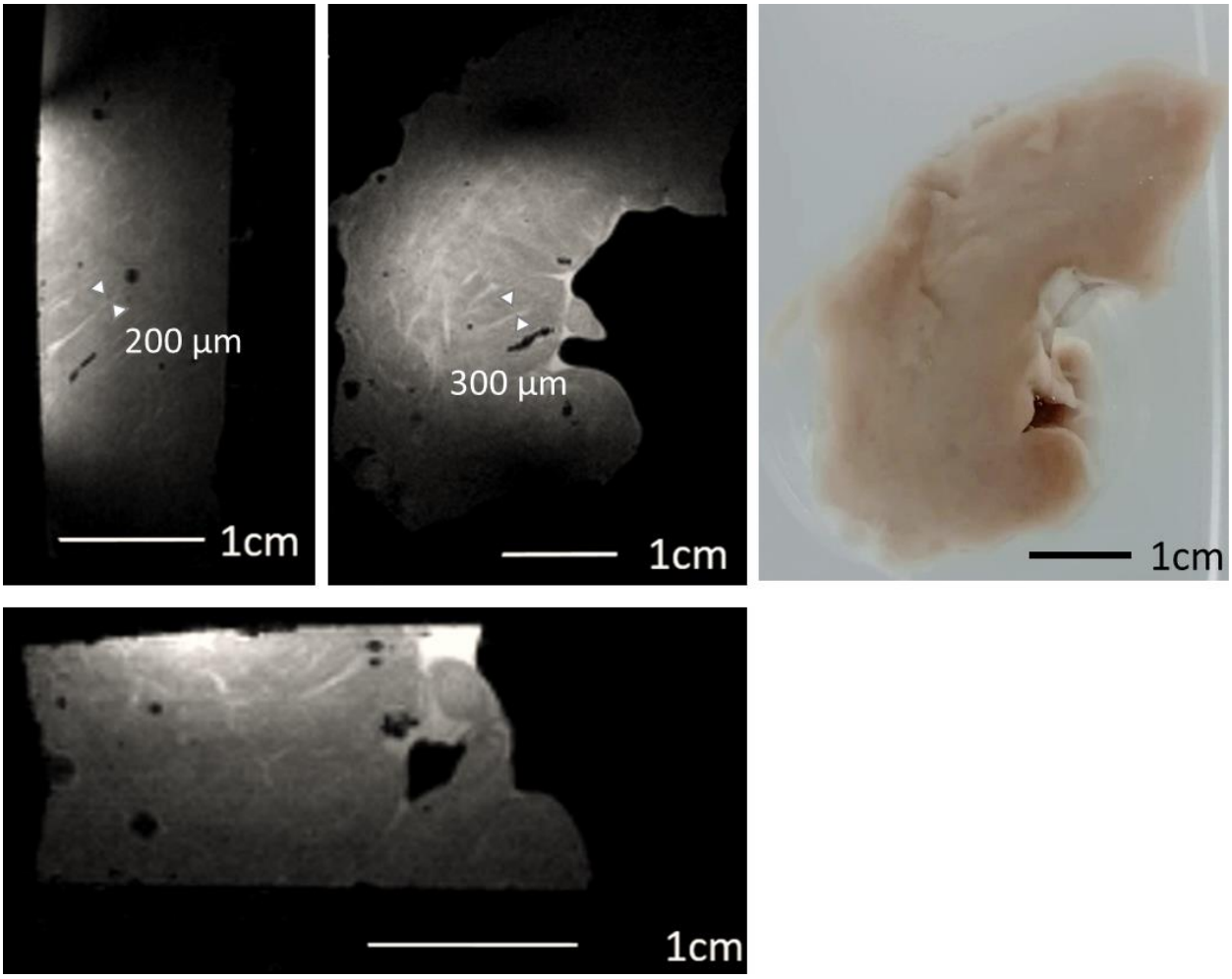

Figure 2-29: In-vitro experiment on a formalin-fixed septum from sheep. Left- 3D GRE T2* weighted images of the septum obtained with the galvanic-detuned coil at 200 µm isotropic spatial resolution. Arrows heads evidenced fine structural details of 200 µm to 300 µm dimension.

2.8.2.3. Isolated heart sample

3D-Truefisp imaging was performed on a static isolated heart, harvested on a pig. Following protocol was applied: FOV = 164 x 164 x 102 mm^3; Matrix size = 384 x 384 x 256 pixels; TR/TE = 1703 / 2.6 ms; FA = 65°; bandwidth = 435 Hz/pixels. Acquisition time = 7 min 15s. Figure 2-30 exhibits the resulting images. Anatomic details such as bicuspid valve, papillary muscles or chordae tendinae could clearly be identified and numerous blood vessels with sections ranging from 400 µm to 600 µm were markedly delineated within the left myocardium wall. The use of our coil clearly empowered the discrimination of fine structural details.

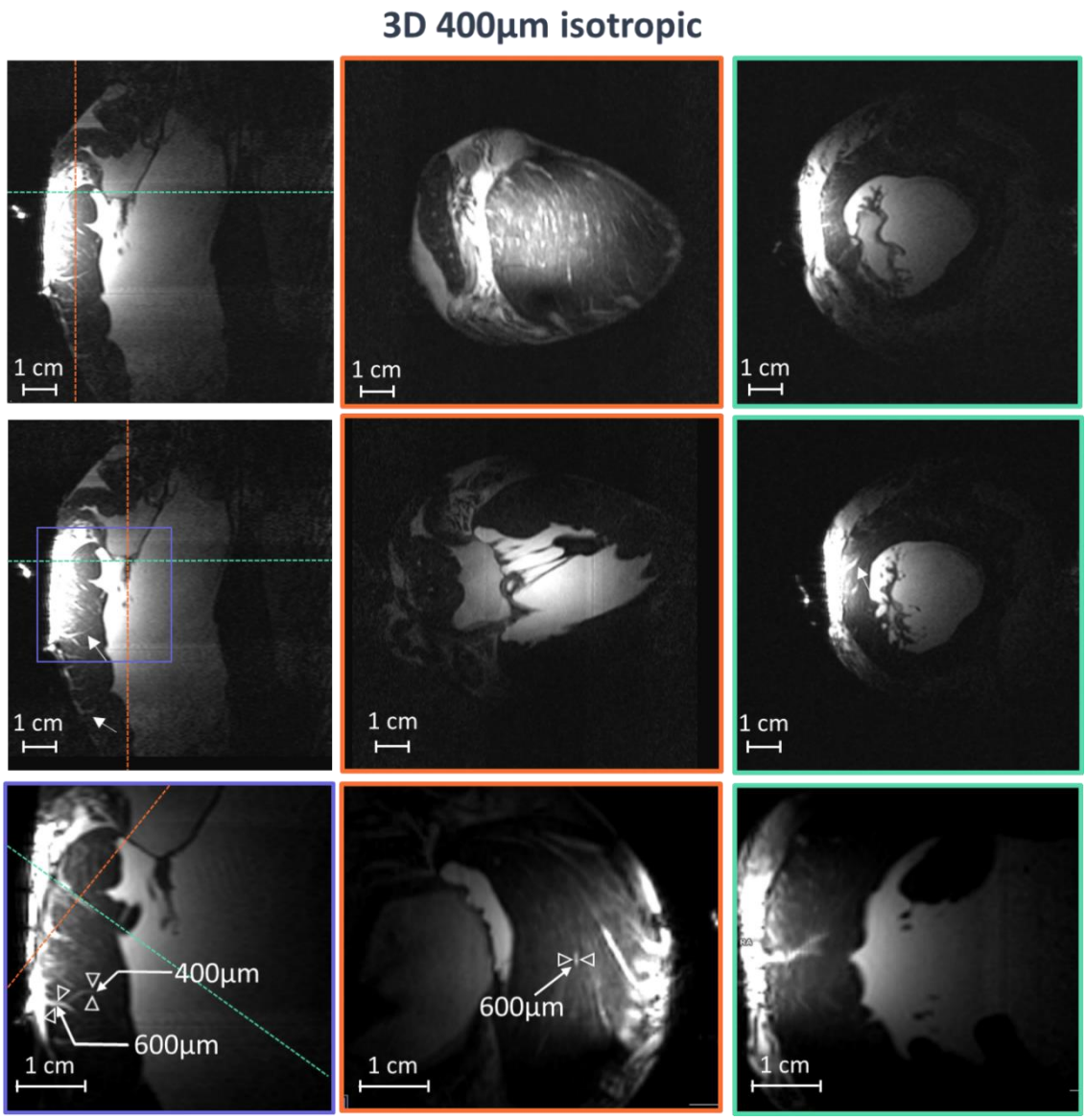

Figure 2-30: In-vitro experiment on a freshly excised heart from pig. First two rows show images acquired with a 3D TrueFisp sequence using the galvanic-detuned coil in the three anatomical planes (three columns) at two different locations (first row and middle row) indicated by the crossed-dotted lines. Last row displays a zoomed-view in the violet square indicated in the second row.

2.9. Application to ex vivo beating heart

The main challenge associated with intravascular high-resolution MR imaging remains the motion. Therefore, a key point of our work was to test the performance of the developed coil in conditions that approaches in vivo conditions where heart is subject to complex motion-induced by a combination of heart contraction and respiratory motion. As at this

time of the project the size and rigidity of the coil did not allow insertion into the vascular tree and thus navigation until the heart cavity, one of the solution was to take advantage of the isolated heart perfusion setup available at the institute and developed by Vaillant et al. [41] (Figure 2-31). This setup allows a heart from large animal to beat inside the magnet. This model was the model of choice to first evaluate influence of the cardiac-motion only on the resulting image acquired with a local coil and to optimize image acquisition in presence of such a motion before integrating a second degree of motion complexity with respiratory. Furthermore, in this isolated heart configuration, it was easier to monitor cardiac pressures at the targeted anatomical site to trigger the acquisition.

2.9.1. Isolated heart perfusion: Material and Methods

Following protocol description is derived from Vaillant et al. [41].

2.9.1.1. Animal Preparation

The protocol was approved by the local Animal Research Ethics Committee (Comité d'Ethique en Expérimentation Animale de Bordeaux - CEEA50) and all experiments were performed in accordance with the approved guidelines. Pigs (Large White x Landrace, ~40 kg, 5 animals for proof of concept) were premedicated with ketamine (20 $mg.kg^{-1}$) and acepromazine (1 $mg.kg^{-1}$) injected IM.Induction of anesthesia was realized with intravenous bolus of ketamine (15 $mg.kg^{-1}$) and midazolam (1.5 $mg.kg^{-1}$). After induction of anesthesia, animals were intubated and ventilated, and received an injection of heparin (2.5 $mg.kg^{-1}$). Anesthesia was maintained with ketamine and midazolam (40 $mg.kg^{-1}.h^{-1}$ and 2 $mg.kg^{-1}.h^{-1}$ respectively).

2.9.1.2. Heart extraction and working perfusion setup

The thorax was opened, and blood from each animal was collected (~3 l) via the introduction of an 8-Fr (2.67 mm) sheath into the right jugular vein. Heparin (15 mg/l) was added in the reservoir to avoid coagulation. Hearts were excised according to a protocol used in humans during heart transplantation. Cardiac arrest was realized in vivo by cross clamping of the ascending aorta and direct injection in the aortic root of 1 l of cold (4°C) cardioplegic Celsior (Genzyme, Saint-Germanen- Laye, France) solution, before a rapid excision and immersion in a cold 0.9% saline solution. The aorta, pulmonary veins, and

pulmonary artery were then cannulated to perfuse the heart in the working mode. Inferior and superior cava veins were sutured to limit leaks and collect the entire coronary sinus outflow through the pulmonary artery.

A specific MR-compatible perfusion setup was used and is represented in Figure 2-1. After the heart was prepared, it was placed into a Plexiglas thermoregulated tank and reperfused in the Langendorff mode for 15–20 min to wash out the cardioplegic solution, gradually rewarm the heart and recover a stable ex vivo cardiac function. This setup offers loaded ventricles with the perfusion medium from the coronary vascular bed, resulting in an isovolumetric contraction. Perfusion of the heart was ensured by the blood collected on the same animal before heart excision, diluted with a Tyrode buffer (vol/vol: 1/3, 38°C), containing energy substrates (16 mM glucose, 0.5 mM pyruvate, 1 mM lactate) and epinephrine (10 nM).

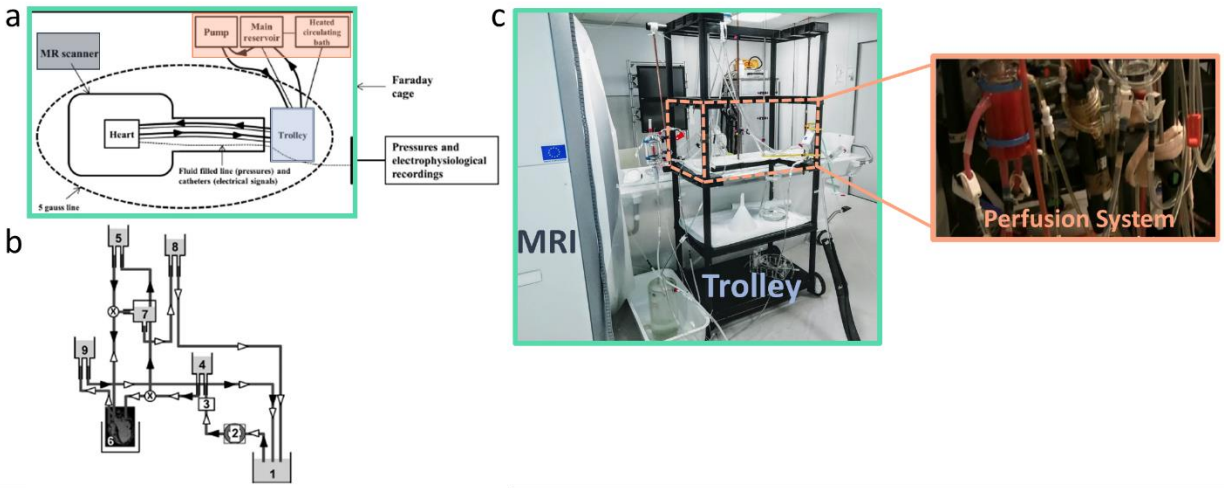

Vaillant et al., *Am J Physiol Heart Circ Physiol*, 2016.

Figure 2-31: Schematic representation of the MR-compatible setup for the isolated working heart modified from Vaillant et al. a) Complete setup inside the Faraday cage including pump and heated circulating bath. b) working perfusion setup in detail: 1: main reservoir, 2: pump, 3: oxygenator, 4: preload, 5: Langendorff reservoir, 6: heart chamber, 7: compliance chamber, 8: left ventricle (LV) afterload, 9: right ventricle (RV) afterload. The reperfusion was only run in Langendorff mode (white arrows). c)Photograph of the setup installation is MR room with the Perfusion system placed on the Trolley. Perfusion system photograph is modified from Bour P. Thesis.

2.9.1.3. Intraventricular pressure measurements

Cardiac contraction was monitored by intracardiac pressure measurement. A homemade intraventricular catheter was inserted into the left ventricle via the apex and connected to a fluid-filled piezoelectric pressure transducer, located outside the Faraday cage, for continuous monitoring of Left Ventricle pressure (EMKA-IOX2 data acquisition system, EMKA Technologies,VA, USA). The pressure was recorded and sent to a LabChart software to generate a TTL trigger. This trigger was used to synchronize the MR-acquisition to the left ventricle contraction (Figure 2-32). Triggering with the pressure instead of ECG brought the advantage of being more accurate since we are triggering relative to a physiologic events that occurs at the place where we are imaging. Besides allowing greater trigger accuracy, using a pressure signal allows us to get rid of the corruption of the ECG signal due to adverse electromagnetic effects such as voltage artifacts and which is a fundamental problem for monitoring cardiac activity during MRI [42][Abi-Abdallah et al., 2006].

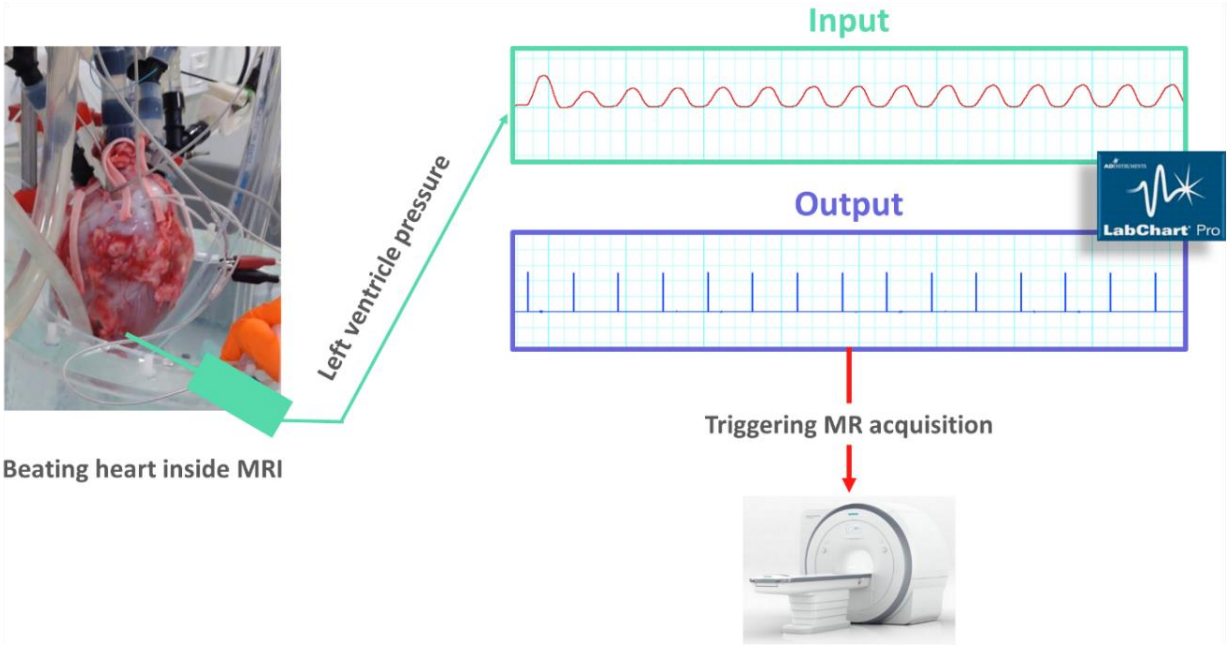

Figure 2-32: Intraventricular pressure measurement and triggering of the MR acquisition. A homemade intraventricular catheter is inserted into the left ventricle via the apex and connected to a fluid-filled piezoelectric pressure transducer. The recorded pressure signal is sent to a LabChart software to generate a TTL trigger and synchronize the MR acquisition with the left ventricle contraction.

2.9.1.4. Coil Positioning

The local galvanic-detuned coil was wrapped in plastic (Parafilm) and inserted into a surgeon glove to ensure its waterproofing and electrical insulation together to keep it from losing its performance characteristics. A dedicated articulated positioning arm was designed to maintain the coil and keep it against the surface of the heart during all the experiment. Using this setup, the coil could follow the beating heart motion without restraining its rhythm.The coil was placed against the outer surface of the left ventricle as illustrated in the Figure 2-33.

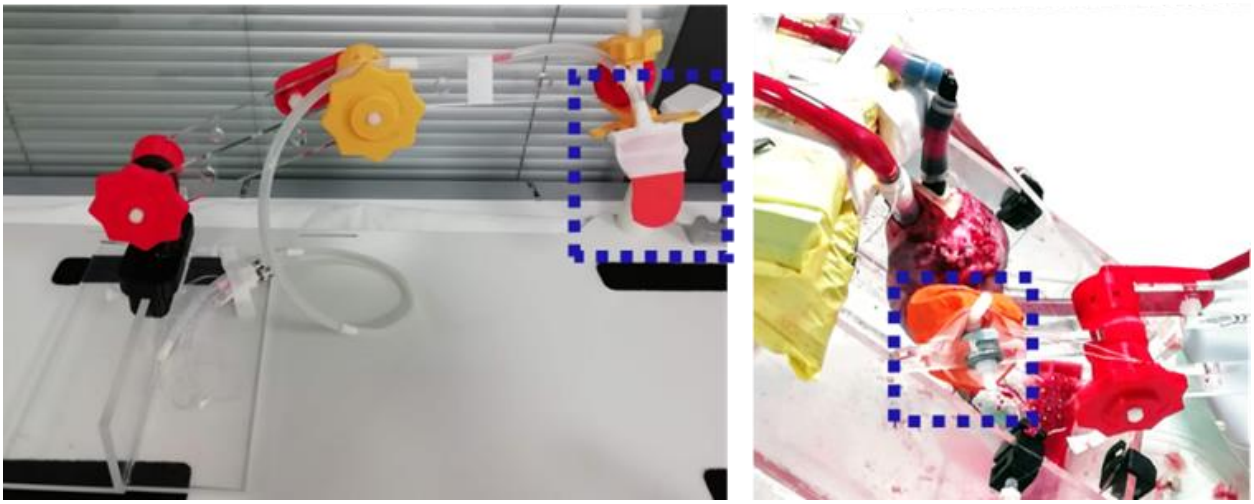

Figure 2-33: Photograph of the setup used to maintain the coil in contact with the left ventricle during beating heart experiment. Left- Coil fixation on the articulated arm. Right- Coil positioning against the outer surface of the left ventricle.

2.9.1.5. Coil Electrical Characterization on isolated heart

Before starting MR experiment, coil was characterized using the same vector network analyzer as introduced earlier in this chapter. The quality factor was determined from the reflection coefficient $|S_{11}|$ when the coil was loaded with the heart (in contact with the left myocardium ventricle). The resonance frequency of the coil was 63.65 MHz and the refection coefficient at this frequency was $|S_{11}|$ = -23.06 dB showing relative good matching. The coil resonance frequency did not change significantly with cardiac motion. The quality factor of the loaded coil was approximately 20 and 35 when unloaded. These quality factor values as well as return loss value are consistent with the values found in [10], [40].

2.9.2. MR acquisition

2.9.2.1. Localization of the coil and optimization of the cardiac gating

The first stage of the imaging protocol involved the detection of the coil spatial location. This was performed with a large FOV imaging sequence with local coil as the receivers. A TrueFisp sequence was acquired with the following parameters: FOV = 245 x 245 mm^2; Matrix size = 208 x 208 pixels; TR/TE = 587.8 / 1.8 ms; FA = 71°; bandwidth = 1200 Hz/pixels. A total of 15 slices were acquired (5 slices in each orientation plane). These images provided a rough map of the 3D spatial orientation of the intravascular coil relative to the myocardium wall.

Second stage of the imaging protocol consisted in optimizing the cardiac gating to minimize motion artifacts in the images. To this end, a cine imaging sequence was performed to find the stationary phase of the cardiac cycle in the region of interest and retrieve the corresponding value for the delay after the TTL trigger. Sequence parameters were as follows: FOV = 70 x 70 mm^2; Matrix size = 128 x 128 pixels; TR/TE = 6.1 / 2.7 ms; FA = 71°; bandwidth = 435 Hz/pixels; slice thickness = 1.5 mm. Resulting spatial resolution was 0.5 x 0.5 x 1.5 mm^3.

2.9.2.2. High-resolution imaging

Initial feasibility and associated limitations of small FOV, high resolution imaging using such a local coil were investigated, including the assessment of the attainable resolution and motion compensation efficiency. The results presented in the following are derived from **5 different isolated heart** experiments. As the MR acquisitions are all triggered, the values of TR given hereafter for each protocol correspond to the mean duration between two triggers and thus two lines of k-space. Indeed, every acquisition was performed with one segment per cycle to minimize the influence of motion.

Acquisition #1

A first set of images consisted in **2D-TrueFisp** sequences. For comparison purpose, three different in-plane spatial resolutions (0.9 x 0.9 mm^2 / 0.7 x 0.7 mm^2/ 0.4 x 0.4 mm^2) were achieved, keeping the same FOV. Each acquisition was triggered relative to the value of

delay found with the cine imaging, as aforementioned. Imaging parameters were as follows: FOV = 70 x 70 mm^2; Matrix size (**900 µm/700 µm/400 µm** in-plane resolution) = 80 x 80 / 96 x 96 / 160 x160 pixels; TR/TE = 510 / 6 ms; FA = 90°; bandwidth = 130 Hz/pixels; slice thickness = 2.5 mm; T2-prep = 40 ms; TTL-triggered every heartbeat; 1 segment, 3 slices. Given the rapid heart cycle (around 117 ± 6 bpm; 512 ms per heartbeat), total acquisition time was 2 min / 2 min 27 s/ 4 min for the 900 µm, the 700 µm and the 400 µm in-plane resolutions, respectively. Resulting images are provided in Figure 2-34 for the slice #3.

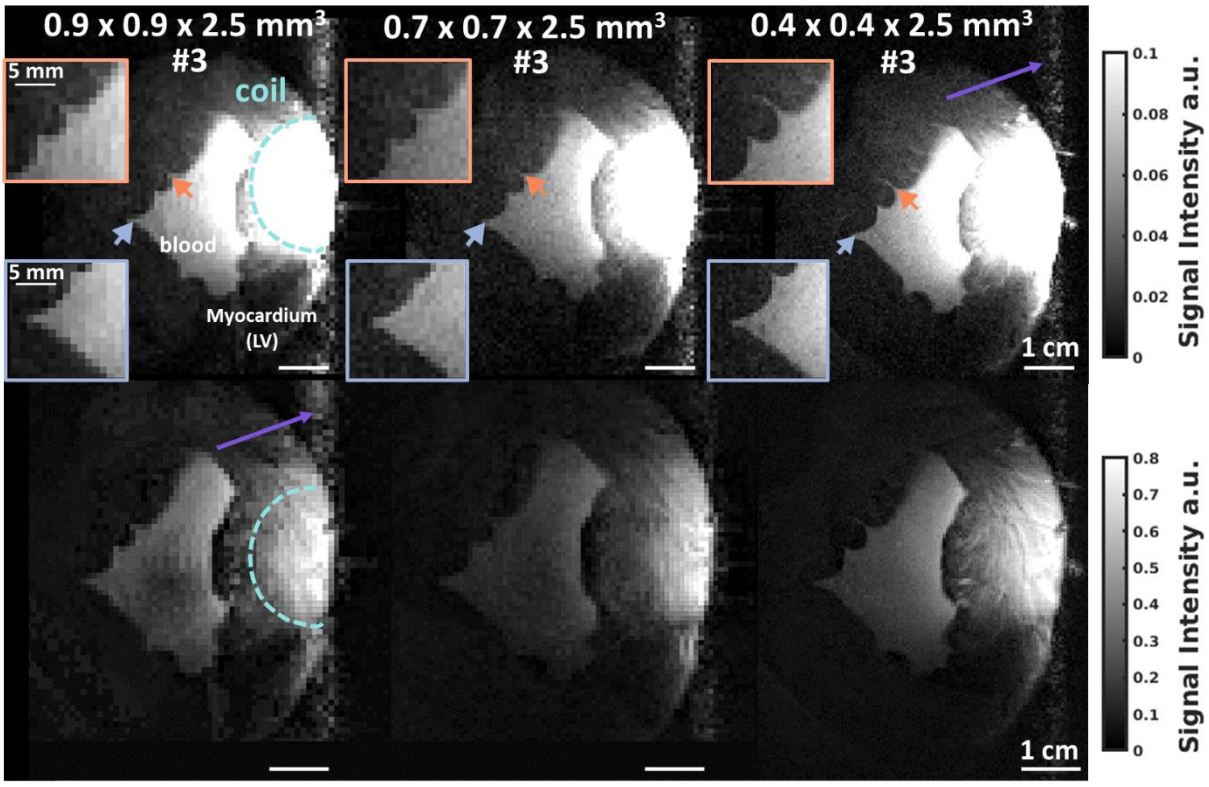

Figure 2-34: Slices #3 of 2D TrueFisp (Acquisition #1) images acquired with the galvanic-detuned coil on a beating heart (117 ± 6 bpm) with three different spatial resolution of 0.9 x 0.9 x 2.5 mm^3; 0.7 x 0.7 x 2.5 mm^3 and 0.4 x 0.4 x 2.5 mm^3. Zoomed-views of anatomical details are provided in orange and blue squares. Coil sensitivity is highlighted with the green dotted curve. Violet arrows depicts motion of the coil, which appears as a trail in the image. **Top-** and **Bottom-** rows differ by their scaling.

The bright signal on first row images attests the coil location against the left ventricle wall (green dotted curve). As expected from our previous coil performance characterization, the sensitivity of the coil covers an approximately **5.5 cm-deep** region with the highest sensitivity found in the immediate vicinity of the coil (< 1 cm). Therefore, myocardium wall

regions close to the coil are brighter, whereas other wall sections remain underexposed. Contrast and brightness were adjusted using the function “adapthisteq” from Matlab that adjusts the contrast of the image using adaptive histogram equalization and resulting images are provided in the bottom row. Adjusting the brightness and contrast allows to highlight fine structures on the 400 µm in-plane resolution image.
Ghosting depicted by the violet arrows may result from blood flowing on the epicardium during acquisition.

The benefits of the coil for high resolution imaging is clearly demonstrated with the achievable in plane resolution of 400 µm. No artifact compromising the appearance of the left myocardium wall was observed and structural details began to be visible while increasing the spatial resolution as shown in the 13 mm x 13 mm portion images (orange and blue frame) and centered at the position of the color-corresponding arrows. Regarding the acquisition time, given a usual clinical FOV of 200 x 200 mm, a matrix size of 500 x 500 pixels would be required to achieve a 400 µm in-plane resolution, resulting in an acquisition time of approximately 12 min(500[encoding lines] x 512[heartbeat] x 3 [slices]) for the same protocol (1 segment per heartbeat). Therefore, our coil shows at least a **3-fold image acquisition acceleration** and a **8-fold FOV reduction** (70 x 70 mm^2 vs 200 x 200 mm^2) compared to conventional chest coils.

Figure 2-35 displays the three slices acquired at **400 µm in-plane resolution**. Corresponding adjusted images are represented in the bottom row and highlight fine structures (of the order of 500 µm) inside the myocardium wall. As demonstrated in the previous Figure 2-34, such details cannot be visualized with the current clinical resolution of 1 mm in-plane, demonstrating the interest of using such a local coil to provide high resolution. Purple frames give a focus on the left endocardium structure. Sharper images, free of motion artifacts, highlight the demarcation between the blood and the myocardium wall, demonstrating the efficiency of the motion compensation at such a high resolution imaging.

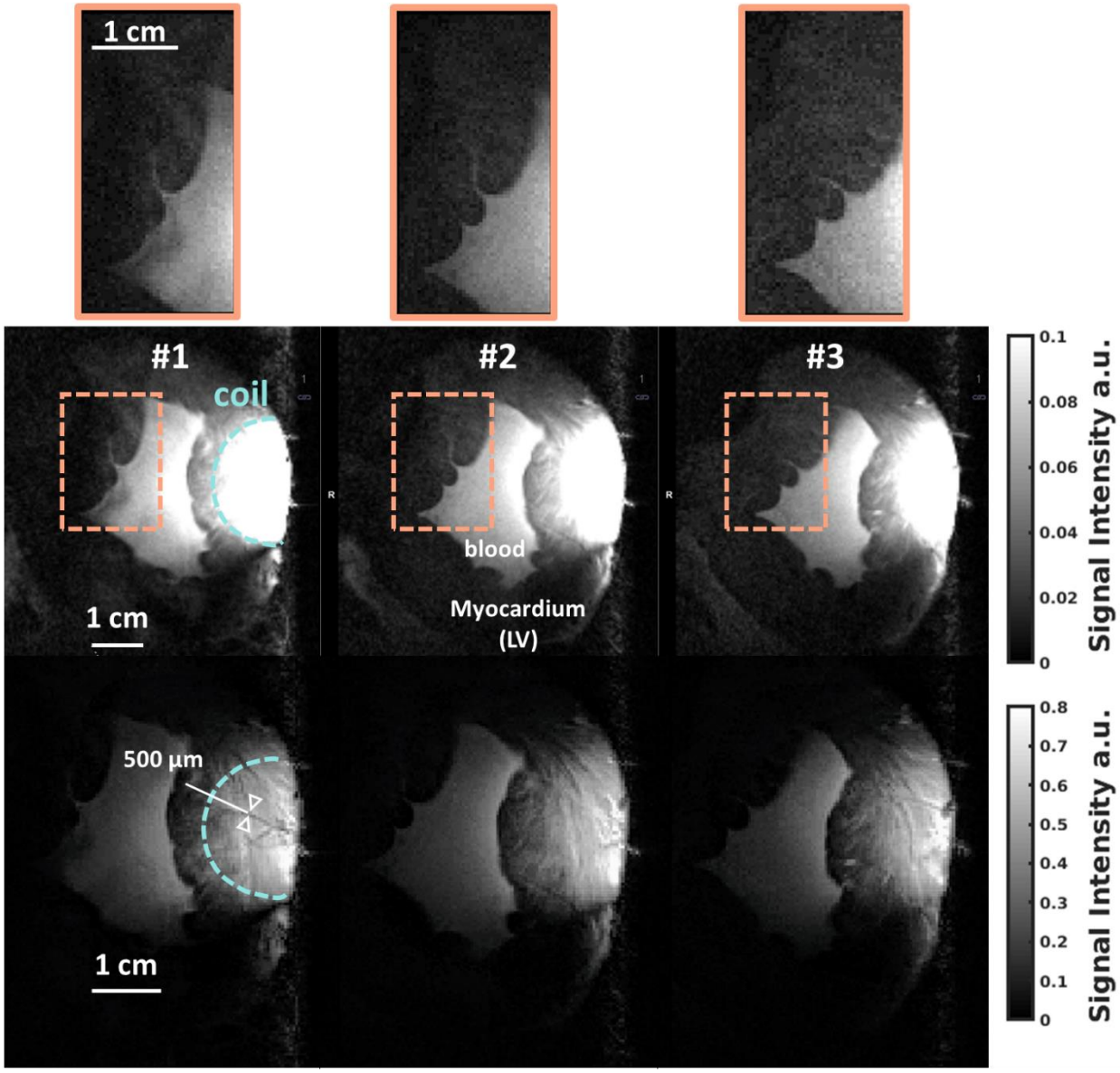

Figure 2-35: Three slices of the left ventricle acquired with a 2D TrueFisp (Acquisition #1) with 400 µm in-plane spatial resolution on beating heart (117 ± 6 bpm). Zoomed-views of the endocardium are provided the orange frames. Images in the bottom row correspond to images in the top row after having adjusted the contrast and brightness. This adjustment allows visualization of structural details.

Acquisition #2

A second set of images with **800 µm in-plane** and **300 µm in-plane** resolution was acquired using **2D-GRE** with the following parameters: FOV = 90 x 90 mm^2; Matrix size (**800 µm** / **300 µm** in plane resolution) = 288 x 288 / 112 x 112 pixels; TR/TE = 580 / 9 ms; FA = 65°; bandwidth = 130 Hz/pixels; slice thickness = 2.5 mm; TTL-triggered every heartbeat (heartbeat of 100 ± 5 bpm); 1 segment; 2 slices; Total acquisition time (**800 µm**

/ **300 µm** in plane resolution) = 2 min 10 s / 5 min 20 s. Resulting images are depicted in Figure 2-36. Comparison between the 800 µm in-plane and 300 µm in-plane spatial resolution images is presented for the slice #1. The 3 cm x 3 cm portion images (blue frames) clearly attests the image quality improvement obtained with a 300 µm in-plane spatial resolution, allowing depiction of fine blood vessels (orange arrow) and marked delineation of the bicuspid (mitral) valve and associated chordae tendinae.

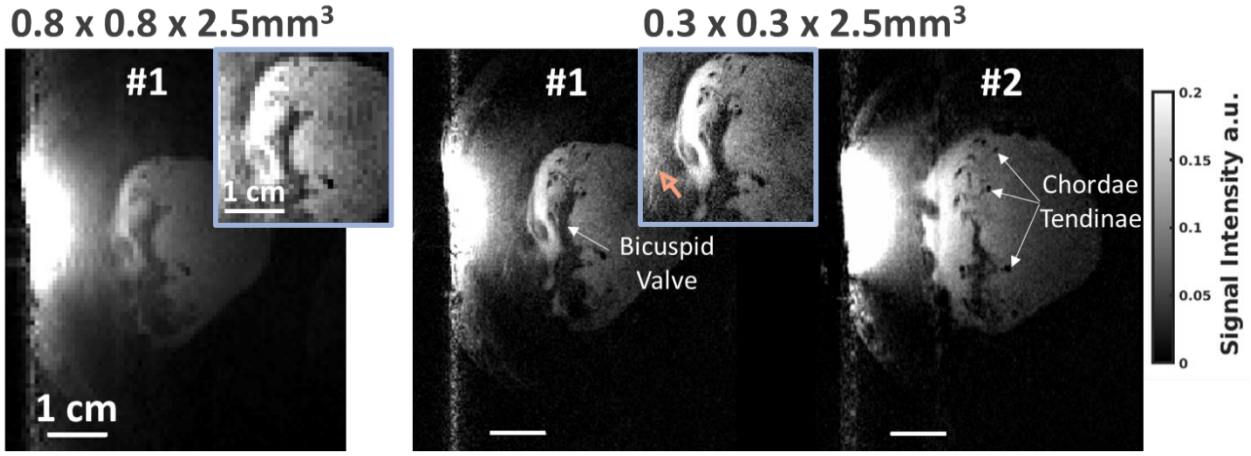

Figure 2-36: 2D-GRE images (Acquisition #2) of the left ventricle. Images were acquired with a 800 µm and a 300 µm in-plane spatial resolution on beating heart (100 ± 5 bpm). Blue frames display zoomed-views focused on the bicuspid valve. Structural details (chordae tendinae, valve) and a vessel (orange arrow) are clearly identified in the image with 300-µm-in-plane resolution.

Acquisition #3

Given these firsts encouraging results, further acquisitions were performed with a better spatial resolution. A 2D-GRE was performed with **0.23 x 0.23 x 2.5 mm³** and **0.16 x 0.16 x 2.5 mm³** with the following parameters: FOV = 70 x 70 mm²; Matrix size (**230 µm** / **160 µm** in plane resolution) = 304 x 304 / 432 x 432 pixels; TR/TE = 518 / 25 ms; FA = 60°; bandwidth = 130 Hz/pixels; slice thickness = 2.5 mm; TTL-triggered every heartbeat (heartbeat of 120 ± 5 bpm); 1 segment; 3 slices; Total acquisition time (**230 µm** / **160 µm** in plane resolution) = 8 min / 11 min.

The first two slices acquired with a spatial resolution of **0.23 x 0.23 x 2.5 mm³** are represented in Figure 2-37. The resolution and signal-to-noise ratio (SNR) were sufficient to depict blood vessels with sections of 400 µm to 500 µm.

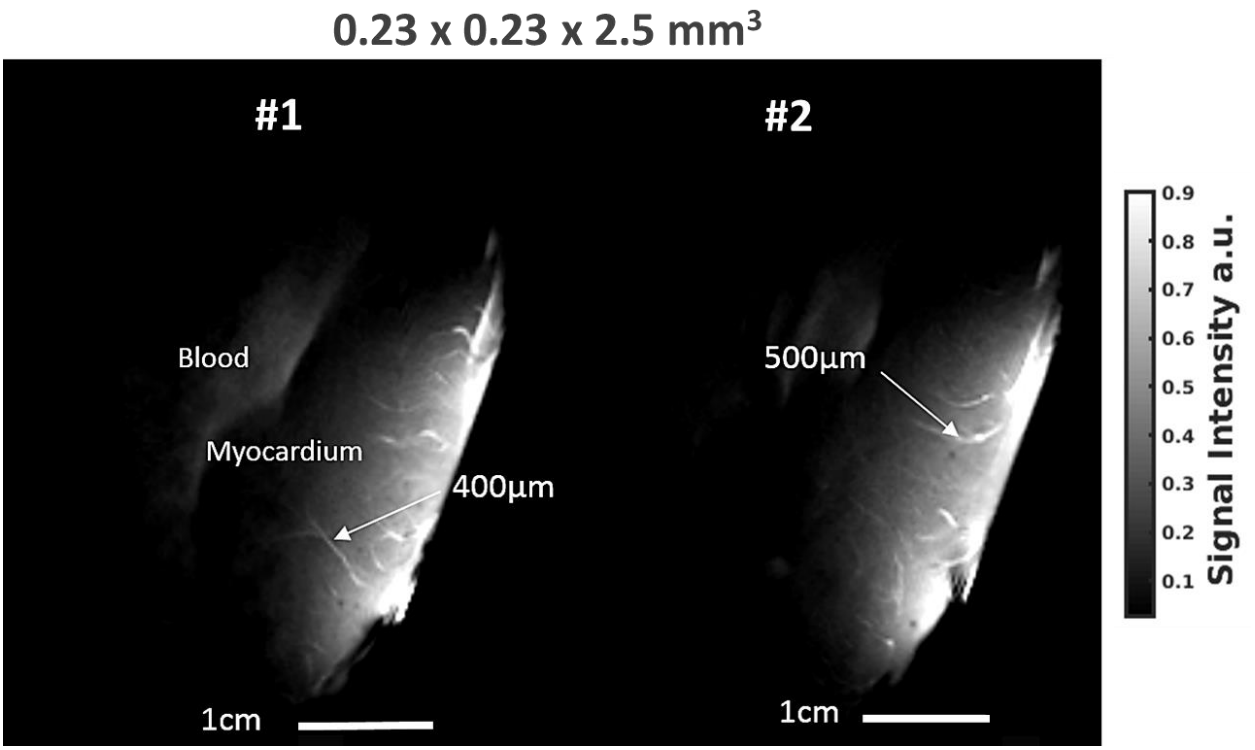

Figure 2-37: 2D-GRE (Acquisition #3) acquired with 0.23 x 0.23 x 2.5 mm3 spatial resolution on beating heart (120 ± 5 bpm). First two slices #1 and #2 are shown and depicted small blood vessels of 400 and 500 µm in section.

Comparison between 0.23 x 0.23 x 2.5 mm^3 and 0.16 x 0.16 x 2.5 mm^3 spatial resolution images is shown in Figure 2-38 for slice #3. In contrast to the two first slices, smeared appearance of ghosting on the myocardium is visible. As aforementioned, this may be due to blood flowing on the epicardium wall during the acquisition (hypothesis). However, this artifact remains acceptable since small and located on a restricted portion of the myocardium wall and did not prevent clear delineation of blood vessels within the wall. Image with the 160 µm in-plane resolution shows enhancement of the sharpness and demarcation of the vessels compared to the 230 µm in-plane spatial resolution image, as indicated with the orange arrow within the zoomed view (2 x 2 cm portion image).

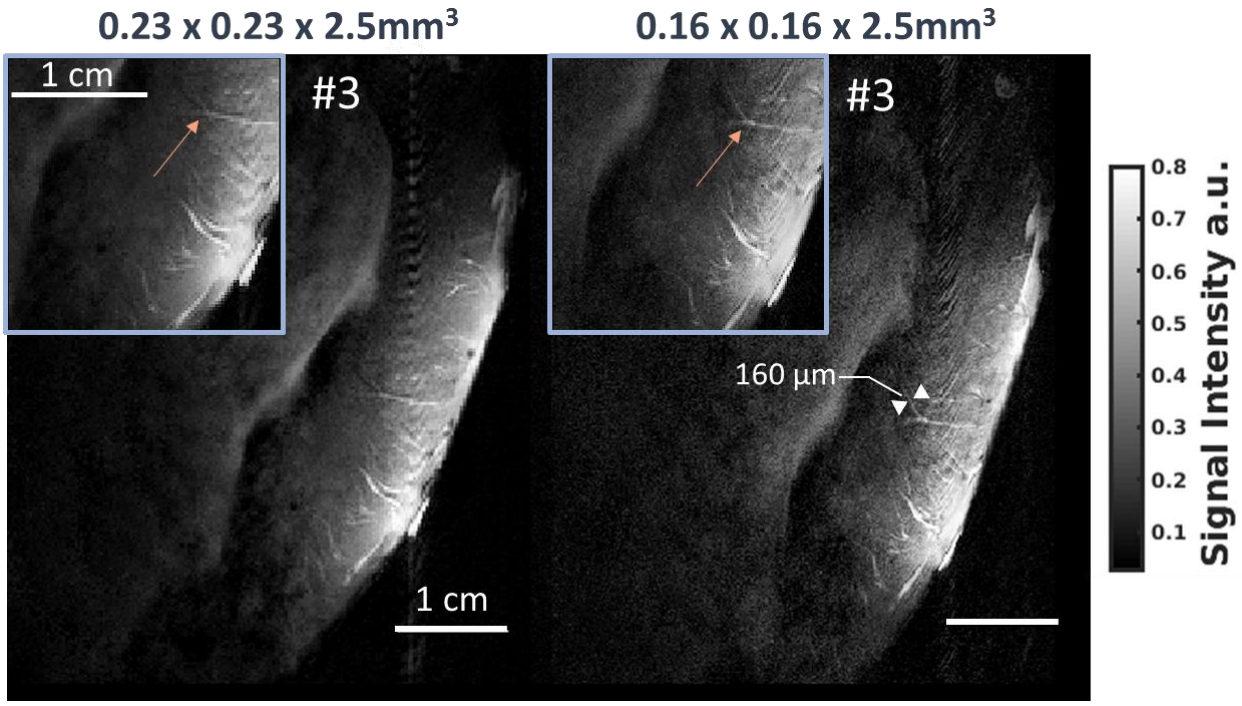

Figure 2-38: 2D-GRE (Acquisition #3) images of the left ventricle acquired with 230 µm and 160 µm in-plane spatial resolution on beating heart (120 ± 5 bpm). A zoomed-view of the blood vessels is provided in blue frames. Orange arrows show a small blood vessel, 160 µm in section.

Acquisition # 4

Another set of images was acquired by reducing the slice thickness to 1.5 mm as well as pushing the FOV to the smallest size that can be attainable with a 2D-GRE imaging sequence configured as follows: FOV = 50 x 50 mm^2; Matrix = 290 x 290 pixels; TR/TE = 593 / 25 ms; FA = 60°; bandwidth = 130 Hz/pixels; slice thickness = 1.5 mm; TTL-triggered every heartbeat (heartbeat of 96 ± 3 bpm); 1 segment; 2 slices; Total acquisition time = 5 min (around 2 min 30 s per slice) . Resulting spatial resolution was: **0.17 x 0.17 x 1.5 mm^3**. Resulting images are presented in Figure 2-39. Position of the coil is denoted (red dots), so that regions at the close vicinity are bright. A clear demarcation between the myocardium and the blood attests of the efficiency of the motion compensation technique even at such a high resolution. After adjusting the contrast and brightness for the two slices (second column), blood vessels of 200 µm to 300 µm in section were identified at the epicardium vicinity.

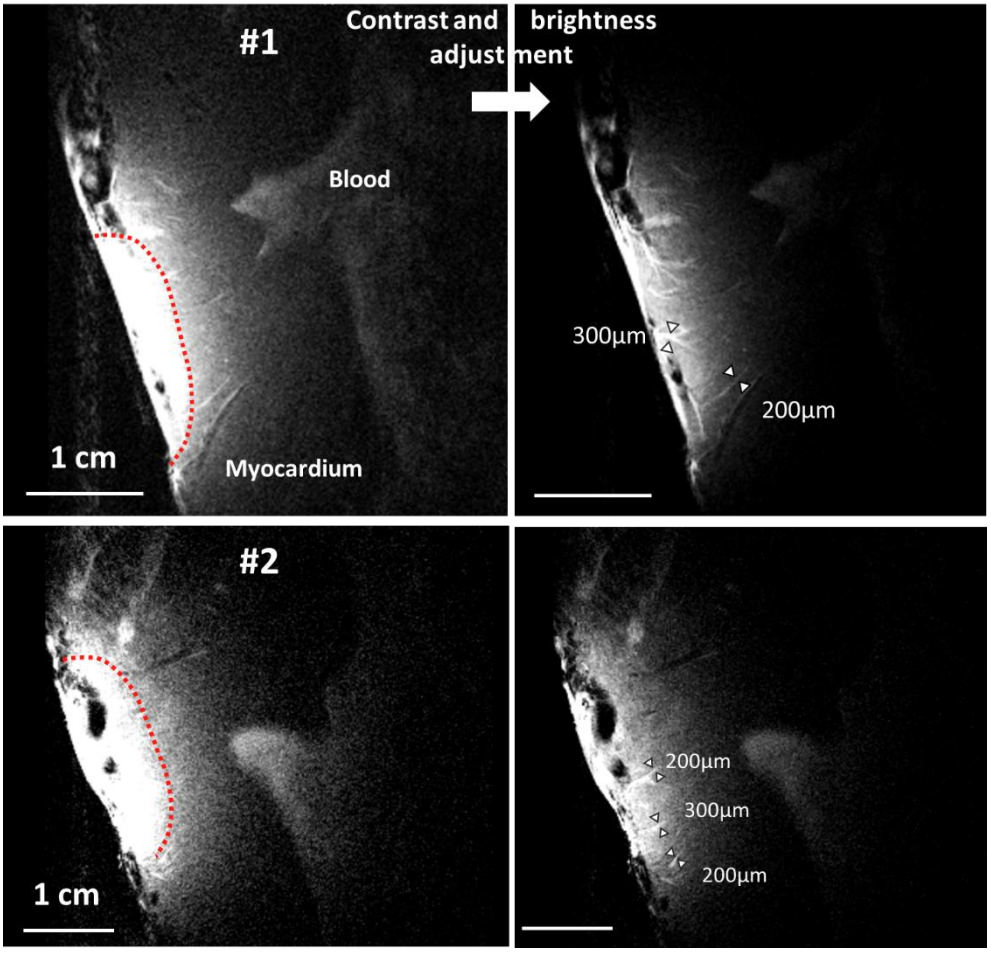

Figure 2-39: #1 and #2 slices of the 2D-GRE sequence (Acquisition #4) acquired on beating heart (96 ± 3 bpm) with a spatial resolution of 0.17 x 0.17 x 1.5 mm3. **Top row-** correspond to the slice #1 with two different contrast and brightness adjustment between left and right images. **Bottom-row**: same as in Top row for the slice #2. Red dotted lines indicate the coil position.

For comparison purpose, an image at a cruder spatial resolution of 0.6 x 0.6 x 1.5 mm^3 was acquired at same location as the slice #1, revealing the merit of high resolution imaging at delineating small vessels and therefore the performance of our coil at providing such a high-resolution in motion condition (Figure 2-40).

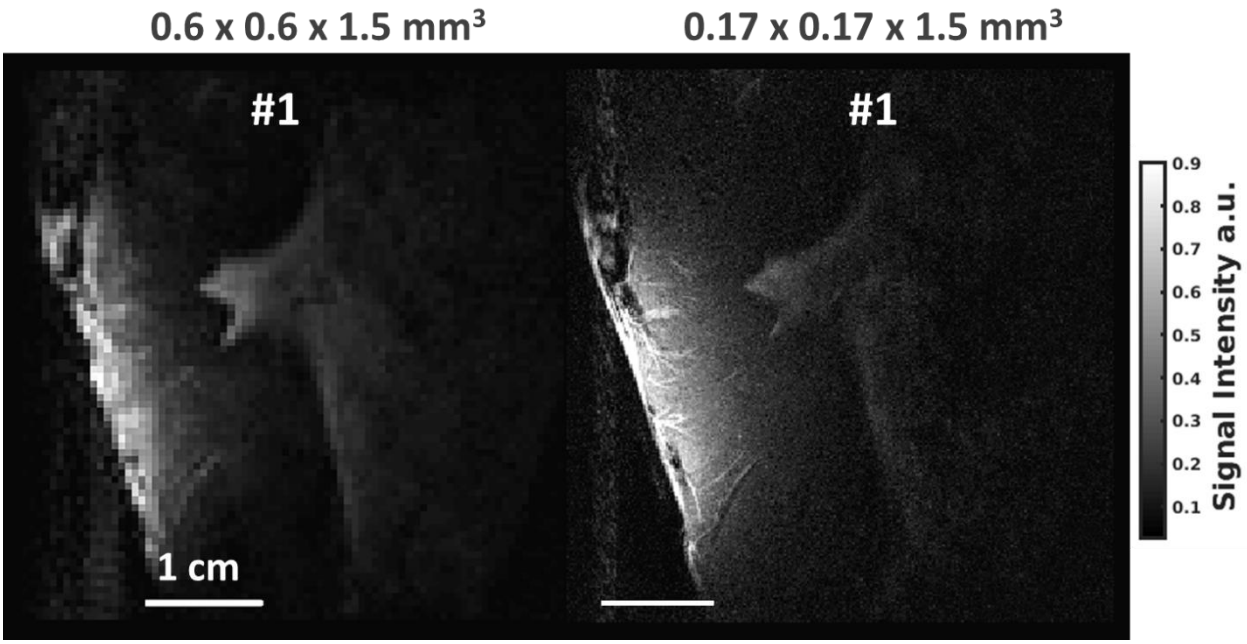

Figure 2-40: 2D-GRE images (Acquisition #4) of the beating heart (96± 3 bpm) at two different spatial resolution: 0.6 x 0.6 x 1.5 mm^3 (left) and 0.17 x 0.17 x 1.5 mm^3. Only the slice #1 is shown.

2.9.2.3. High resolution imaging: initial feasibility of T1 mapping

In cardiac magnetic resonance imaging, the T1 relaxation time in myocardial tissue may represent a valuable biomarker for a variety of pathological conditions. By quantifying tissue characteristics through T1 mapping, small variations of T1 within the myocardium can highlight tissue pathology. This possibility has driven our interest to evaluate the feasibility of obtaining high resolution T1 maps using our local coil in isolated heart. Current imaging spatial resolution of common T1 mapping MOLLI is 1.6 x 2.3 x 8 mm^3. Here, we evaluated the feasibility of obtaining T1 maps at **0.8 x 0.8 x 2 mm^3** and **0.7 x 0.6 x 2 mm^3 on a beating heart**, taking advantage of the reduced FOV to increase the spatial resolution while choosing the larger matrix size that could fit the time window between two TTL-triggers. The achievable matrix size is limited by the RR interval. Two additional T1 maps of **0.4 x 0.4 x 2 mm^3** and **0.3 x 0.3 X 2 mm^3** were acquired **after the heart contraction was stopped**.

Acquisition on beating heart

A first T1 map was acquired with the following parameters: FOV = 76 x 76 mm^2; Matrix = 96 x 96 pixels; TR/TE = 705 / 2.7 ms; FA = 35°; bandwidth = 345 Hz/pixels; slice thickness = 2 mm; 9 segments; Acquisition time = 58 s. Resulting spatial resolution was 0.8 x 0.8 x 2 mm^3. Images were acquired in diastole over 5 heartbeats, followed by a period of 3 heartbeats. After another inversion, another 3 images were acquired, resulting in the acquisition of 8 images.

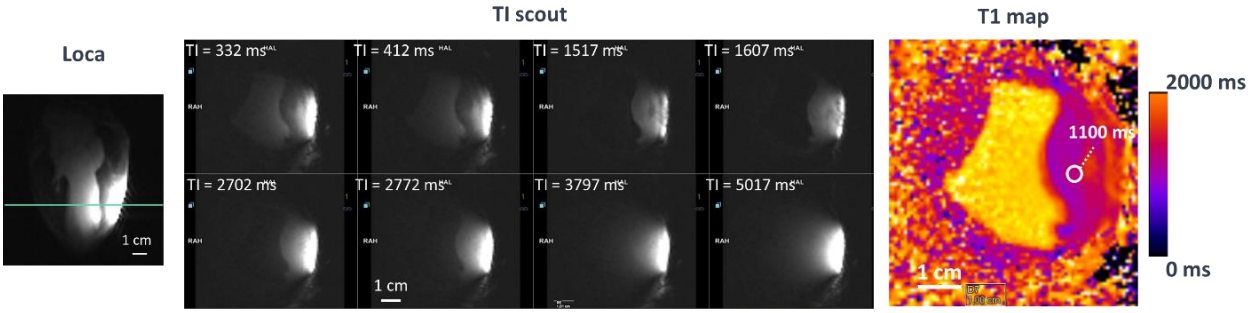

Figure 2-41: T1 mapping of the left ventricle with 0.8 x 0.8 x 2 mm^3 spatial resolution acquired on a beating heart (80 ± 5 bpm). **Left-** Localization image indicates the coil location and the position of the slice for T1 mapping (green line). **Middle-** TI scout with TI ranging from 332 ms to 5017 ms. **Right-** T1 map. T1 value of the myocardium was found to be 1100 ms.

Figure 2-41 shows the T1 map obtained with a resolution of 0.8 x 0.8 x 2 mm^3 on an isolated heart beating at 80 ± 5 bpm. Localization image of the left indicates (green line) the position at which T1 map was acquired. Corresponding TI scout is depicted in the middle and reveal images free from motion artifacts when looking at the interface between blood and myocardium. The T1 value of the healthy unenhanced myocardium was found to be 1100 ms in the displayed ROI, consistent with the expected value of approximately 1000 ms found in literature [43].

A second T1 map was acquired in an orientation such as a coronary blood vessel could be contained within the slice and thus evaluate the feasibility to discriminate it in the resulting T1 map. The imaging protocol was identical to that described above except the FOV was: 50 x 60 cm^2 and Matrix size was 71 x 96 pixels. Acquisition time was 44 s.

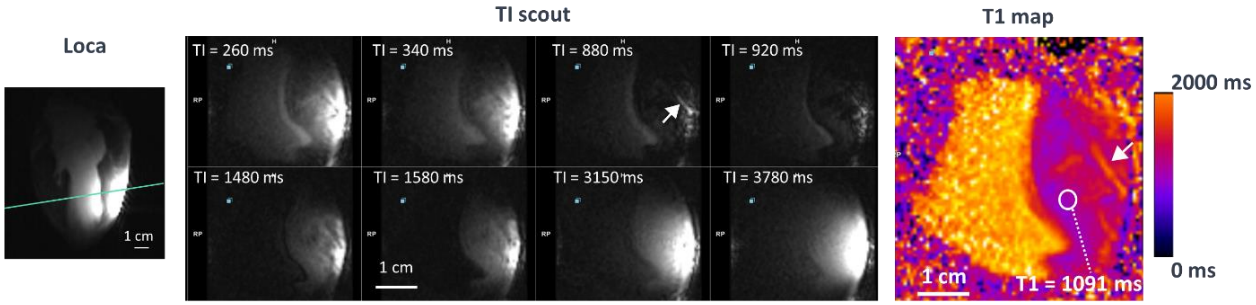

Figure 2-42: T1 mapping of the left ventricle with 0.7 x 0.6 x 2 mm^3 spatial resolution acquired on a beating heart (80 ± 5 bpm). **Left-** Localization image indicates the coil location and the position of the slice for T1 mapping (green line). **Middle-** TI scout with TI ranging from 260 ms to 3780 ms. White arrow shows a blood vessel. **Right-** T1 map. T1 value of the myocardium was found to be 1091 ms. White arrow points out the blood vessel.

Figure 2-42 demonstrates that the coronary blood vessel (white arrow) can clearly be distinguished from the dark myocardium at a TI = 880 ms. T1 map highlights the difference between the blood vessel and myocardium (white arrow). The T1 value for the unenhanced myocardium was found to be 1091 ms in the indicated ROI, consistent with the previous value. No artifact compromising the appearance of the vessel was observed and sharp myocardium contours on the TI scout indicate the efficiency of the gating at freezing the motion.

These two results demonstrate the feasibility of pressure-gated, high-resolution T1 mapping using our local coil.

Acquisition on a static heart

At the end of the experiment, the heart contraction was stopped and two additional T1 maps with **0.4 x 0.4 x 2 mm^3** and **0.3 x 0.3 x 2 mm^3** were acquired to investigate the possibility of discriminating fine blood vessels and structures using T1 characteristics, and for comparison with T1 maps acquired during beating. T1 maps were acquired at the same location as the high-resolution images acquired in (see acquisition #1, section 2.9.2.2). The T1 maps were acquired with the following parameters: FOV = 50 x 60 mm^2; Matrix size (**400 µm** / **300 µm** in-plane resolution) = 120 x 144 pixel / 148 x 176 pixels; TR (**400 µm** / **300 µm** in-plane resolution) = 1407 / 1854 ms; TE = 4 ms; FA = 35°; bandwidth = 130 Hz/pixels; slice thickness = 2 mm; 21 segments; Acquisition time = 1 min 25 s / 2 min.

Figure 2-43 depicts the two T1 maps, acquired at two different spatial resolution (400 µm in-plane and 300 µm in-plane resolution) at the position indicated by the green line on the localization image (left).

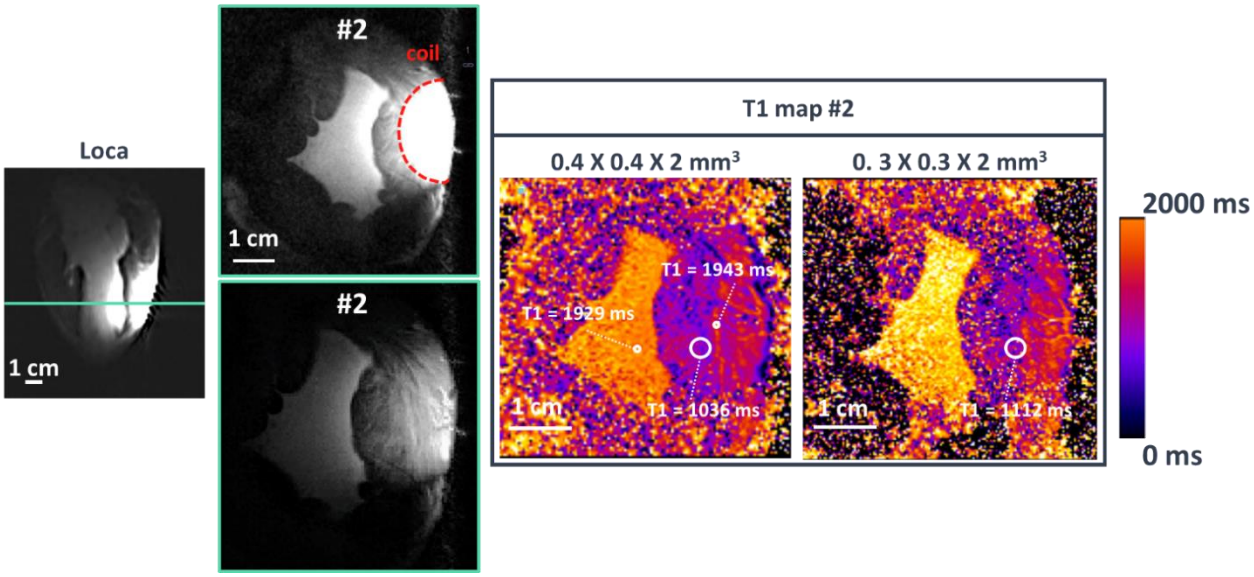

Figure 2-43: T1 maps with 0.4 x 0.4 x 2 mm^3 and 0.3 x 0.3 x 2 mm^3 spatial resolution acquired on a static heart, right after the heart contraction was stopped. **Left-** Localization image showing the position/orientation of the T1 maps slices relative to the myocardium. **Middle-** Corresponding high-resolution images acquired at the same location when heart was beating (section 2.9.2.2) with different scaling (Top / Bottom). **Right-** High-resolution T1 maps with ROIs indicating the mean T1 value in it.

These T1 maps correspond to the images collected earlier on a beating heart (acquisition slice #1, section 2.9.2.2) with a spatial in-plane resolution of 400 µm and a slice thickness of 2.5 mm. Structural details and blood vessels at the vicinity of the coil are visible on these images (Top: before adjustment, Bottom: after contrast and brightness adjustment). T1 maps reflect the structural changes in the myocardium wall and highlight blood vessel presence. The T1 value of 1943 ms found within the myocardium wall at the location of what seems to be a blood vessel is consistent with the T1 value found for the blood within the cavity of left ventricle (T1 = 1929 ms in the T1 map with 400 µm in-plane spatial resolution). T1 values found in both the T1 maps (T1 = 1036 ms / T1 = 1112 ms for the 400 µm and 300 µm in-plane spatial resolution respectively) were consistent with the expected values from the literature [43]. However, a marked difference in the T1 value found for the blood compared to the clinical expected value (approximately 1430 ms [44]) is observed. This can be attributed to the blood composition within the perfusion setup that differs a bit

from in vivo composition. Indeed, a Tyrode buffer (vol/vol: 1:3, 38°) as well as Dobutamine to maintain heart function during ex vivo perfusion were added to the blood collected on the animal [41]. This variation in blood composition may explain the difference obtained in T1 blood value.

These two T1 maps demonstrate the potential of high-resolution imaging for T1 mapping as they highlight the structural changes as well as fine blood vessels. This could be used to depict small details in the myocardium tissue to distinguish diffuse fibrosis from the viable tissue. However, these two maps were obtained on a static heart and therefore, no gating was performed. Extrapolation of these first results toward in-vivo suffer from the ECG-gated limitation (pressure gating in our case) that constraint the maximal matrix size achievable. One of the solutions is thus to reduce the FOV at the minimum but depending on the gradient strength provided by the scanner, FOV cannot always be reduced to the desired one. In our case, **we were able to perform a minimal FOV of 50 x 60**. This limited the matrix size to 71 x 96 when acquisition was gated and therefore limited the spatial in-plane resolution to 0.7 x 0.6 mm^2.

2.10. Application to high resolution MR-thermometry

In patients presenting with persistent atrial fibrillation, one of the reference treatments is radiofrequency ablation which consists in inducing a local necrosis of the arrhythmogenic tissue. In this context, temperature mapping is of major importance to deliver the appropriate amount of energy to the targeted tissue and help determine the quality of lesions (place, size, depth and extent of damage). Previous studies have demonstrated the possibility to monitor temperature changes in the ventricles of sheep with a spatial resolution of 1.6 x 1.6 X 3 mm^3 [45], [46]. However, in the context of atrium imaging, where the wall thickness ranges from 2 to 5 mm, such a spatial resolution remains insufficient for precise monitoring of temperature changes. A submillimeter spatial resolution (of 300 µm isotropic or better) is desirable to characterize the cardiac substrate and precisely monitor the radiofrequency procedure. Such an improvement in spatial resolution results in a reduction of the Signal-to-Noise ratio (SNR) by two orders of magnitude, leading to insufficient image quality. As the precision on temperature images depends on MRI phase accuracy, which is inversely proportional to SNR on magnitude images [47], increasing the SNR becomes thus mandatory. Taking advantage of the higher SNR achieved with our

developed local coil (SNR gain of 35), we conducted experiments in order to evaluate the maximal spatial resolution one is possible to achieve on phantom while keeping a good temperature precision (<= 1°).

2.10.1. Experimental setup

A plastic cylinder filled with agar (3% with 0.9% NaCl to match tissue electrical conductivity) was used for experiments. A RF ablation catheter (Imricor Medical Systems, Burnsville, Minnesota, USA) equipped with 2 electrophysiology (EP) electrodes (3.7-mm tip electrode and 3.5-mm inter-electrode spacing) was inserted vertically in the agar gel, close to the left cylinder bore. The 2 cm-in diameter loop coil was positioned against the cylinder left bore, with its axis aligned with the catheter tip, where radiofrequency energy is emitted (Figure 2-44). The tip electrode of the catheter was connected to a clinical RF ablation generator (Stockert Medical Solution, Freiburg, Germany). RF ablation of 40 s each was performed with an RF power of 15 W.

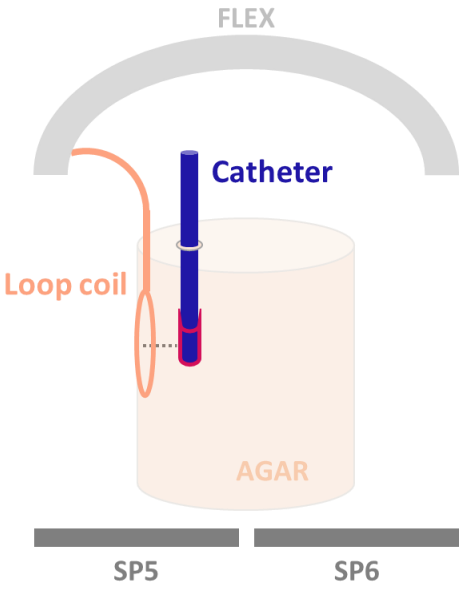

Figure 2-44: Setup used for high-resolution MR thermometry experiment

2.10.2. MR-Thermometry using a local coil combined with conventional coils

All measurements were performed on a 1.5T clinical imaging system (MAGNETOM, Aera Siemens Healthcare Erlangen, Germany) equipped with a maximum gradient strength of 45 mT/m and a maximum slew rate of 200 T/m/s. Acquisition was first performed with conventional coils, namely the FlexSmall_4 (FL, 4 elements) and the Spine (SP, 2 coils with 4 elements each). In a second experiment, the conventional coils were combined with the local coil (Loop), for a total of 13 elements.

Two spatial resolutions were performed: **1.6 x 1.6 x 3 mm^3** and **1.4 x 1.4 x 2 mm^3**

The acquisition sequence was a single-shot gradient echo planar imaging (EPI) sequence, with the following parameters: FOV = 123 x 123 mm^2, TR/TE = 1000/23 ms, matrix size = 78 x 78 and 86 x 86 pixels (zero filled to 156 x 156 and 172 x 172 pixels) with slice thickness = 3 and 2 mm for a spatial resolution of 1.6 x 1.6 x 3 mm^3 and 1.4 x 1.4 x 2 mm^3 respectively, bandwidth = 1455 Hz/pixel, FA = 53°, GRAPPA 2, 7/8 Partial Fourier. For each experiment, 120 dynamics were acquired. The sequence as well as the thermometry pipeline implemented to compute and display temperature maps are described in Chapter4.

2.10.2.1. Temperature precision measurement

In order to assess the thermometry precision, a first acquisition with no ablation (no heating) was performed. The temporal standard deviation (σ_T) of temperature was computed in a region of interest of ~45 x 45 mm^2 for each pixel within the sensitivity region of the local coil over the 120 dynamic acquisitions, as shown in Figure . This analysis was performed before and after filtering using the filter described in Chapter 4 section.

Figure 2-45 shows the resulting temperature precision for the two experiments for a spatial resolution of **1.6 x 1.6 x 3 mm^3**. Magnitudes images evidence the intense bright region at the close vicinity of the local coil, which corresponds to the local coil sensitivity. In this region, the ROI of 45 x 45 mm^2 selected for the temporal standard deviation computation is represented by a blue frame. Corresponding temporal standard deviation maps are displayed below.

σ_T values (mean ± std) were **0.83 ± 0.16 °C** and **0.25 ± 0.08 °C** without filtering for conventional coils only and conventional coils combined with the local coil respectively. After filtering, the σ_T values were **0.22 ± 0.08 °C** and **0.07 ± 0.03 °C** respectively. Similarly,

σ_T values were computed for the acquisition with 1.4 x 1.4 x 2 mm^3 spatial resolution and were found to be: **1.28 ± 0.27 °C** and **0.28 ± 0.07 °C** before filtering for conventional coils only and conventional coils combined with the loop coil respectively. After filtering, σ_T were**:** **0.33 ± 0.12 °C** and **0.07 ± 0.03 °C** respectively. These results demonstrate a marked improvement in temperature precision even when no filtering is applied and that this precision is far below the requirement of 1°C (0.25°C in average). Furthermore, going higher in spatial resolution (1.4 x 1.4 x 2 mm^3) does not affect the precision of the temperature when loop coil is combined with conventional coils. Conversely, when only the conventional coils are used, temperature accuracy is **4 times lower** than when the loop coil is added to the reconstruction. Filtering the data yields to a greater temperature accuracy and allows a precision of 0.07°C in average.

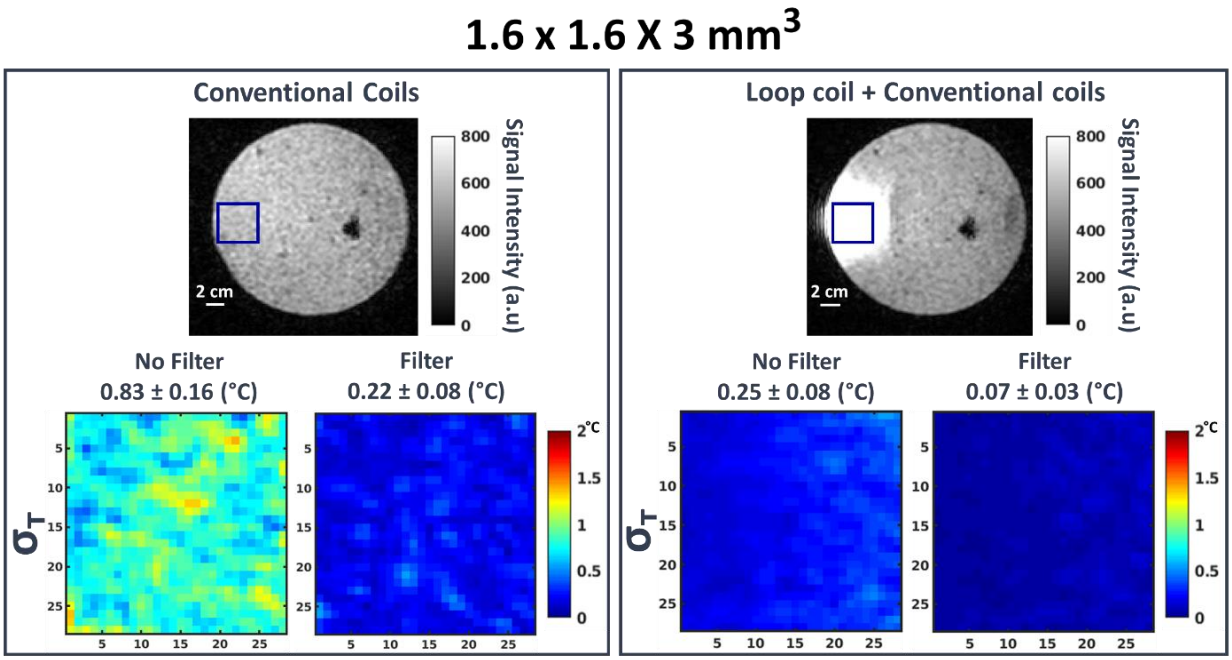

Figure 2-45: Evaluation of the temperature precision obtained when only conventional coils (FlexSmall_4 and Spine elements) are used (left) and when a local coil is combined with conventional coils (right). Spatial resolution of the images is 1.6 x 1.6 x 3 mm3. Top images display the magnitude image with the ROI used for statistical analysis overlaid on it (blue frame). Bottom images show the resulting temporal standard deviation (σ_T) maps computed over the ROI before (left) and after (right) filtering for both experiments.

2.10.2.2. Heating experiment

Radiofrequency was delivered 30 s after beginning of the MR-thermometry sequence, for a duration of for 40 s. The first 30 slices were averaged together to create reference phase images for temperature computation (see chapter 4 for details). For each acquisition (with or without the local coil), the temperature evolution in the same pixel was analyzed before and after filtering. The selected pixel corresponded to the pixel with the maximum temperature over the time. A temporal window (purple frame) of 5 dynamic acquisitions was used to compute the mean temperature and the temporal standard deviation at the end of the radiofrequency energy deposition (at t = 70s).

Figure 2-46 displays the evolution of the temperature in the selected pixel for the experience with 1.6 x 1.6 x 3 mm^3 spatial resolution.

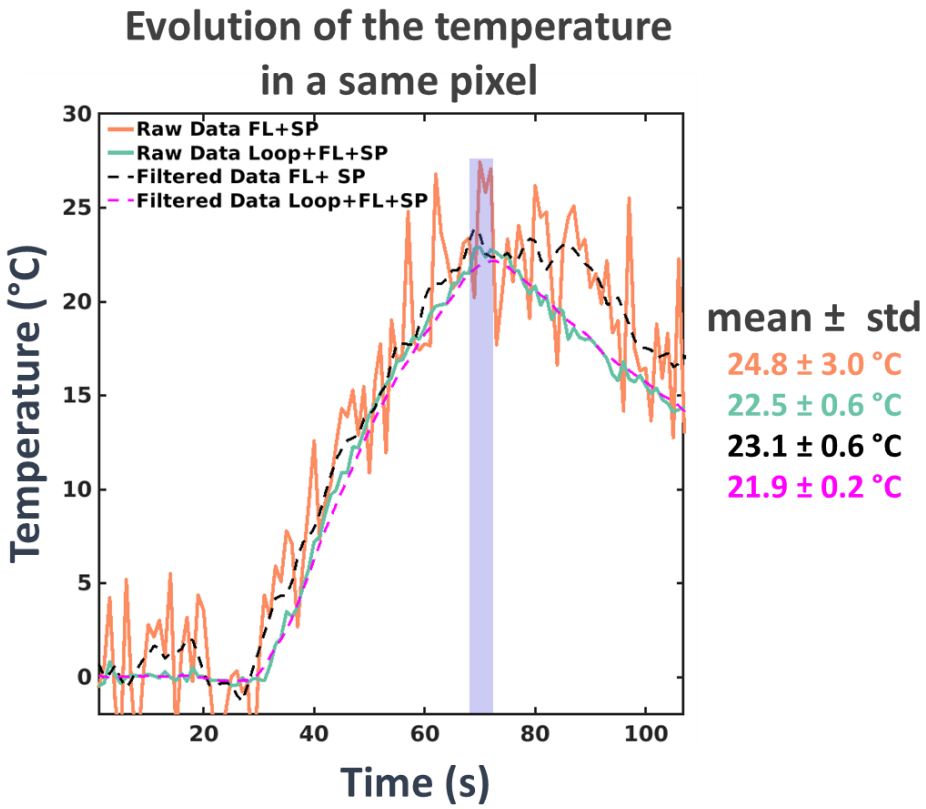

Figure 2-46: Evolution of the temperature over the time in a same pixel for experiment with 1.6 x 1.6 x 3 mm spatial resolution. Orange curve corresponds to the temperature data obtained when only conventional coils (FL+SP) are used as receivers and without filtering the data (raw data). Black dotted curve represents the same data after filtering. Green curve correspond to the raw temperature data obtained when combining the local loop coil with conventional coils (Loop+FL+SP). Pink dotted curve corresponds to the filtered temperature data acquired with Loop+FL+SP coils. Mean maximal temperature values for each curve were computed over the temporal window displayed in violet.

Original data (not filtered) acquired with the conventional coils presents large temperature variations all along the acquisition (orange curve) with an uncertainty of ± 3.0°C in the estimation of the maximal temperature attained. After filtering these data (black curve), uncertainty is markedly reduced (± 0.6°C). In comparison, adding the loop coil element directly allows an uncertainty of 0.6°C in the estimation of the maximum temperature without filtering, demonstrating thus the gain in temperature precision one can obtain using such a coil. Filtering the original data acquired with combination of the loop coil and conventional coils enable precision of 0.2°C.

2.10.3. Evaluation of the temperature precision at different spatial resolution

In this experiment, only the loop coil was used and we evaluated the temperature precision obtained when going higher in spatial resolution. The same sequence as well as the thermometry pipeline were used, except that no Grappa acceleration was used. Four experiments were conducted with the following parameters:

Number	FOV (mm^2)	Matrix size (pixels)	Slice thickness (mm)	Spatial resolution (mm^3)
#1	100 x 100	64 x 64	3	1.6 x 1.6 x 3
#2	61 x 61	64 x 64	3	0.8 x 0.8 x 3
#3	61 x 61	64 x 64	2	0.8 x 0.8 x 2
#4	53 x 53	76 x 76	2	0.7 x 0.7 x 2

Table 2-2: MR experiments parameters

All acquisitions were performed with TR/TE = 340/38 ms, bandwidth = 1455 Hz/pixel, FA = 53°,and 7/8 Partial Fourier. For each experiment, a total of 500 dynamics was acquired.
Heating experiments were performed with a Laser (975 nm, LuOcean Mini 4, Lumics,Berlin, Germany) inserted vertically in the agar gel (2 min 24s heating, 0.4 W). As in the previous experiment, the loop coil was placed against the plastic box containing the gal with its axis perpendicular to the laser's tip. The temporal standard deviation (σ_T) of temperature was computed for each pixel in a region of interest of ~12 x 12 mm^2 around the laser (orange

frame in Figure 2-47) over the 20 dynamics preceding heating. This analysis was performed before and after filtering. Temporal standard deviations are given in Table 2-3.

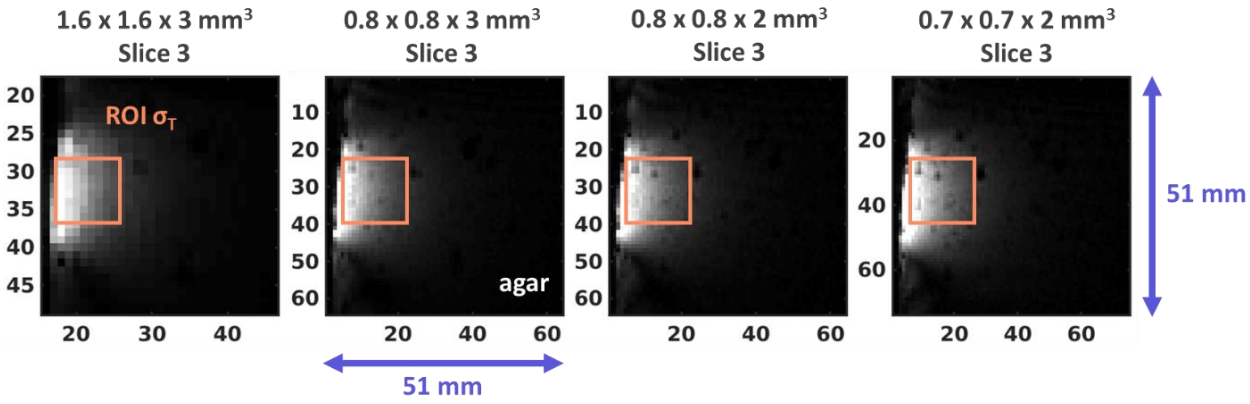

Figure 2-47: Magnitude images of the gel agar for each MR acquisitions described in Table 2-2. Overlaid orange frames indicate the ROI for statistical analysis.

Acquisition	σ_T before filtering (°C) (mean ± std)	σ_T after filtering (°C) (mean ± std)
#1	0.35 ± 0.02	0.13 ± 0.01
#2	0.45 ± 0.07	0.15 ± 0.02
#3	0.58 ± 0.09	0.18 ± 0.04
#4	0.87 ± 0.07	0.32 ± 0.04

Table 2-3 : Temporal standard deviation (mean ± std) obtained for each of the four MR acquisitions within the ROI

We observe a decrease in temperature precision while increasing the spatial resolution. However, after filtering, the precision is maintained below 0.2 °C even with a voxel size of 0.8 x 0.8 x 2 $mm^{3.}$

Figure 2-48 displays the resulting temperature maps over a 16 x 16 mm^2 region for each of the investigated spatial resolutions. The white dashed cross represent the pixel with the maximal temperature increase. Evolution of the filtered temperaure in this pixel was plotted over the time for each of the four acquisitions and is shown below.

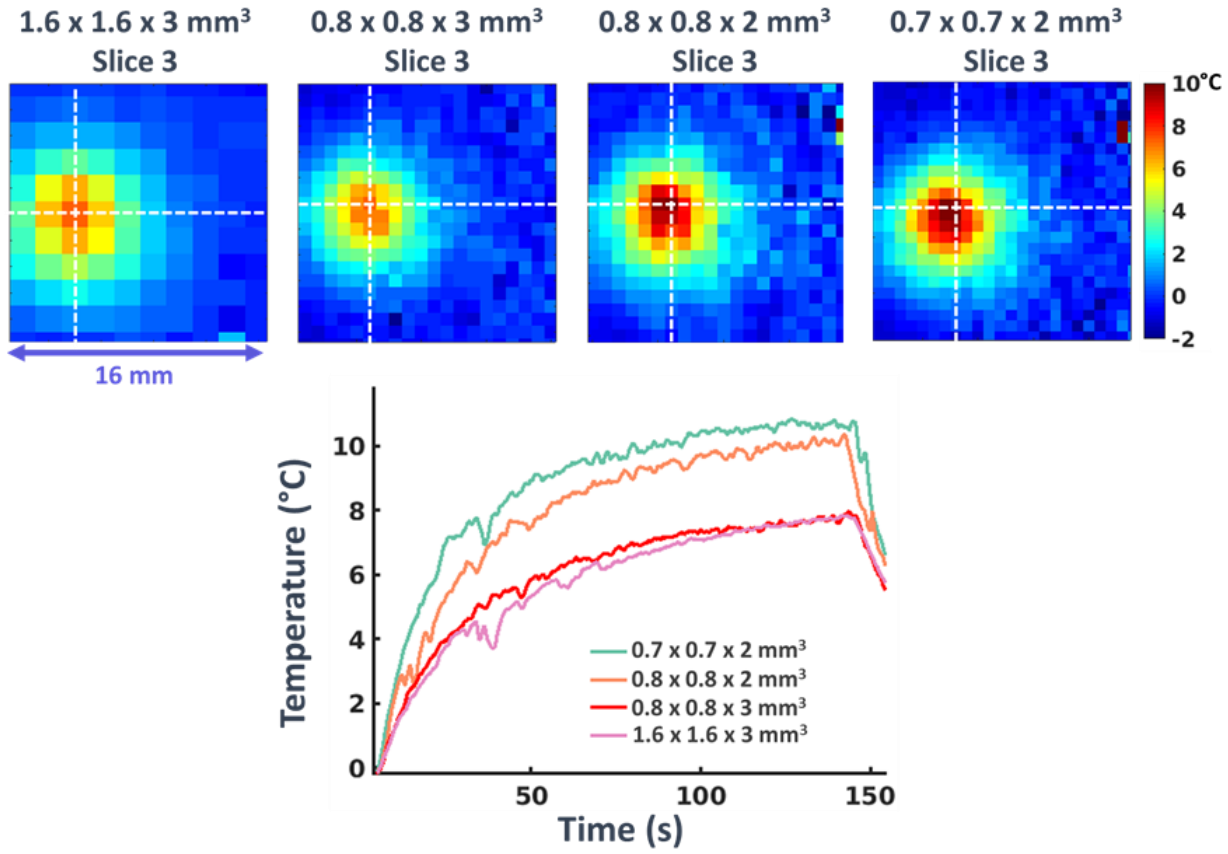

Figure 2-48: **Top-** Temperature maps at the end of the heating over a 16 x 16 mm^2 region around the heating source (laser) for the four investigated spatial resolutions. The white dashed cross indicate the pixel with the maximal temperature increase over the time. **Bottom**- Filtered temperature evolution in the selected pixel for the four spatial resolutions.

A temporal window of 5 dynamic acquisitions was used to compute the mean temperature and the temporal standard deviation at the end of the heating experiment (at t = 144s). Resulting maximal temperature (mean ± std) was: **10.6 ± 0.5 °C; 9.5 ± 0.6 °C; 7.9 ± 0.3 °C** and **7.8 ± 0.1 °C** for acquisition #4,#3, #2 and #1 respectively. From these results, we show that for a same location, a difference in temperature of 2.8 °C exists between a temperature map with voxel size of 7.68 mm^3 and a temperature map with 0.98 mm^3. Reduction of partial volume effect is of particular importance for very focal heating such as for thermal ablation of structures like the atrium wall.

2.11. Discussion and conclusion

The conducted work aimed at developing a coil prototype to improve the spatial resolution in cardiac MRI, at clinical field (1.5 T). The prototype introduced here was based on a single-loop design that seems the easiest local surface loop to implement, as a first approach. The manufacturing of intravascular imaging coils raises several challenges among which the major problem lie in the heat induced by the RF current into conductors such as coaxial cables linking the coil (deeply introduced into the patient) to the connecting plug of the MR system [12], [48]. In order to alleviate this safety issue, an optical detuning circuit was implemented, based on previous works [15]. Efforts were made to adapt this solution to our tuning/matching network. In our design, we found that only one photodiode was sufficient to feed the PIN diode, therefore, that only one optical fiber is required which is an important point when converging toward a practical implementation of the intravascular coil, especially to meet the small size constraints. We demonstrated that such an optical detuning circuit provides an efficient decoupling strategy while allowing the same sensitivity and selectivity performances than a coil that would be actively detuned by galvanic means. We however observed that a tiny bright spot was remaining at the location of the coils when the latter were detuned. This can be explained by the close proximity of our coils with the sample which increases the sample resistance. One of the solutions is to wrap our coil in an insulated housing. Moreover, refinement of the detuning circuit should improve the detuning efficiency and lower the reflection coefficient close to 0 dB when detuning the coil. In our workbench experiment, calculated reflection coefficient values were close to -1dB, indicating a residual coupling at the operating frequency when coils were detuned. Regarding the optical detuning circuit, a variability in the detuning efficiency may subsist due to misalignment between the optical fiber and the sensitive area of the photodiode. This could be solved by implementing a fixation to maintain the optical fiber perpendicularly centered to the sensitive area, achieving thus the required optical power to properly activate the PIN diode.

This pilot study highlights the possibility of amplifying the signal to noise ratio of a factor of **35** in the close vicinity of the coil, compared to conventional chest coil. This increase in SNR can be used to decrease the voxel size without acquisition time penalties, by reducing the FOV accordingly. The performance of our local coil was evaluated on 5 isolated beating

hearts. Results highlights first the feasibility of a small FOV, high resolution imaging and second the repeatability of our method. Use of gated acquisitions relying on intraventricular pressure recording allowed acquisition of images free from motion artifacts resulting in clear delineation of myocardium wall structures and blood vessels. At clinical field, the highest achievable spatial resolution was **0.16 x 0.16 x 2 cm^3** and the smallest performed FOV being **50 x 50 mm^2** for the tested acquisition sequences. The spatial coverage of our loop was large enough to acquire multi-slice imaging in-vivo and even 3D images ex-vivo. The diameter of the coil could, however, be smaller to further reduce the spatial coverage of our coil which in our case was around 6-cm deep. Performance of the loop coil was also exploited for MR-thermometry experiments. At the current spatial resolution of MR-thermometry (1.6 x 1.6 x 3 mm3), a **precision of 0.25°C** (0.07°C after filtering) was obtained using the local loop coil combined with conventional coil, which is 3 times greater than with conventional coils only. Using the local coil alone, it was possible to perform a reduced FOV (53 x 53 mm^2), high-resolution (0.7 x 0.7 x 2 mm3) temperature mapping while maintaining a temperature precision < 1°C (0.87°C / 0.32°C before/after filtering). From these observations, local loop coil could be used in conjunction with external RF coils to either enhance the temperature accuracy in the combined image or provide high-resolution temperature maps when used alone exploiting reduced FOV. As these results were obtained in a static gel, they therefore cannot simply be generalized to in vivo where motion still remains the main challenge and source of temperature errors.

Despite the encouraging results obtained on a beating heart with our coil, the gap between the prototype and the practical implementation is nevertheless not yet bridged. Indeed, several challenges have to be raised before converging toward intravascular design.

- **First, our coil has to become flexible**. One of the solutions relies on expandable elongated loop. This design provides the best quality images when the axis of the catheter is along the main magnetic field compared to loopless antenna [18]. Several different designs were developed. Zimmerman et al. [26] conceived a receive-only loop mounted on a ballon catheter for ex-vivo imaging of the vascular wall. Martin et al. [49] used an intravenous RF coils made off copper-berrylium material to assess the arterial wall indirectly. Quick et al. [27] employed a balloon catheter with a copper coil and a catheter with an expandable Nitinol coil to image the iliac artery. Homagk

et al.[50] proposed a self-expandable catheter loop without any balloon that may block the blood flow. More recently, Schmidt et al. [7] developed a novel manifold push-pull mechanism to expand an imaging loop coil inside the heart cavity, Volland et al. [10] developed a catheter-mounted expandable loop balloon for high-resolution intracardiac MR imaging. Alternative catheter-mounted allowing coil deployment via pre-shaped filament was also proposed [9]. Nevertheless, none of these papers proposed a solution that merges this elegant and practical design with a network including an efficient detuning strategy, which meets the safety requirement.

The critical point of such a loop design relies on the lumped components (capacitors, inductors, resistors, diodes) that reduces the flexibility and increases the diameter of the design besides raising safety. To overcome these issues, tuning and matching strategies, as well as the circuit design were discussed in the literature. Remote tuning and matching network was considered [27] to avoid bulky, active components and not compromising the flexibility of the coil. Additional advantage of such a configuration is that SNR less depends on imperfect tuning and matching and tuning less depends on coil loading and expansion. However, this strategy achieves a lower quality factor [49] and was found to led to a drop of 75% in image SNR as compared to having a local tuning/matching (at the distal part), since the SNR in this configuration is greatly limited by the losses associated with the coaxial cable [51]. Therefore, if one wants to achieve the maximum SNR, the tuning and matching capacitors should be placed at the end of the loop before connecting it to the coaxial cable [50]. As placing the tuning/matching network at the distal part of the catheter coil is not always feasible due to physical size constraints and poses the issues of safety with introduction of active components inside the body, one alternative is the loopless antenna. An important property of the loopless antenna indeed is that its optimum impedance is close to that of a typical coaxial cable, and therefore, the tuning and matching can be placed remotely without significant loss of performance [18]. However, one of the main problems with this loopless design, besides the fact that the sensitivity along its length shows a significant variation, is that its sensitivity is very low at its distal end and therefore seems not optimal in our case when we rather want to image a disk-shaped plane. To solve this issue, Qian et al. [52] demonstrated that tapered insulation for the whip could be used to increase the

sensitivity near the tip. Another solution to overcome the distal tuning/matching network while benefiting of the sensitivity of a loop coil may reside on coaxial RF coils. Such a technology, relying on auto-resonant structures such as transmission line resonators implemented using coaxial cables, allow more flexibility, close-fitting design, light, weight, and robustness to coil overlap variations. Multi-turn multi-gap coaxial RF coils exhibit outstanding mechanical flexibility while offering more degrees of freedom in the coil diameter [53], [54]. This type of coil could also be embedded inside a catheter sheath for insertion and navigation and unfolded inside the heart cavity. However, currently, no coaxial coil match the required diameter of 2-cm or less at our operating frequency of 63.6 MHz. Moreover, if the matching of such a coil can be done remotely, there is sometimes the need of a fine tuning at the distal part. Other solutions could be considered such as manufacturing our coil on a flexible circuit board such as Kapton foil or 3D printing with selective metalization [55]. At present, we were not able to miniaturize the coil to converge toward intra-cardiac one. However, in the light of these improved thin foil technologies, this problem could be overcome in future refinements of the coil design.

- **Second key challenge of our coil is to make it safe**. Detuning is an important aspect of a safety design as it helps in reducing the current induced on the coil during transmission of RF pulses to the body. Whatever the coil design (loopless antenna, loop coil), the detuning has to be handled with care. As mentioned earlier, PIN diode-based decoupling circuits needs to be supplied by a direct current. This represents a safety issue since in case of tuning/matching network in the distal part, this current is circulating inside a coaxial cable, potentially in contact with the heart of the patient. In our case, where we chose to place the tuning/matching network at the distal part for higher SNR performance, we replaced the galvanic connection of the decoupling circuit by an optical connection. Nevertheless, galvanic connection is still required to connect the coil to the receive port and this optical detuning solution should be associated with an optical method of NRM signal transmission to fully remove coaxial cable from the intravascular probe and therefore to fully ensure patient safety [34], [56], [57]. Other solutions were also proposed to diminish the unwanted induced currents like coaxial chokes [14], transformer coupled

transmission lines [58], baluns matching circuits and traps [39]. Evaluation of the potential RF-related heating of the coil during MRI scanning is therefore a crucial step of the development.

- Third, the most challenging problem in intravascular imaging is **the issue of flow and motion artifacts.** The major problem associated with the blood stream is ghost artifacts, as was shown in Martin et Henkelman [23]. In addition, possible vibration of the coil due to pulsatility may increase blurring artifacts. Our solution to generate images free from these artifacts rely on gated acquisition by deriving the left intravascular pressure signal. In our study, the coil was not directly put within the blood flow and was not subjected to the respiratory motion-induced which certainly reduced the artifacts. Another attempt to compensate for cardiac motion during imaging process could rely on MR-tracking coils. Ideal is to converge toward “an all-in-one” probe that is capable of performing tracking and imaging [1], [7], [59]. To avoid multiple coaxial cables connected to the external system, Kurpad et Unal [60] implemented a multi-mode coil design that allows both tracking of the catheter and high-sensitivity, limited FOV for imaging the vessel wall and cardiac chambers. This implementation was not tested in vivo.

- Finally, perspective of the coil array could be envisioned to improve both the spatial resolution and reducing the acquisition through subsampled k-space acquisitions. Recently, Schmidt et al. [61] converge toward a RF coil assembly capable of self-expansion that includes two RF coils and a tracking coil to indicate the location and movement of the RF coils within an imaging subject.

2.12. References

1] J. de Arcos et al., ‘Motion-corrected high-resolution intra-cardiac imaging using MR-Tracking coils: reducing the effect of noise on motion estimation’, Proceedings of the 25th ISMRM Annual Meeting, Honolulu, HI, USA 2017.

[2] A. F. Thomsen, ‘Left Atrial Wall Thickness and Pulmonary Vein Size are Increased in Patients with Atrial Fibrillation Compared to Healthy Controls - A Multidetector Computed Tomography Study’, International Journal of Clinical Cardiology, vol. 4, no. 2, Jun. 2017.

[3] K. P. Pruessmann, M. Weiger, M. B. Scheidegger, and P. Boesiger, ‘SENSE: Sensitivity encoding for fast MRI’, Magnetic Resonance in Medicine ,pp. 952–962, Nov 1999

[4] S. Giusti et al., ‘Preoperative rectal cancer staging with phased-array MR’, Radiation Oncology, vol. 7, no. 1, p. 29, Dec. 2012.

[5] R. Frass-Kriegl, S. Hosseinnezhadian, M. Poirier-Quinot, E. Laistler, and J.-C. Ginefri, ‘Multi-Loop Radio Frequency Coil Elements for Magnetic Resonance Imaging: Theory, Simulation, and Experimental Investigation’, Frontiers of Physics, vol. 7, p. 237, Jan. 2020.

[6] H. L. Kantor, R. W. Briggs, and R. S. Balaban, ‘In vivo 31P nuclear magnetic resonance measurements in canine heart using a catheter-coil.’, Circulation Research, vol. 55, no. 2, pp. 261–266, Aug. 1984, doi: 10.1161/01.RES.55.2.261.

[7] E. J. Schmidt et al., ‘Intra-Cardiac MRI Catheter for EP Ablation Monitoring: Preliminary Studies’, Proceedings of the 19th ISMRM Annual Meeting, Montreal, Canada 2011.

[8] N. A. Volland, E. G. Kholmovski, J. R. Hadley, and D. L. Parker, ‘Limited FOV MR thermometry using a local cardiac RF coil in atrial fibrillation treatment’, Proceedings of the 19th ISMRM Annual Meeting, Montreal, Canada 2011.

[9] N. A. Volland, R. Merrill, J. R. Hadley, and D. L. Parker, ‘Development of a catheter-mounted cardiac RF coil for temperature imaging in atrial fibrillation treatment’, Proceedings of the 21th ISMRM Annual Meeting, Salt Lake City, Utah, USA 2013.

[10] N. A. Volland, J. R. Hadley, E. G. Kholmovski, N. F. Marrouche, and D. L. Parker, ‘Catheter-mounted expandable loop (CAMEL) balloon RF coil for high-resolution intracardiac MR imaging’, Proceedings of the 22th ISMRM Annual Meeting, Milan, Italie, 2014.

[11] M. F. Dempsey, B. Condon, and D. M. Hadley, 'Investigation of the factors responsible for burns during MRI', Journal of Magnetic Resonance Imaging, vol. 13, no. 4, pp. 627–631, Apr. 2001.

[12] V. Detti, D. Grenier, E. Perrin, and O. Beuf, 'Assessment of radiofrequency self-heating around a metallic wire with MR T1-based thermometry', Magnetic Resonance in Medicine, vol. 66, no. 2, pp. 448–455, Aug. 2011.

[13] M. K. Konings, L. W. Bartels, H. F. M. Smits, and C. J. G. Bakker, 'Heating Around Intravascular Guidewires by Resonating RF Waves', Journal of Magnetic Resonance Imaging, vol. 12, no. 1, pp. 79–85, Jul. 2000.

[14] M. E. Ladd and H. H. Quick, 'Reduction of resonant RF heating in intravascular catheters using coaxial chokes', Magnetic Resonance in Medicine, pp. 79-85, 2000.

[15] I. Saniour et al., 'Active optical-based detuning circuit for receiver endoluminal coil', Biomedical Physics & Engineering Express, vol. 3, no. 2, p. 025002, Feb. 2017.

[16] A. J. Martin, D. B. Plewes, and R. M. Henkelman, 'MR imaging of blood vessels with an intravascular coil', Journal of Magnetic Resonance Imaging, vol. 2, no. 4, pp. 421–429, Jul. 1992.

[17] E. Atalar et al., 'High resolution intravascular MRI and MRS by using a catheter receiver coil', Magnetic Resonance in Medicine, vol. 36, no. 4, pp. 596–605, Oct. 1996.

[18] E. Atalar, 'Catheter Coils', in Encyclopedia of Magnetic Resonance, R. K. Harris, Ed. Chichester, UK: John Wiley & Sons, Ltd, Dec. 2011.

[19] J. L. Cavalcante and E. Larose, 'Intravascular MRI for Plaque Characterization: Are We Close to Reality?', Current Cardiology Reports, vol. 18, no. 9, p. 89, Sep. 2016.

[20] M. D. Schnall, R. E. Lenkinski, D. Hill, H. Y. Kressel, and H. M. Pollack, 'Intracavity Probe and Interface Device for MRI Imaging and Spectroscopy', U.S. Patent No. 5,476,095, Dec. 1995.

[21] K. Kandarpa, P. Jakab, S. Patz, F. J. Schoen, and F. A. Jolesz, 'Prototype Miniature Endoluminal MR Imaging Catheter', Journal of Vascular and Interventional Radiology, vol. 4, no. 3, pp. 419–427, May 1993.

[22] G. C. Hurst, J. Hua, J. L. Duerk, and A. M. Cohen, 'Intravascular (catheter) NMR receiver probe: Preliminary design analysis and application to canine iliofemoral imaging: CATHETER PROBE', Magnetic Resonance in Medicine, vol. 24, no. 2, pp. 343–357, Apr. 1992.

[23] A. J. Martin and R. M. Henkelman, ‘Intravascular MR imaging in a porcine animal model’, Magnetic Resonance in Medicine, vol. 32, no. 2, pp. 224–229, Aug. 1994.

[24] O. Ocali and E. Atalar, ‘Intravascular magnetic resonance imaging using a loopless catheter antenna’, Magnetic Resonance in Medicine, vol. 37, no. 1, pp. 112–118, Jan. 1997.

[25] X. Yang, B. D. Bolster, D. L. Kraitchman, and E. Atalar, ‘Intravascular MR-monitored Balloon Angioplasty: An In Vivo Feasibility Study’, Journal of Vascular and Interventional Radiology, vol. 9, no. 6, pp. 953–959, Nov. 1998.

[26] G. G. Zimmerman, P. Erhart, J. Schneider, G. K. von Schulthess, M. Schmidt, and J. F. Debatin, ‘Intravascular MR Imaging of Atherosclerotic Plaque: Ex Vivo Analysis of Human Femoral Arteries with Histologic Correlation’, Radiology, pp. 769–774, Sep. 1997.

[27] H. H. Quick et al., ‘Single-loop coil concepts for intravascular magnetic resonance imaging’, Magnetic Resonance in Medicine, vol. 41, no. 4, pp. 751–758, Apr. 1999.

[28] B. Gruber, M. Froeling, T. Leiner, and D. W. J. Klomp, ‘RF coils: A practical guide for nonphysicists: RF Coils’, Journal of Magnetic Resonance Imaging, vol. 48, no. 3, pp. 590–604, Sep. 2018.

[29] C. E. Hayes and L. Axel, ‘Noise performance of surface coils for magnetic resonance imaging at 1.5 T: Surface-coil noise for MRI at 1.5 T’, Med. Phys., vol. 12, no. 5, pp. 604–607, Sep. 1985.

[30] R. Kriegl, ‘A flexible coil array for high resolution magnetic resonance imaging at 7 Tesla’, Thesis, Dec. 2014.

[31] D. I. Hoult and R. E. Richards, ‘The Signal-to-Noise Ratio of the Nuclear Magnetic Resonance Experiment’, Journal of Magnetic Resonance, pp. 71–85, Oct. 1976.

[32] J. Mispelter, M. Lupu, and A. Briguet, ‘NMR Probeheads For Biophysical And Biomedical Experiments Theoretical Principles And Practical Guidelines’. Imperial College Press, 2015.

[33] S. H. Nezhadian, ‘A flexible transceiver array employing transmission line resonators for cardiac MRI at 7 T’, Thesis, Chapter2, Dec. 2017.

[34] I. Saniour, ‘Exploitation des effets électro-optiques pour la sécurité en IRM: applications des liaisons optiques pour des capteurs RF endoluminaux et des sondes de mesure du TAS’, Thesis, Chapter1, Dec. 2018.

[35] W. A. Edelstein, C. J. Hardy, and O. M. Mueller, ‘Electronic decoupling of surface-coil receivers for NMR imaging and spectroscopy’, Journal of Magnetic Resonance, vol. 67, no. 1, pp. 156–161, Mar. 1986

[36] B. Keil and L. L. Wald, ‘Massively parallel MRI detector arrays’, Journal of Magnetic Resonance, vol. 229, pp. 75–89, Apr. 2013.

[37] M. Burl and M. X. Zou, ‘Transmit mode coil detuning for MRI systems’, U.S. Patent No 6,850,067, Feb. 2005.

[38] W. R. Nitz, A. Oppelt, W. Renz, C. Manke, M. Lenhart, and J. Link, ‘On the heating of linear conductive structures as guide wires and catheters in interventional MRI’, J Magn Reson Imaging, vol. 13, no. 1, pp. 105–114, Jan. 2001.

[39] D. M. Peterson, B. L. Beck, G. R. Duensing, and J. R. Fitzsimmons, ‘Common mode signal rejection methods for MRI: Reduction of cable shield currents for high static magnetic field systems’, Concepts in Magnetic Resonance, vol. 19B, no. 1, pp. 1–8, Oct. 2003.

[40] N. A. Volland, E. G. Kholmovski, D. L. Parker, and J. R. Hadley, ‘Initial feasibility testing of limited field of view magnetic resonance thermometry using a local cardiac radiofrequency coil: Limited FOV MR Thermometry with Local Coil’, Magnetic Resonance in Medicine, vol. 70, no. 4, pp. 994–1004, Oct. 2013.

[41] F. Vaillant et al., ‘Magnetic resonance-compatible model of isolated working heart from large animal for multimodal assessment of cardiac function, electrophysiology, and metabolism’, American Journal of Physiology-Heart and Circulatory Physiology, vol. 310, no. 10, pp. H1371–H1380, May 2016.

[42] D. Abi-Abdallah, E. Chauvet, L. Bouchet-Fakri, A. Bataillard, A. Briguet, and O. Fokapu, ‘Reference signal extraction from corrupted ECG using wavelet decomposition for MRI sequence triggering: application to small animals’, BioMed Eng OnLine, vol. 5, no. 1, p. 11, 2006.

[43] J. R. Burt, S. L. Zimmerman, I. R. Kamel, M. Halushka, and D. A. Bluemke, ‘Myocardial T1 Mapping: Techniques and Potential Applications’, Radiographics, vol. 34, no. 2, p. 20, Apr. 2014.

[44] X. Zhang, E. T. Petersen, E. Ghariq, W. M. Teeuwisse, and J. Hendrikse, ‘In vivo blood T1 measurements at 1.5 T, 3 T, and 7 T’, Magnetic Resonance in Medicine, pp. 1082–1086, Oct. 2013.

[45] S. Toupin et al., ‘Feasibility of real-time MR thermal dose mapping for predicting radiofrequency ablation outcome in the myocardium in vivo’, Journal of Cardiovascular Magnetic Resonance, vol. 19, no. 1, Dec. 2017.

[46] V. Ozenne et al., ‘Improved cardiac magnetic resonance thermometry and dosimetry for monitoring lesion formation during catheter ablation’, Magnetic Resonance in Medicine, vol. 77, no. 2, pp. 673–683, Feb. 2017.

[47] T. E. Conturo and G. D. Smith, ‘Signal-to-noise in phase angle reconstruction: Dynamic range extension using phase reference offsets’, Magnetic Resonance in Medicine, vol. 15, no. 3, pp. 420–437, Sep. 1990.

[48] C. J. Yeung, R. C. Susil, and E. Atalar, ‘RF safety of wires in interventional MRI: Using a safety index’, Magnetic Resonance in Medicine, vol. 47, no. 1, pp. 187–193, Jan. 2002..

[49] A. J. Martin, R. F. McLoughlin, K. C. Chu, E. A. Barberi, and B. K. Rutt, ‘An expandable intravenous RF coil for arterial wall imaging’, Journal of Magnetic Resonance Imaging, vol. 8, no. 1, pp. 226–234, Jan. 1998.

[50] A.-K. Homagk et al., ‘An expandable catheter loop coil for intravascular MRI in larger blood vessels’, Magnetic Resonance in Medicine, vol. 63, no. 2, pp. 517–523, Feb. 2010.

[51] N. Yak, K. J. T. Anderson, and G. A. Wright, ‘Tuning and amplification strategies for intravascular imaging coils: Matching Circuits and LNAs in Intravascular MRI Coils’, Magnetic Resonance in Medicine, vol. 68, no. 5, pp. 1675–1680, Nov. 2012.

[52] D. Qian, A.-M. M. El-Sharkawy, E. Atalar, and P. A. Bottomley, ‘Interventional MRI: Tapering improves the distal sensitivity of the loopless antenna’, Magnetic Resonance in Medicine, vol. 63, no. 3, pp. 797–802, Mar. 2010.

[53] L. Nohava et al., ‘Flexible multi-turn multi-gap coaxial RF coils (MTMG-CCs): design concept and bench validation’, Proceedings of the 27th ISMRM Annual Meeting, Montreal, Canada 2019.

[54] B. Zhang, D. K. Sodickson, and M. A. Cloos, ‘A high-impedance detector-array glove for magnetic resonance imaging of the hand’, Nat Biomed Eng, vol. 2, no. 8, pp. 570–577, Aug. 2018.

[55] R. A. Horch and J. C. Gore, ‘3D-printed RF coils for solution-state NMR: Towards low-cost, high-throughput arrays’, Proceedings of the 23th ISMRM Annual Meeting, Toronto, Canada 2015.

[56] R. Ayde, ‘Potentialities of an Electro-Optic Crystal Fed by Nuclear Magnetic Resonant Coil for Remote and Low-Invasive Magnetic Field Characterization’, IEEE Sens. J, pp. 12-74–1280, Apr. 2013.

[57] R. Ayde et al., ‘Unbiased Electro-Optic Waveguide as a Sensitive Nuclear Magnetic Resonance Sensor’, IEEE Photon. Technol. Lett., vol. 26, no. 12, pp. 1266–1269, Jun. 2014.

[58] S. Weiss, P. Vernickel, T. Schaeffter, V. Schulz, and B. Gleich, ‘Transmission line for improved RF safety of interventional devices’, Magnetic Resonance in Medicine, pp. 182–189, Jul. 2005.

[59] C. M. Hillenbrand et al., ‘Active device tracking and high-resolution intravascular MRI using a novel catheter-based, opposed-solenoid phased array coil’, Magnetic Resonance in Medicine, vol. 51, no. 4, pp. 668–675, Apr. 2004.

[60] K. N. Kurpad and O. Unal, ‘Multimode intravascular RF coil for MRI-guided interventions’, J. Magnetic Resonance Imaging, vol. 33, no. 4, pp. 995–1002, Apr. 2011..

[61] E. J. Schmidt, ‘Self-Expanding Multi-Channel RF Receiver Coil for High Resolution Intra-Cardiac MRI and Method of Use’, Patent US9232920, Jan. 2016.

Chapter 3

Motion Compensation

High-resolution imaging of atria incurs several difficulties due to the submillimeter spatial resolution that is required and the rapid and complex motion of the myocardium, which is a combination of cardiac contraction and respiration. If not compensated for, this results in significant blurring and ghosting in the reconstructed image. In this chapter, we therefore focus on strategies to compensate for 3D respiratory and cardiac motion. We remind the reader that the final objective of the research plan will be to provide 3D high-resolution (objective 200 µm isotropic) images of the atria. In this context, the requirements for motion description and subsequent compensation on reconstructed images must be in the same order of magnitude as the targeted spatial resolution. Moreover, the instantaneous position determination should be in 3D and describe local displacement at the vicinity of the targeted anatomical region.

3.1. Literature

In the following paragraph, we briefly review the methods already developed to account for respiratory and cardiac motion:

- **Use of external physiological sensors**

  A simple solution, which remains the mainstay in current clinical cardiac MRI, is the use of external physiological sensors to synchronize k-space data collection in the same physiological state. In this approach, MR-compatible ECG electrodes positioned on the thorax and respiratory bellows [1] provide instantaneous surrogates of the organs positions and can be used to trigger/gate the sequence in prospective or retrospective approaches [Lenz et al. 1989]. They are compatible with any acquisition sequence, provide a continuous recording and do not interfere with image contrasts, which in turn make them ease-of use. However, they do not provide actual measurements of organ displacements and ECG readings are often

distorted by magneto-hydrodynamic effect and by high switching of the gradients, yielding to potential erroneous triggering. This is problematic for triggering on the atria, particularly in the context of arrhythmia where a proper cardiac gating is difficult to obtain or even impossible.

- **Use of Navigators (NAVs)**

  Navigator [2] positioned on the diaphragm can measure a 1D profile at the liver-lung interface to trigger the acquisition or to track the slice continuously. A scaling factor (usually 0.57 - 0.6)[3] is then applied to compensate the change in position of the slice located on the heart. It has to be considered, however, that the relationship between diaphragmatic and heart displacement is not constant over the complete organ [4]. Moreover, this factor can be patient dependent and vary during the acquisition. In addition, such 1D NAV only monitors superior inferior (SI) translational motion although respiratory-induced motion may extend in three dimensions. More advanced method, based on 2D “navigator images” (iNAVs) has also been exploited [5]. The method proposes to create a 2D low-spatial resolution prescans for parameter estimation of an affine motion model and apply correction during the reconstruction process. While the advantage is that non-rigid motion is taken into account, this approach remains sophisticated and may not be adapted for very localized motion estimation (of the order of 300 µm).

- **Self-gating (SG) techniques**

  Such techniques directly extract motion information from the k-space data themselves and offer the advantage to operate with 100% scan efficiency and improved ease of use. Existing SG strategies can be roughly divided into two categories:

  In the first category, images at different respiratory phases are combined using an image registration algorithm. For that purpose, a readout oriented along the superior-inferior (SI) direction is placed before each acquisition of interleaves for respiratory self-navigation while the cardiac motion signal is extracted retrospectively from the recorded ECG time stamps that are synchronized with data acquisitions [6], [7]. In another approach, a Butterfly navigator is used to provide

motion estimates, which further enable estimation of data weighting factors from the distance to a reference respiratory phase. This information is then used in a weighted iterative reconstruction to suppress image artifacts from motion through soft-gating [8]–[10]. Such technique has been extensively tested in volunteers and patients. However, they still suffer from limitations related to the motion model employed for correction (e.g. translation, affine, or non-rigid).

Instead of either discarding or co-registering data with assumptions about motion models as in the first strategy (registration-based correction method), a recent approach, called extra-dimensional golden-angle radial sparse parallel MRI (XD-GRASP) has been introduced. The method proposes to sort the acquired data into multiple undersampled motion states and then reconstructs them as multidimensional image series by exploiting Compressed Sensing (CS) [11], [12]. The five dimensions in this framework therefore include the three spatial dimensions plus two distinct temporal dimensions corresponding to cardiac and respiratory phases. However, these concepts still mandate an ECG recorded by the scanner, which is difficult for the atrium. Alternative cardiac synchronization methods have thus been implemented to provide motion-compensated cardiac images without the need of an ECG [13], [14]. However, in the context of imaging with a small coil, the intercepted volume inherent to coil sensitivity is not expected to vary significantly with physiology.

- **Use of micro coils**

Several papers reported the use of micro-coils to measure the 3D positions of a catheter. Dumoulin et al [15] first introduced the concept of active tracking. A single or a set of micro receive coils is mounted to the tip of an interventional device. As the resonance frequency within a given volume changes monotonically with position when adding a linear gradient field to the main magnetic field, the frequency of the detected signal provides a direct measure of the micro coils positions. Some papers proposed a dual-purpose catheter device that could be used for both tracking and imaging application. Hillenbrand et al. [16]performed device tracking (15 ms / tracking) and automated slice positioning for high resolution (240 µm) imaging of the abdominal artery with an opposed-solenoid phased array catheter coil. They reported a tracking accuracy of 2 mm. Homagk et al. [17] proposed a catheter

system that consists in an expandable coil for abdominal aorta imaging. Using the position information, they retrospectively compensated the motion. Other groups proposed to integrate a tetrahedron tracking coil array into an imaging coil for motion detection and real-time prospective motion correction in real-time. Tracking accuracy was found to be less than one millimeter [18], [19].

In the present work, we have chosen to exploit micro-coils for motion compensation as they provide an absolute, local and 3D position measurements. A dedicated sequence was implemented that integrates a tracking module into a gradient echo imaging sequence. Golden-Angle (GA) radial sampling scheme presents an intrinsic robustness to motion and offers the potential benefit of retrospective self-gating. These reasons motivated our choice for this sampling scheme. Combining tracking and radial acquisition, we also developed an image reconstruction framework that continuously acquire k-space data and sort it into multiple sets of undersampled data with distinct motion states. With the goal of combining the motion robustness and the acceleration capabilities, in an attempt to accelerate the

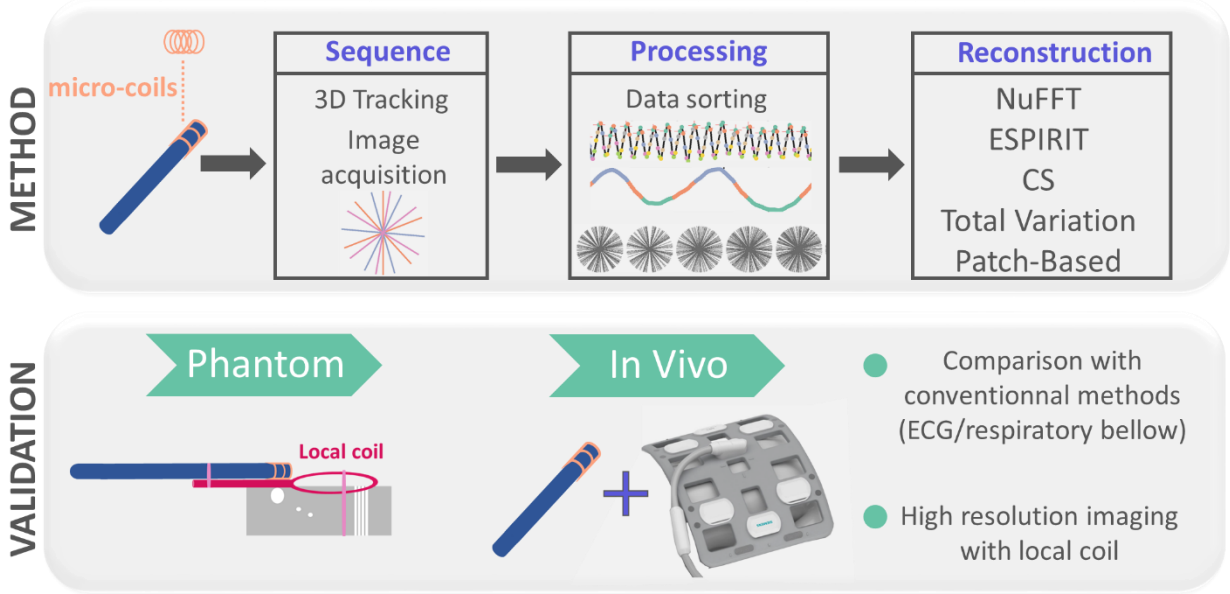

Figure 3-1: Schematic of the architecture of the Chapter. A catheter integrating micro-coils was used for tracking the motion. Using the micro-coils position information, an algorithm that sorts the data into multiple sets of undersampled data was implemented and reconstruction methods were exploited to recover images from the sorted k-space data. Method was first tested *ex vivo* on phantom with the developed local coil introduced in Chapter 2 as a receiver-only. Second step was to investigate potentials of the method *in vivo*, using the external coil arrays as receivers. Preliminary *in vivo* study was finally conducted wherein the local coil was directly positioned against the ventricle wall for high-resolution, motion compensated imaging of the ventricle.

acquisition time while maintaining a targeted image quality, we also exploited existing iterative optimization techniques to reconstruct the motion-sorted, undersampled datasets by exploiting sparsity along the corresponding motion-state dimensions. The chapter can therefore be schematically summarized in Figure 3-1.

3.2. Instrumentation and software implementation

3.2.1. Catheter design

A 9 F MR-compatible catheter (Imricor Medical Systems, Burnsville, Minnesota, USA) equipped with 2 micro-receive coils (one proximal C_p, one distal C_d as indicated in Figure

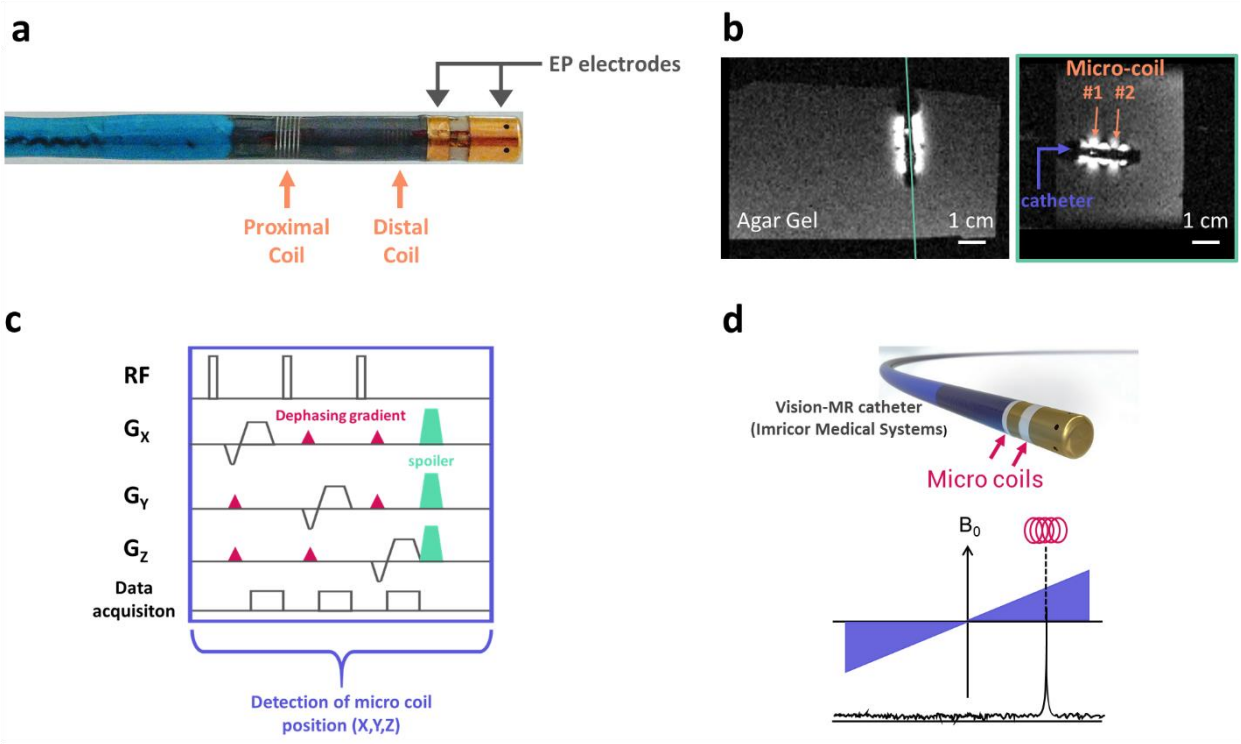

Figure 3-2: Active catheter tracking and tracking module. a) A catheter embodied with two micro-coil receivers, one proximal, one distal (orange arrows) and two EP electrodes (gray arrows) including an ablation tip. b) The associated magnitude image of the catheter evidences the two micro-coils that appear hyperintense whereas the catheter body remains hypointense. c) a tracking module was implemented that consists in three non-selective RF pulses followed by a gradient-recalled echo. Spoiler gradients are added at the end of the tracking module to avoid cross-talk between consecutive tracking modules. d) The signal received by the micro-coil exhibits a sharp peak in the frequency spectrum that is proportional to the spatial location of the micro-coil along the applied gradient direction.

3-2a, Left) and 2 electrophysiology (EP) electrodes (3.7-mm tip electrode and 3.5-mm inter-electrode spacing) was used both for the active device visualization and the micro coils signal recording for retrospective motion correction. Imaging with the two micro-receive coils was performed in gel using a 3D GRE sequence with 0.6 mm^3 voxel size. The associated magnitude images given in Figure 3-2b right illustrate the utility of the two active markers, which appear hyperintense whereas the catheter body stays hypointense. The micro-receive coils consist in two small solenoids which provide a limited receive sensitivity profile and allow thus to detect MR signals from the spins in the immediate vicinity of the micro coil. Therefore, they act as a nearly point-source signal (received from surrounding tissue) allowing a precise determination of the position of the devices (Figure 3-2d) [20].

3.2.2. Tracking Module implementation

For real-time device localization of the catheter and recording of the micro-coils signal, a 3D device tracking was implemented with custom-written ICE/IDEA tracking software (Siemens, Erlangen, Germany). The tracking module consists of a single pulse-echo sequence [15], [17]. This sequence features a non-selective RF pulses applied with the body coil to excite all spins within the FOV followed by a gradient-recalled echo with readout gradient along one axis. [15], [16], [18]. Additional dephasing gradients were added along the two other orthogonal directions to suppress the MR-signal. Spoiler gradients were added at the end of the tracking module to avoid cross-talk between consecutive tracking modules along different axes. Strength of these spoilers could be tuned within the user interface to adjust background suppression. This process is repeated for the three axes (X, Y and Z). No coil other than the two-channel catheter coils is used for the signal reception during this module. Typical acquisition parameters of the tracking module are: FOV = 450 mm, matrix = 512 data points, TE = 2.8 ms, TR = 4.8 ms, FA = 3°, bandwidth = 152 Hz/px, background suppression = 6 $mT.m^{-1}$. Total 3D tracking module duration with this set of parameters is 24.47 ms. The small flip angle was applied to minimize changes in spin magnetization for imaging (see 3.4.2). The sequence diagram of the implemented tracking module is given in Figure 3-2c.

3.3. Tracking measurements: Micro coils signals and determination of the catheter position

The signal recorded by the micro-coils is a complex signal acquired in the spatial frequency domain. For each of the three orthogonal axes (in the physical x-,y- and z-directions of the magnet coordinate system), the magnitude and the phase of the signal are derived from the tracking module frequency measurement. Two approaches can be used to compute the position of the catheter. One is based on the Fourier transform of the signal and works in the image space while the other directly works in the k-space and exploits the phase component of the acquired signal. In the following, we describe the two methods.

3.3.1. Position derived by Fourier Transforming the signal

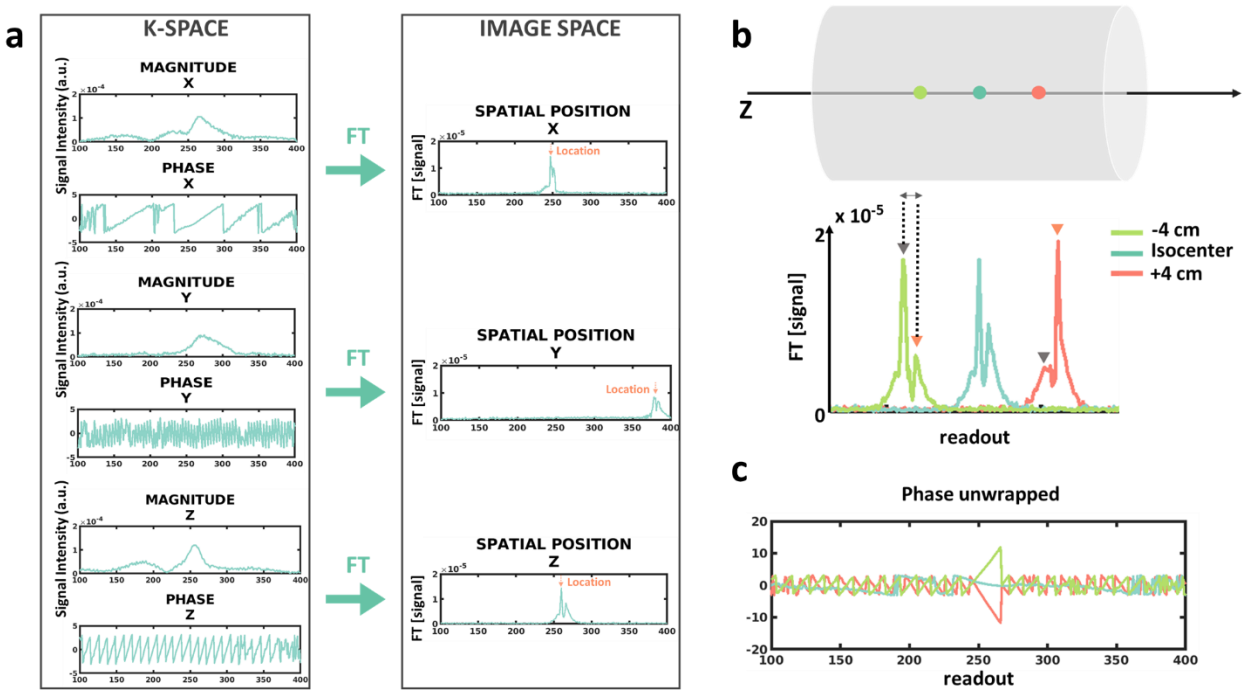

Figure 3-3: Position derived by Fourier Transforming. a) For each direction, the associated magnitude and phase of the tracking signal is retrieved and corresponding spatial position is obtained after Fourier transforming the k-space data. b) Three different spatial positions along Z-axis generate three different spatial profiles. c) Difference in spatial location translates into a phase shift in k-space domain, yielding to a change in phase's slope.

Position of each micro-coil can be retrieved in the image domain after Fourier transformation of the k-space. This requires identification of the peak signal within each projection (x,y and z) (Figure 3-3a) [15], [16], [21] Figure 3-3b shows an example of a

catheter inserted into an agar gel, for 3 different positions (-4 cm, isocenter, + 4cm) in the z direction, together with the resulting spatial profiles.

3.3.2. Position derived by analysis of the phase's slope

Due to the shift property of the Fourier Transform, any motion in the image space translates into a phase ramp in the k-space. Therefore, each position can be retrieved by analyzing the phase of the k-space. Let's g(x) and G(k) the Fourier Transform pair with:

$$\mathrm{G(k)} = \mathrm{FT[g(x)]} = \int_{-\infty}^{+\infty} \mathrm{g(x)e^{-2\pi ikx}dx} \tag{3-1}$$

then a shift in the spatial domain results in:

$$\mathrm{g(x - x_0)} \leftrightarrow \mathrm{G(k)e^{-2\pi ikx_0}} \tag{3-2}$$

Thus, the phase slope of the signal acquired in the k-space is proportional to the position of the sensor. Figure 3-3c shows the phase profiles for the three positions mentioned above, showing the three different slopes. In our implementation, the phase of the central 21 points of the k-space was selected and unwrapped prior to linear fitting to derive the slope s. The position P was retrieved using the following equation:

$$P = s.\frac{FOV}{2\pi} \tag{3-3}$$

The process was repeated for each direction and coil elements as illustrated in Figure 3-4.

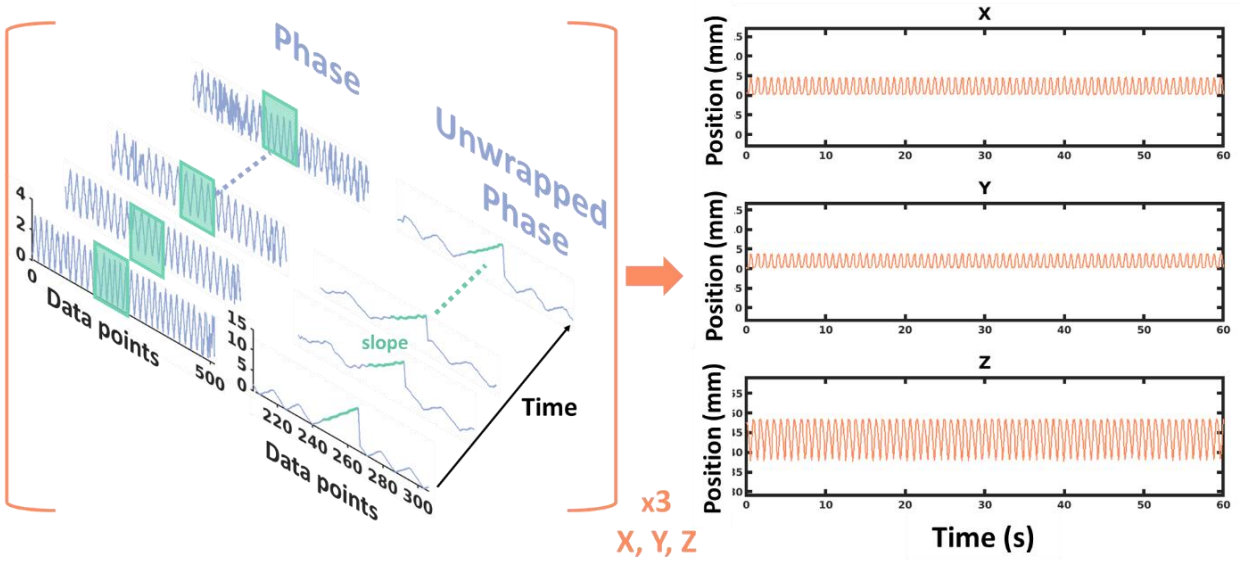

Figure 3-4: Position information from phase's slope. The phase of the central 21 points of the k-space is selected (blue frame) and unwrapped prior to linear fitting to derive the slope s. The process is repeated 3 times, for each direction (X,Y and Z). Finally, the slope over the time is plotted, which gives position information over the time.

This method was preferred since analysis of peak position appeared more difficult due to variation in the profiles according to catheter position, as illustrated in Figure 3-3c. Indeed, as explained in Qin et al. [18], the signal detected by the solenoid micro coil is highly dependent on the orientation of the coil with respect to the readout gradients. A single peak is observed if the gradient is applied perpendicular to the tracking coil while two peaks are observed if the readout gradient is applied along the length of the along the length of the tracking coil, with each local maximum corresponding to an end of the coil (Figure 3-5). Moreover, fitting the phase of the central portion of the k-space with a linear function required no sophisticated implementation.

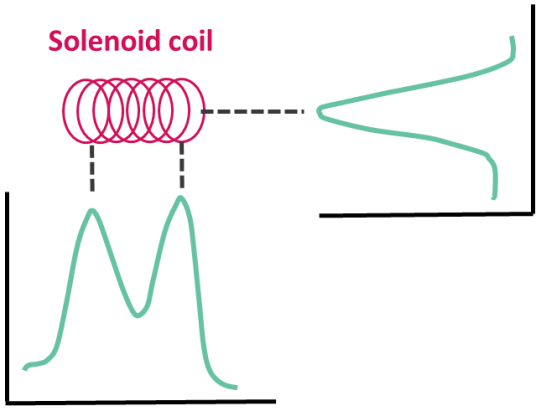

Figure 3-5: Sensitivity profiles of a solenoid coil in two orthogonal directions. Modified from Qin et al., *Magn Reson Med*, 2013

3.3.3. Comparison of the two methods

The two aforementioned methods were compared ex vivo in a moving phantom (translational along Z axis and rotational around Z axis) and in vivo in a sheep's heart. In phantom, tracking coils embodied on the catheter were inserted into a flask of water and tightly attached to a piston rod system. The piston was controlled by a software driving two pneumatic air lines which simultaneously allowed for control of translation and torsion (Shelley Medical Imaging Technologies, Ontario). In vivo, the catheter was inserted into the left ventricle via a femoral access. Both tracking measurements were performed using the tracking sequence introduced in 3.2.2. 2000 and 4000 tracking measurements were recorded in Phantom and in vivo respectively. These tracking measurements were then processed using our method (orange) and compared to the position retrieved by Siemens method (green). Resulting positions of the catheter over time are displayed in Figure 3-6 for the two experiments. In phantom as in vivo, position measurements do not show significant differences between the two methods. However, in phantom experiment, the position retrieved by Siemens algorithm shows little perturbances with shift of the maximal motion plateau along Y. Along X direction, at the bottom motion plateau, Siemens method presents a threshold effect while our method displays fluctuations. In vivo, the position retrieved using our method was found to be less noisy along X. In both experiments, the shift between the two position curves is explained by the fact that while we compute the

position of one micro-coil (here the distal micro-coil), Siemens algorithm computes the tip's position of the catheter. The latter is located 1 cm away from the distal micro-coil.

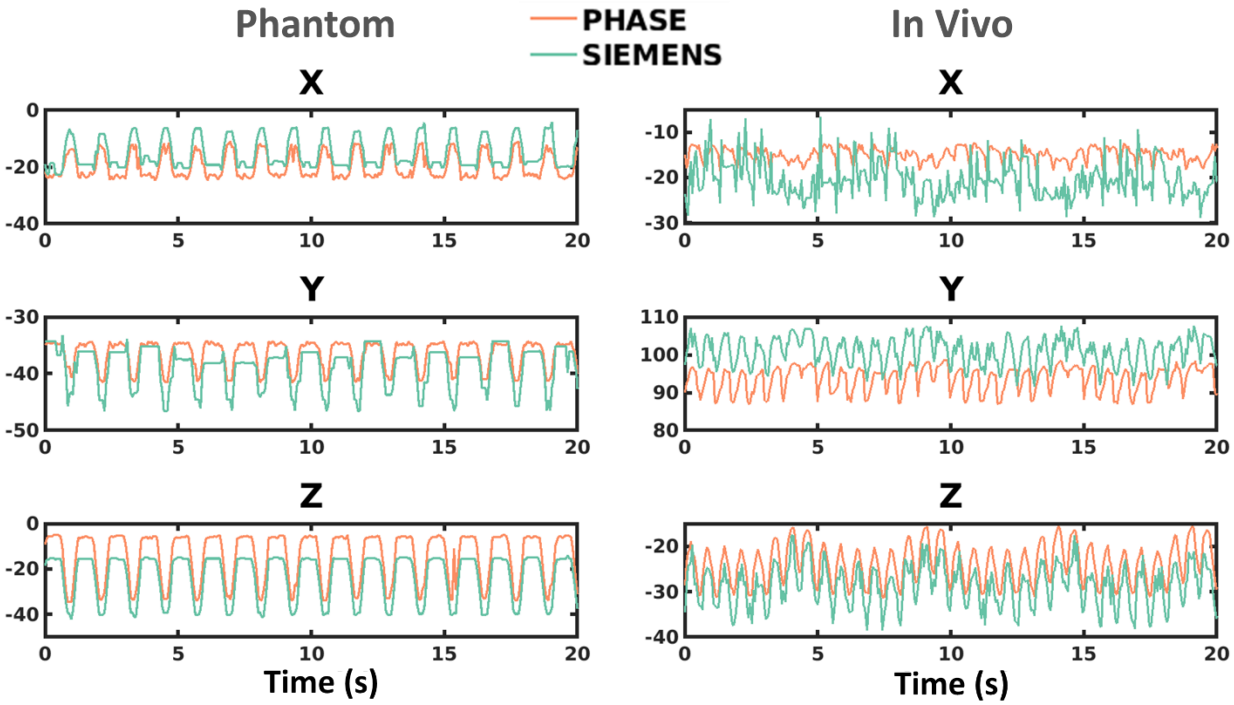

Figure 3-6: Comparison between the methods based on Fourier Transform (green curves) and the method relying on the phase's slope of the tracking signal (orange). Both methods were compared on a moving phantom (left) and in vivo on a sheep heart (right). No significant difference between the two methods is observed. In vivo, our method provides less noisy position information along X direction.

3.3.4. Precision of the position measurement retrieved by the MR tracking-coils

The positional accuracy of the tracking retrieved by the phase slope was measured for different matrix size of the tracking acquisition module. For that purpose, a catheter was inserted into a static gel and tracking signals were recorded. The tracking module was set up with the following parameters: FOV = 450 mm; FA = 3°; bandwidth = 152 Hz/px. Matrix sizes were: 100 / 128 / 256 and 512 data points. For each acquisition, the temporal standard deviation σ_T was computed over 100 tracking measurements and retrieved in Table 3-1.

Matrix size (data points)	σ_T (mm) along X direction	σ_T (mm) along Y direction	σ_T (mm) along Z direction
100	0.13	0.22	0.13
128	0.12	0.24	0.15
256	0.20	0.20	0.18
512	0.25	0.31	0.13

Table 3-1: Temporal standard deviation along X,Y and Z directions for different matrix size of the tracking acquisition

We observed a directional difference in the standard deviation. The error in Y is comparable but larger than observed along X and Z. These results evidence that no significant difference in the temporal standard deviation was observed between different matrix sizes demonstrating the independency of the positional accuracy with the matrix size. This also demonstrates the feasibility to correct motion with a submilimeter order of magnitude (~ 0.3 mm at least), which is required for high-resolution imaging.

3.3.5. Positional errors: origin and correction

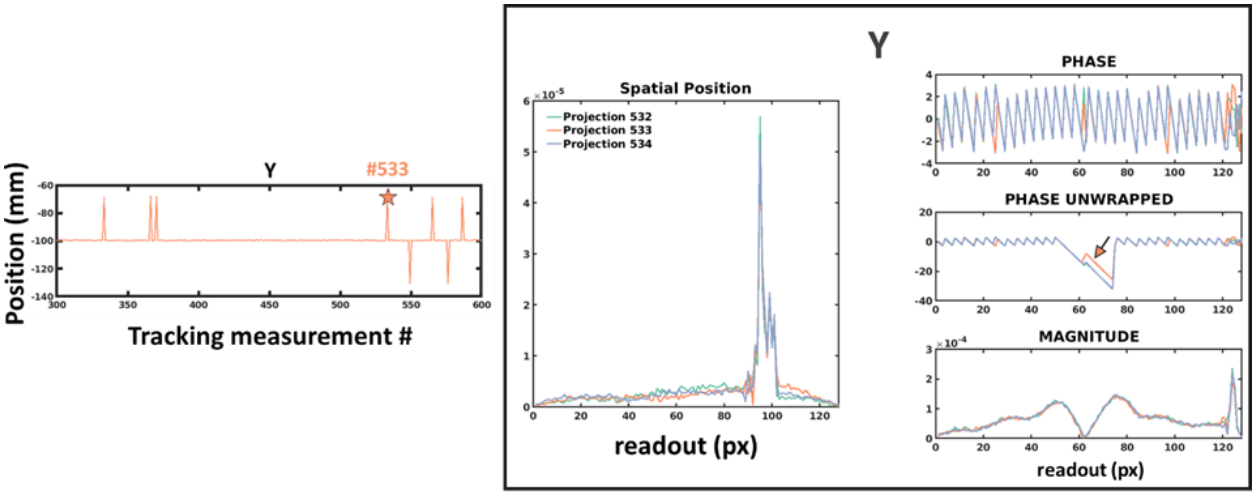

Figure 3-7: Origin of the punctual positional errors. Example is given along Y direction (**left**). Considering tracking measurement #533, we observe the phase signal is not well defined (orange star) when compared to the previous and the following measurements (#532 and #534). This results in an incorrect phase unwrapping (**Right**, orange arrow), directly affecting the slope fitting and leading to erroneous position measurement.

Even though the phase slope-based localization algorithm is able to provide consistent position measurements with an accuracy of 0.3 mm, some punctual positional errors can occur. Figure 3-7 gives an example of such a positional error occurring at the tracking measurement #553 during a static phantom experiment. When considering the phase signal of the consecutive tracking measurements #532 #533 and #534, we see that these punctual positional errors come from a poor phase definition at the tracking measurement #533. The resulting phase unwrapping is thus not correctly achieved which leads to an incorrect phase slope and therefore an erroneous position measurement.

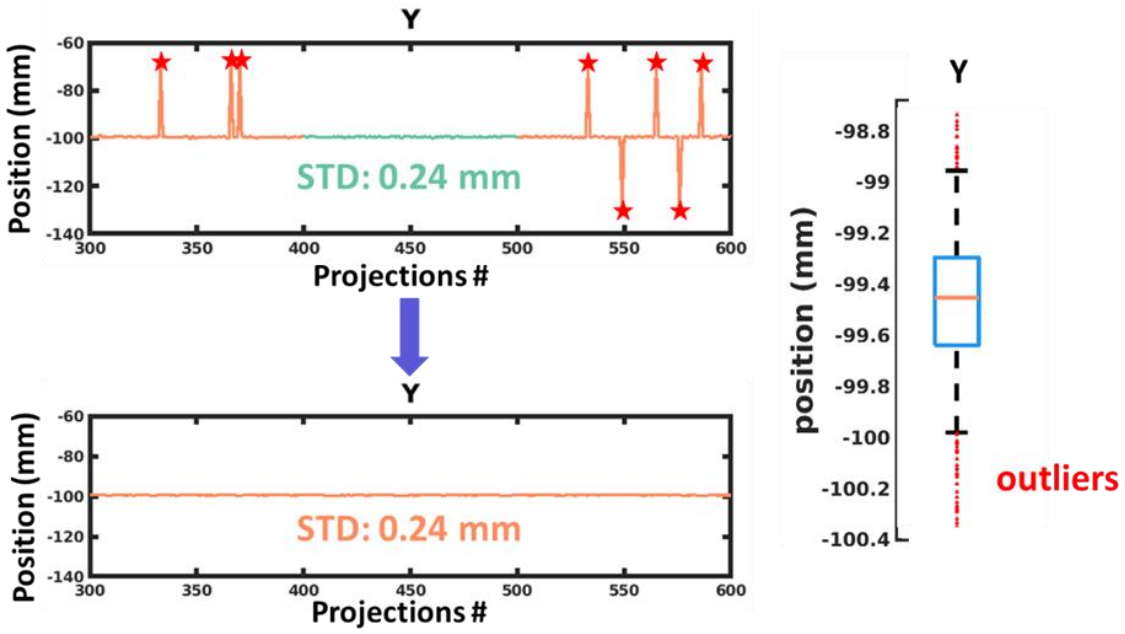

Figure 3-8: Positional errors correction of a static phantom experiment. The punctual errors indicated with red stars are removed using a statistical approach. A box and whisker plot of the original signal is derived that allows removing of the outliers (values below the 0.025 percentile and upper 0.975 percentile). Values considering as outliers are set to the previous position value. This allows to remove punctual positional errors while keeping the core signal unchanged.

In order to remove these punctual positional errors, a statistical approach based on quantiles values was used. Box and whisker plots were produced and outliers (values below the 0.025 percentile and upper 0.975 percentile) were removed. Each outlier value was set to the previous position. The method was first tested on a static phantom experiment were positional errors occurred (Figure 3-8). It allowed removing punctual

positional errors without modifying the core signal (the σ_T of the core signal remained unchanged after applying our correction). Efficiency of our correction method was also evaluated during a motion phantom experiment to evaluate its ability to preserve the main position information (Figure 3-9).

3.3.6. Evaluation of the tracking accuracy on motion phantom experiments

The tracking accuracy and precision was further evaluated on a moving phantom. Goal of this experiment was to assess the ability of our position estimation method, combined with the statistical-based correction at retrieving a known motion frequency and amplitude. We first introduce the set-up and trajectories used for the experiments conducted all along this chapter. In this experiment where only the tracking accuracy is investigated, without acquiring k-space lines to generate images.

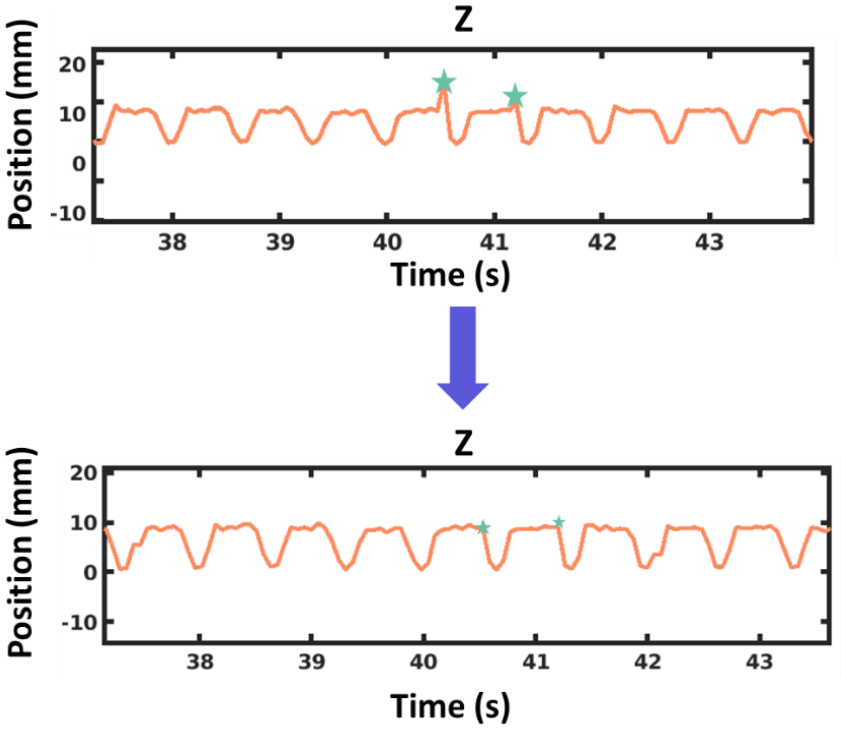

Figure 3-9: Positional errors correction of a moving phantom experiment. Example of erroneous position measurement is highlighted by the two green stars on the original signal. After applying the statistical-based correction, these two errors are removed while keeping the core signal unchanged.

3.3.6.1. Set-up

A 3D-printed calibration phantom (introduced in chapter 2), immersed in water was attached to the rod system of a pneumatic piston. The piston was tightly fixed to the MR-table with a plastic holder. The catheter, equipped with the two small micro-coils was inserted into a flask filled of water and attached to the local loop coil previously developed (chapter 2), together with the phantom as illustrated in Figure 3-10.

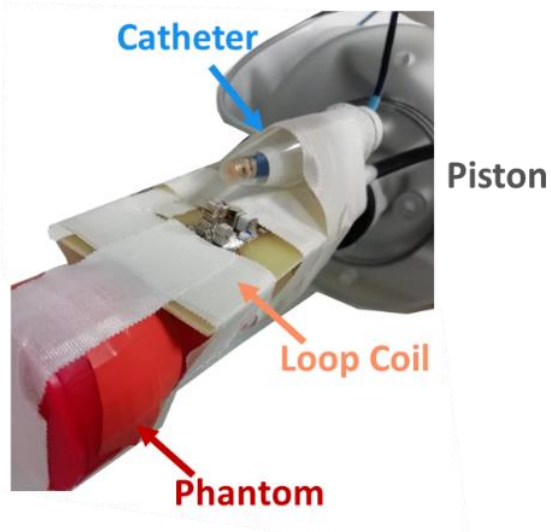

Figure 3-10: Set-up used for the phantom experiments. The catheter equipped with the two micro-coils is attached together with the phantom and the loop coil. The system {loop coil + catheter + phantom} is fixed on the piston rod system.

3.3.6.2. Motion trajectories

Two different motion patterns were used (Figure 3-11): an oscillating translational motion along Z-axis (1) and a combined translational (along Z-axis) and rotational motion (around Z-axis) to mimic the heart contraction (2). Amplitude of the motion ranged from 1 to 3 cm. The motion frequency was defined via a remote computer controlling the two airlines of the pneumatic piston. Frequency values ranged from 20 to 90 beats per minute (bpm).

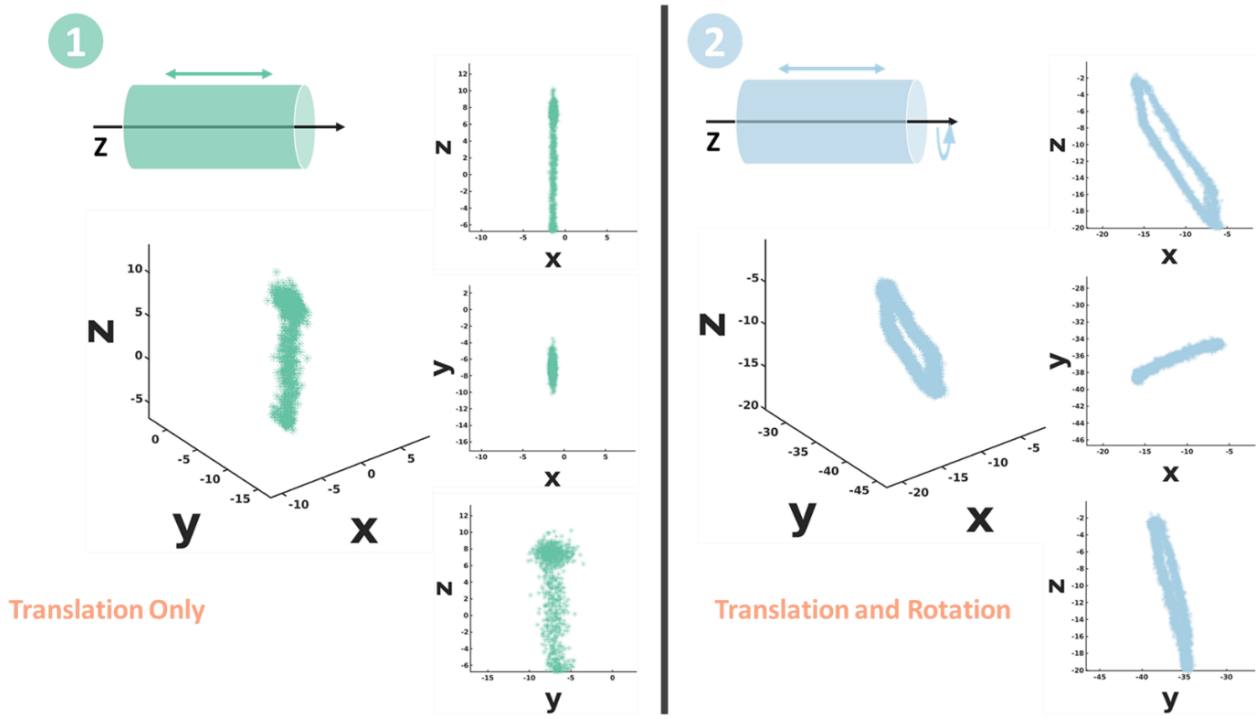

Figure 3-11: Motion trajectories generated by the piston. **1)** translational-only motion along Z-axis. **2)** Combination of a translational (along Z-axis) and a rotational (around Z-axis).

3.3.6.3. Tracking accuracy on motion phantom

A translational motion at 50 bpm and 1.5 cm in amplitude was generated. Tracking module parameters were same as in 3.2.2. 3000 tracking measurements were acquired and processed to retrieve the 3D position of the catheter using method described in 3.3.2. Photograph of the experiment is given in Figure 3-12. The resulting positions recorded by the distal micro-coil are shown for each direction (X,Y and Z). A motion of 1.5 cm in amplitude at a rate of 50 beat per minutes (bpm) was measured along the Z axis while no motion along X and Y axes was observed, which is consistent with the motion parameters induced by the piston. The small difference in amplitude over the time can be attributed to the motion induced by the piston which may differ a little between two consecutive back and forth movements. In addition, vibration of the holder may add some extra motion in the other directions. Nonetheless, this result emphasized that an accurate measurement of the motion (both in amplitude and in frequency) can be retrieved using micro-coils and our method based on the phase slope analysis.

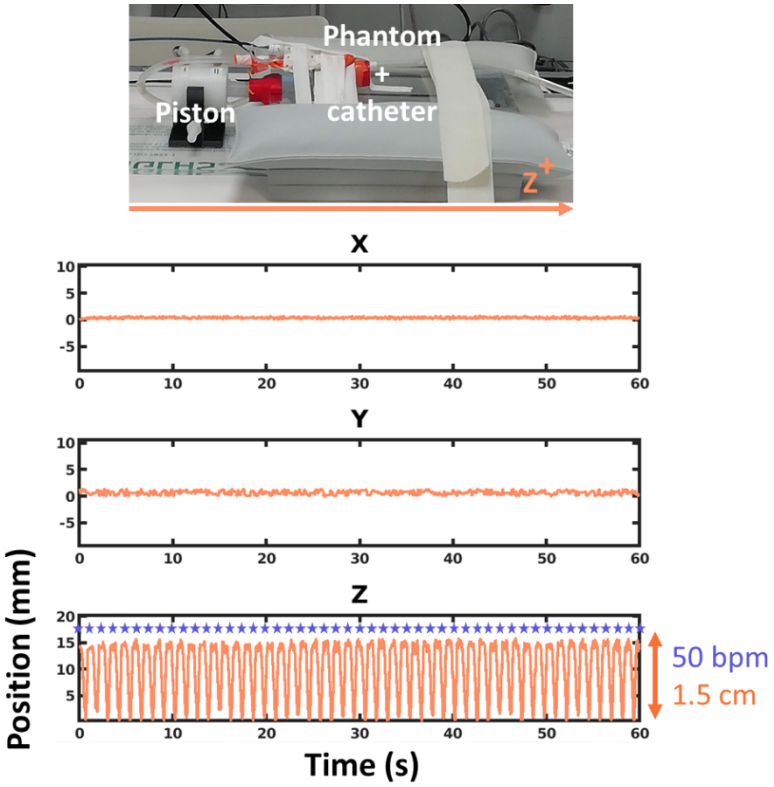

Figure 3-12: Photograph of the moving phantom experiment. **Top-** A phantom filled of water was attached to the rod system of a pneumatic piston. The catheter, equipped with two-micro-coils was inserted into the phantom. A translational motion at a rate of 50 bpm and 1.5 cm in amplitude was generated. **Bottom-** Position was retrieved with the phase's slope method and plotted for each direction. Violet stars evidences

3.4. Combining a tracking module with an imaging sequence

3.4.1. Implemented sequence

A two-dimensional (2D) gradient-recalled sequence (GRE) was modified to integrate the MR-tracking module describe above. Radial scheme (also called projection acquisition) was preferred as it offers the continual passage of the radial lines (projections) through the center of k-space and is therefore well suited for retrospective gating. In addition, the overlap of the spokes in the k-space center averages the object information in time and reduces sensitivity to motion and flow. Another advantage of this scheme is that artifact from undersampling consist of streaks instead of wraparound that results from undersampled phase encoding with rectilinear trajectory. This allows scan time reduction with artifacts that are much less objectionable for the image. The tracking module was

added before acquisition of N (adjustable parameter from the user interface) imaging segments. Radial lines were acquired using a golden-angle (GA) scheme since it allows the possibility of arbitrary data sorting with approximately uniform k-space coverage in each motion state while maintaining sufficient incoherence in the sampling patterns along the new motion-state dimension for robust iterative non-linear optimization reconstruction. In our study, 3 radial lines were acquired after every tracking module and this scheme was repeated until the total number of desired projections was reached (Figure 3-13). In the rest of this chapter, the sequence is referred as 2D-GA.

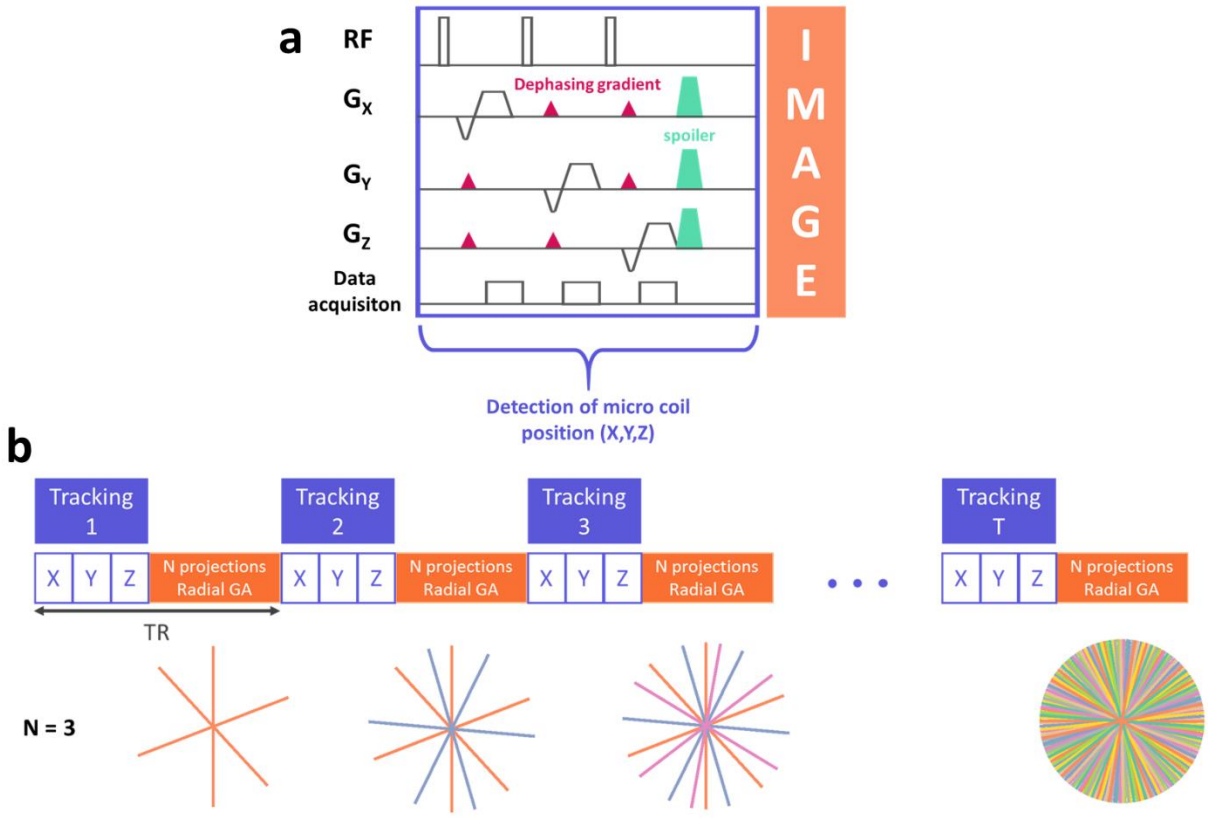

Figure 3-13: Schematic of the Pulse Sequence used and acquisition pattern. (a) Integration of a Tracking module inside an imaging sequence (GRE) for retrospective gating. Before the acquisition of N radial k-space projections, a non-selective excitation followed by the acquisition of Projection data is applied for each axis (X,Y,Z) to determine the position of the catheter.(b)One tracking module gives the positions of N projections. N is the number of segments fixed in the sequence. In our case, the number of segments was 3 which implies that every tracking index is associated with 3 index of projections acquired in the radial k-space.

3.4.2. Influence of the Tracking Module on image quality

Influence of the tracking module was first evaluated to verify if artifacts were generated on the resulting image. For that purpose, different flip angle (FA) values of the tracking module were tested and resulting images were compared. Experiment was conducted on a 3D-printed calibration phantom described in Chapter 2. Imaging sequence parameters were set as follows: FOV = 150 x 150 mm^2; Matrix size = 288 x 288 pixels; TR/TE = 60/6.4 ms; FA = 15°; bandwidth = 250 Hz/pixels; slice thickness = 3 mm; 3 segments; 2001 projections, Acquisition time = 40 s and tracking module parameters were: FOV = 450 mm, 512 data points, TR/TE = 4.8/2.8 ms and FA values were successively: 10°, 7° and 3°, background suppression was set to 1 $mT.m^{-1}$. In the last experiment, the same acquisition with same tracking parameters was performed, for all the aforementioned FA values, this time setting background suppression gradient strength to 6 $mT.m^{-1}$. An image without tracking module was acquired for comparison purpose (reference image).

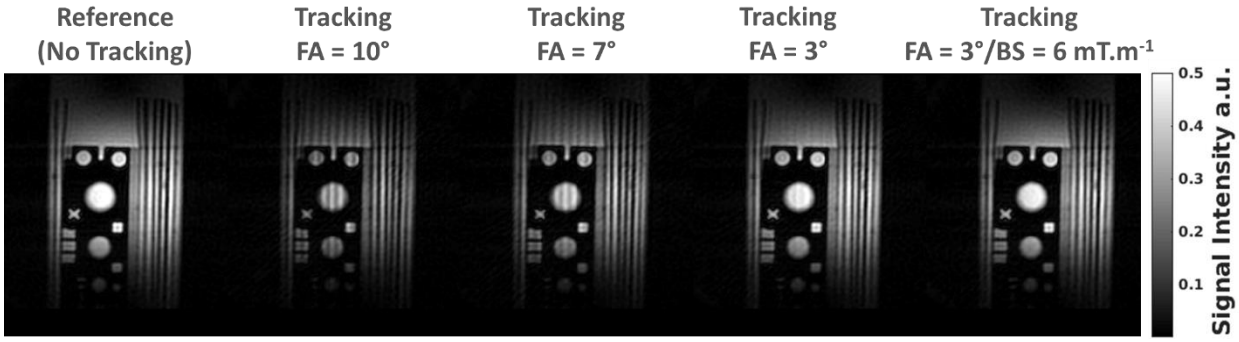

Figure 3-14: Influence of the FA value of the Tracking Module on the resulting image quality. FA superior to 3° induce stripes in the resulting image. Adding background suppression allow a higher reduction of these stripes. The combination of FA value and background suppression value yielding to the targeted image quality (reference image) was selected for the rest of the experiment.

Resulting images demonstrate apparition of stripes in the phantom image if the FA is too high (> 3°). Increasing the spoiler strength (to 6 $mT.m^{-1}$ at least) improves the resulting image, leading to a similar quality as the reference imaging (Figure 3-14). Acquisition with FA > 3° and background suppression set to 6 $mT.m^{-1}$ were performed but only demonstrated a weak reduction of stripes in the resulting images compared to the acquisition performed with a FA set to 3° (data not shown). The set of parameters (FA = 3° and 6 $mT.m^{-1}$) was therefore retained for the following experiments.

3.4.3. Influence of an inversion recovery (IR) pulse on the tracking measurement precision and on the image quality

As IR is widely used in cardiac MRI (Late gadolinium enhancement for example), influence of such a magnetization preparation pulse on the position measurement accuracy was evaluated. Goal of the following experiment was therefore to assess the feasibility of imaging with such a contrast while correcting the motion using tracking measurements with a sufficient accuracy (< 1 mm). Experiment was conducted on the same 3D printed phantom mentioned earlier. An IR pulse was set up before the tracking module with an inversion time (TI) of 800 ms. Image acquisition was performed with the following parameters: FOV = 150 x 150 mm^2; Matrix size = 288 x 288 pixels; TI/TR/TE = 800/914/6.4 ms; FA = 15°; bandwidth = 250 Hz/pixels; slice thickness = 3 mm; 3 segments; 2001 projections, Acquisition time = 40 s Tracking module was set-up as follows: FOV = 450 mm, FA = 3°, 512 data points, TR/TE = 4.8/2.8 ms; total Tracking module time = 24.47 ms, bandwidth = 152 Hz/px. The same acquisition was performed without any IR pulse for comparison purpose. Tracking signal was recorded and processed. For both acquisitions, magnitude of the tracking signal was plotted and the standard deviation of the position σ_T was computed in each direction, over 300 tracking measurements.

σ_T values of the acquisition with tracking only were 0.10 mm, 0.18 mm and 0.14 mm for X,Y and Z directions respectively.

σ_T values of the acquisition with an IR pulse were 0.18 mm, 0.62 mm and 0.31 mm for X,Y and Z directions respectively.

In both acquisitions, a maximal standard deviation was observed for Y direction. The reported σ_T values demonstrate a decrease in tracking accuracy when adding an IR pulse before the tracking measurement. This is explained by the drop in signal-to-noise ratio induced by the IR pulse as demonstrated in Figure 3-15 (top). This reduction in SNR, which is well known when using an IR pulse preparation is observed in the resulting images where images acquired with an IR pulse is noisier Figure 3-15 (bottom). Nonetheless, the tracking precision remains below 1 mm (0.6 mm at least).

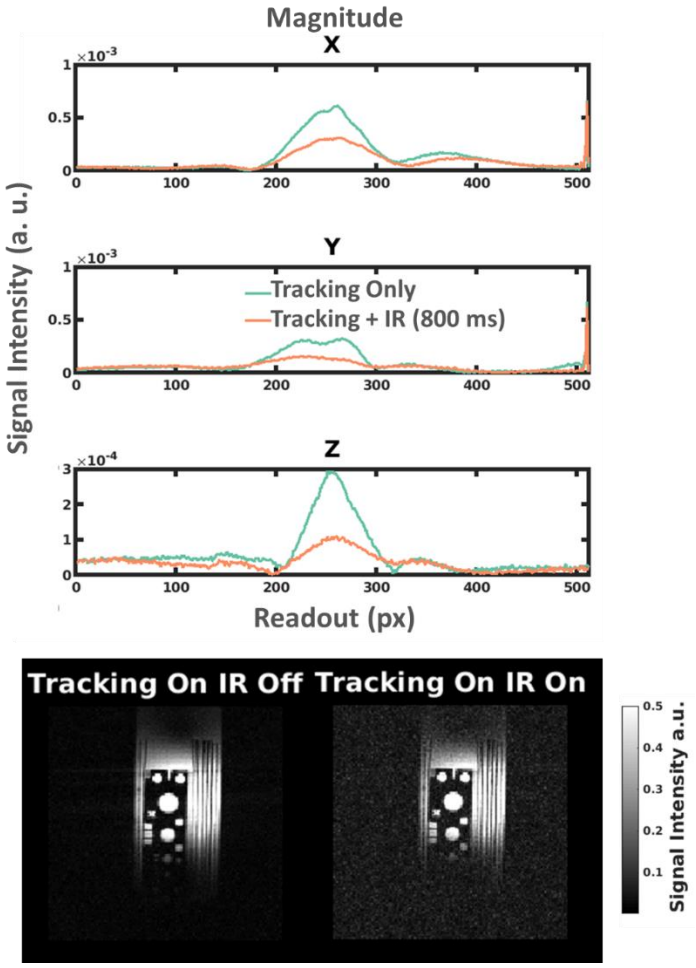

Figure 3-15: Influence of an IR preparation pulse on both tracking accuracy and image quality. An IR pulse (TI = 800 ms) was added before each tracking measurement Magnitude of the tracking signal is plotted for both acquisition and evidences a drop of signal when an IR pulse is played out. This drop of signal is observed in the resulting image, which is noisier. Nonetheless, details remain visible.

3.5. Data sorting

In our implementation, the position signal, retrieved from the micro-coils, is used to retrospectively sort the acquired data into different motion states. Extraction of these motion states can be realized by either partitioning the signal into amplitude intervals (green bars) or dividing the signal into time intervals (orange bars) as for cine imaging (Figure 3-16). The radial profiles are then assigned into different motion states, yielding a set of N different k-spaces.

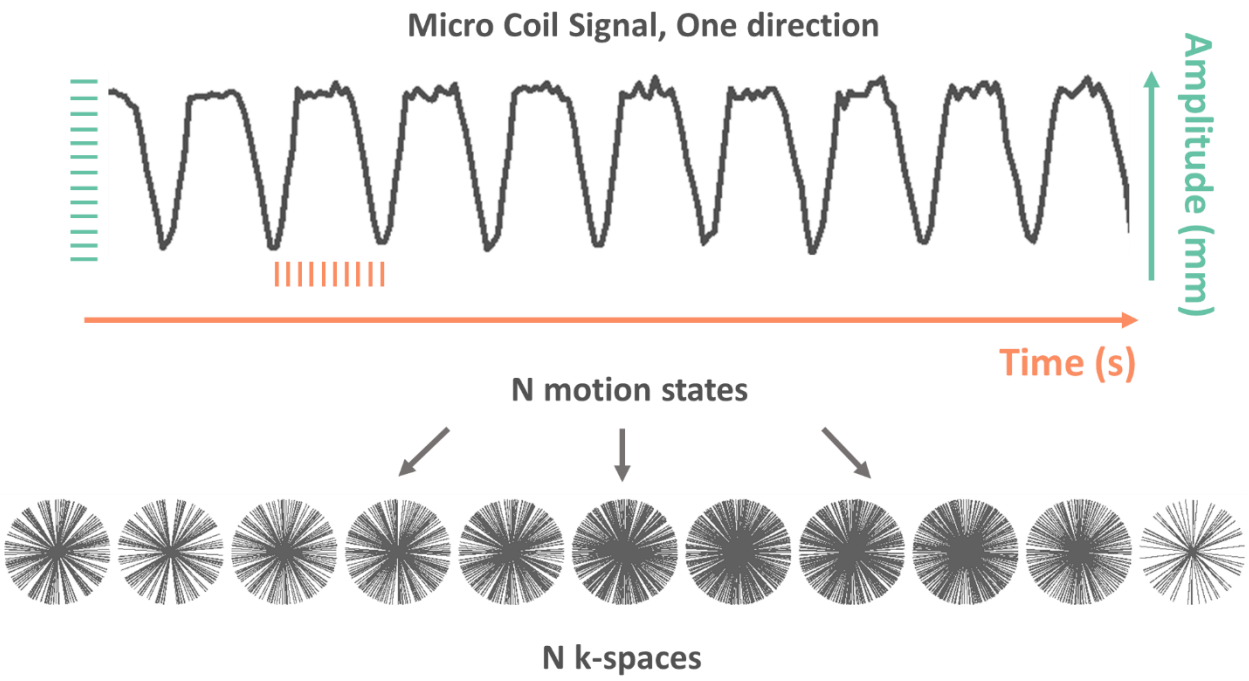

Figure 3-16: Schematic representation of the data sorting procedure. In a first step, referred as sorting, the position signal is either partitioning in amplitude intervals (green bars) or time intervals (orange). In a second step, the sorted projections belonging to a same motion state are binned together, yielding to N k-spaces (corresponding to N motion states).

Experiments were conducted with the set-up described in section 3.3.6.1 and the 2D-GA acquisitions were performed with the following parameters: FOV = 150 x 150 mm^2; Matrix = 288 x 288 px; slice thickness = 3 mm; FA = 15°; TR/TE = 60/6 ms; BW = 250 Hz/px; 3000 radial views; 3 segments (1000 shots); Acquisition time = 1 min. Tracking module parameters were set as follows: FOV = 450 mm, matrix = 512 data points, TE = 2.8 ms, TR = 4.8 ms, FA = 3°, bandwidth = 152 Hz/px, background suppression = 6 $mT.m^{-1}$, total tracking duration 24.47 ms. The same dataset was exploited for the two sorting algorithms. Resulting corrected images were reconstructed using ESPIRIT algorithm while original data (without correction) were reconstructed with NuFFT. These two reconstruction methods will further be explained in section 3.6.

3.5.1. Amplitude-based sorting

1D case

First method consists in sorting the position retrieved from micro-coils into N bin windows of equal width. Example of such a sorting is given in Figure 3-17a for a phantom performing a translation motion along the Z axis of the MRI.

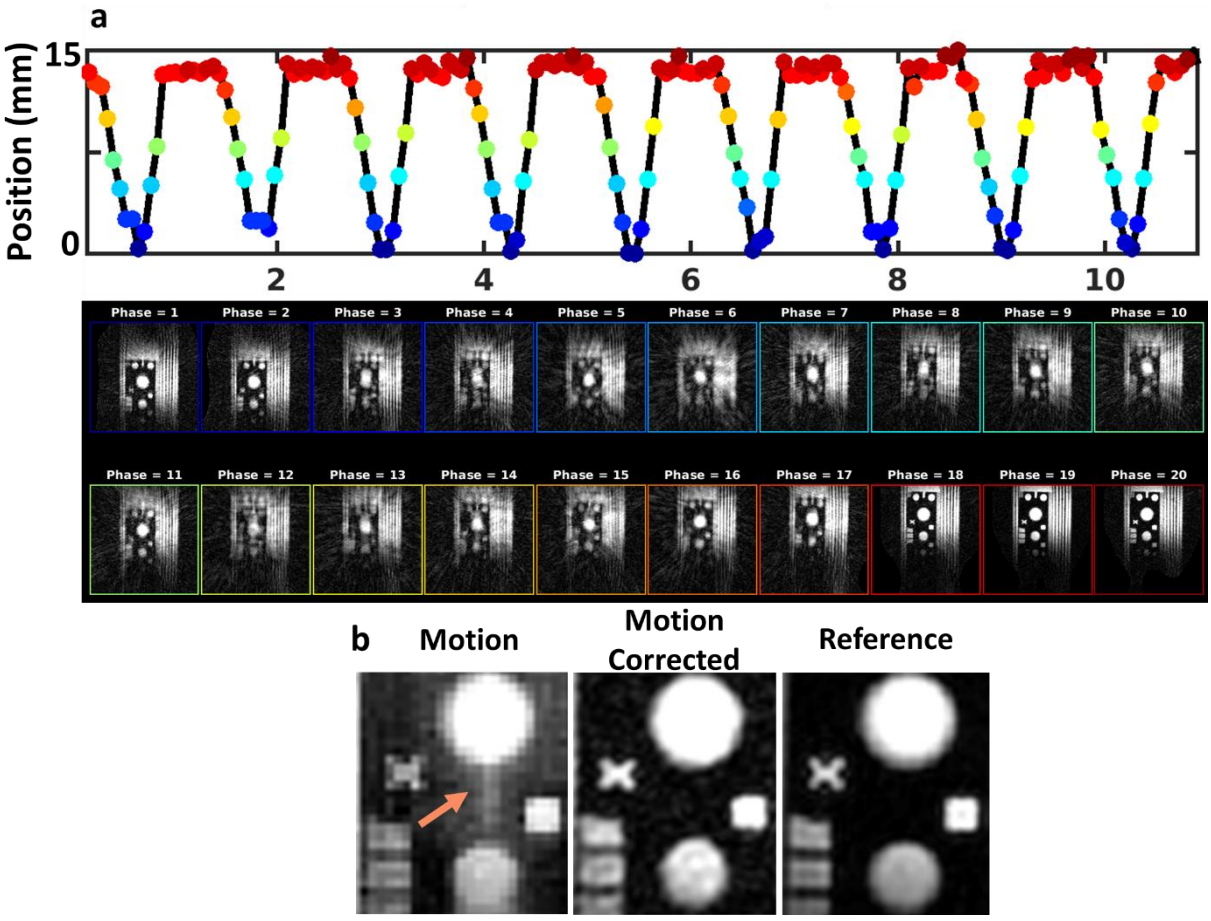

Figure 3-17: Illustration of the amplitude-based sorting algorithm. a) The position signal is partitioned into N phases along the position dimension. Each phase is then reconstructed. Here, 20 motion phases were derived. Phases corresponding to a motion plateau (phases 18 to 20) exhibit a good image quality whereas intermediate phases (acceleration phases) demonstrate a high artifact level with severe image degradation. b) Comparison of uncorrected image (motion) together with corrected and reference images demonstrates removing of blurring artifact (orange arrow) after sorting the data. The motion-corrected image displays a quality equivalent to the reference one.

Twenty phases (colored points) were derived from the position signal (black curve). Images corresponding to each motion state are displayed below and color-framed according to the same color code. As illustrated, high-quality, motion-corrected images (phases 18, 19 and 20) are recovered. Comparison between motion (no correction), motion-corrected (phase 20) and image without any motion (reference image) demonstrates correction of blur artifacts (orange arrow) and recovering of contrast and sharpness of details (Figure 3-17b). However, we observe uneven image quality between image corresponding to the motion plateau and intermediate phases (Phase 2 to Phase 17), the latter being strongly affected by streaking and blurring artifacts. This is explained by the fact that these phases correspond to an acceleration phase (when the phantom is moved back and forth at high speed). Compared to “plateau” phases, a greater displacement occurs within the bin window, yielding to more intra-bin motion. In the meantime, less radial profiles are acquired which results in higher undersampled data and therefore higher streaking artifacts. One of the solution would be to perform an adaptive binning, as proposed in Cruz et al [7], which would automatically detect acceleration phase and reduce the window size accordingly to ensure a more reliable motion compensation. However, in our case, we only search for one image in the stable phase of the motion. Therefore, in practice, only the phase corresponding to the motion plateau (phase 19 for example) may be reconstructed.

3D extent of the amplitude-based algorithm

A 3D version of the amplitude-based algorithm is proposed. The dataset presenting in the following was collected in vivo, on a sheep (**animal experiment #1**, see section 3.8.2) with the same tracking parameters as the one used in phantom experiment. The 3D position was derived from one of the micro-coils and plotted before being processed. In this approach, processing is divided into 3 steps and is illustrated in Figure 3-18. In the first step, position amplitude along each direction is computed to determine the primarily direction of the motion. In step 2, only the direction with the greatest motion amplitude is considered to find the most recurring position using a histogram. This phase corresponds to the motion plateau described above. The associated coordinates in the two other directions are then derived to define the center of a sphere. Finally (step 3), only the positions belonging to the sphere whose radius, called the acceptance radius (AR), corresponds to the motion amplitude tolerated within a single bin are retained to reconstruct

an image free from motion. It is possible to reconstruct another phase of the motion by simply selecting with the histogram the new center of the sphere. However, in practice, as aforementioned, only the phase corresponding to the most stable phase is reconstructed.

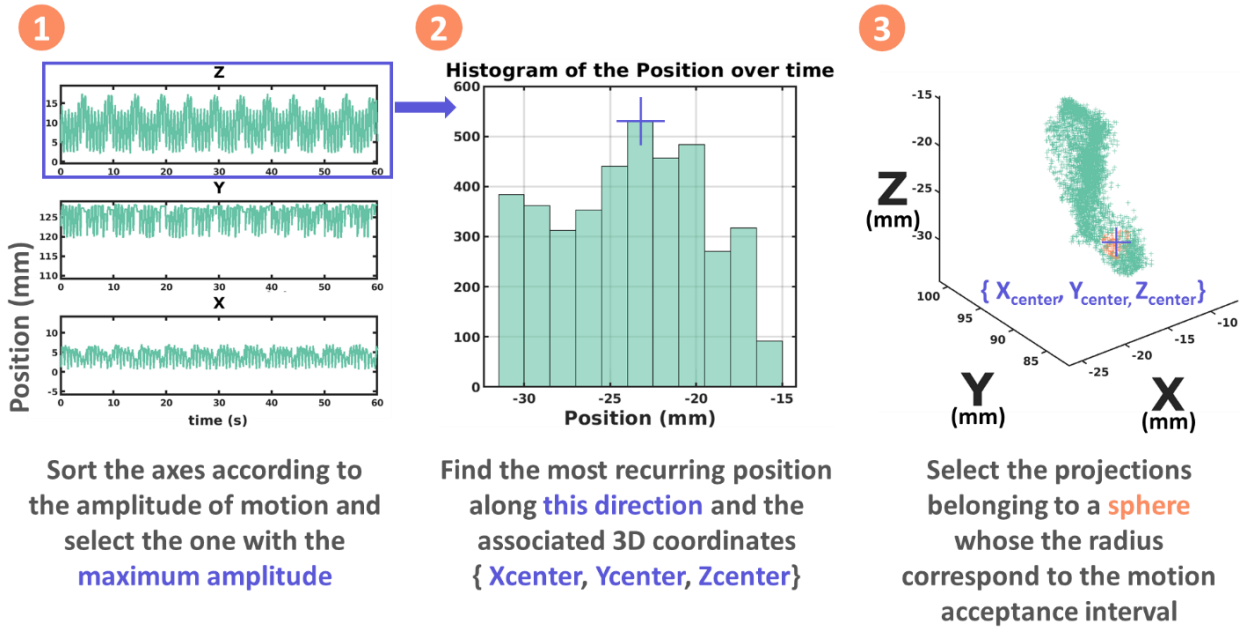

Figure 3-18: 3 steps of the 3D amplitude based algorithm. First, the direction with the largest motion amplitude is selected (Z-axis in this example). In a second step, histogram of the positions is plotted for the selected direction which gives the most recurrent position over the time. Finally, the associated coordinates of this most recurring position are retrieved and described the center of a sphere whose radius corresponds to the acceptance motion amplitude.

3.5.2. Temporal-based sorting

The second method consists in grouping the projections according to the time interval they belong to, following the same principle as retrospective gating in cardiac cine imaging. A peak detection algorithm is performed and returns the associated time. Time interval is therefore defined according to the time between two consecutive peaks and the number of desired phases. Example of this sorting algorithm is provided in Figure 3-19a.

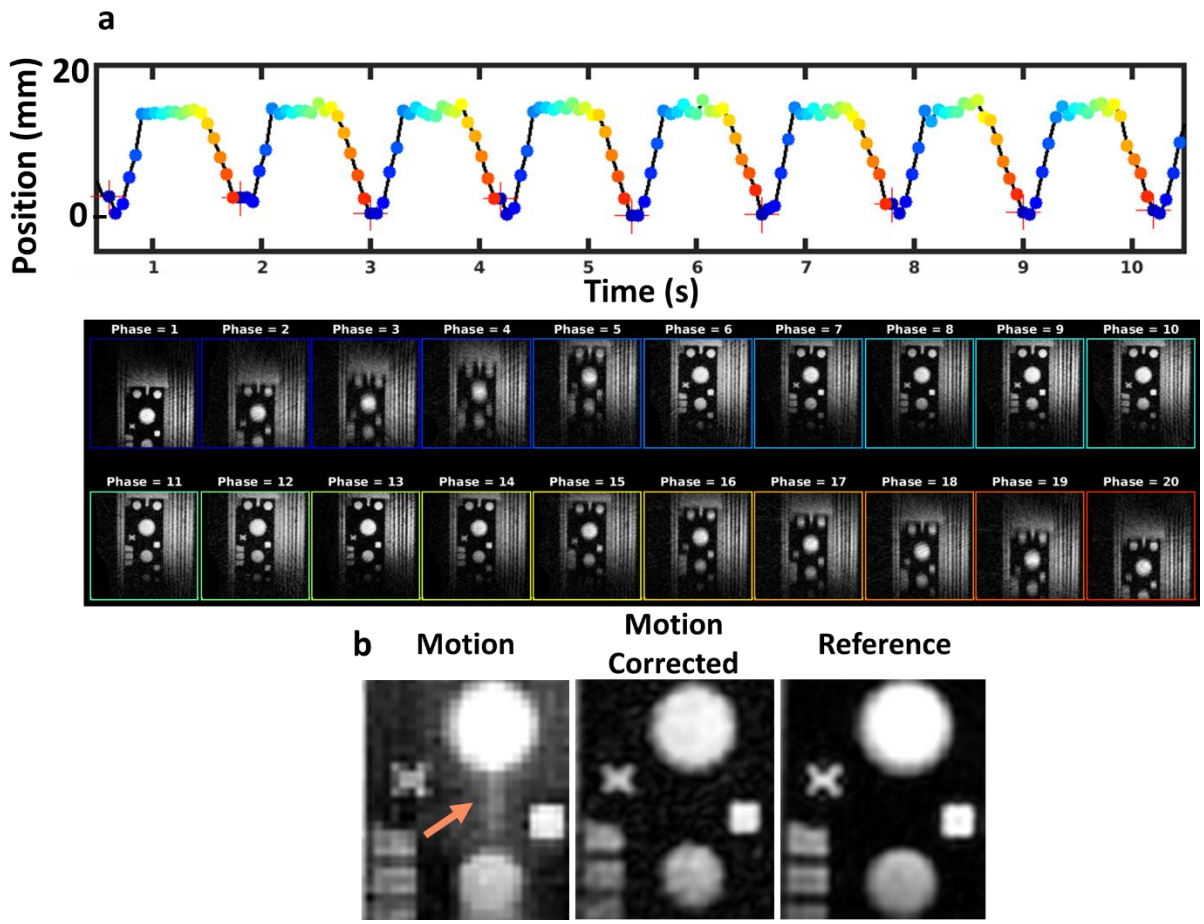

Figure 3-19: Illustration of the temporal-based sorting algorithm. Each motion cycle is divided into N time intervals. Projections that belong to the same interval time are binned together and resulting k-space are reconstructed. In this example, 20 phases were derived from the sorting data procedure. Phases corresponding to a motion plateau (phases 18 to 20) exhibit a good image quality whereas intermediate phases (acceleration phases) demonstrate severe blurring artifacts. b) Comparison of uncorrected image together with corrected and reference images demonstrates removing of blurring artifacts (orange arrow) after sorting the data. The motion-resolved image displays a quality equivalent to the reference one.

Twenty phases were derived for direct comparison with the amplitude-based algorithm previously described. Motion states are overlaid (colored dots) on the position measurement (black curve) and peaks are identified with a red cross. Images corresponding to motion plateau (phases 6 to 14) demonstrates a good image quality with correction of blur artefacts (orange arrow) and restitution of contrast and sharpness (Figure 3-19b) when compared to the reference image. In opposite, images corresponding to acceleration phases (phases 3 to 5 and phases 15 to 20) demonstrates a poor image

quality with blurring and streaking artifacts with a more severe alteration for phases 3 to 5. This is because the piston acceleration is higher when moving the phantom forth than back.

Compared to the images resulting from the amplitude-based algorithm, images obtained with the temporal-based one showed better results for phases outside the motion plateau (intermediate phases). This is explained by the fact that in the time division algorithm, distinction between the back-and-forth motion is made. In our phantom experiment, even if the motion is considered as rigid, a shift in the trajectory between the back and forth motions can occurs, yielding to a mix of two motions if no distinction is made, increasing thus the intra-bin motion.

3.5.3. Application to in vivo

We further investigated the position retrieved by the micro-coil signals in vivo. Experiment was conducted on the same dataset as in the 3D version of the amplitude-based sorting (**animal experiment #1** see 3.8.2). The catheter was in contact to the left ventricle apex. Physiological signals were recorded by external sensors (ECG leads and respiratory below) and indicated a heart rhythm comprised 96-100 beats per minutes (bpm) throughout the study and a respiratory rate of 12 cycles/min. The position signal was retrieved as described in section 3.3.2 and plotted over time for each direction (Figure 3-20,left). Analysis of these signals evidenced that the catheter motion is composed of two oscillating movements with different frequencies: a lower frequency, and a higher frequency. The 3D plot of the catheter position over time clearly highlighted the twisting motion, which is characteristic of the cardiac contraction (Figure 3-20, middle): the latter consists of a clockwise rotation at its base and a simultaneous counter clockwise rotation at its apex. Frequency spectrum of the direction presenting the dominant modulation (here Z) was derived and demonstrated two main frequencies (0.2 Hz and 1.6 Hz) that correlated with the respiratory rate and the heart rhythm (Figure 3-20, right). These frequencies were used to build a Butterworth filter of a 1^{st} order to extract both motions components.

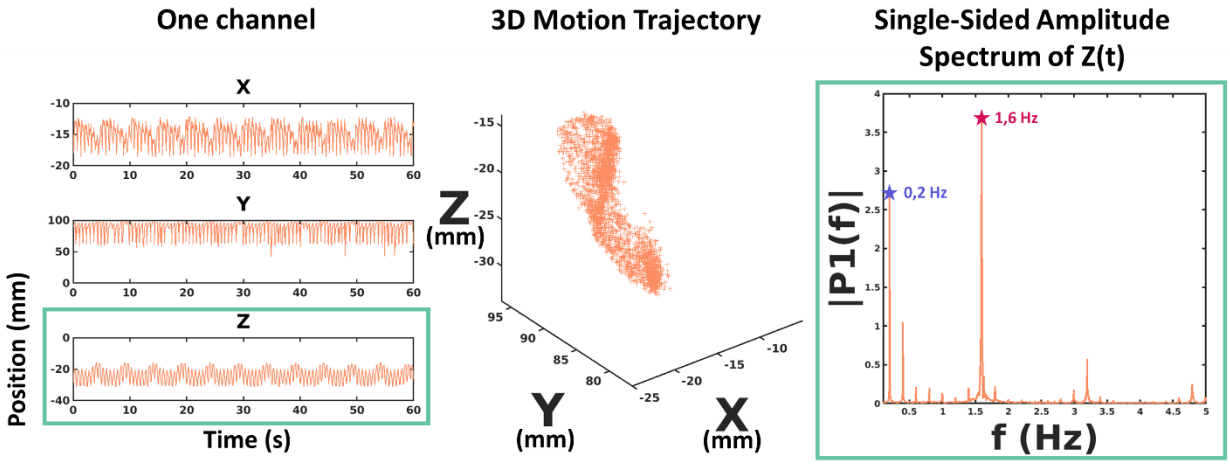

Figure 3-20: Analysis of the frequency components of the position signal. **Left-** The 3D position is retrieved after analysis of the phase's slope of one micro-coil and plotted for each direction. The signal position reveals a modulation with two oscillating motions: a slow one and a faster one. **Middle-** The 3D plot of the position evidences a twisting motion pattern, which is characteristic of the heart motion. **Right-** The single-sided amplitude spectrum in the direction presenting the dominant modulation depicts two main frequencies at 0.2 Hz and 1.6 Hz. These frequencies feed the input of a Butterworth filter for extraction of the two motion components.

The resulting extracted motions components were compared to the physiological recorded signals. Overlay of both the physiological signals and the catheter signals is shown in Figure 3-21.

We only display the ECG trigger initiated by the MR scanner, which coincides with the R-wave of the ECG signal. A good correspondence is observed between the signal recorded by the catheter (orange curve) and the QRS trigger generated from the ECG leads (green curve) by the scanner. Same observation is made for the respiratory signal although a slight difference can be noticed between both curves. This is explained by the fact that the signals do not record the same information. While micro-coils inform about the motion inside the cardiac chamber, the respiratory bellow detect the chest expansion. This result highlights the feasibility to derive a cardiac and a respiratory signal from the signal recorded by the micro-coils. These two signals can further be used at the input of the temporal-based sorting to derive cardiac and respiratory phases.

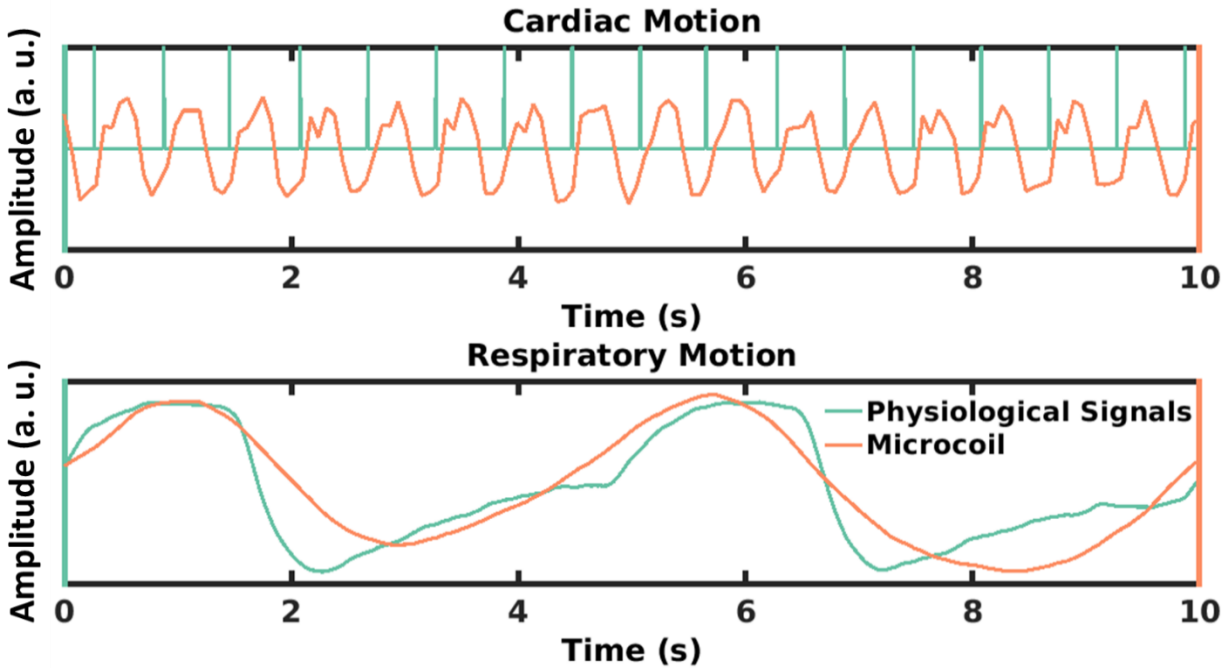

Figure 3-21: Comparison between extracted motion signal components from micro-coil recordings and physiological signal recorded by external sensors. The motion component with the frequency of 1.6 Hz derived from the frequency spectrum correlates with the cardiac triggering generated by the scanner. Likewise, the motion component with 0.2 Hz correlates with the respiratory bellow signal. A slight lag between respiratory bellow signal and the signal extracted from micro-coils is observed and is due to the fact that the signal are not recorded at the same location.

3.5.4. Characterizing the projections repartition within the k-space

3.5.4.1. Sampling of radial trajectory – The Nyquist-Shannon criterion

To prevent from any aliasing in images, a minimum number of spokes have to be acquired and the distance between spokes at the edge of k-space have to comply with the Nyquist-Shannon criterion [22]. For 2D scan, this translates into the following mathematical formulation:

$$k_{max}\Delta\Phi \leq \frac{1}{L} \qquad (3\text{-}4)$$

Where k_{max} is the maximum k-space radius, $\Delta\Phi$ the angular sampling interval which is determined by the desired spatial resolution and L the FOV, which is assumed to be the

same in all direction. For a 2D trajectory that samples over π radians, the number of equiangular spokes required to satisfy the Nyquist-Shannon criterion is:

$$N_s = \frac{\pi}{\Delta\Phi} = \pi k_{max} L \quad (3\text{-}5)$$

For comparison, in case of a 2D Cartesian acquisition, with the same FOV and resolution (i.e, the acquisition matrix size, not including zero filling), the number of phase encode lines N_{phase} would be :

$$N_{phase} = 2k_{max} L \quad (3\text{-}6)$$

Combining equations 3.5 and 3.6 gives the minimum number of diametral spokes that have to be acquired relative to the matrix size:

$$N_s = \frac{\pi}{2} N_{phase} \quad (3\text{-}7)$$

The 2D radial trajectories, sampling over π, therefore require 57% more Fourier lines relative to a comparable 2D Cartesian acquisition in order to sufficiently sample the data space. According to these equations, the angular sampling interval to comply with the criterion is:

$$\Delta\Phi(^\circ) = \frac{2}{\pi \,.\, N_{phase}} * 180 \quad (3\text{-}8)$$

Practically, it is often tolerable to acquire only a reduced number of spokes and therefore increase the angular sampling interval. This is because the region of interest is frequently located inside the object so that the streaking is located at the border of the image and are therefore not objectionable for interpretation. Reducing the number of spokes is further appreciable to decrease the scan time. However, in certain scenarios, the number of spokes and therefore the angular interval does not meet the recommended requirement so that the degradation in the image is too pronounced. This is a well-encountered issue, especially in motion-compensation strategy where only a subspace of the total acquisition projections are considered to recover a motion-free image. To overcome this limitation,

development of methods exploiting only a reduced number of acquisitions were introduced (see section).

3.5.4.1. K-space filling analysis

Golden-angle ratio exhibits advantageous coverage of the k-space. In this radial acquisition scheme, the angle of the acquired spokes is continuously increased by 111.25 degrees, resulting in a series of complementary radial spokes with large angular distance that always add up to approximately uniform angular coverage of the k-spaces [23]. However, sorting the acquired radial lines into different motion phases may drastically alter the effective golden-angle repartition. In this situation, gaps and clusters of samples in k-space may arise, yielding to more or less coarse streaking in the image. In order to characterize the sampling density and attempt to predict the artifact level in the resulting image, we proposed a representation that inform about the compliance of each k-space with the Nyquist angular criterion. For that purpose, we computed the angular interval between each of the radial profiles belonging to a sorted k-space and plotted the histogram of the angular distribution. Example of such a representation is given in ***Figure 3-22***Figure 3-22 for images sorted with the **time-based algorithm**.

Density sampling was plotted for the phase #11, corresponding to the plateau and the phase #5 corresponding to an acceleration phase. A red line delineates the angular interval to comply with Nyquist criteria. The orange cross indicates the number of projections satisfying the Nyquist angular interval. The corresponding k-space is plotted to schematically represent the radial lines distribution while the histogram provides a quantitative metric of the distribution (total number of projections and percentage of projections satisfying Nyquist criteria).

Figure 3-22 further highlights that at equivalent density sampling, image corresponding to the motion plateau displays a good quality whereas image corresponding to the acceleration phase depicts severe blurring artifacts. This is because, within a same window time, the motion amplitude is greater in the phase #5 (pink arrow) phase than in the phase #11 (green arrow) introducing thus more intra-bin motion. This demonstrates that, in addition to the sampling density, the notion of motion acceleration has also to be taken into account in the resulting image quality. Therefore, the projections not only have to meet the Nyquist angular criterion but also be chosen so as to minimize the intra-bin motion.

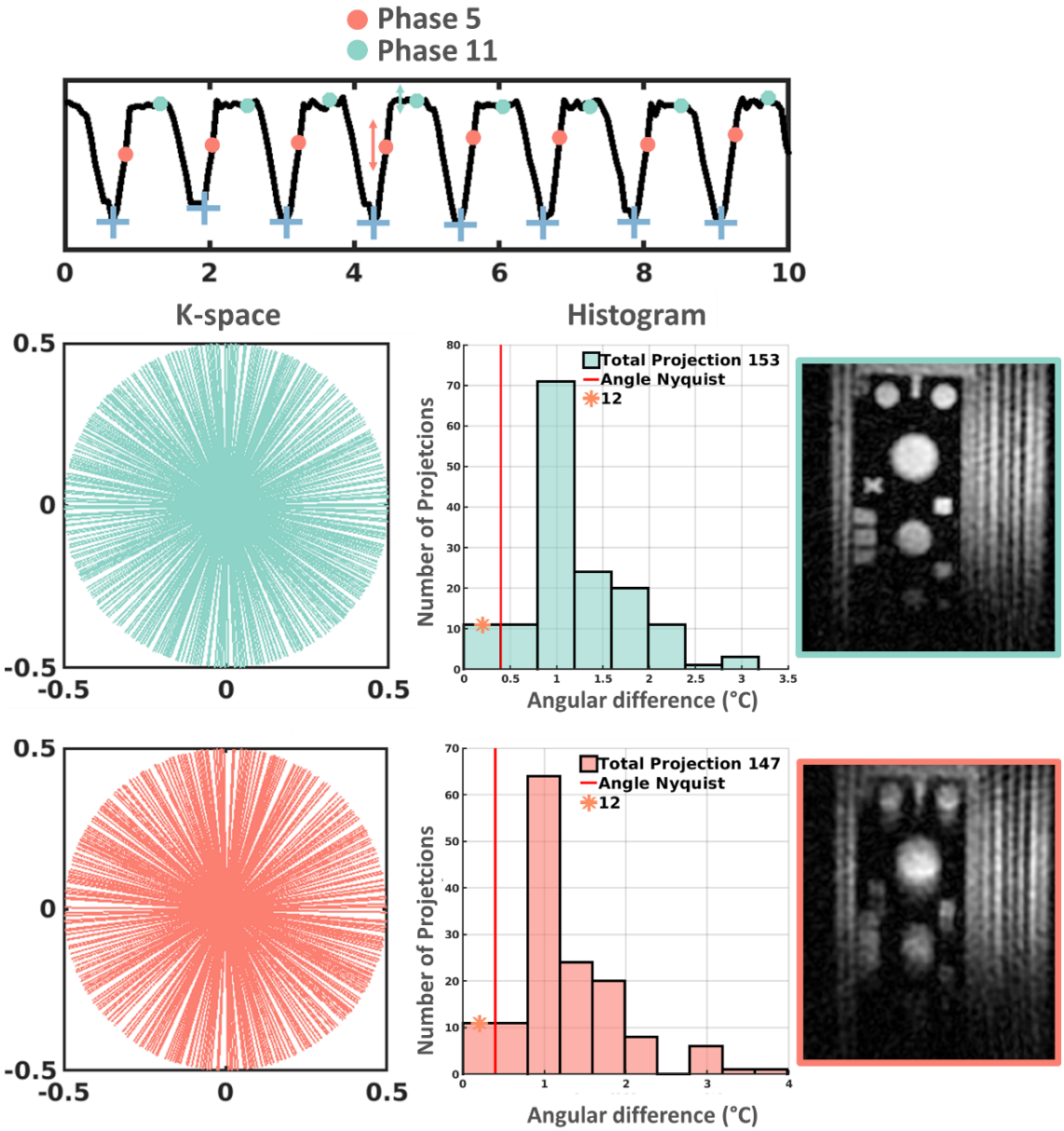

Figure 3-22: Density sampling representation. In order to quantify the coverage of the k-space after data sorting procedure, a histogram is plotted (**middle**) that represents the angular interval distribution. A red line indicates the Nyquist angular criterion. The associated k-space is plotted (**left**). The density sampling of a phase corresponding to the motion plateau (green dots on the curve, phase #11) and a phase corresponding to an acceleration (pink dots on the curve, phase #5) were derived. An equivalent density sampling is found between the two k-space datasets. However, resulting images demonstrate an uneven image quality. This is because, within a same window time, the motion amplitude is greater in the phase #5 (pink arrow) than in the phase #11 (green arrow) introducing thus more intra-bin motion.

3.5.5. Data sorting and image quality: conclusion

From these results, we demonstrated that the resulting image quality would depend on multiple parameters:

- **Acceleration**: at equivalent density sampling, the k-space encapsulating the largest motion amplitude (ex: acceleration phase vs motion plateau) will result in a poor image quality. Consequently, the faster the motion is the thinner the bin window size should be to minimize intra-bin motion. One of the solutions would rely on an adaptive binning that adjust the bin window size with the motion amplitude, as proposed in Cruz et al. [7]

- **The bin window size**: has to be a compromise between the motion acceptance and the minimum data required to comply with Nyquist criteria. The smaller this window is, the more data are rejected and the less radial views are included in the reconstruction, which in turns yields to a poor image quality.

- **The temporal resolution of the tracking**: Increasing the temporal resolution can be invested either for a higher motion subdivision (reducing the window size) or to increase the number of motion states. The tracking acquisition rate has to be chosen in accordance with the motion frequency (slow motion do not need a high refresh rate).

- **The sorting algorithm type**: A temporal division would permit distinction between cardiac phases in vivo. Limitation of the amplitude-based sorting algorithm is the risk to mix cardiac phases: the heart position during diastole and systole could be the same at a certain respiratory phase, which will introduce blurring in the resulting image and skew the interpretation.

3.6. Image reconstruction

This section introduces the methods used to reconstruct the radial acquisition from the basic Non-uniform Fast Fourier Transform (NuFFT) reconstruction to more sophisticated compressed sensing algorithms when data are strongly undersampled. In this situation, the

Nyquist criterion is not satisfied and images may exhibit intense and coarse streaking artifacts, which preclude from good interpretation. This is due to the unmeasured gaps in k-space between spokes. The reconstruction problem is therefore clearly undetermined and conventional techniques such as gridding fail to provide a proper image. One of the solutions is to address it in the form of an inverse problem, which is solved with an iterative nonlinear optimization technique. In order to compensate the missing data, prior knowledge about the object are incorporated in the process. This is realized by adding suitable penalty terms to the cost function that prevent the selection of implausible solutions and drive the optimizer to find a solution complying with both, the measured data and the prior knowledge. This regularization term is a trade-off between reduction of noise and preservation of images structures and edges. The choice of this term is therefore decisive in the reconstruction process. In particular, incorporating sparsity and statistical properties of images into the reconstruction problem have demonstrated a valuable improvement in image quality and sharpness. In addition, the approach exploits localized sensitivities of receiving coils to gain additional object information in a similar manner to parallel imaging, like GRAPPA or SENSE.

3.6.1. Non-uniform Fast Fourier Transform (NuFFT)

When the data set is not acquired along a uniform sampled-rectilinear k-space trajectory, the sampling positions are neither on a grid nor equidistant, which precludes a straightforward use of the Fast Fourier Transform (FFT) [24]. Additional complication comes from the sample density which is much higher in the center of k-space than in the outer area (for radial acquisition scheme). As the Discrete Fourier Transform (DFT) does not account for this locally varying distance between samples, severe blurring artifacts occult the image. Therefore, it is necessary to cope with both. First, radial sampling data must be morphed to fit into a rectangular array for data processing. This technique is called “gridding” or “regridding” and are a special case of the NuFFT. This can be done with different approaches [25]–[27]. Succinctly: after the raw data has been density compensate and resampled onto the Cartesian grid, a 2D Discrete Fourier Transform (DFT) takes the data to the image domain. The gridding reconstruction can mainly be divided into three steps: convolution (multiplication of the image by the FT of the gridding kernel), Fast Fourier Transform (FFT) and division by the inverse Fourier transform (IFT) of the kernel. Steps in

gridding are further detailed in Handbook of MRI pulse sequences [22] In the present work, the NuFFT was implemented using the open-source GPU library written in C++ with a Matlab mex interface proposed in Knoll et al. [28] and exploiting computation power of NVIDIA CUDA GPUs.

3.6.2. Eigenvector-based SPIRiT (ESPIRIT) and Compressed Sensing (CS) using BART toolbox

Data resulting of the sorting algorithm were reconstructed using ESPIRIT and CS for optimal image recovery. This was achieved with the Bekerley Advanced Reconstruction Toolbox (BART), which is a free and open-source image reconstruction framework. The library and command-line program offer efficient implementations of many calibration and reconstruction algorithms for MRI [29]. Briefly, ESPIRIT is an auto-calibrating parallel imaging method. It recovers the sensitivity maps of the receive coils from an eigen decomposition of a calibration matrix constructed from auto-calibration data. This method is an extended SENSE-based reconstruction algorithm that links both GRAPPA and SENSE methods and combines benefits of both [30]. ESPIRIT can be extended to integrate regularization terms such as $\ell 1$-norm with a wavelet transform for CS reconstruction [31]. CS takes advantage of the fact that an MR image is usually sparse in some appropriate transform basis. Sparsity means that there is only a few number of significant pixels with nonzero values within the data set. Hence, this transform allows to enforce the distinction between the significant information with the background noise. In a holistic approach, CS states that the measured signal can be accurately recovered from few samples if the following requirements are satisfied: (**1**) the desired image has a sparse representation in some basis (transform sparsity), (**2**) the measured samples are randomly chosen (incoherent measurements in the image or transform domain) and (**3**) a nonlinear reconstruction must be performed to enforce both sparsity and consistency with the acquired MR data. The sparsity of a solution is obtained using the $\ell 1$-norm whose minimum solution yields the sparsest solution. Operationally, the reconstructed image must be consistent with the Fourier transform of the acquired k-space data and have few large-valued coefficients when sparsely transformed. Mathematically, this entails solving an optimization problem, i.e. finding the image that minimizes this form [32]:

$$\underset{\hat{x}}{\operatorname{argmin}} = \|E\hat{x} - s\|_2^2 + \lambda\|\mathcal{W}\hat{x}\|_1 \qquad (3\text{-}9)$$

where $\hat{x}$ is the reconstructed image, E the encoding matrix including coil sensitivities, gridding and Fourier Transform, s the acquired k-space data. The constraint $\|E\hat{x} - s\|_2^2 < \varepsilon$ enforces data consistency. λ is the parameter that controls the degree of regularization in the reconstructed image, adapted to the noise level. The recovered image is here supposed to have a sparse representation in the basis $\mathcal{W}$ which can be, for example a wavelet transformation. Wavelet transform consists of generating a sparse representation by decomposing an image into its low and high frequency. Its performances have been demonstrated for image compression and denoising problems.

In practice, we used the following command lines for **ESPIRIT**: **'pics –l iter -S -rλ -t'**. And the following command line for **CS**: **'pics –l iter -l1 -rλ -s step'** using the ℓ1-regularized reconstruction (wavelet basis) with **iter** the number of iterations, adapted to the level of noise and **step** the iteration step size. The regularization parameter was empirically optimized. Specifically, a range of values (0,00005 – 0.0001) were tested and compared visually. The value generated the best image quality (sharpness, delineation of the myocardium wall) was selected.

3.6.3. Total Variation regularization using BART toolbox

In a third approach, we exploited the total variation (TV) regularization available in BART toolbox. This TV has been successfully employed in image restoration [24] and was first introduced in 1992 by Rudin, Osher and Fatemi as a spatial sparsity measure, limiting noise amplification while preserving sharp edges and small features in the images. TV penalty can be considered as requiring the image to be sparse by both the specific transform and finite-differences at the same time. In mathematical form, this penalty can be described as follows:

$$\underset{\hat{x}}{\operatorname{argmin}} = \|E\hat{x} - s\|_2^2 + \lambda_t \mathrm{TV}_t \qquad (3\text{-}10)$$
$$\text{with } \mathrm{TV}_t = \|\nabla\hat{x}\|_1$$

where ∇ represents the 1D temporal gradient and TV_t the temporal total variation in cardiac-dimension for example (inter-bin) which is, in other words, the sum of absolute differences between adjacent bins. The parameter λ_t defines the balance between total variation regularization and data consistency. In our experiments, we used a combination of wavelet transform with finite differences to reconstruct all motions states simultaneously as it has been shown to provide better performance than either of them alone. [33]. This allowed restitution of cardiac time-resolved motion-compensated image of undersampled radial MR data. In practice, we used the following BART command line: **'pics -e -S -d5 -RW:7:0: λ -RT:1024:0: λ_t -p dcf_file -t'** where 1024 corresponds to the 10th dimension (the cardiac dimension in our case), λ and λ_t the regularization parameters for the wavelet transform and total variation respectively and dcf_file is a file containing the compensation density coefficients. We used small value of λ_t to avoid blurring in regions with large motion and better distinguish motion states, as explained in Cruz et al. [7]. Typically, values of both λ and λ_t was 0.00025. TV was further extended to the respiratory-phase dimension.

3.6.4. Patch-based image reconstruction

In a last approach, patch-based image reconstruction was used with help of Dr. Bustin to denoise images obtained with TV. This reconstruction exploits local redundancies and low-rank matrix structures to obtain a sparser representation. Further details are provided in [34], [35].

3.6.5. How much can we undersample? The reconstruction limits

Speeding up the acquisition time is the key challenge of high-resolved cardiac MRI in that it reduces the risk of motion artifacts in images while the gain in time can be invested in increasing the spatial resolution. Moreover, in catheter ablation, accelerated acquisitions are critical for real time visualization of rapid physiological changes such as the lesion formation or tissue temperature changes during thermal ablation. More specifically, in our study, accelerating the acquisition is required to achieve high-resolution imaging of the arrhythmogenic substrate within an acceptable time window. This involves the search for the maximum acceleration factor one may achieve, in other words: ***what is the minimum number of spokes we can acquire to gain in time while maintaining a diagnostic***

***image quality*?** This is a delicate question as numerous parameters affect the quality of an iterative reconstruction such as Compressed Sensing [36]. Notably, an empirical study was conducted by Lazarus [37], to quantitatively derive the maximum undersampling factor preserving a targeted image quality as function of the image matrix size and the input SNR. Results emphasized that: (1) a minimum SNR has to be reached in order to meet the expected image quality, (2) going higher in resolution (increasing the matrix size) allow larger acceleration factors. Nevertheless, this second point is subjected to the available SNR in practice. As the proposed question[1] is theoretically inextricable, we focused in our study on empirically finding the best set of parameters at the input of ESPIRIT algorithm (section 3.4) to recover a desired image quality from a highly undersampled data set. In addition, as the final goal is to provide high-resolution imaging using our developed local coil (see chapter 2), we tested if only one coil could be used to perform such a reconstruction, although multiple receivers with different spatial sensitivities are favorable for those iterative reconstruction processes.

3.7. Evaluation of the implemented methods on Phantom

The aim of this section is to investigate if the implemented algorithms, combined with the reconstruction methods are efficient in practice at correcting different motion trajectories (the simplest as well as the most sophisticated) at different frequencies while evaluating the maximum undersampling factor allowing to retrieve a good image quality.

3.7.1. Maximum undersampling factor in static images

A first experiment was conducted to estimate the maximal undersampling factor achievable given our coil sensitivity (available SNR) and our reconstruction method.

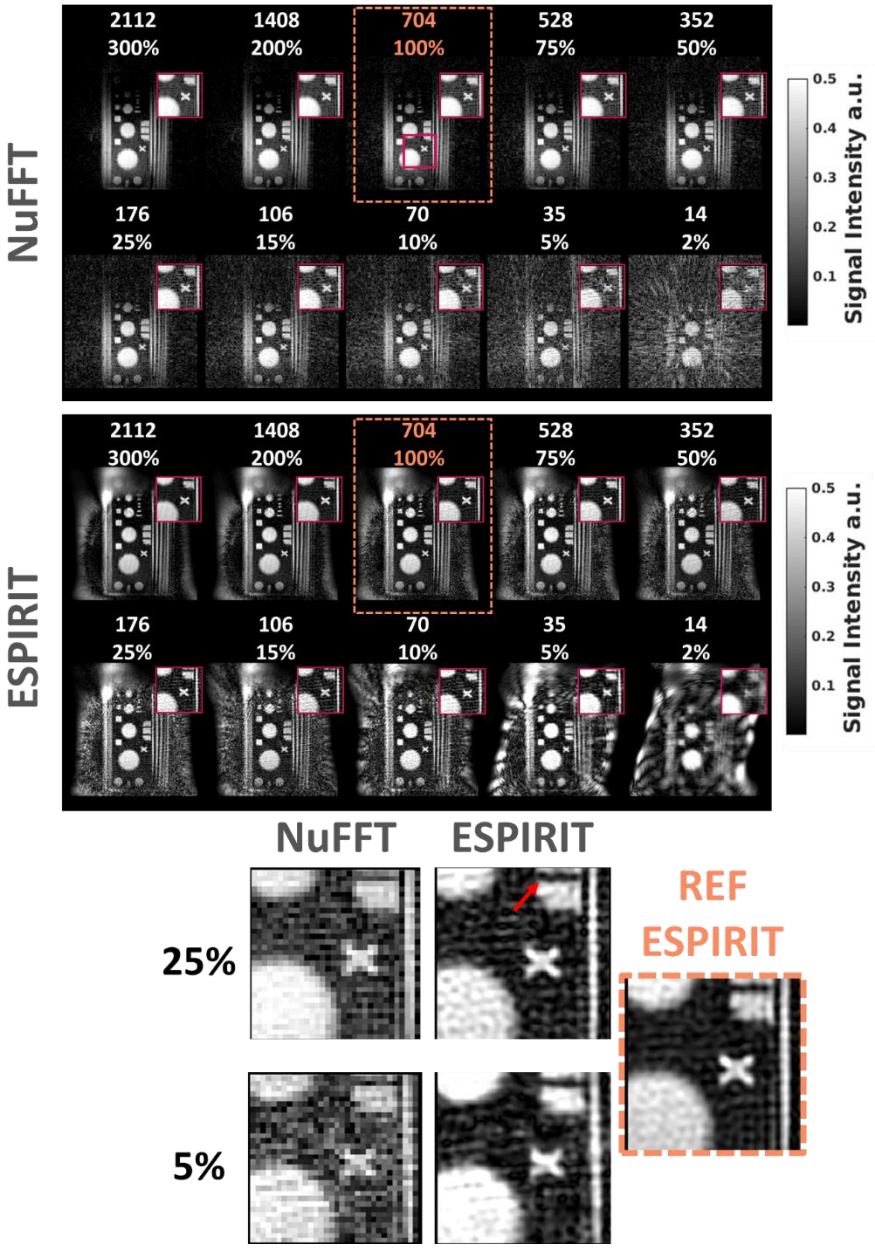

Figure 3-23 : Comparison between NuFFT and ESPIRIT reconstruction methods on data with different sampling. An acquisition was performed on a static phantom using the implemented sequence (2D-GA). The effect of both over and under-sampling on resulting image quality was evaluated. **Top-** For each image, the total number of projections included in the reconstruction and its equivalence in percentage (related to the minimum required number) is displayed. A dashed orange frame indicates the reference image, corresponding to the image reconstructed with the theoretical required number of projections (704). A zoom view that focus on the cross is given for each sampling. **Bottom-** ESPIRIT algorithm is compared to NuFFT for data with only 25% and 5% of the required data. Image acquired with all the required data (REF) and reconstructed with ESPIRIT is provided for comparison purpose. Results demonstrate efficiency of ESPIRIT at maintaining the targeted image quality until 25% of the requested data.

For that purpose, a 2D-GA acquisition was performed on a static phantom (3D-printed phantom, see Chapter 2) with the following image parameters: FOV = 150 x 150 mm^2; Matrix size = 448 x 448 pixels; TR/TE = 66/8 ms; FA = 10°; bandwidth = 255 Hz/pixels; slice thickness = 3 mm; 3 segments; 3000 projections, Acquisition time = 1 min. Only the local coil (2 cm in diameter) was used as a receiver. The later was directly positioned on the phantom as described in section 3.3.6.1. The theoretical minimum number of projections was computed using the equation (3-7**Erreur ! Source du renvoi introuvable.**) and was found to be 704 (448 x π/2). We deliberately acquired much more projections than needed to assess both the effects of oversampling and undersampling on the resulting image quality. The number of projections was iteratively decreased from 2112 to 14 projections (300% to 2% of the required data) and resulting images were first reconstructed using the NuFFT before applying ESPIRIT algorithm. Figure 3-23 displays the resulting images obtained with NuFFT (two top rows) and ESPIRIT (two bottom rows) reconstruction methods.

For each image, the total number of projections included in the reconstruction and its equivalence in percentage (related to the minimum required number) is displayed. A dashed orange frame indicates the reference image, corresponding to the image reconstructed with the theoretical required number of projections (704). A zoomed view focused on the cross of the phantom is displayed at the top right of each image. From these results, we show that oversampling the data does not lead to a superior image quality, except increasing the SNR. Conversely, as expected from the theory, streaking artifacts increase when decreasing the number of projections. Nevertheless, these artifacts remain not objectionable for image interpretation even if only 50% of the data is used for the reconstruction. In addition, we show that ESPIRIT clearly enhances the image quality and allows a higher undersampling factor (<50%). Indeed, details such as the cross and the bar (500 µm-width, red arrow) appear sharper and remain distinguishable even when only 25% of the required data is used. Furthermore, compared to NuFFT, ESPIRIT allows recovering details within an image reconstructed with only 5% of the data. However, in this last situation, the details are not restituted with as much precision, demonstrating that undersampling limit has been reached. The “halo” effect surrounding the phantom in the ESPIRIT reconstructed images is due to the sensitivities estimation and the choice of the

calibration matrix size and therefore depends on the coil and on the parameters set in the algorithm.

The sampling distribution of the k-spaces corresponding to 100%, 50% and 25% of the theoretical required data were plotted in Figure 3-24 in order to quantify how far it is possible to violate the Nyquist criterion while maintaining an acceptable image quality.

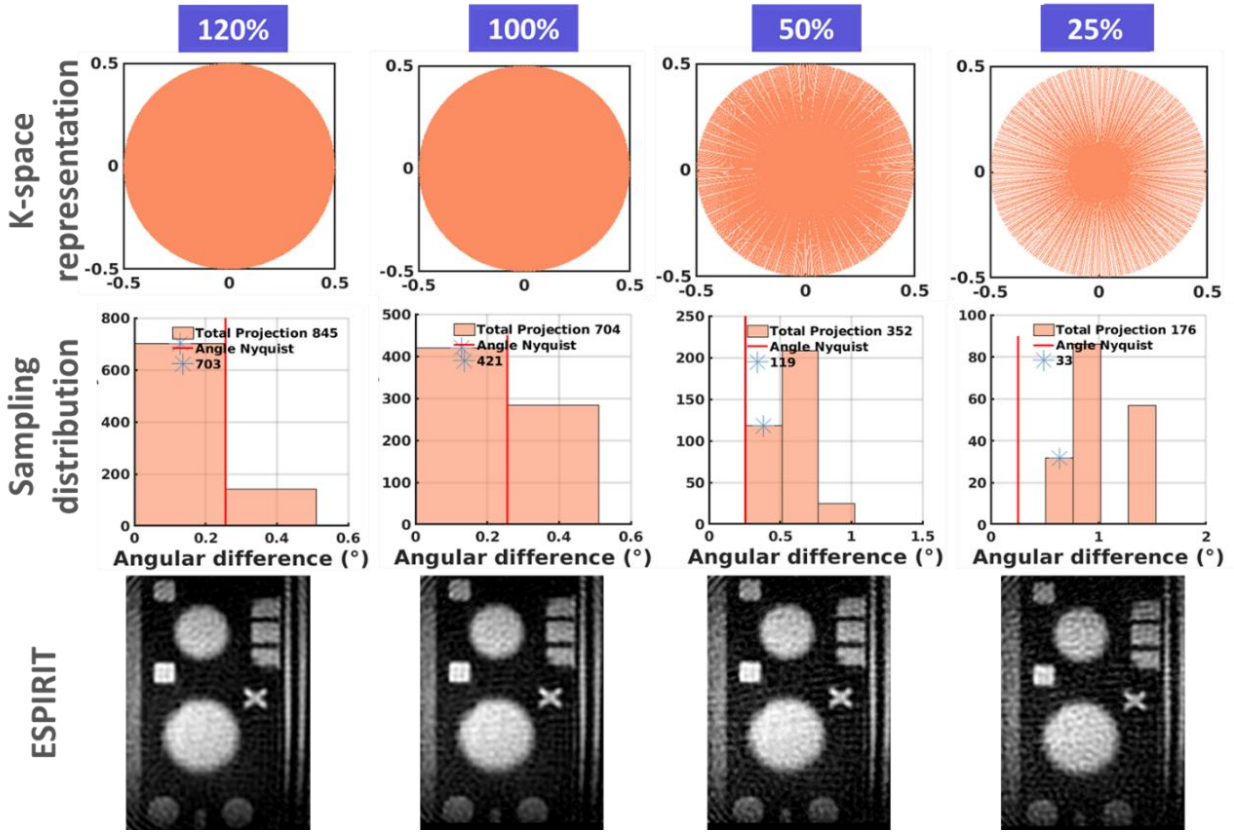

Figure 3-24: Evaluation k-space with different undersampling degree on image quality. **Top row-** K-space with 120%, 100%, 50% and 25% of the theoretical required data respectively were reconstructed using ESPIRIT. **Middle row-** For each k-space, histogram of the angular distribution is plotted. We observe that 120% of the theoretical data are required to meet 100% of the Nyquist angular criterion using our acquisition scheme. **Bottom row-** However, using only 25% of the theoretical data yields to the same image quality, demonstrating the possibility of high undersampling with ESPIRIT added to the reconstruction.

We observed that even when 100% of the theoretical required data were used for reconstruction, only 60% of the total projections satisfied the Nyquist angular interval. This is explained by the fact that GA only promotes a uniform coverage by adding 111.25 degrees between two consecutive projections without any constraints about angular sector

they should belong too. Therefore, unless computing the number of repetitions which ensures that there is at least one projection per angular sector or constraining the acquisition scheme, GA, as currently implemented, does not guarantee that each angular sector corresponding to the Nyquist angular interval is filled. In our experiment, we found that at least 120% of the theoretical required data have to be acquired to fulfill the Nyquist angular criterion. However, as illustrated in Figure 3-24, we show that with only 25% of the theoretical required projections among which 0% satisfy the Nyquist angular criterion, it is possible to reconstruct an image of equivalent quality than the one complying with Nyquist (120%). These results therefore emphasize the possibility to drastically shorten scans without sacrificing spatial resolution by taking advantage of ESPIRIT to recover a high image quality.

3.7.2. Correction of different motion trajectories

3.7.2.1. Translational-only motion

A first experiment was conducted using the previously described set-up (3.3.6.1) and a translational motion at a rate of **50 beat per minute** (motion 1 in Figure 3-11**Erreur ! Source du renvoi introuvable.**) along Z. Position was computed from the phase analysis of the micro-coils signal, as described in section 3.3.2 and corrected using the statistical approach proposed in section 3.3.5 to remove the outliers. The 2D-GA Acquisition was performed with the following parameters: FOV = 150 x 150 mm^2; Matrix = 288 x 288 px; slice thickness = 3 mm; FA = 15°; TR/TE = 60/6 ms; BW = 250 Hz/px; 3000 radial views; 3 segments (1000 shots); Acquisition time = 1 min. Resulting voxel size was **0.5 x 0.5 x 3 mm^3**. Tracking parameters were: FOV = 450 mm, 512 data points, FA = 3°; background suppression = 6 mT.m-1; TR/TE = 4.8/2.8 ms; bandwidth = 152 Hz/px.

After the position was derived (Figure 3-25a), the motion was corrected using the 3D amplitude-based algorithm described in section 3.5.1 and projections belonging to the more stable phase were grouped together. In this experiment, the AR was set to 0.5 mm to fit with the spatial resolution of the image (the smallest structure is of an order of 500 µm). The binned k-space was successively reconstructed using NuFFT and ESPIRIT. Acquisition without any motion was also performed and image was reconstructed using the

same methods to provide a reference. Images resulting from the two experiments are juxtaposed in Figure 3-25a for comparison purpose.

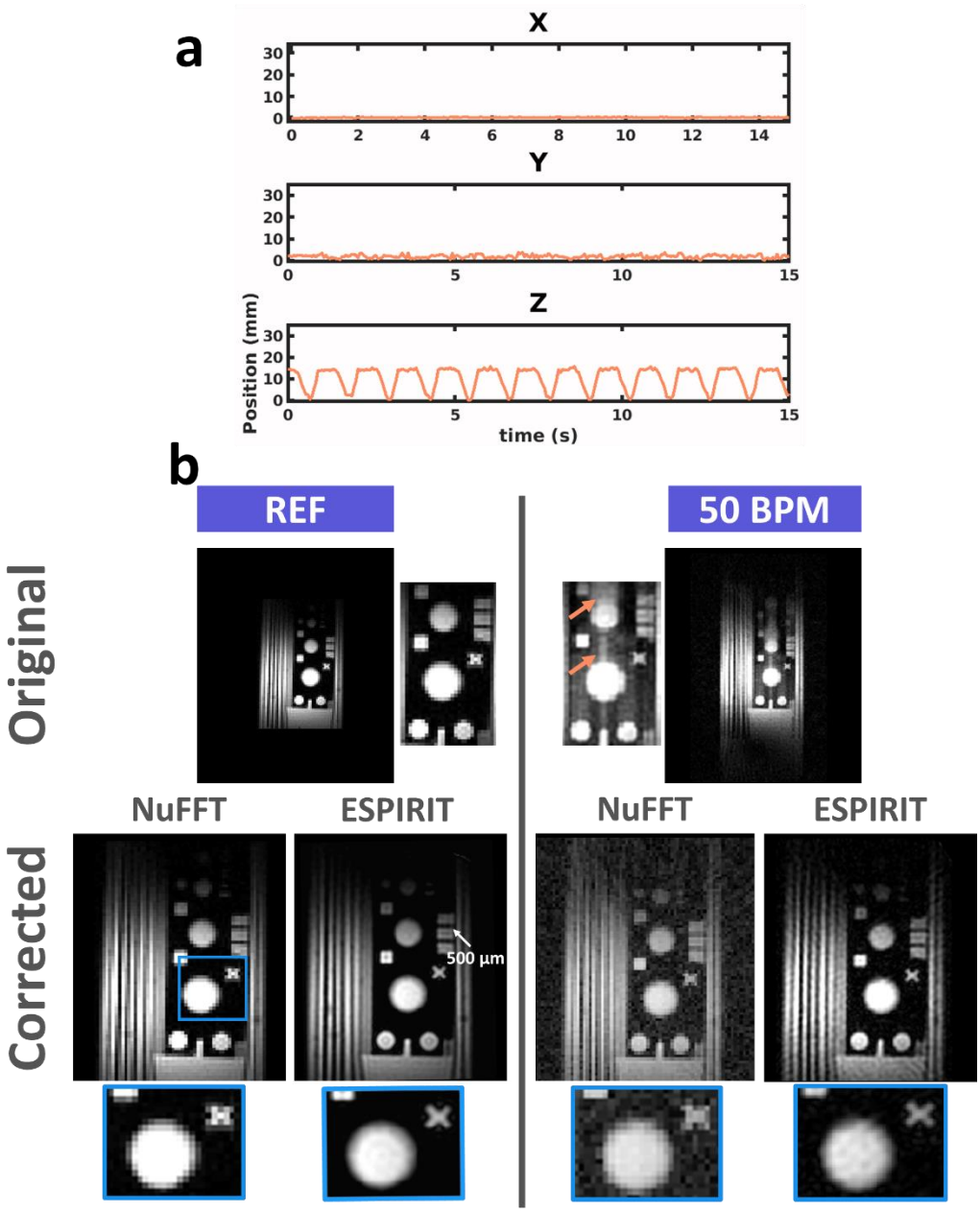

Figure 3-25: Correction of a translational motion along Z-axis at 50 bpm. **a)** Plot of the positions over time for each direction (X, Y and Z). Only a modulation along Z-axis is observed, which is consistent with the motion induced by the piston. **b) Left-** Reference image (static image) reconstructed with either NuFFT or ESPIRIT. **Right-** Top image displays the image when motion is induced with a zoomed-view focusing on geometric details. White trails are observed (orange arrows), resulting from motion artifacts. Bottom images show motion-corrected image reconstructed with either NuFFT or ESPIRIT. Motion-corrected image and reference image reconstructed with ESPIRIT demonstrate similar quality. Blue frames provide a zoomed-view of the circle and cross for sharpness comparison purpose.

We show that motion at this rate induces blurring artifacts and trails in the resulting image (orange arrows). These artifacts are removed after the application of our sorting algorithm and the resulting image, reconstructed with NuFFT method is similar to the reference one although less contrasted. ESPIRIT reconstruction drastically enhances the image quality of the reference image by improving the sharpness and spatial resolution (blue frames). Applying such an ESPIRIT in the motion corrected image yields to an image with same contrast and sharpness as the reference image reconstructed with ESPIRIT. This result demonstrates the efficiency of our motion correction pipeline (including data sorting and reconstruction) at restoring a motion –resolved image with an equivalent quality as an image without motion.

3.7.2.2. Combination of translational and rotational motion

In a second experiment, a combination of translation and rotation motion was induced to the phantom (motion 2, Figure 3-11) at a rate of **50 bpm**. Imaging parameters were as follows: FOV = 150 x 150 mm^2; Matrix = 448 x 448 px; slice thickness = 3 mm; FA = 15°; TR/TE = 60/6 ms; BW = 250 Hz/px; 6000 projections; 3 segments; Acquisition time = 2 min and same tracking parameters as previously described were set. Resulting voxel size was **0.3 x 0.3 X 3 mm^3**. An image without motion was acquired and reconstructed using the same protocol and served as reference.

Figure 3-26a represents the position over the time along each direction. It can be noticed that the motion induced by the piston rod system is not uniform and generates a position that is more stable (longer stay) at the end of the piston stroke (green frame) than at the start (purple frame). Resulting image with motion is displayed in Figure 3-26b-right. The rotation around Z-axis conducts to the superposition of these two positions (corresponding to purple and green frames) within the image. Of note, this rotation of the phantom around Z-axis results in the apparition of ellipsoid forms in the image, which occurs at the end of the piston stroke (green frame). In this motion state, a bright spot (orange arrow) is depicted and corresponds to the coil sensitivity, which on average is more frequently at this position. Although more stable, we chose to reconstruct the phase corresponding to the start of the piston stroke for more immediate comparison with the reference image. The acceptance radius was kept to 0.5 mm since structures dimension of the phantom are about 0.5 mm at minimum.

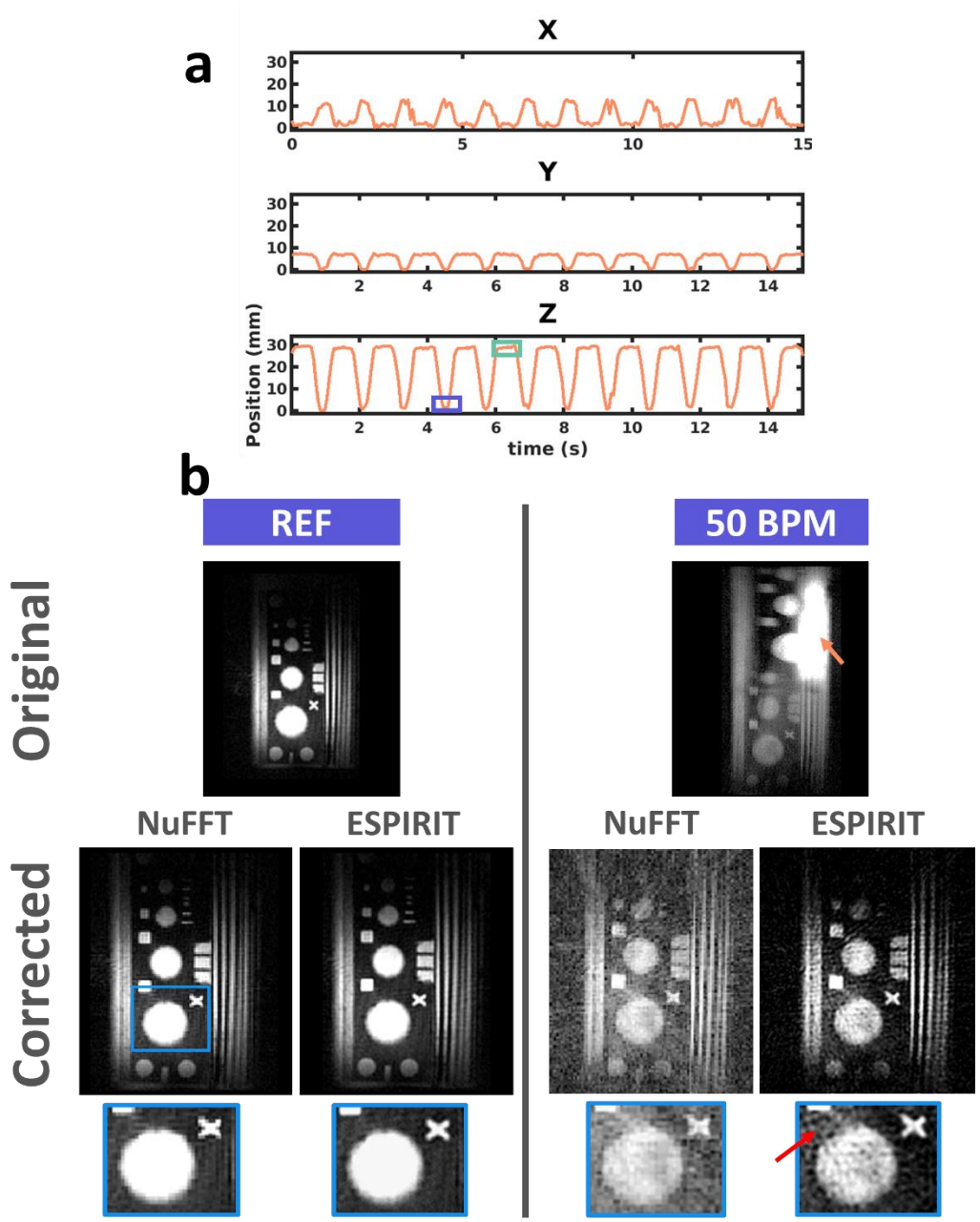

Figure 3-26: Correction of a translational (along Z-axis) and rotational (around Z-axis) motion at 50 bpm. **a)** Plot of the positions over time for each directions (X, Y and Z). Overlaid purple and green frames correspond to the start and the end of the piston stroke respectively. **b) Left-** Reference image (static image) reconstructed with either NuFFT or ESPIRIT with 704 projections (satisfying Nyquist criteria). **Right-** Top image displays the image with motion. Ghosting artifacts is clearly visible (orange arrow). Bottom images show motion-corrected image reconstructed with either NuFFT or ESPIRIT with 183 projections. Motion-corrected image and reference image reconstructed with ESPIRIT demonstrate a residual trail within the image (red arrow) as well as less signal due to undersampling (183 = 26% of the theoretical number of projections). However, it can be noticed that cross sharpness is preserved.

Image obtained after motion correction shows suppression of the ghostings. Adding ESPIRIT to the reconstruction clearly improves the quality by recovering sharpness and contrast of the structures. Although similar to the reference one, the corrected image still exhibits a trail (red arrow). This is due, on the one hand, to the high-undersampling factor (only 183 projections included in the reconstruction with only 58 projections satisfying the Nyquist criterion against 704 required at least) and, on the other hand, because this phase corresponds to an acceleration phase (see section 3.5.4) and not a plateau. Nevertheless, considering the cross in the motion-corrected image, the spatial resolution is preserved and exhibits similar sharpness than the reference one, which highlights the feasibility to freeze the motion while retaining the information on the small structures.

3.7.3. Correction of motions at different frequencies and amplitudes

Efficiency of our algorithm was evaluated for different motion frequencies on a phantom moved translationally along Z. Motion was successively induced at **20 bpm**, **50 bpm** and **90 bpm** with an amplitude of approximately 25 mm, 15 mm and 5 mm for 20bpm, 50bpm and 90 bpm respectively. The 2D-GA acquisition was performed with the following image tracking parameters: FOV = 150 x 150 mm^2; Matrix = 288 x 288 px; slice thickness = 3 mm; FA = 15°; TR/TE = 60/6 ms; BW = 250 Hz/px; 3000 radial views; 3 segments (1000 shots); Acquisition time = 1 min. Tracking acquisition parameters were the same as the one set above. Resulting spatial resolution was 0.5 x 0.5 x 3 mm^3. An image without motion was also acquired to provide a reference. Position of the phantom over the time was retrieved and motion was corrected using the 3D amplitude-based algorithm with an acceptance radius of 0.25 mm. Reconstruction was performed using NuFFT for basic reconstruction and ESPIRIT for image quality improvement. The reference image was reconstructed using the theoretical number of projections required (Matrix size*π/2 = 452).

Images without motion compensation (Figure 3-27b top row) display ghosting and blurring artifacts that are frequency dependent (purple arrows). At slow rate (20 bpm) a duplication effect is observed which is in accordance with the oscillation pattern (green curve) that depicts two motion plateaus, corresponding to two stable phases of motion. At 50 bpm, we observe a trail in the image. At high rate (90 bpm), ghosting and blurring artifacts appear as vibration effect, which is in accordance with the more jerky motion described by the position curve (blue curve) in Figure 3-27a. After data sorting, the number of projections in

each k-space was 291, 306 and 342 for 20 bpm, 50 bpm and 90 bpm cases respectively. Images obtained after reconstruction with ESPIRIT method are displayed in the second row and demonstrate reduction and even suppression (20 bpm and 50 bpm) of ghosting artifacts. Moreover, a marked improvement in sharpness and contrast is observed in the three motion-corrected images. A residual artifact, however, remains in the 90 bpm motion-corrected image (red arrow). This may be explained by the vibrations and jerky motions of the piston that are more complex to compensate at this rate.

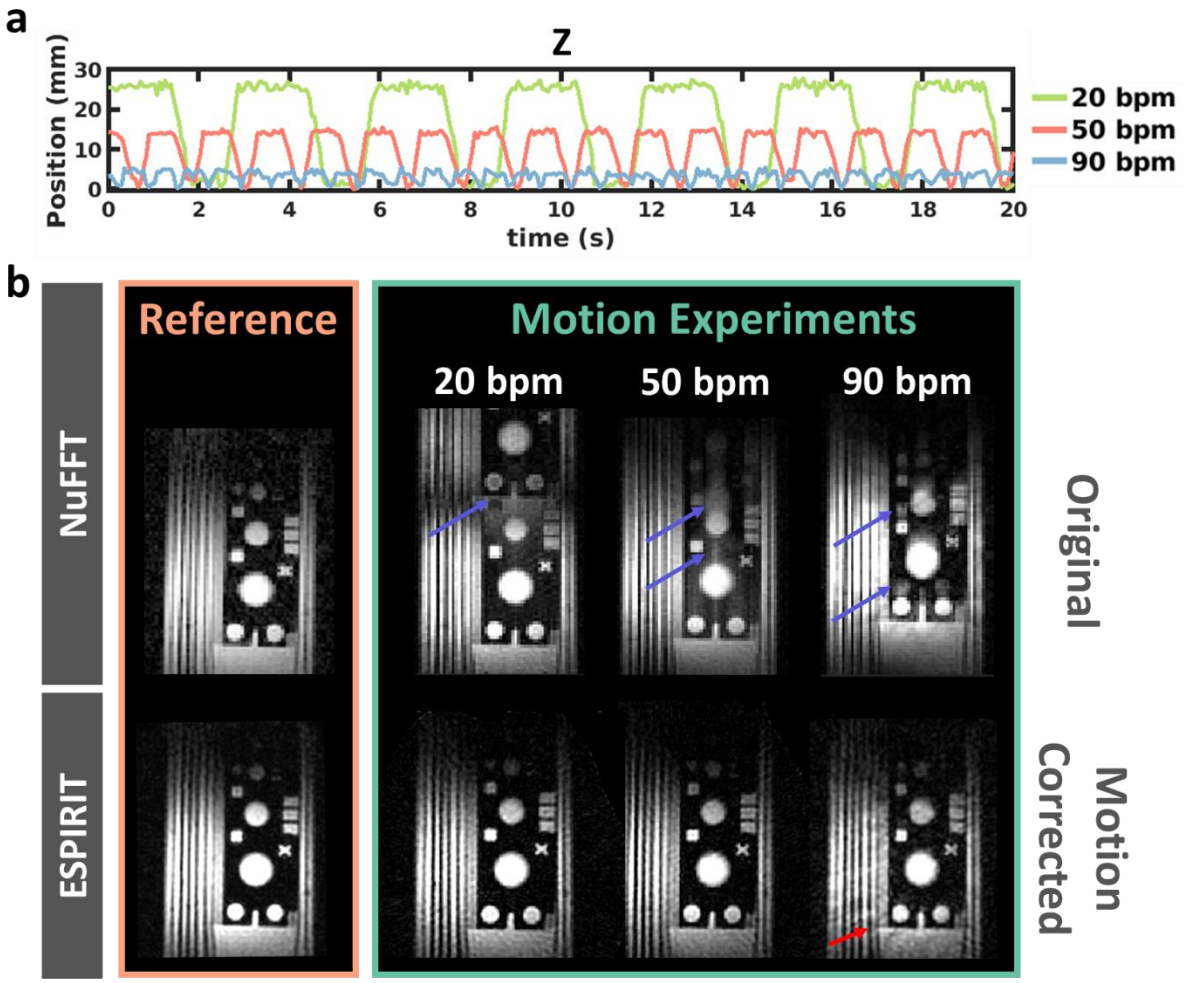

Figure 3-27: Correction of a translational motion along Z at different frequencies and amplitudes. a) Position over the time for a motion at 20 bpm (green), 50 bpm (pink) and 90 bpm (blue). b) **Top row-** Original images. Purple arrows show ghosting and blurring artifacts within images of motion experiments. **Bottom row-** Motion-corrected images reconstructed with ESPIRIT. For comparison purpose, reference images reconstructed wit 452 projections is displayed on the left. Red arrow shows a residual artifact in the motion-corrected image.

For each case, difference maps were computed (Figure 3-28). For that purpose, image before correction was registered and normalized to the reference image before being subtracted to the reference. Same process was performed for the image after correction. These maps demonstrate the marked reduction of motion artifacts in the images after correction. We observe a more important difference after correction for the experiment at 90 bpm than for the experiment at 20 bpm. This is mainly due to the jerky motion that induces vibrations and out of plane motions that are more complicated to compensate. Moreover, the tiny residuals observed in images after correction may also be attributed to small registration errors (especially at the edges) and/or small differences in SNR. These results nonetheless highlight the efficiency of our motion compensation algorithm, associated with the ESPIRIT reconstruction method in recovering an image without (or at least drastically reduced) motion artifacts at a spatial resolution of 500 µm in plane for a wide range of motion frequencies.

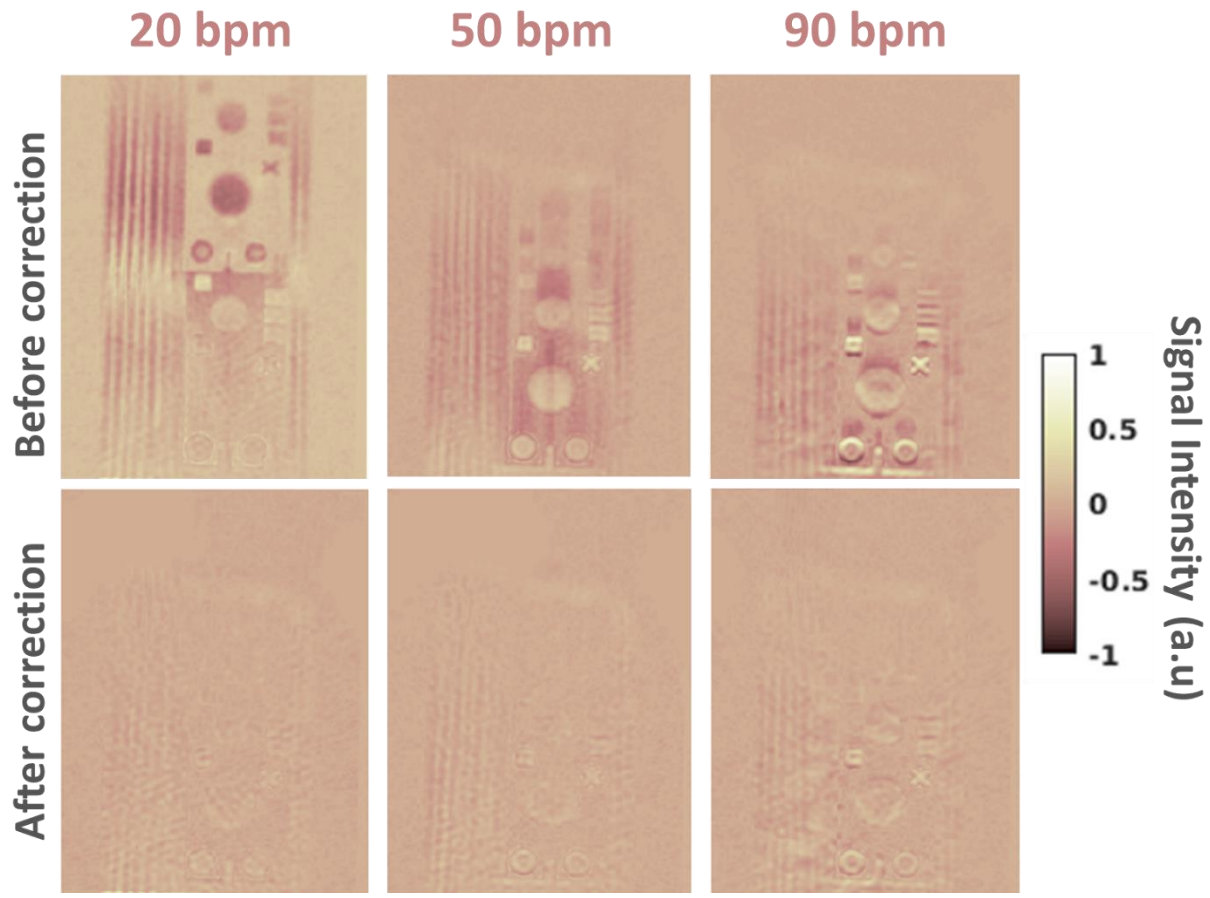

Figure 3-28: Difference maps. **Top row-** difference between motion images at 20 bpm, 50 bpm and 90 bpm and reference image. **Bottom row-** difference between motion-corrected images and reference image.

3.7.4. Maximum acceleration factor allowing maintaining the desired image quality: analysis on moving phantom experiments.

After having demonstrated the effectiveness of our algorithm at correcting different motion trajectories in a frequency range from 20 to 90 bpm, we evaluated how restrictive we could be in the motion acceptance (how small the AR could be) and therefore how much could the maximum acceleration factor be in order to maintain an acceptable image quality. **Data set was the same as the one acquired in section 3.7.2.2** with a translational and rotational motion at 50 bpm. Nyquist provides quantitative upper-bounds on the number of measurements necessary for optimal reconstruction, however, in practice, as already illustrated in section 3.7.1, theses bounds are not clearly defined and can be lowered. Moreover, these bounds are established for images without motion. In our case, due to data binning, the radial profiles in each bin will not be equally spaced by the golden angle as they depend on the motion cycle. Thus, a quasi-uniform k-space distribution is not guarantee for any bin and the number of radial profiles may no more comply with Nyquist.

In this section, we therefore evaluate the degree of undersampling that can be perform and attempt to establish lower bounds as a function of the image size and the total acquired projections using the proposed density sampling representation described in section 3.5.4.

For that purpose, we iteratively decreased the acceptance radius (AR) set in the amplitude-based algorithm (3D-extended) and reconstructed the resulting binned data with NuFFT and ESPIRIT methods. Associated k-space and density sampling (histogram) were plotted for each case, together with the motion trajectory indicating in orange the accepted data and the center of the motion acceptance sphere (purple cross). Percentage of the radial lines included in the final reconstruction relative to the theoretical requested number (in this experiment, a theoretical number of 702 projections) are displayed in the purple frame and percentage of these projections complying with the Nyquist angular criteria are displayed in the pink frame for each case. Results are displayed in Figure 3-29.

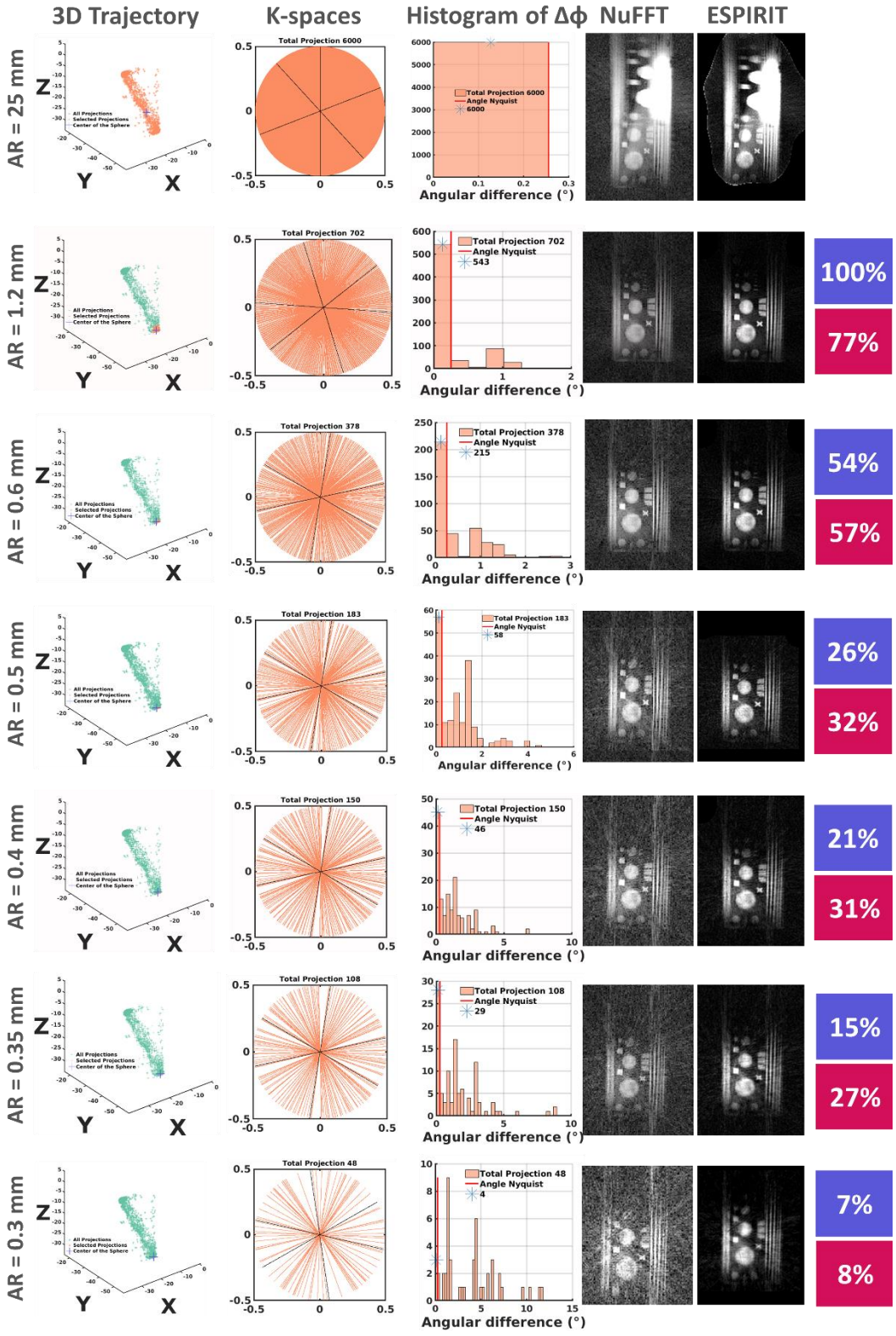

Figure 3-29: Evaluation of the maximum allowed undersampling factor on a moving phantom. Purple frames indicate percentage of projections relative to the theoretical number provides by Nyquist while pink frames indicate the percentage of the projections complying with Nyquist angular criterion (inform about the coverage of the k-space).

The first reconstruction uses all the data (6000 projections) and resulting image evidences the motion artifact. As the bin window size (AR) decreases, gaps in the k-spaces increases with larger angular intervals. This is confirmed by the histograms analysis. Indeed, the largest angular difference goes from approximately 1° to 12° for 100% and 7% of the theoretical requested data respectively. These gaps in k-space yield in the apparition of streaking artifacts in the resulting image, which become more pronounced and coarse as the undersampling increases. However, as illustrated in Figure 3-30, using ESPIRIT yields a certain recovery of missing k-space information up to an acceleration factor of 5 (21% of the requested data and only 31% of them fulfilling Nyquist angular criterion) and allows maintaining the targeted image quality (sharpness and resolving power) **until an acceleration factor of 4** (26% of the requested data with only 32% of them satisfying Nyquist angular criterion).

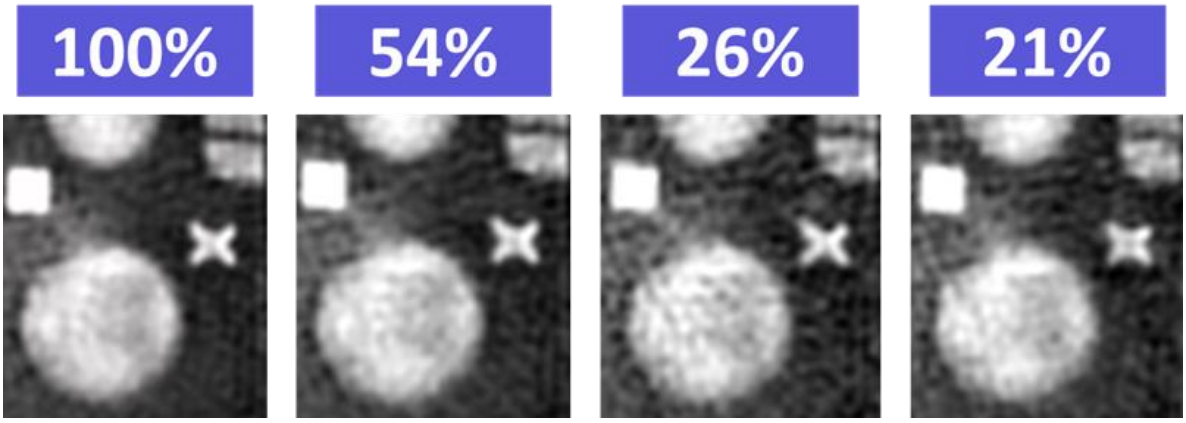

Figure 3-30: Zoomed-views of motion-corrected phantom images reconstructed with ESPIRIT with different acceleration factors (1, 2, 4 and 5).

In this experiment, we therefore demonstrated efficiency of our method in compensating motion within an acceptance window of 0.8 mm - 1 mm (AR between 0.4 mm and 0.5 mm) and recovering the desired image quality with **only 26% of the theoretical required data** and only 32% of them complying with Nyquist angular criterion

3.7.5. Conclusion

In this section, we demonstrated the tremendous potential of our processing, combining with ESPIRIT reconstruction method to provide highly resolved, motion-free images. We especially emphasized the ability of our technique at correcting motion of different types from most simple (translational motion only) to most sophisticated (translational and rotational motion) trajectories within a wide frequency range. In addition, we exhibited the feasibility to recover an image with 300 µm in-plane resolution, devoid of any motion artifact from a high-undersampled k-space using our local coil only, demonstrating thus efficiency of ESPIRIT with only one coil and meeting the requirements set for later in vivo applications.

3.8. Application to in vivo

In this section, we tested efficiency of our method at retrospectively compensating for cardiac motion after the imaging process to deliver non-blurred cardiac images. In this section, conventional chest coils were used as a receiver.

3.8.1. Experimental setup

Animal preparation

Cardiac Magnetic Resonance guided catheterization was performed in 3 sheep (50 ± 4 kg). The protocol was approved by the local Animal Research Ethics Committee according to the European rules for animal experimentation. After premedication of pigs with ketamine (20 $mg.kg^{-1}$) and acepromazine (1 $mg.kg^{-1}$) by an intramuscular injection, the induction of anesthesia was realized with intravenous bolus of ketamine (15 $mg.kg^{-1}$) and midazolam (1.5 $mg.kg^{-1}$). This step was followed by intubation, ventilation and shaving of the thoraco-abdominal region. An MR-compatible catheter (see section 3.1.1) was inserted through the femoral vein and maneuvered by an experimented operator into the epicardial space using X-ray angiography system. After positioning the catheter, the animals were moved to the MR room and installed in a supine position in the MR scanner. The animal was assisted for ventilation using a MR-compatible ventilator (Aestivia, General Electric, Fairfield, CT, U.S.A.) with a respiratory rate of 12-15 breaths per minute (bpm). Conventional surface ECG electrodes and respiratory bellow were used to respectively record cardiac rhythm and respiratory signal of the animals.

Imaging Protocol

The entire interventions were performed within a 1.5 T scanner (MAGNETOM Aera, Siemens Healthcare, Erlangen, Germany). MR data were acquired using two 18-element antennas (Body-18, Siemens, Erlangen) positioned anterior and posterior around the chest of the animal. Pre-procedure scans included an interactive sequence made of a b-SSFP pulse sequence (TE/TR = 1.93/183 ms, resolution = 1.8 x 1.8 x 4 mm^3, Field of view (FOV) = 300 x 300 mm^2, FA = 45°) interleaved with the catheter tracking module (BEAT IRTTT: Interactive Real Time Tip Tracking, Siemens Healthcare, Erlangen, Germany). This sequence was used to navigate the catheter until the left or right (depending on the experiments) ventricle (Figure 3-31a). Following the catheter navigation, a 3D b-SSFP image was acquired and served to generate an anatomical roadmap, as illustrated by the Figure 3-31b.

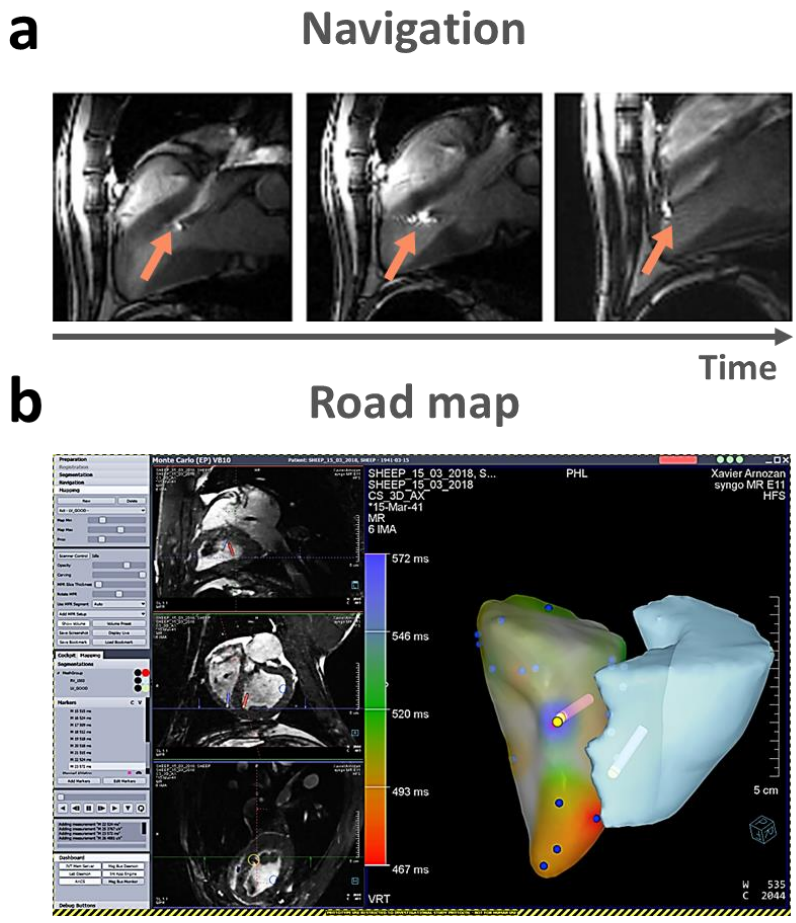

Figure 3-31: Pre-procedure scans. a) An interactive sequence made of a b-SSFP pulse sequence is used to navigate the catheter until the heart cavity. b) A 3D b-SSFP is then acquired and serve as an anatomical roadmap. From this 3D image, a whole heart shell is generated by segmenting it with a dedicated segmenting software.

The 3D whole heart shell was obtained with a manual segmentation performed using MUSIC software (multimodality software for specific imaging in cardiology, L'Institut de Rythmologie et de Modélisation Cardiaque, University of Bordeaux, Institut National de Recherche en Informatique et Automatique Sophia Antipolis, Sophia Antipolis, France) [38].

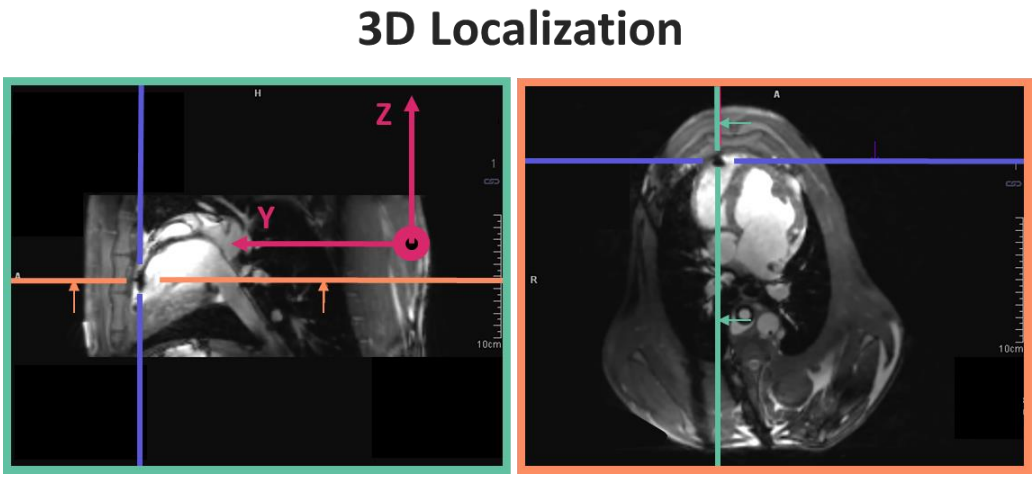

Figure 3-32: 3D b-SSFP acquired in vivo on a sheep. The sagittal (left) and transversal (right) views evidence the catheter at the apex of the right ventricle. The latter allows identification of the catheter position and placement of the slices for the 2D-GA acquisition.

Figure 3-32 displays one of the 3D b-SSFP image acquired on a sheep and used to position the 2D GA slice. In the following experiments, imaging parameters varied from one to anther acquisition and are therefore given separately. Tracking parameters were kept unchanged between the experiments and were as follows: FOV = 450 mm; 512 data points; FA = 3°; background suppression = 6 $mT.m^{-1}$; bandwidth = 152 Hz/px; TR/TE = 4.8/2.8 ms and a duration of 24.47 ms.

3.8.2. Comparison between retrospective gating using external sensors or micro-coils signals

In this study, we compared the cardiac phases obtained after a retrospective sorting using either external sensors signals or micro-coil signals. Experiment was conducted on a sheep (48 kg), named **animal experiment #1**. The 2D-GA was acquired with the following

parameters: FOV = 200 x 200 mm^2; Matrix = 128 x 128 px; TR/TE = 70/4 ms; FA = 65°; bandwidth = 250 Hz/Px; slice thickness = 4mm; Radial views = 12000; 3 segments. Total acquisition time was 4 min 36 s. Resulting spatial resolution was therefore 1.6 x 1.6 x 4 mm^3. The catheter was inserted into the right ventricle for pacing while another was inserted into the left ventricle for micro-coils recording. Simultaneously, physiological signals were recorded using ECG leads fixed on the chest of the animal and a respiratory bellow placed around the diaphragm of the animal. The heart rhythm was 96 bpm and the respiratory rate was 12 cycles/min. The micro-coil signals were processed as described in section 3.5.3. Given the extracted cardiac and respiratory signals, it was possible to sort the data into both cardiac and respiratory motion-resolved states. Specifically, the series of 2D radial lines was first binned into different cardiac phases with a desired temporal resolution using the cardiac motion signal, and each cardiac phase was further sorted into multiple respiratory phases spanning from end-expiration to end inspiration using the respiratory motion signal. Practically, the number of desired cardiac phases was selected and gave the resulting temporal resolution. In this experiment, the series of continuously acquired 2D radial lines was first sorted into 8 cardiac phases, generating an image series with temporal resolution of approximately 60 ms. In the next step, each cardiac phase was further sorted into three respiratory motion phases, thus generating a 4D dataset with a matrix size of 128 x 128 x 8 x 3. Although the conventional number of cardiac phases in clinic is ~ 20 [12], we considered in the scope of this study that 8 phases were sufficient to compare the two methods, the intend here being not to provide cine images.

The sorted 4D images were reconstructed using ESPIRIT method. Same process was applied this time using the physiological signals recorded by the conventional sensors (ECG leads and respiratory bellow, corresponding to the green curve) at the input of the sorting algorithm. Example of this data sorting process is illustrated in Figure 3-33a for the cardiac and respiratory signals extracted from the micro-coil recordings. The red cross indicates the start of the cardiac cycle. Each colored-point represents a selected cardiac phase within the cycle. The respiratory signal is segmented into three phases spanning from end-expiration to end-inspiration with the first phase corresponding to the end-expiration. Images resulting from the physiological sorting (green framed) and the micro-coils based sorting (orange framed) are compared in Figure 3-33b for a fixed respiratory phase (first phase) and all the cardiac phases.

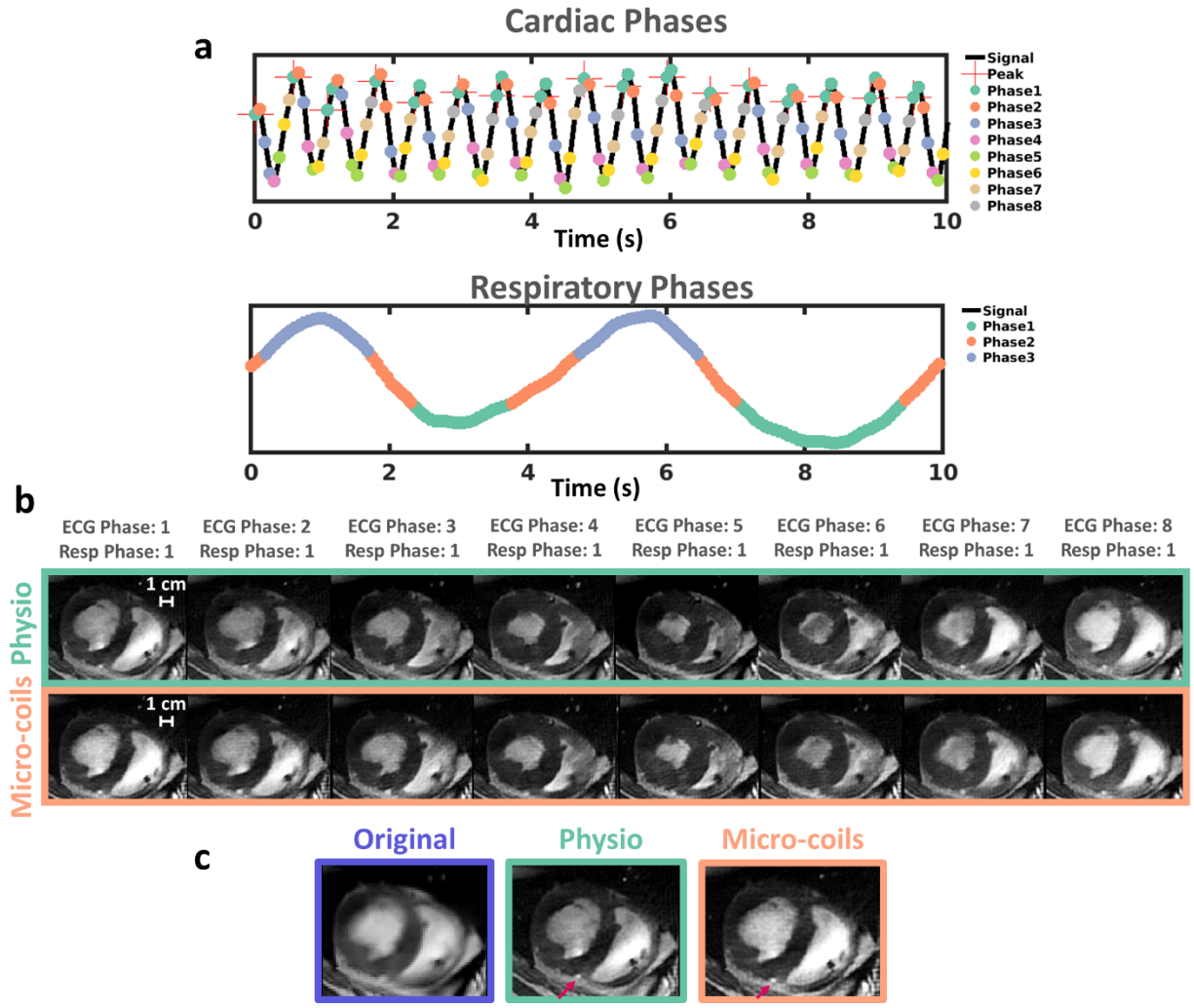

Figure 3-33: Comparison of cardiac phases obtained after retrospective sorting using either external sensors (ECG electrodes – "Physio") or micro-coil signal. a) Cardiac and respiratory signals extracted from the micro-coil recordings. b) Eight cardiac phases were retrospectively reconstructed using either the "Physio" method (relying on external sensors) or micro-coils method. c) Comparison between original image (with motion), motion-corrected image (Cardiac Phase #1, Respiratory Phase #1) using external sensors and motion-corrected image (Cardiac Phase #1, Respiratory Phase #1) using micro-coils. Pink arrows show a coronary vessels.

Similar cardiac phases were obtained between both methods. The difference between the systolic and the diastolic phases of the cardiac cycle can be visually appreciated in the size of the left ventricle blood pool and myocardium. Using this data sorting process, we were able to provide cardiac and respiratory motion-corrected images as shown in Figure 3-33c. Due to the intrinsic robustness of the radial acquisition original image does not present

strong motion artifacts but evidence blurring and the myocardium wall is not clearly delineated. Conversely, sorting the data yields to a marked improvement in the left ventricle wall sharpness as well as a drastic reduction of blur regions. Coronary vessel that was within the blurred region on the original image is revealed (pink arrow). We observed an equivalent image quality between external sensor-based sorting and micro-coils-based sorting. Hence, this result emphasizes the synchronicity of catheter motion with the beating heart and demonstrates the ability of our method to recover cardiac phases as effectively as the retrospective conventional method does.

3.8.3. Validation of the method in a second animal

We further tested the efficiency of the aforementioned method in **a second animal experiment (#2)**. Acquisition was performed with the following parameters: FOV = 200 x 200 mm^2; Matrix = 208 x 208 px; TR/TE = 60/5 ms; FA = 60°; bandwidth = 250 Hz/Px; slice thickness = 3 mm; Radial views = 12000; 3 segments. Total acquisition time was 4 min 36 s. Resulting spatial resolution was 1 x 1 x 3 mm^3. The catheter was inserted into the right ventricle. The heart rhythm recorded by the ECG leads was 95 bpm and the respiratory rate recorded by the respiratory bellow was 12 cycles/ min. The cardiac motion signal and the respiratory motion signal were extracted from the micro coils recordings and the acquired k-space was sorted into a 4D dataset (k_x-k_y-cardiac phase-respiratory phase) following the same procedure as in 3.8.2. It was possible to bin the data into 11 cardiac phases and 5 respiratory phases. Sorted k-space were then reconstructed using ESPIRIT. Figure displays the images corresponding to each couple of (ecg/resp motion state) obtained after the data sorting procedure.

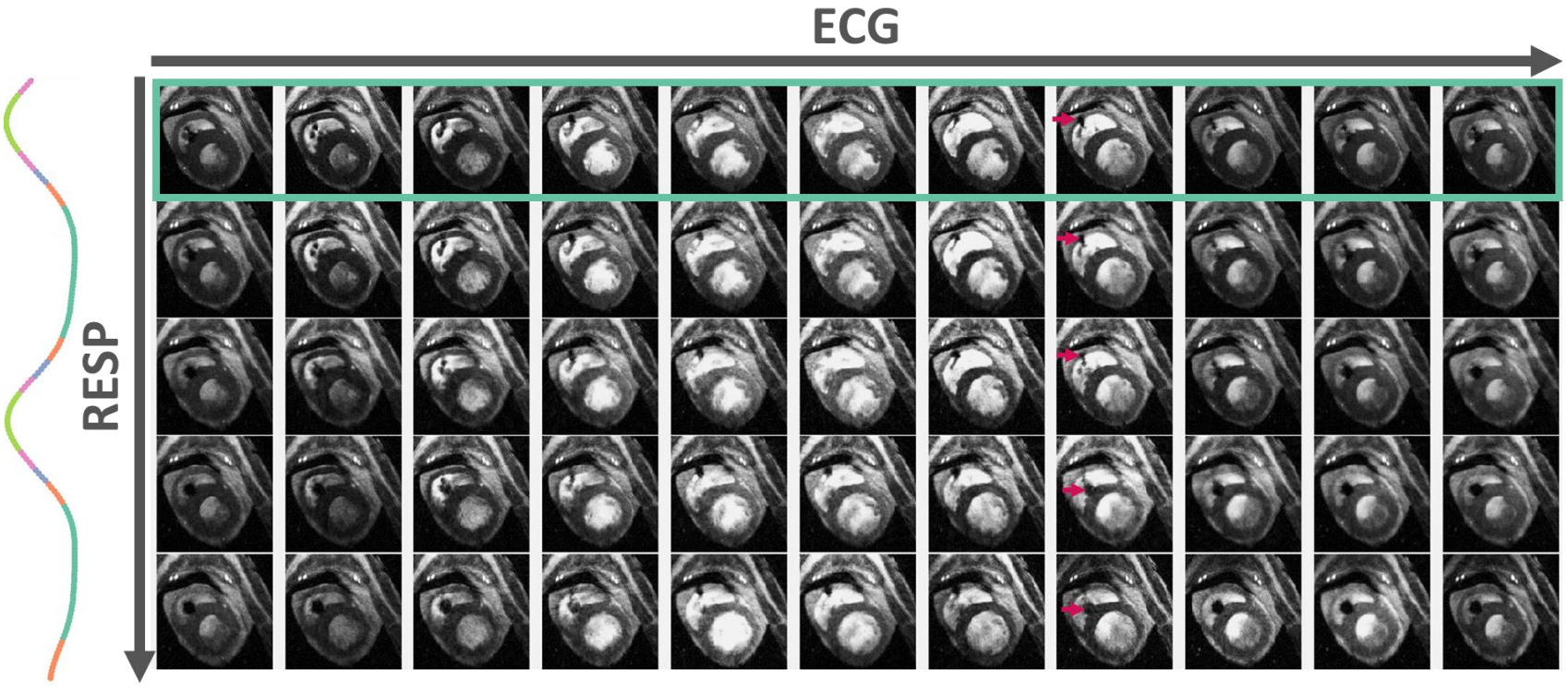

Figure 3-34: Reconstructed cardiac and respiratory phases. The cardiac motion signal and the respiratory motion signal were extracted from the micro coils recordings and the acquired k-space was sorted into 11 cardiac phases and 5 respiratory phases. Sorted k-space were then reconstructed using ESPIRIT. Spatial resolution is 1 x 1 x 3 mm3. Pink arrows help visualize the catheter displacement over the respiratory phases.

Difference between systolic and diastolic phases of the cardiac cycle can be visually appreciated in the size of the left ventricle blood pool and myocardium. The first respiratory phase, corresponding to end-inspiration, shows better image quality with a sharp and well-defined margin of the papillary muscles (cardiac phase #7) together with a good delineation of the myocardial wall. This is because this phase is the most stable (see the respiratory motion signal, left), collecting more radial views without important motion acceleration. Pink arrows help visualize the catheter displacement within the right ventricle cavity over the respiratory phases.

3.8.4. Maximum acceleration factor allowed in vivo imaging

As in phantom experiment (section 3.7.4), we further investigated the maximum acceleration factor allowed. Experience was conducted on the same dataset as in the previous section, namely **animal experiment #2**.

Motion was resolved using the 3D amplitude-based algorithm (section 3.5.1). The acceptance radius (AR) was iteratively decreases from 2 mm to 0.3 mm. Images were reconstructed with ESPIRIT. For each case, k-spaces and density sampling are displayed, together with the 3D trajectory of the heart motion depicting in orange the accepted positions. For each case, percentage of the selected projections relative to the theoretical requested number (here 327) is displayed in the purple frame and percentage of these projections satisfying Nyquist angular criterion are displayed in the pink frame. The red line in the histogram indicates the angle value complying with Nyquist angular criterion (here 0.55°) and the blue cross indicate the number of projections among the selected projections that respect this angular shift. The results are displayed in Figure 3-35.

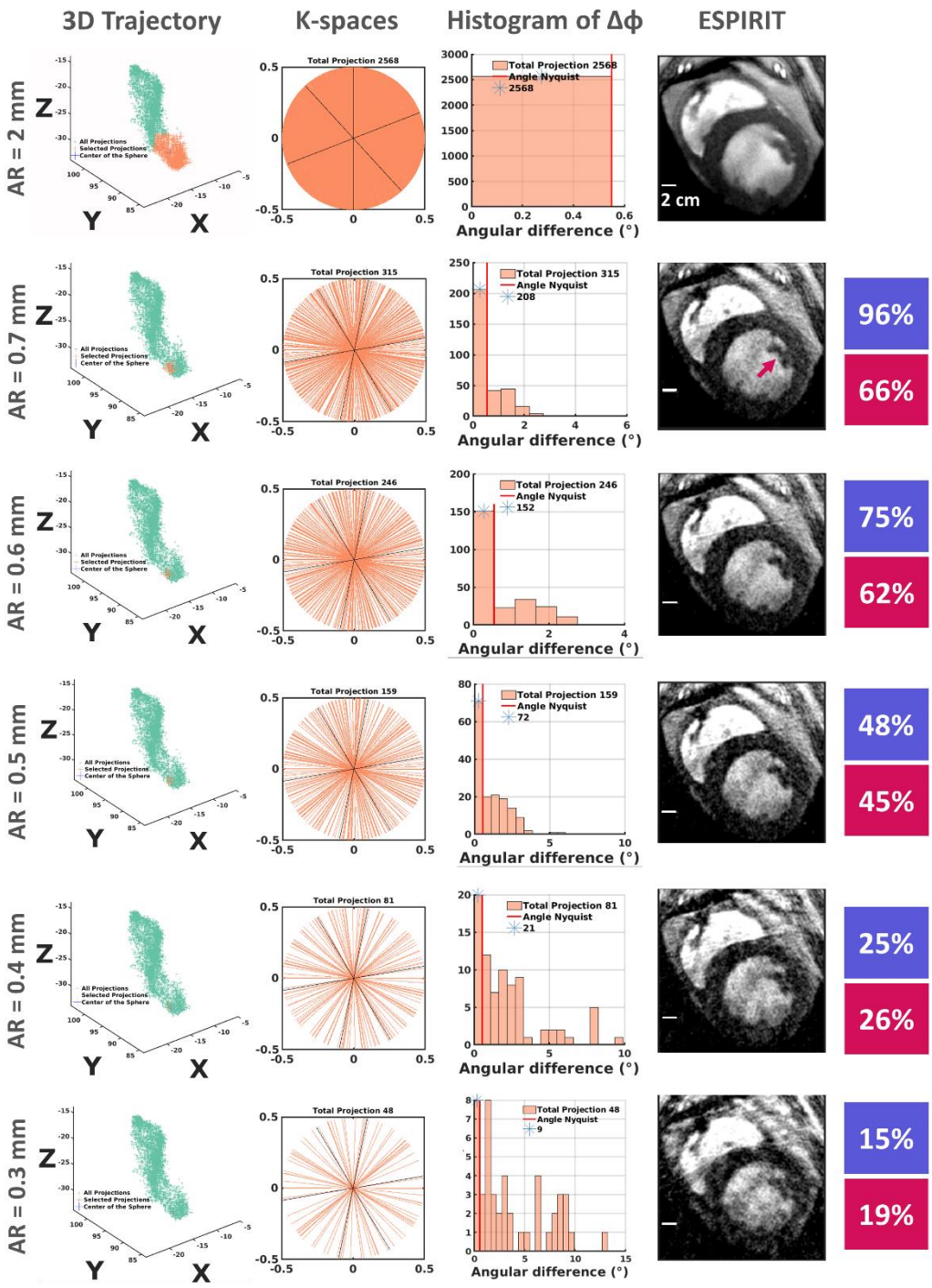

Figure 3-35: Evaluation of the maximum allowed acceleration factor in vivo. Purple frames indicate the percentage of projections relative to the theoretical number and pink frames indicate the percentage of projections. Pink arrow shows a papillary muscle.

The first reconstruction is voluntarily performed with a large AR (2 mm) to demonstrate effect of motion within the image. As the AR decreases, gaps in k-spaces occur and angular intervals between projections increase from approximately 2° to 12 ° between k-spaces with 96% and 15% of the required data. These gaps in k-spaces translate into streaking artifacts and signal loss, which appears as pepper and salt noise within the reconstructed images. ESPIRIT allows an acceleration factor of 2 (48% of the required data) while maintaining the targeted image quality (depiction of the papillary muscle, pink arrow). A degradation of the image quality is observed beyond an acceleration factor of 2 (< 48% of the required data). This poor image quality can be anticipated by analysis of the density sampling histogram. Indeed, the later demonstrates large angular intervals (until approximately 8° compared to the requested angular interval of 0.55°), which creates large gaps in k-space.

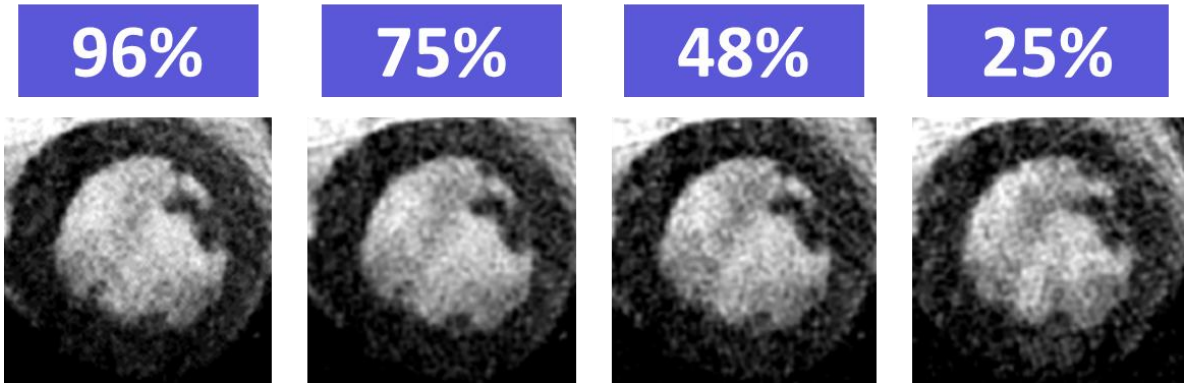

Figure 3-36: Zoomed-views of the left ventricle. Image is reconstructed with ESPIRIT with different acceleration factors (1, 1.3, 2, 4). Spatial resolution is 1 x 1 x 3 mm^3.

Figure 3-36 displays a cropped view of the left ventricle to make the comparison more easily between the different undersampling images. No significant difference in image quality is observed between the image reconstructed with 100% of the theoretical requested data and the image reconstructed with only 48% of the data. Although sharpness is lower and streaking artifacts are more present within the image reconstructed with only 25% of the data, it is possible to depict the papillary muscle. Hence, an acceleration factor of 3 could be considered as a compromise between a short acquisition time and the maintenance of the image quality.

Compared to phantom acquisition where an acceleration factor of 4 could be achieved, in this in vivo experiment, the percentage of projections complying with Nyquist angular criterion is smaller (26% versus 32%) for 25% of the requested data selected. This may explain the difference in image quality. Difference can also arise from the coils used in vivo, which are not the same as the one used in phantom experiment. In vivo, the coil arrays were placed far from the heart in opposite to phantom experiment were a local loop coil was directly in contact with the object to be imaged and coil moved together with phantom. As ESPIRIT relies on coil sensitivity, a change in coil interferes directly with the final image quality. Moreover, as mentioned in section 3.5.4, the available SNR also plays a key role in maximal allowed acceleration factor and resulting image quality.

3.9. Image Improvement using different iterative reconstructions

3.9.1. Comparison of different methods

In this section, we handle the issue of reconstructing high-resolution images (we remind the reader that final objective is a submillimeter spatial resolution) from undersampled k-spaces while simultaneously take into account the acquisition speed (maximal allowed acceleration factor). The dataset from **animal experiment #2** (short axis view) was used and this time binned with **the time-based algorithm** (3.5.3). From sections (0) we demonstrated that at least an acceleration factor of 2 could be performed while maintaining the targeted image quality using ESPIRIT algorithm. Of the 12,000 projections initially acquired, only 4,200 were kept before binning to enforce the subsampling of the sorted data. 11 cardiac phases and 5 respiratory phases were provided by the data sorting procedure. Only the first respiratory phase (end-expiration) was retained as it was the more stable one. Density sampling was plotted using histogram to provide statistics upon the number of projections contained in each sorted k-space together with the number of projections complying with the Nyquist angular criterion. Images were reconstructed using NuFFT, ESPIRIT, Compressed Sensing (CS), total variation (TV) regularization added to CS in the cardiac-phase dimension and Patch-based (PB) algorithms (Figure 3-37a).

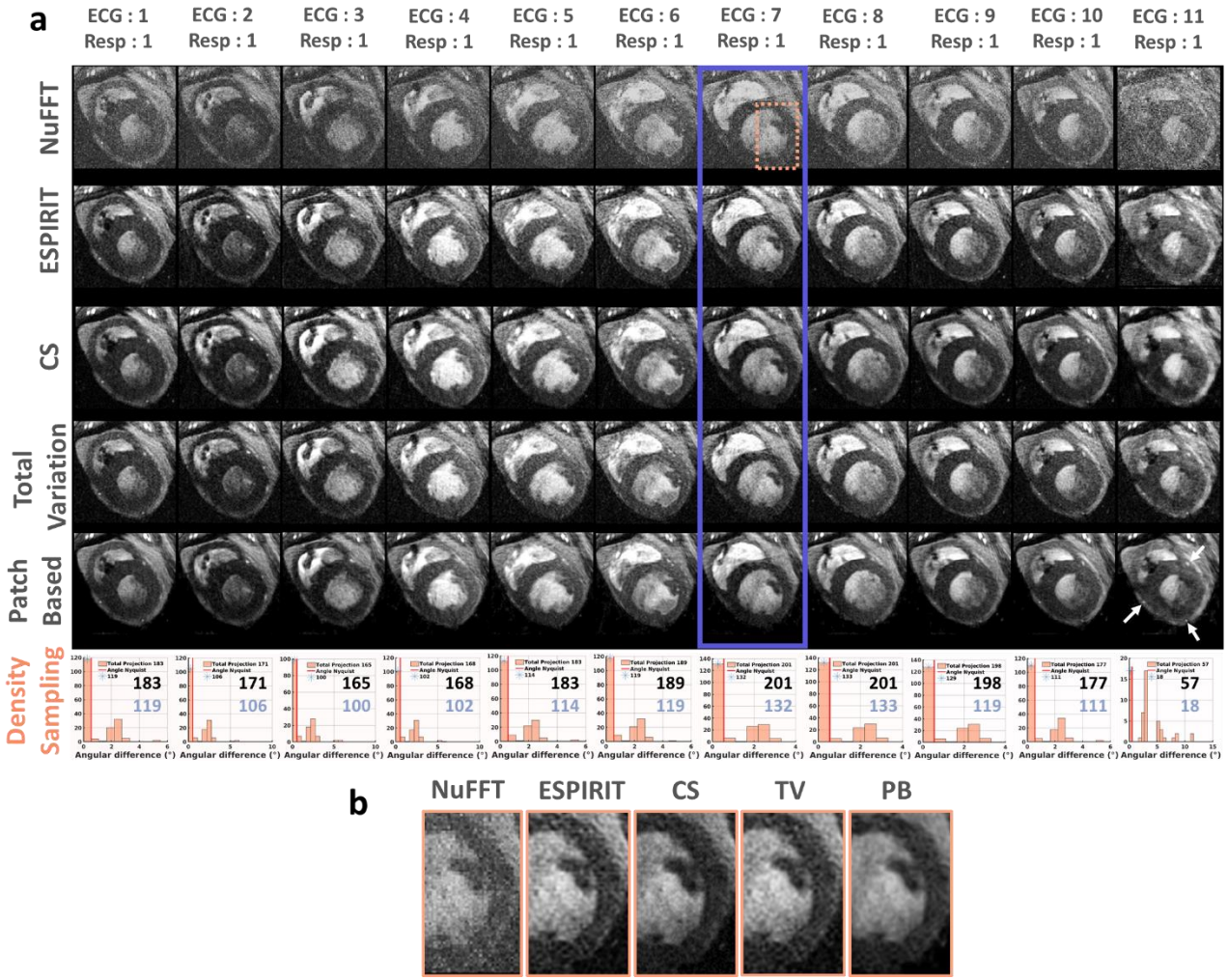

Figure 3-37: Comparison of different reconstruction methods on a same dataset (#2). a) 4,200 projections were initially acquired and binned into 11 cardiac phases and 5 respiratory phases. The eleven cardiac phases of the first respiratory phase were reconstructed successively with NuFFT, ESPIRIT, CS, TV and Patch-based methods. White arrows show coronary vessels. The density sampling of each cardiac phase's k-spaces is shown with the number of projections selected after sorting (black) and the number of projections complying with Nyquist angular criterion (blue). b) Zoomed-view of the left ventricle wall.

From the density sampling histogram, we observe that in average, 170 projections were grouped in each sorted k-space (acceleration factor of 2) with a maximal number of 201(corresponding to 61% of the theoretical required data, for phases 7 and 8) and a minimal number of 57 (corresponding to 17% of the theoretical required data, phase 11). In each sorted k-space, approximately 60 to 66% of the projections complied with Nyquist angular criterion (except for cardiac phase #11 where only 30% satisfied it). Images reconstructed with NuFFT display non-uniform image quality, which is directly related to the density sampling of the corresponding k-spaces. For example, cardiac phase (ECG phase in figure) number #7 displays a satisfactory image quality with a clear delineation of the myocardium wall and depiction of the papillary muscle. In opposite, phase #11 (worst-case with only 57 radial views) displays a poor image quality with coarse striking, due to a higher undersampling (hence larger values of angular intervals).

As already evidenced, using ESPIRIT yields to higher image quality with a marked reduction of the pepper and salt noise present in NuFFT reconstruction. Furthermore, ESPIRIT partially helps recover missing-information of the phase #11 and blood vessels are rendered more visible. Using CS helps remove some streaking and globally renders the images smoother than in ESPIRIT. Contrast within images is also slightly improved. Tiny difference is observed between TV and CS although TV seems to sharpen edges and improves the delineation of small blood vessels (see phase #11). Adding Patch-based to the TV reconstruction smoothen the images and denoises them, especially ventricle walls appear with a more uniform intensity. However, we do not notice a significant difference for image analysis between CS, TV and Patch-based reconstructions.

We nevertheless demonstrated through this example the potential of these iterative reconstructions in recovering information of highly undersampled data. Considering phase #11, employing such an iterative method allows depiction of blood vessels (coronary vessels) within the left ventricle, which could not have been revealed without (white arrows). We have introduced here multiple iterative reconstruction methods that give us a flexibility, which with we can play in order to improve image quality.

3.9.2. Motion-corrected cardiac images: results in two animals

In this section, the effectiveness of our method to compensate for the motion was tested in three different animals. Motion was compensated using the algorithm relying on cardiac and respiratory signal extraction. **#2** corresponds to the animal experiments #2 earlier detailed. In this experiment, two acquisitions were performed: one in short axis and a second in sagittal orientation. Of the 12,000 projections acquired, only 4,200 projections and 6,000 were considered before sorting the data for short axis and sagittal orientation acquisition respectively. Data were binned into 11 cardiac phases and 5 respiratory phases. Displayed images in Figure 3-38 correspond to the 1st respiratory phase, 7th cardiac phase for short axis / 1st respiratory phase, 1st cardiac phase for sagittal orientation.

#3 was performed in sheep with the following parameters: FOV = 300 x 300 mm^2; Matrix = 352 x 352 px; TR/TE = 70/7.5 ms; FA = 65°; bandwidth = 250 Hz/Px; slice thickness = 3 mm; Radial views = 12,000; 3 segments. Total acquisition time was 4 min 36 s. Resulting spatial resolution was **0.8 x 0.8 x 3 mm^3**. The heart rhythm was 60 bpm and the respiratory rate was 10 cycles/min. A catheter was inserted into the right ventricle and a second catheter, inserted in the left ventricle served for micro-coils recording. Data were binned into 15 cardiac phases and 4 respiratory phases. The 1st respiratory phase and the 6th cardiac phase image is displayed

For each experiment, images after data sorting procedure were reconstructed with TV applied along the cardiac dimension. Figure 3-38 displays the resulting original images reconstructed using NuFFT together with the motion-resolved images reconstructed using TV.

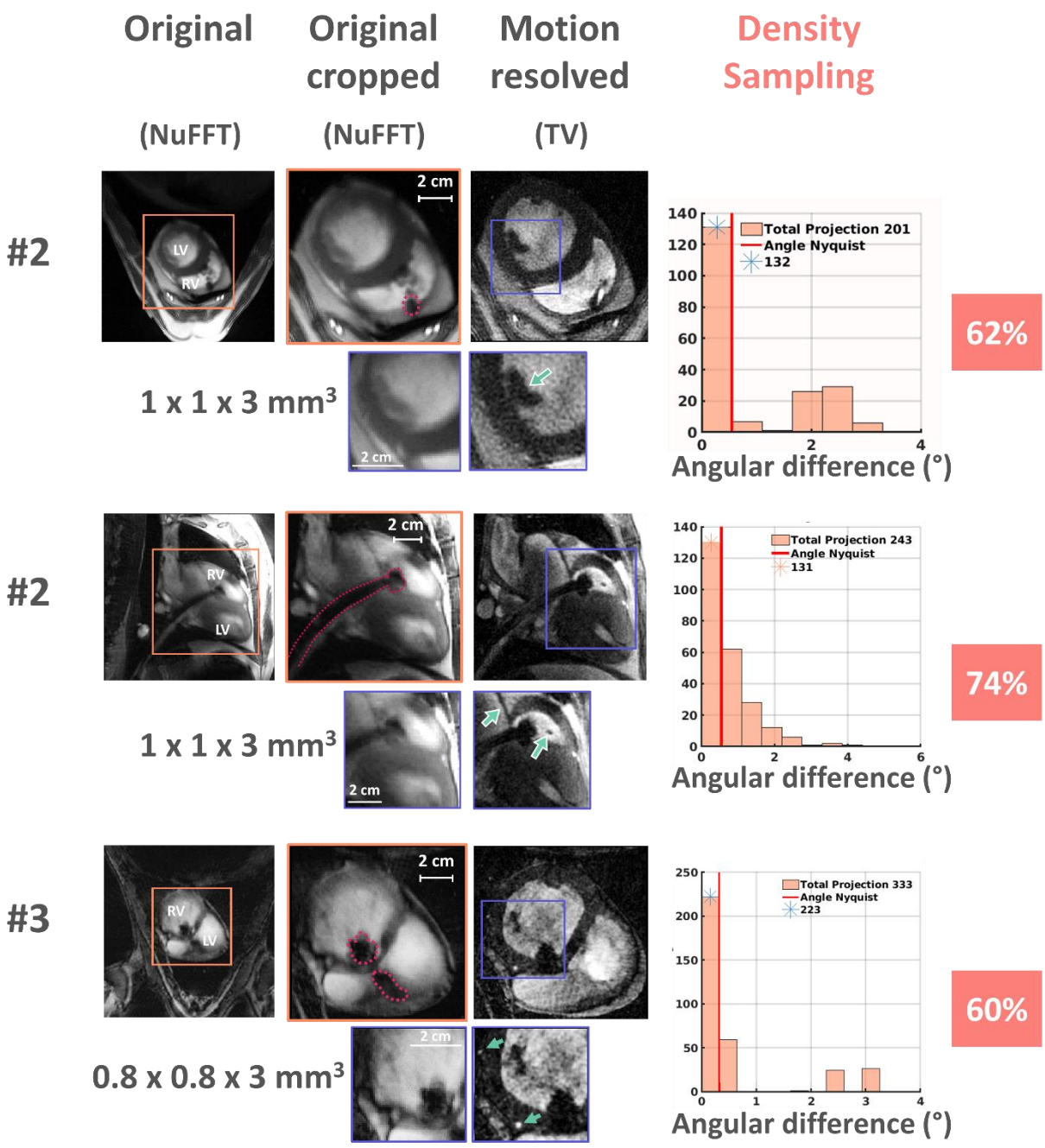

Figure 3-38: Motion-corrected images from two in vivo experiments. **Left-** Original images with motion. **Middle-** cropped view of the heart with motion. The pink dotted line indicate the catheter. **Right-** Motion-corrected images. Purple frames are zoomed-views of both the motion and the motion-corrected images for each case. Green arrows depict anatomic details (papillary muscle, wall, blood vessels). Associated k-spaces density sampling are displayed with the percentage of projections (pink frames).

Anatomical view displayed in the left image corresponds to the original image (without motion compensation). A cropped view focusing on the two ventricles (RV and LV) is displayed in the middle and framed in orange. Catheters position within the ventricles are surrounded by a pink dotted line. The images on the right correspond to the motion-resolved images obtained after data sorting and TV reconstruction. Cropped view of the motion-resolved images is given below and framed in purple. For comparison purpose, the same crop is applied to the original image and also framed in violet. The blue arrows point small structures within the motion-resolved images (vessels and anatomical structures such as papillary muscle). Density sampling is provided for each image and indicates the percentage of selected projections relative to the theoretical number (pink frame). Over the three cases, between 60% to 74% of the theoretical data were included in the final reconstruction after the data sorting procedure. The percentage of inclusion depends on the selectivity of the sorting algorithm (number of cardiac and respiratory phases). An example of how a higher acceleration factor for #2 in sagittal orientation is given in Figure 3-39.

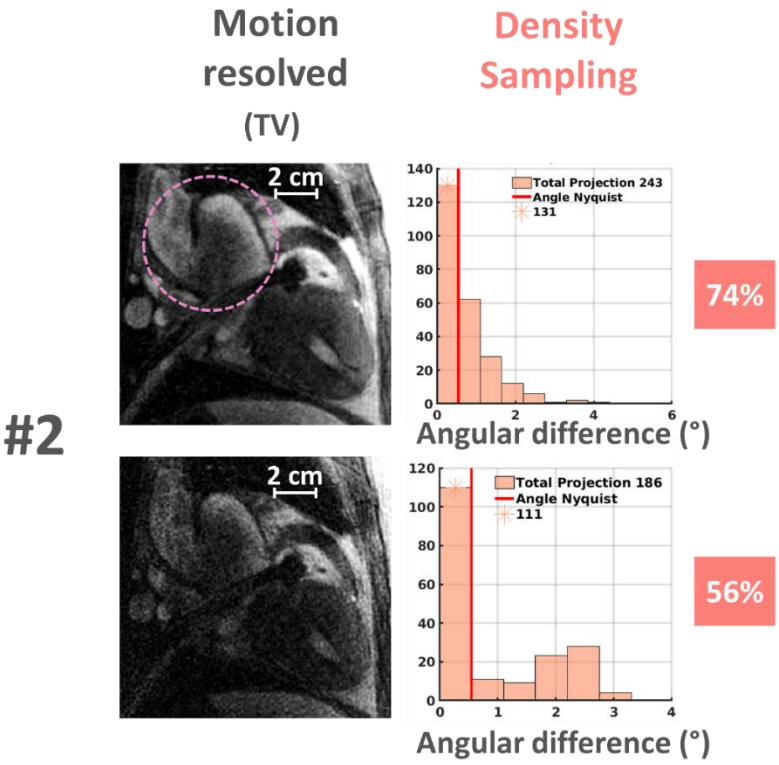

Figure 3-39: Influence of the undersampling degree on the resulting image quality. A loss in SNR is observed in the pink ROI. However, right ventricle wall together with the blood vessel at the apex are is still clearly delineated.

In this experiment, we demonstrated that an acceleration factor of ~2 (56% of the theoretical required data) was feasible but at the price of the SNR and yields to more noisy images (pink ROI). For these reasons, we kept the percentage of accepted data between 60% to 74% in Figure 3-38.

Results from sections 3.8.4 and 3.9 clearly emphasize the ability of our method to provide motion-resolved images with a marked improvement in both sharpness and contrast. Using TV reconstruction, resolution power is enhanced and depiction of small anatomical features (vessels, papillary muscles) is possible. The maximal allowed acceleration factor was found to be between 2 and 3 depending on acquisitions. We also demonstrate efficiency of our method to freeze the motion at a spatial resolution of 800 µm in-plane resolution even with only 60% of the data used in the reconstruction (Figure 3-38).

3.10. Motion-corrected, high-resolution cardiac imaging using MR-tracking coils and a local receive-only coil: Preliminary results

In a last study, we attempted to **combine hardware developments** of Chapter 2 with **motion-correction algorithm** introduced in this chapter to provide high-resolution cardiac MR images retrospectively compensated for motion. For that purpose, in vivo experiment was conducted on an open-chest pig.

Preparation and MR measurements were completed following the described procedure in section 3.8.1 (animal preparation). The animal vital signs were monitored continuously during the MR experiment. Heart rate was 96 bpm and respiratory rate was maintained to 12 cycles /min. The local coil, 2 cm-in diameter was wrapped in plastic to keep it from getting wet and potentially losing its performance characteristics. It was then positioned against the outer surface of the left ventricle through the open chest access with little to no pressure on the heart wall. In this configuration, the coil could follow the beating heart motion. The catheter embedded with MR-tracking coils was inserted into the right ventricle. Figure 3-40-left shows the localization images (1.5 x 1.5 x 4.5 mm^3 spatial resolution) performed before acquisition of the 2D-GA sequence.

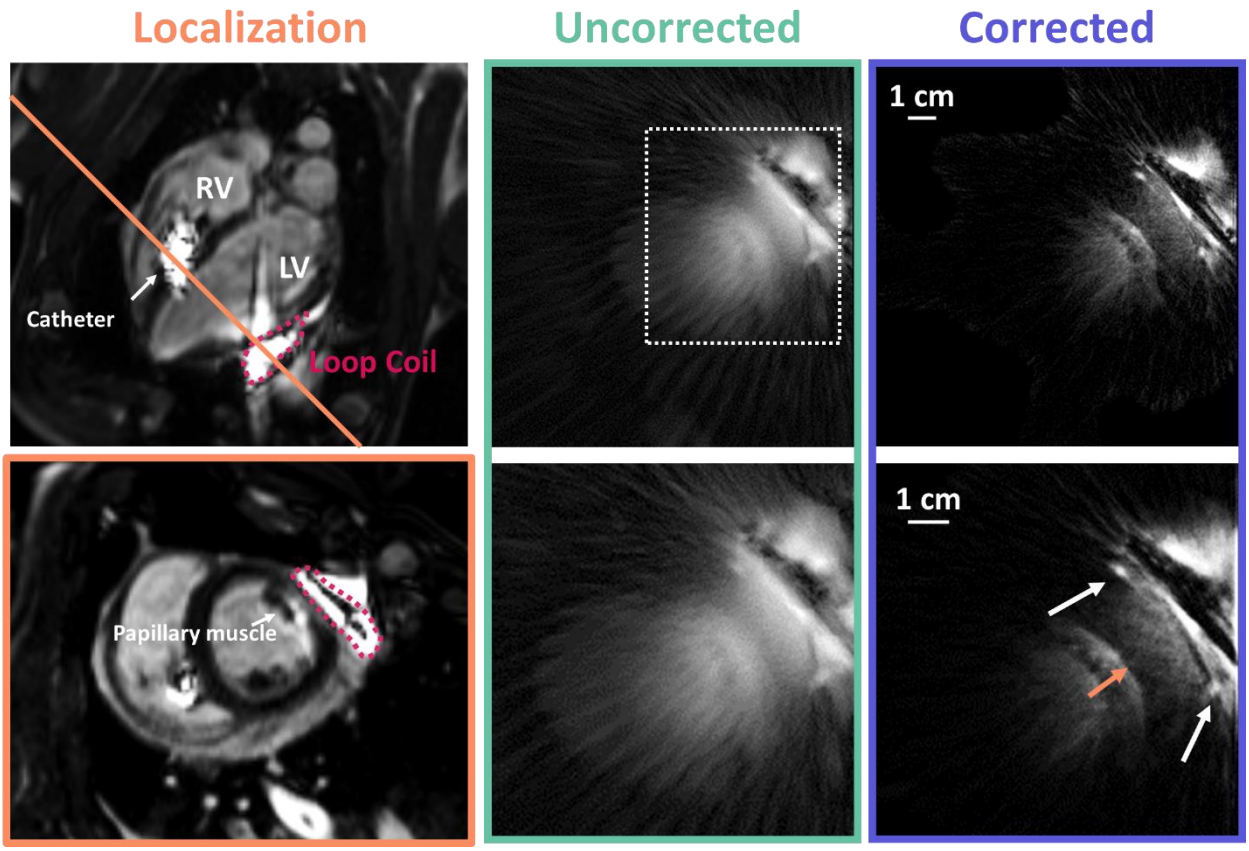

Figure 3-40: In vivo motion-corrected, high-resolution (300 µm in-plane resolution) image of the left ventricle acquired with the local loop coil as a receiver only. **Top and Bottom left-** localization image acquired with the chest coil array shows position of the loop coil (against the left epicardium wall, Pink ROI) and the catheter with the two micro-coils (bright signal in the right ventricle cavity). **Top middle-** Original image (with motion) depicts severe streaking and blurring artifacts. **Top right-** motion-corrected image. **Bottom middle and right**- images are zoomed-view (white frame on top image) of the motion and motion-corrected image respectively. Motion corrected image show a marked improvement in both sharpness and contrast (clear delineation of the left ventricular endocardial border-orange arrow and depiction of blood vessels-white arrows)

Image on the top evidences the catheter located close to the inter-ventricular septum in the right ventricle and the loop coil positioned on the left ventricle wall. The cut plane (orange line) perpendicular to the inter-ventricular septum and passing through the catheter and the loop coil is shown below. Papillary muscle can be visualized on this view. Position of the loop coil is highlighted by a dotted pink circle on the two views. After position of the coil relative to the ventricle wall was verified, the 2D-GA sequence was performed with the following parameters: FOV = 150 x 150 mm^2; Matrix = 448 x 448 px; TR/TE = 65/8 ms; FA = 65°; bandwidth = 255 Hz/Px; slice thickness = 3 mm; Radial views

= 12,000; 3 segments. Total acquisition time was 4 min 23 s. Resulting spatial resolution was **0.3 x 0.3 x 3 mm^3.** Tracking parameters were kept unchanged: FOV = 450 mm, matrix = 512 data points, TE = 2.8 ms, TR = 4.8 ms, FA = 3°, bandwidth = 152 Hz/px, background suppression = 6 mT.m-1, total tracking duration 24.47 ms. 4000 tracking measurements were therefore acquired and processed to retrieve the 3D position of the catheter. Data were then sorted according to the respiratory state and the cardiac phase they belonged to using the data sorting procedure described in 3.5.3. The sorted data were then fed into TV regularization, which operates in the cardiac-phase dimension, as mentioned in section 3.9. Image obtained for a fixed respiratory state (phase #1, corresponding to end-expiration) and a fixed cardiac phase (phase #9, corresponding to end-diastole) are displayed in the same figure and labeled “Corrected”. This image was reconstructed with 483 projections (68% of the requested theoretical data, from Nyquist theorem). For comparison purpose, uncorrected image is juxtaposed to the corrected image. Bottom row corresponds to the crop view (white dotted frame) of the top row images. Streaking artifacts arising from physiological motion are clearly visible on the uncorrected image, which hinder its interpretation. Using our motion-correction algorithm, a marked improvement in image quality is performed. Sharpness is significantly improved, which makes possible a clear delineation of the myocardium wall as well as depiction of blood vessels (white arrows) together with papillary muscles (orange arrow). Hence, this preliminary result highlights the feasibility to combine our loop coil with MR-tracking coils to correct motion for high-resolution cardiac imaging (300 µm in-plane resolution).

3.11. Discussion

In this chapter, we sought for solution to compensate for 3D cardiac and respiratory motions using micro-coils embodied on a catheter to track internal motion and not use conventional surrogates of motion descriptor (e.g. such as ECG, respiratory belt or 1D navigator).

Here, our approach was to make use of an available catheter integrating MR-tracking coils. Our decision was motivated by the several advantages offered by the micro-coils,

in compliance with the technical requirements of the project: First micro-coils are small, and thus require a tiny footprint, which allows them to be integrated to an imaging catheter coil, as already proposed in [16], [17], [39], [40]. Second, small size of such sensors is a double advantage is that it also limits their receive sensitivity profile, which directly impact the tracking accuracy (micro-coils therefore act as a point-source signal). These feature is essential as the accuracy of the motion sensor has to be of the same order of magnitude as the resolution if the image (in our case a desirable spatial resolution of 200-300 µm isotropic). In our results, we report a positional accuracy ranging from 130 to 300 µm, which complied with the accuracy requirement. The implemented MR-tracking process allowed for 3D position localization at a frame rate of 24.47 ms. This frame rate could be further reduced to 15 ms by changing the matrix size (from 512 to 100 data points) of the tracking module, since that matrix size do not influence the tracking accuracy. Although the results presented here show image quality with 3 segments per TR, the sequence implementation offers flexibility between tracking update time and the number of segments acquired between two consecutive tracking modules. This would therefore allow flexibility in temporal resolution and allow a trade-off between temporal resolution requirement and speed of the acquisition.

Although two micro-coils were available on the catheter, only one micro-coil is sufficient to sort the k-space data, which is in favor of a small footprint for future technical implementation of a catheter combining imaging and tracking coils.

The position information provided by the micro-coils offered a great flexibility in data sorting strategies (amplitude, 3D position, cardiac and respiratory phase's extraction). Taking advantage of it, two motion-correction algorithms based either on amplitude or time were implemented. Both were tested on a moving phantom and demonstrated efficiency at compensating motion with different trajectories, frequencies and amplitudes to image a moving phantom with 300 µm in-plane resolution. In vivo, we showed the ability of the method to recover structural details on a 2D 300 µm in-plane image acquired with the local loop coil used and reconstructed with ESPIRIT algorithm. However, only one experiment combining local loop coil and micro-coils in vivo was carried out and further

experiments need to be performed to evaluate the performances of the method, although this primarily result is very encouraging.

Although iterative reconstruction methods such as ESPIRIT and Compressed Sensing benefit from coil arrays [7], [12], [33], these non-linear optimization algorithms showed good performances with a single loop coil.

In order to analyze the compliance of the sorted k-spaces to the Nyquist criterion, we proposed a representation of its density sampling. Using such an analysis during acquisition, it would be possible to dynamically adjust the k-space lines in order to properly fill the missing angular sectors and avoid excessive sampling in the same angular sectors in order to optimize acquisition time.

Alternatively, the 3D position information provided by the micro-coils may be used to perform an interactive motion gating, by acquiring k-space data at the same state using a predefined acceptance window. Cruz et al. [7] proposed an adaptive binning relying of such a gating to both correct for motion and accelerate the acquisition. They were able to reduce the average scan time of a 3D non-Cartesian acquisition by 2.6x when compared to a gated conventional acquisition.

In our study, only 2D radial acquisitions were performed. Next step would concentrates on extrapolating these results to 3D imaging, since results obtained on ex vivo fixed sample of sheep septum show good image quality. The prolonged acquisition times inherent to 3D encoding can be compensated by subsampling strategies (e.g. 3D golden angle radial sampling with Poisson-disk density [41], wave-caipi Cartesian sampling [42] (REF), G-CASPR [43]) combined with iterative reconstruction algorithms such as compress sensing or patch-based presented in our results.

An important consideration relies on the desire contrast that is possible to obtain using our method. Indeed, although we studied the influence of an Inversion Recovery pulse on positional accuracy and resulting image quality, no in vivo images were acquired with preparation pulses. In future developments, we could consider triggering an inversion recuperation sequence with the position information from the micro coils.

We also evaluated the acceptable undersampling factor without degrading image quality. Regarding the results in phantom, we found that and acceleration factor of 4 could lead to a reasonable image quality even at 300 µm in-plane resolution. However, in vivo, this acceleration factor was found to be a compromise between 2 and 3, but limited number of acquisitions were performed. In the experiment conducted on an open-chest of a pig, with the local coil in contact with the myocardium, we were able to reconstruct an image at 300 µm in-plane resolution with only 68% of the theoretical data.

Overall, these results highlight the potential of the proposed method at providing high-resolution motion-corrected imaging of the myocardium. Nevertheless, the reconstruction method needs further optimization to increase the acceleration factor, as the one promote in literature(between 2x [7] to 4x[43] [32]).

Along with the technical improvements of the coil, using a multicoil array for data reception, the combination of compressed sensing and parallel imaging would enable additional acceleration [33].

Regarding the targeted anatomic region, we only applied our method to the left ventricle imaging. Further evaluations need to be done in vivo on atrium wall.

3.12. References

[1] R. Ehman, M. McNamara, M. Pallack, H. Hricak, and C. Higgins, ‘Magnetic resonance imaging with respiratory gating: techniques and advantages’, American journal of Roentgenology, pp. 1175–1182, 1984.

[2] Y. Wang, R. C. Grimm, J. P. Felmlee, S. J. Riederer, and R. L. Ehman, ‘Algorithms for extracting motion information from navigator echoes’, Magnetic Resonance in Medicine, vol. 36, no. 1, pp. 117–123, Jul. 1996.

[3] Y. Wang, S. J. Riederer, and R. L. Ehman, ‘Respiratory Motion of the Heart: Kinematics and the Implications for the Spatial Resolution in Coronary Imaging’, Magnetic Resonance in Medicine, vol. 33, no. 5, pp. 713–719, May 1995.

[4] S. Roujol, E. Anter, M. E. Josephson, and R. Nezafat, ‘Characterization of Respiratory and Cardiac Motion from Electro-Anatomical Mapping Data for Improved Fusion of MRI to Left Ventricular Electrograms’, PLoS ONE, vol. 8, no. 11, p. e78852, Nov. 2013.

[5] M. Henningsson, P. Koken, C. Stehning, R. Razavi, C. Prieto, and R. M. Botnar, ‘Whole-heart coronary MR angiography with 2D self-navigated image reconstruction: 2D Self-Navigated Image Reconstruction’, Magnetic Resonance in Medicine, vol. 67, no. 2, pp. 437–445, Feb. 2012.

[6] S. Coppo et al., ‘Free-running 4D whole-heart self-navigated golden angle MRI: Initial results: Free-Running 4D Whole-Heart MRI’, Magnetic Resonance in Medicine, vol. 74, no. 5, pp. 1306–1316, Nov. 2015.

[7] G. Cruz, D. Atkinson, C. Buerger, T. Schaeffter, and C. Prieto, ‘Accelerated motion corrected three-dimensional abdominal MRI using total variation regularized SENSE reconstruction: Accelerated Motion Corrected Abdominal MR’, Magnetic Resonance in Medicine, vol. 75, no. 4, pp. 1484–1498, Apr. 2016.

[8] C. Forman, D. Piccini, R. Grimm, J. Hutter, J. Hornegger, and M. O. Zenge, ‘Reduction of respiratory motion artifacts for free-breathing whole-heart coronary MRA by weighted iterative reconstruction: Weighted Iterative Reconstruction for CMRA’, Magnetic Resonance in Medicine, vol. 73, no. 5, pp. 1885–1895, May 2015.

[9] J. Y. Cheng et al., ‘Free-breathing pediatric MRI with nonrigid motion correction and acceleration: Free-Breathing Pediatric MRI’, Journal of Magnetic Resonance Imaging, vol. 42, no. 2, pp. 407–420, Aug. 2015.

[10] J. Y. Cheng et al., ‘Comprehensive motion-compensated highly accelerated 4D flow MRI with ferumoxytol enhancement for pediatric congenital heart disease: Motion-Compensated Accelerated 4D Flow’, Journal of Magnetic Resonance Imaging, vol. 43, no. 6, pp. 1355–1368, Jun. 2016.

[11] D. Piccini et al., ‘Four-dimensional respiratory motion-resolved whole heart coronary MR angiography: Respiratory Motion-Resolved Coronary MRA’, Magnetic Resonance in Medicine, vol. 77, no. 4, pp. 1473–1484, Apr. 2017.

[12] L. Feng et al., ‘5D whole-heart sparse MRI’, Magnetic Resonance in Medicine, vol. 79, no. 2, pp. 826–838, Feb. 2018.

[13] J. Pang et al., 'ECG and navigator-free four-dimensional whole-heart coronary MRA for simultaneous visualization of cardiac anatomy and function: Self-Gated 4D Coronary Imaging', Magnetic Resonance in Medicine, vol. 72, no. 5, pp. 1208–1217, Nov. 2014.

[14] L. Di Sopra, D. Piccini, S. Coppo, M. Stuber, and J. Yerly, 'An automated approach to fully self-gated free-running cardiac and respiratory motion-resolved 5D whole-heart MRI', Magnetic Resonance in Medicine, vol. 82, no. 6, pp. 2118–2132, Dec. 2019.

[15] C. L. Dumoulin, S. P. Souza, and R. D. Darrow, 'Real-time position monitoring of invasive devices using magnetic resonance', Magnetic Resonance in Medicine, vol. 29, no. 3, pp. 411–415, 1993.

[16] C. M. Hillenbrand et al., 'Active device tracking and high-resolution intravascular MRI using a novel catheter-based, opposed-solenoid phased array coil', Magnetic Resonance in Medicine, vol. 51, no. 4, pp. 668–675, Apr. 2004.

[17] A.-K. Homagk et al., 'An expandable catheter loop coil for intravascular MRI in larger blood vessels', Magnetic Resonance in Medicine, vol. 63, no. 2, pp. 517–523, Feb. 2010.

[18] L. Qin et al., 'Prospective motion correction using tracking coils', Magnetic Resonance in Medicine, vol. 69, no. 3, pp. 749–759, Mar. 2013.

[19] J. de Arcos et al., 'Motion-corrected high-resolution intra-cardiac imaging using MR-Tracking coils: reducing the effect of noise on motion estimation', Proceedings of the 25th ISMRM Annual Meeting, Honolulu, HI, USA 2017.

[20] W. Wang, 'Magnetic Resonance–guided Active Catheter Tracking', Magnetic Resonance Imaging Clinics of North America, vol. 23, no. 4, pp. 579–589, Nov. 2015.

[21] C. Flask et al., 'A method for fast 3D tracking using tuned fiducial markers and a limited projection reconstruction FISP (LPR-FISP) sequence', Journal of Magnetic Resonance Imaging, vol. 14, no. 5, pp. 617–627, Nov. 2001.

[22] M. A. Bernstein, K. F. King, and X. J. Zhou, Handbook of MRI pulse sequences. Elsevier, Chapter 13, 2004.

[23] H. Chandarana et al., 'Free-Breathing Contrast-Enhanced Multiphase MRI of the Liver Using a Combination of Compressed Sensing, Parallel Imaging, and Golden-Angle Radial Sampling':, Investigative Radiology, vol. 48, no. 1, pp. 10–16, Jan. 2013.

[24] K. T. Block, 'Advanced Methods for Radial Data Sampling in Magnetic Resonance Imaging', Thesis, 2008.

[25] J. O'sullivan, 'A Fast Sinc Function Gridding Algorithm for Fourier Inversion in Computer Tomography', IEEE Transactions on Medical Imaging, pp. 200–207, 1985.

[26] S. Matej and I. Bajla, 'A high-speed reconstruction from projections using direct Fourier method with optimized parameters-an experimental analysis', IEEE Trans. Med. Imaging, vol. 9, no. 4, pp. 421–429, Dec. 1990.

[27] D. Rosenfeld, 'An optimal and efficient new gridding algorithm using singular value decomposition', Magnetic Resonance in Medicine, vol. 40, no. 1, pp. 14–23, Jul. 1998.

[28] F. Knoll, A. Schwarzl, C. Diwoky, and D. K. Sodickson, ‘gpuNUFFT - An open source GPU library for 3D regridding with direct Matlab interface’, Proceedings of the 22th ISMRM Annual Meeting, Milan, Italia, 2014.

[29] M. Uecker et al., ‘Berkeley advanced reconstruction toolbox’, Proceedings of the 23th ISMRM Annual Meeting, Toronto, Canada 2015.

[30] M. Uecker et al., ‘ESPIRiT-an eigenvalue approach to autocalibrating parallel MRI: Where SENSE meets GRAPPA’, Magnetic Resonance in Medicine, vol. 71, no. 3, pp. 990–1001, Mar. 2014.

[31] M. Lustig, D. Donoho, and J. M. Pauly, ‘Sparse MRI: The application of compressed sensing for rapid MR imaging’, Magnetic Resonance in Medicine, vol. 58, no. 6, pp. 1182–1195, Dec. 2007.

[32] O. N. Jaspan, R. Fleysher, and M. L. Lipton, ‘Compressed sensing MRI: a review of the clinical literature’, The British Journal of Radiology, vol. 88, no. 1056, p. 20150487, Dec. 2015.

[33] L. Feng, T. Benkert, K. T. Block, D. K. Sodickson, R. Otazo, and H. Chandarana, ‘Compressed sensing for body MRI: Compressed Sensing for Body MRI’, Journal of Magnetic Resonance Imaging, vol. 45, no. 4, pp. 966–987, Apr. 2017.

[34] A. Bustin et al., ‘Isotropic Reconstruction of MR Images Using 3D Patch-Based Self-Similarity Learning’, IEEE Trans. Med. Imaging, vol. 37, no. 8, pp. 1932–1942, Aug. 2018.

[35] A. Bustin et al., ‘Five-minute whole-heart coronary MRA with sub-millimeter isotropic resolution, 100% respiratory scan efficiency, and 3D-PROST reconstruction’, Magnetic Resonance in Medicine, vol. 81, no. 1, pp. 102–115, Jan. 2019.

[36] K. G. Hollingsworth, ‘Reducing acquisition time in clinical MRI by data undersampling and compressed sensing reconstruction’, Phys. Med. Biol., vol. 60, no. 21, pp. R297–R322, Nov. 2015.

[37] C. Lazarus, ‘Compressed Sensing in MRI: optimization-based design of k-space filling curves for accelerated MRI’, Thesis, Chapter 2, 2019.

[38] H. Cochet et al., ‘Cardiac Arrythmias: Multimodal Assessment Integrating Body Surface ECG Mapping into Cardiac Imaging’, Radiology, vol. 271, no. 1, pp. 239–247, Apr. 2014.

[39] K. N. Kurpad and O. Unal, ‘Multimode intravascular RF coil for MRI-guided interventions’, Journal of Magnetic Resonance Imaging, vol. 33, no. 4, pp. 995–1002, Apr. 2011.

[40] E. J. Schmidt et al., ‘Intra-Cardiac MRI Catheter for EP Ablation Monitoring: Preliminary Studies’, Proceedings of the 19th ISMRM Annual Meeting, Montreal, Canada 2011.

[41] E. Levine, B. Daniel, S. Vasanawala, B. Hargreaves, and M. Saranathan, ‘3D Cartesian MRI with Compressed Sensing and Variable View Sharing Using Complementary Poisson-Disc Sampling’, Magnetic Resonance in Medicine, p. 12, Apr. 2016.

[42] B. Bilgic et al., ‘Wave-CAIPI for highly accelerated 3d imaging’, Magnetic Resonance in Medicine, p. 11, Jun. 2015.

[43] M. Usman, B. Ruijsink, M. S. Nazir, G. Cruz, and C. Prieto, ‘Free breathing whole-heart 3D CINE MRI with self-gated Cartesian trajectory’, Magnetic Resonance Imaging, vol. 38, pp. 129–137, May 2017.

Chapter 4
Evaluation of the devices safety using MR-Thermometry

In this chapter, focus of our attention is made on safety inherent to insertion of a MRI receiver coil inside the body. **Our work was driven by the need to provide an accurate, in-situ method to better quantify the safety hazards of implants**. The developed method was initially thought to evaluate and address potential heating issues of the intravascular coil during MRI scanning but is likely to extend for the other implanted devices such as pacemakers of neuro-stimulator.

We first describe the risks associated with MRI systems, including potential interaction of radiofrequency waves with biological tissues and potential hazards associated with the presence of an implanted devices (pacemaker, DBS) or monitoring device (EEG, ECG leads). We then introduce the dosimetric terms and recall the general regulatory limits. Finally, after briefly reviewing the current methods to handle safety issue in MR environment and after giving some prerequisites, we present the MR-thermometry method implemented during the PhD to quantify temperature evolution in the vicinity of a metallic device.

4.1. Introduction

With an aging population, large joint replacements and cardiac implantable devices are becoming increasingly prevalent. Millions of patients benefit from passive implants, like hip or knee replacements, spine stabilization devices, vascular stents, clips or coils. Many others depend on active implants or devices, requiring electrical power and logic components to operate, like pacemakers, neuro-stimulators, insulin pumps, spine pain-relief stimulators, and cochlear implants. By now, an estimated 4 million patients carry a

cardiac electronic implantable device (CEID) worldwide [1] and over 75.000 patients have undergone a Deep Brain Stimulation (DBS) procedure worldwide [2].

Along with MRI becoming the gold standard for many common medical conditions, the number of implant recipients requiring diagnostic MRI is continuously increasing [3].

While MRI is generally perceived as a safe imaging modality [4], the strong electromagnetic fields used during an acquisition can lead to potential safety hazards, especially for patients implanted with a medical device. A hazard is defined as a potential source of harm, which may lead to health impairment or loss of the quality of life. An adverse event is defined by the United States Food and Drug Administration (FDA) as “any undesirable experience associated with the use of a medical product in a patient” [3]. Several theoretical [5]–[7] and experimental studies [8]–[11] have shown, indeed, that tissue temperature increase can easily reach several tens of degrees Celsius, potentially leading to severe safety hazards such as burn injuries [12], [13].

The MR environment involves a large static magnetic field, pulsed gradient magnetic fields, and radiofrequency (RF) fields, all of which can interact with body tissues and devices, leading to serious risks to individuals or patients. Recently, the rapid growth of interventional MRI has raised new concerns about safety since surgeons are introducing metal instruments (e.g. biopsy needles, catheters, vascular guidewires, and other wire-shaped devices) into the patient during MR scanning. Even for a non-ferromagnetic device, there is the potential for unwanted coupling of the RF EM field with the device, causing a local amplification of RF heating near the device. This therefore represents an ongoing challenge for clinicians for the management of patients with implants (or during intervention) so they can undergo imaging and treatments in a manner that balances benefit and risk [14].

Considering the importance of using MRI for the care and management of patients, major technical evolutions have occurred over the past ten years to alleviate the contraindications of implant within MR environment. Mainly consisted in **modifying the imaging hardware** to make it less interactive with conductive implants [15]–[18], **modifying the implant structure and material** itself to reduce the antenna effect (4.2) [19]–[21] and **modifying**

the implant trajectory – through surgical planning – to reduce the coupling and the antenna effect. Regarding cardiac electronic implantable devices (CEIDs), pacemakers with MR Conditional labeling have been released into the EU market since 2008 [22] and into the US market since 2011. However, safety hazards still exist.

In the followings, we only focus on RF-related heating since it represents the biggest risk in MRI[9], [23].

4.2. Risks associated with the Radiofrequency field B_1

During a clinical magnetic resonance procedure, patients are subjected to the magnetic field component of the transmitted RF field (often referred to as B_1). B_1 varies rapidly in time, with a frequency range of 64 MHz at 1.5 T. The maximum strength of B_1 is only a few microTesla (μT), an order of magnitude lower than the Earth's magnetic field at the surface and many orders of magnitude smaller than B_0. However, even though the B_1 field is small in magnitude, its high frequency leads to safety concerns. Indeed, during an MRI acquisition, the patient's body will absorb the RF energy that is emitted by the acquisition sequence, which may convert into temperature increase of the tissue.

Most reported accidents involved burns due to excessive local heating in the presence of conducting materials close to the patient such as the leads of equipment for monitoring physiological parameters [24]–[27] or presence of metallic implant in the patients (such as ICD, pacemaker or DBS) [7]. Indeed, metallic passive and active implants can collect the RF power like antennas, resulting in induced currents along the conductive structure and creating local hotspots at the implant-tissue interface [28]. Active implants with electrically long and insulated leads, such as pacemakers or DBS, are of particular concern since they pick up electromagnetic (EM) energy along their entire length and deposit it at their distal electrodes in the form of a displacement current. This gives rise to a highly localized increase in the electric field strength, which in turns causes local temperature increase of the surrounding tissue [29].

The magnitude of the locally deposited power of RF heating is a complex interaction that depends on many variables, including:

- the **characteristics of the emitting RF coil** of the MR system (e.g., geometry, materials, physical properties)
- the **RF transmit mode** (e.g., circularly polarized, multi-channel-2 (MC-2))
- the **patients' anatomy, tissue properties, and position with respect to the RF coil** (i.e., imaging landmark).

In addition, for implant carriers, the RF heating also depends on the **medical device characteristics** (e.g., geometry, materials, and physical properties) and **location** within the field and within or on the patient.

The Maxwell-Faraday equation is directly relevant when considering interactions with the RF field. It is written as follows:

$$\oint_c \vec{E}.d\vec{l} = -\iint_S \frac{\delta \vec{B}}{\delta t}.\ \overrightarrow{dS} \qquad (4\text{-}1)$$

where the field $\overrightarrow{B}$ considered here is the magnetic field generated by the RF coil, $\overrightarrow{B_1}$. Equation (4-1 expresses the fact that an electric field is generated such that the electromotive force (emf) or voltage around a stationary closed loop (integral of $\vec{E}$) is equal to (the negative of) the time rate of change of the magnetic flux density integrated over the surface enclosed by the loop [30]. This equation can be stated more simply as:

$$V \propto \frac{dB}{dt} \qquad (4\text{-}2)$$

where V is the voltage induced in the loop and t is time. In the case of heating, it is not directly the transmitted $\overrightarrow{B_1}$ that causes problems, but rather **the associated electric field**, represented by $\vec{E}$. In a conductive medium, $\vec{E}$ drives a conduction current density equal to $\sigma\vec{E}$ (where σ is the conductivity of the medium). This induced current in turn generates a

new magnetic field as described by another Maxwell's equation, Ampere's law, which connects $\vec{E}$ and $\vec{B}$ as follows [30]:

$$\oint_c \vec{B} \cdot d\vec{l} = \iint_S \mu \vec{J} \cdot d\vec{S}, \qquad \vec{J} = \overrightarrow{J_C} + \overrightarrow{J_D} = \sigma\vec{E} + \varepsilon\frac{\partial \vec{E}}{\partial t} \tag{4-3}$$

Where $\overrightarrow{J_C}$ and $\overrightarrow{J_D}$ are the conduction and displacement current densities, respectively ε is the permittivity of the medium and σ is the conductivity of the medium. Thus, there is a new induced $\overrightarrow{B_{induced}}$ field that combines with the original source RF field and the magnitude of the generated electric field no longer has a simple dependence on the magnitude of the transmitted RF only. This equation comes into play to explain the electromagnetic induction heating [31].

Previous publications have investigated in detail the physics and causes of thermal injuries during MRI due to the RF electromagnetic field. Three possible mechanisms were highlighted:

The Electromagnetic induction heating

RF electromagnetic fields can induce voltages in conductive media forming conductive loop such as pacemaker lead or ECG electrodes leads and causes current to flow. As a consequence of the high electrical resistance of the surrounding media (e.g. human tissue), resistive heating is thus generated. The most important heating occurs where the electrical resistance is strongest, thus at the metal/tissue interface [11]. Also, it has been demonstrated that a variation in the input impedance at the side of interface circuit connected to a wire (or micro(coaxial cable) had an effect on the RF-induced heating at the tip of this same wire [32]. Dempsey et al [31] demonstrated that there is actually very little heating of the metal resulting from direct induction in electrically conductive loops (0.6 ± 0.1°C in their study). The heating does not happen because according to the above equation (4-3), the current in the loop will itself generate a magnetic field that will counter the driving B_1 field. If the current induced in the loop grows large enough to generate a field that exactly cancels B_1, then no more current can be induced [30]. Before wrongly conclude

that loops metal pose no risk in MRI, Panych et Madore [30] simulated the case where a small break is present in the loop and showed that even if the effect on the magnetic field ($\overrightarrow{B}$ in the above equations) is not much different than if the ring were intact, the electric field ($\overrightarrow{E}$) is perturbed in the region of the ring gap, leading to an elevated SAR and a potential local tissue damage. Plus, Bennett et al [33] observed a significant heating at the tips of screws that clamp a radiosurgery head frame due to the resistive dissipation of currents induced by the RF field passing perpendicularly through the area enclosed by electrically conducting loop head frame.

The electromagnetic Induction Heating of a Circuit in Resonance:

Although a less likely scenario, the mechanism described above can be enhanced if the loop-containing implanted device acts as a circuit in resonance. A conducting coil exposed to time-varying magnetic fields is equivalent to an electric circuit having an inductance L, a capacitance C, a resistance R, and a voltage oscillating at an angular frequency ω. Peak current in the circuit occurs when the circuit is in resonant condition ($\omega = \frac{1}{\sqrt{LC}}$). Thus, should a large loop be formed during MRI that will by coincidence have the appropriate values of inductance and capacitance so that the resonant frequency matches the frequency of the MRI machine, significant amount of energy may be transferred, possibly resulting in destruction of the device and damage to surrounding tissue. A non-detuned receive coil would be an example. Dempsey et al found a very high temperature rises of up to 61.1°C in loops with appropriately valued inductance and capacitance to cause resonance [31]. This mechanism therefore provided enough heat to induce thermal injury.

The heating due to antenna effect:

The mechanism for RF heating discussed to this point has only involved the generation of current via induction in conductive loops. Straight wires (not bent into loops) can also provoke significant hazard. Antenna effect is considered as the primary safety concerns in MRI [18]. Lengths of the monitoring cable can be considered as RF wire antenna that will be sensitive to the electric component rather than the magnetic component of the radiofrequency wave. The long conductive wire (DBS or pacemaker leads for example) will couple with the RF electric field and wire currents will be produced, terminating in the

surrounding tissue producing thus a high local SAR. This is explained by the fact that resonant antenna exhibit current and voltage standing wave patterns formed by reflections from the open ends of the wire. When resonance is achieved, the electrical energy remains confined to the immediate vicinity of a given antinode. Thus, the highest electric field of the antenna is at the tip. This phenomenon occurs when the length of the wire is such as to support the formation of standing waves. Typically, wire lengths of a half wavelength are most likely to result in the maximum heating [31], [34], [35]. However, this resonance phenomenon is determined by the operating frequency f and the dielectric properties of the media surrounding the antenna since both the relative permittivity ε_r and relative permeability μ_r influence the phase velocity of the electromagnetic field [5]:

$$\lambda = \frac{c}{f.\sqrt{\varepsilon_r}} \text{ and } c = \frac{c_a}{\sqrt{\varepsilon_r \,.\, \mu_r}} \qquad (4\text{-}4)$$

where c_a is the phase velocity in air and c the corresponding phase velocity in the surrounding media. Panych and Madore [30] illustrated this dependence with operating frequency and dielectric properties of the media: considering the speed of the light in the void is 3.10^8 m.s^{-1} and a wave with f = 122.7 million oscillations per second (3T field strength). According to (4-4), the wave would cover 2.35 meters per oscillations, which results in about 1.17 meters for half the wavelength. However, RF waves in MRI do not travel in void but passes through several tissue types (each with different electrical properties). Therefore, one must take into account the relative permittivity of tissue. Considering approximate value of relative permittivity of the heart muscle is $\varepsilon_r \sim 80$ [36], the half wavelength in tissue is reduced compared to its value in the void by $\sqrt{\varepsilon_r}$ down to about 13 cm in the present example. The conductivity of tissues also comes into play and brings the half wavelength value even further down, for example close to 12 cm here if one assumes a conductivity of 0.5 S.m^{-1}. Thus, at 3T, an implanted wire in the range of 12 cm in length should be worrisome. Moreover, as aforementioned, the operating frequency has to be take into account: a longer implant may be safe at 3T but unsafe at 1.5T as shown in the reported results from Luechinger et al. [37].

Nevertheless, one should not assume there will be or not heating based on the wire length alone. Indeed, determination of the wavelength on an insulated antenna in a conductive medium is a complicated function of insulation thickness and medium properties [19]. Moreover, boundary conditions have also been shown to be important in this regard. During interventional procedure, the fraction of catheter inserted into the patient and the fraction in air outside the patient will vary, yielding change in the boundary conditions. As a result, the resonant length will change so will the safer length. Langman et al. [38] showed in vitro, the influence of termination condition on the resonant behavior of the pacing lead at 1.5T. Pacemaker lead tip heating was evaluated using three different conditions: pacemaker-attached, abandoned-capped and abandoned gel-exposed. Each leads lengths were chosen to encompass clinical lead (40 to 60 cm). The most substantial difference in pacemaker lead tip heating occurred for a lead length of 60 cm at which the abandoned-capped lead exhibited a greater heating (+96%) than pacemaker-attached lead. This changing in termination condition correspond to a change from a short to an open circuit. Regarding the transmission lines theory, this change in termination condition causes a 90° phase shift in the standing wave. As a consequence, the resonant heating condition will be shifted and will not occur at the same length. Thus, while lead length of 60 cm was safe for a pacemaker-attached lead, it becomes worrisome as soon as the lead is abandoned. These results indicate that finding the safer lead length for one termination condition does not suggest it is the lead length that will minimize heating for any termination condition. Balasubramanian et al. [39] investigated the heating of EEG with a focus on the antenna effect and found a substantial temperature increase (over 15°C) for electroencephalography (EEG) electrodes wire lengths that were odd multiples of ¼ RF wavelength, at 3T. Armenan et al [40] did not find a maximal temperature increase at classical length (λ/4, λ/2), showing again the difficulty of predicting the resonant phenomenon. They explained their result by the fact that the excitation RF field did not cover the whole wire length in their experiment, which led to standing waves that differed from the classical case in which the excitation covers the whole wire length. These differences across literature are attributed to the change in the boundary conditions, showing again the importance of considering the terminated conditions of the wires. In addition to wire length and terminal conditions, the geometric structure of the lead, its position inside the RF coil, its location within the body and the lead path have also been shown to be significant [5], [11], [41]. For example, Nitz et al demonstrated that the closer

the wire is located toward the resonator wall, the further it is dislocated from the isocenter of the magnet, the larger the temperature increase at the tip of the wire after execution of an imaging protocol. A solution to reduce heating associated with antenna effect was proposed by Ladd et Quick [19]. They demonstrated that the resonant RF heating in elongated conductive wires such as intravascular catheters could be reduced by avoiding a resonant length of cable and by including coaxial chokes on the cable. They obtained a significant reduction of the temperature increase in a 0.7 mm diameter triaxial cable, from 55°C without any choke to 3.4°C with one choke.

4.3. Dosimetric terms and Safety Regulation

4.3.1. Specific Absorption Rate (SAR) and established standards

In order to prevent the risks of inducing thermoregulatory imbalance and causing local hyperthermic tissue damage with RF energy during MRI, strict regulations were imposed by FDA and the International Electrotechnical Commission (IEC) to regulate both the maximum tissue temperature (see Table 4-1) and the Specific Absorption Rate (SAR, described hereafter). These safety guidelines especially recommend limiting localized heating to < 39 °C for “normal” operating mode and 40 °C for “first level controlled” operating mode while maintaining body core temperature change less than 0.5 °C for normal mode and 1 °C for first level controlled mode (as defined in IEC 60601-2-33:2010) [42]. Because local temperature is generally difficult to assess, more tractable SAR thresholds were derived to ensure compliance with the guidelines. In the IEC standard, regarding particular requirements for basic safety of MR equipment (IEC 2015), SAR limits are specified with regard to global (whole-body) and local aspects as shown in Table 4-2 Local SAR is averaged over tissue masses of 10 gram or 1 gram and is considered to prevent excessive localized heating that are actually the cause of burns. It is stated that these temperature and SAR limits are conservative and that higher values may be accepted for specific tissues if no unacceptable risk occurs.

Operating Mode	Maximal body core temperature in °C	Maximal local tissue temperature in °C	Maximal body core temperature elevation in °C
Normal	39	39	0.5
1st Level Controlled	40	40	1
2nd Level Controlled	> 40	> 40	> 1

Table 4-1: Maximal tissue temperature. Modified from Fiedler et al., 2018

Averaging time	6 minutes		
Operating mode	Normal	1st Level Controlled	2nd Level Controlled
Global SAR aspects (W/kg)		Volume Transmit Coils	
Whole Body	2	4	> 4
Partial Body *	2 - 10	4 - 10	> 4 - 10
Head	3.2	3.2	> 3.2
Localized SAR (W/kg)		Local Transmit Coils	
Trunk	10	20	> 20
Limbs	20	40	> 40

*Determination of partial body SAR according to (International Electrotechnical Commission (IEC), 2015).

Table 4-2: Global and Local SAR limits. Modified from Fiedler et al., 2018

The RF transmit coil induces an electric field inside the lossy human body tissue and the absorbed RF energy is converted into heat (Faraday's law, (4-1)). Standards regarding human exposure to RF electromagnetic fields (IEEE International Committee on Electromagnetic Safety (SCC 28), 2003), (IEEE International Committee on Electromagnetic Safety (SCC39), 2006) as well as the standard regarding particular requirements for basic safety of MR equipment (International Electrotechnical Commission (IEC), 2015) have introduced the metric SAR.

SAR corresponds to the rate at which energy is absorbed by the body when exposed to the RF electromagnetic field (B_1) and is measured in units of Watts per kilogram (W/kg) of body weight. It is determined by the dissipated RF power P_V in a tissue element ΔV divided by its mass Δm:

$$SAR = \frac{\Delta P_V}{\rho \Delta V} = \frac{d}{dt}\left(\frac{\Delta W_V}{\Delta m}\right) = \frac{1}{2\Delta V}\iiint_{\Delta V} \frac{\sigma(\vec{r})}{\rho(\vec{r})} \left|\vec{E}(\vec{r})\right|^2 dV \qquad (4\text{-}5)$$

with the absorbed energy ΔW_V in tissue element ΔV, the specific tissue density ρ, the electrical conductivity $\sigma = \omega\varepsilon_0\varepsilon_r''$ (ε_0 corresponds to the vacuum permittivity and ε_r'' is the imaginary part of the relative permittivity : $\varepsilon_r(\omega) = \frac{\varepsilon(\omega)}{\varepsilon_0}$) and the magnitude of the electric field $\left|\vec{E}(\vec{r})\right|$, which is determined by the transmit RF coil and the exposed body region [43].

SAR is patient dependent and varies depending on the patient's size and mass (weight and shape). Of note is that there is no direct way to measure SAR prior to or during an MRI procedure. As a result, MR system manufacturers rely on numerical models to conservatively estimate the SAR for a particular scan sequence and each manufacturer uses their own conservative assumptions for their SAR models (patients size and tissue composition) to ensure that no patient is exposed to RF energy that exceeds the specified limits [44].

If the estimated SAR value exceeds the regulation safety limit, the scanner cannot perform the examination until the operator changes some sequence parameters, such as TR, to reduce the energy deposition on the subject. The admitted whole body SAR is 2 W/kg for normal mode and 4 W/kg for first level controlled mode and superior to 4 W/kg for second level controlled mode. This acknowledged upper limit is established from observed behavioral changes in animal studies: the average metabolic rate, as a conversion of chemical into mechanical and thermal energy in the human body, is estimated to be 115 W at rest and 295 W for moderate activity. Thus, 2 W/kg for a 100 kg person represents a situation of homeostasis without undue stress and is chosen as acceptable exposure for Normal Operating Mode of MRI systems.

4.3.2. Most critical SAR aspects

In practice, it is difficult to determine the SAR from the equation (4-5) since it supposes to know the value of the local electric field. Local effects are typically underestimated by global SAR aspects [43]. Also, obtaining accurate SAR estimate is complicated by the fact that the human body has a complex geometry and is not uniform in terms of its dielectric properties (conductivity, permittivity). Since these parameters can vary considerably for different tissues (conductivities for example can vary by as much as an order of magnitude between tissue types), the SAR is non-uniform in heterogeneous tissue distributions even for the potential case of a uniform electric field. Moreover, these dielectric properties of biological tissues show a distinct frequency dependence [45] in addition to vary from patient to patient. In addition, it has been demonstrated that conductivity changes with pathologies. This finally results in a frequency dependence and a subject-dependent SAR distribution.

With regard to radiofrequency heating, it has been suggested that control of the whole body averaged SAR alone is not sufficient to estimate local energy deposition in human tissues [46]. However, while whole body SAR is routinely monitored in practice with measures of the power delivered to the transmit coil (and estimates of the power delivered to the subject), local SAR remains a concern as its measurement and tracking calls for more advanced methodology and is thus more challenging to monitor [47]. Local SAR is even more complicated to estimate if the pattern of power loss density in the human body varies with time during RF transmission[48].

Originally, SAR metric was designed for heating in biological tissue devoid of metallic or conductive implants. However, patients with implants - particularly those that are conductive and have elongated configurations- raise additional safety concerns, as mentioned in the previous section. In addition, several other parameters involved in MRI induced heating of implants such as the length and the geometric structure of the lead, or the implant location are not reflected by SAR estimation [11]. It is thus still a debate whether this metric is appropriate as a general predictor of implant heating as currently applied or calculated within MR systems. Studies led by Baker et al [49], [50] revealed a marked differences in the RF-induced heating profile of a DBS implant across two different MR system from the same manufacturer. In [50], the ratio of temperature changes to SAR values for the head (SAR-H) $\Delta T/SAR\text{-}H$ for the implant ranged from 3.5 to 5.5 times higher

on one MR system as compared to the other, depending on the measurement site. The data used in this study were derived using a configuration of the MR system and the implant hardware consistent with the FDA-approved safety guidelines provided by the manufacture. Hence, these findings underscore the notion that console-reported SAR values do not constitute a reliable index of heating for elongated, conductive implants such as DBS hardware system even if safety recommendations provided by manufacturers are respected. Moreover, Massire et al [51] showed that a peak 10-g SAR value of 10W/kg could lead to a wide range of possible temperatures values, confirming that the relationship between SAR and temperature is not straightforward.

4.3.3. B1+rms

Therefore, from these findings, when active implants and devices are present in patients, the use of SAR appears to be an insufficient and even unreliable metric to predict RF-induced heating. To this end, the Joint Working Group comprised of scientists and scientists affiliated with MR system and device manufacturers, along with the FDA and IEC 60601-2633 standard recommended that B_{1+rms} be used as a metric for implant heating in complement to SAR [52], [53].

$$B_{1,rms}^{+} = \sqrt{\int_{0}^{t_x} \frac{(B1^{+}(t))^2 \, dt}{t_x}} \qquad (4\text{-}6)$$

$B_{1,rms}^{+}$ is the root-mean-square (rms) value of the MRI effective component of the RF magnetic (B1) field emitted by the transmit coil of the MRY system:

$B_{1,rms}^{+}$ is measured in units of micro-Tesla (μT). The MR scanner measures the B_1^+ field (the positively rotating RF magnetic field produced by the scanner) needed for an imaging sequence and uses the time averaged B_1^+ field, or $B_{1,rms}^{+}$, that will occur due to a particular imaging sequence. Thus, the $B_{1,rms}^{+}$ value is calibrated by the MR system's software during the preparation phase of any measurements of an MRI exam. It is then updated during the acquisition. An important characteristic of $B_{1,rms}^{+}$ is that it is not an estimated

value but it is a measured quantity based on the pulse sequence and the associated parameters. Furthermore, $B_{1,rms}^{+}$ is not patient-dependent nor is it calculated differently based on a given MR system manufacturer. For these reasons, this quantity is a much more consistent approach to assess RF-induced implant heating than whole-body SAR [23]. As a consequence, device manufacturers have begun to have labeling approved with a given B_{1+rms} value not to be exceed. As an example, Medtronic recommend a $B_{1,rms}^{+}$ ≤ 2.0 μT in case of a patients with DBS systems that are full-body MRI scan eligible. [22]. In the latest version of IEC 60601–2-33, the so-called fixed-parameter option (FPO) was introduced for 1.5T systems (FPO:B), which specifically addresses the scanning of implant carriers and fixed limit value of $B_{1,rms}^{+}$ = 3.2 μT.

4.3.4. Regulation - Safety guidelines

Along with the incoming technical solutions performed in both implants design and MR hardware, research studies have been performed to determine risks associated with using MRI in the patients with certain electronically activated implants. These investigations typically defined safety guidelines and good practices with respect to the conditions that must be used for the device (e.g., setting the device to the “off ” mode of operation and resetting after MRI) and the parameters for the MR examinations [3], [14], [54]–[56]. Several guidelines for MRI safety practices have also been issued by radiological societies, eg, the American College of Radiology (ACR), Canadian Association of Radiologists and European Union. In fact, certain electronically activated implants have labeling claims approved by the FDA that permit MRI to be performed as long as specific guidelines are followed to ensure patient safety [9].

Plus, concerns regarding the compatibility of MRI and implants have led to standardization of medical device testing, labeling, and terminology by ASTM International (including but not limited to F2503, F2052, F2189), while implantable portions of active device standards fall under the International Organization for Standardization, Technical Standard (ISO/TS; latest guidelines, ISO/TS 10974:2018) [56]. ASTM published test methods for the evaluation of MR interaction with medical devices including force and torque, RF heating and artefacts. These test methods are fundamental for the labelling of medical implants in three MR compatibility categories “MR safe”, “MR conditional” and MR unsafe”.

4.4. MR-thermometry method for safety assessment

Although B1+rms was proposed as a more precise metric of RF exposure, it does not provide a measurement of local temperature change. In this section, we present the method developed to quantify temperature evolution in tissue surrounding an implanted wire. Intend of this work was to address the safety challenge raised by insertion of an intravascular coil within the body, especially the potential RF-related heating.
At the beginning of this PhD thesis an MR thermometry method for real time temperature mapping of the heart and liver was already available, resulting from previous work of Senneville et al [57], Ozenne et al.[58], Toupin et al.[59], Bour et al. [60]. During the first year of PhD, I closely worked with Dr. Pierre Bour to modify this pre-existing method into a method for RF-related heating assessment.

Personal contribution:

- Participating in sequence development (with strong help and contribution of Dr. Bour)
- Management of ex vivo and in vivo experimentations
- Data post-treatment and production of figures

This section corresponds to a paper published by Marylène Delcey et al., in PLOS One. In April 2021. Few modifications relative to the original paper are add to comply with the thesis manuscript (such as Literature and Prerequisites).

4.4.1. Literature

Numerous methods have been proposed to handle the safety issue and investigate the potential risk of burn injury during an MRI procedure.

Methods exploiting Fluoroptic temperature or Electric fields probes

In the past two decades, measurements in gelled saline phantoms with **fluoroptic temperature measurement systems** have become the gold standard in basic research of RF-related implant heating in MRI [9], [19], [61]. Although rapid and giving access to absolute temperature value, a major drawback to this method, besides its invasiveness, is

that these probes can only measure the temperature at a single point, making it difficult or at least time-consuming to investigate heating effects of implants with complex geometries. Plus, as RF-related heating is often focused at one spot (local hot spots), misplacing the probe results in missing the heating zone. Furthermore, prior results showed that temperature measurements obtained using temperature probes are subject to variation depending on the exact probe location, probe contact configuration, sensitive probe volume, and so forth, leading to an uncertainty in the calculated temperature value. For example, Matei et al [62] showed that positioning errors of fluoroptic probes may lead to an error of up to 45%, even if the probe is directly attached to the heating source. Lottner et al [63] demonstrated that systematic errors occur if the fiber optic temperature probes are placed in the vicinity of implants and if their size are comparable. They further showed that temperature sensors with a significant size compared to the samples influence the RF absorption of energy and can distort the temperature distribution and hence affect the measured temperature, yielding to incorrect certification of implants.

A different approach consists in **measuring the electrical currents** induced inside the implant by the absorbed RF energy, as they are held to be directly responsible for heating at high resistance locations within the circuit, as well as at small device-to-tissue interfaces [7]. Detection and measurement of the RF E-field has been performed using different methods [41], [64]–[66]. Although accurate, these techniques require a calibration step in order to preserve isotropy of the probe measurements, and measurement of E field components within a few millimeters of the surface is challenging due to the thickness of the probe and the interaction of the EM field with phantom edges [67]. Plus, there is no direct in-situ evaluation of the temperature. The method proposed by Saniour et al require the analysis of both refractive index modifications and optical axis orientation Thus, for each desired medium, two probe prototypes has to be developed (using a single isotropic crystal) and calibrated outside the MR system in order to measure precisely the three components of the E-field. Moreover, electric field values depend on the MR system (especially on the RF antenna: volumic or surfacic) and on the biological media. Thus, the use of a probe adapted to the environment (air or biological environment) is very important for accurate results.

Methods relying on temperature probes and E-field probes both present the disadvantage of being invasive and localized. Hence, these methods are not efficient to depict hotspots

or temperature gradients in case the local hot spot occurs in a region outside the probe location. In addition, Saniour showed that electric field measurement uncertainties were principally associated to positioning errors of the E-field probe within the biological medium as well as the positioning of the sample within the MR scanner.

Methods relying upon numerical simulations

Since the local SAR is difficult to measure in vivo, data describing local energy deposition can be reconstructed from complex mapping of B+1 field through suitable algorithms based on simplifying assumptions [68], or acquired from experiments performed in vivo on animals or on phantoms [69], [70]. In addition, the numerical approach presents the ability to simulate several configurations (type of coils, field strength…) and to take into account the variability between patients (age, type of implants, position of the implant, metabolism, morphology…). Numerical simulation is an invaluable tool for MRI safety and can help for the development of new devices. For example, [71] used numerical simulations (finite-differences time-domain) to assess the effects of a high dielectric material on the induced heating at the tip of an endocardial lead. Several medical implants have been studied through computational models, like stents [72] and orthopedic devices [73].

Repeatedly, agreement in transmit magnetic B1+ fields distributions between two geometries has been used to suggest agreement in heating distributions. However, [47] showed that relatively small differences in sample geometry resulted in relatively minor differences in the distribution of B1+, but in greater differences in SAR and temperature change. They also confirmed that changes in B1+ distribution underestimate changes in local SAR or temperature change. This was explained by the fact that B1+ fields are primarily produced by currents in the copper coil, while SAR in the sample is very dependent on the distributions of conductivity and permittivity throughout the sample. Changes in conductivity of the tissue properties of the phantom can create new regions of high SAR with relatively little effect on the B1+ field distribution. Thus, reliance on B1+ distribution alone for validation of simulation with a sample or subject for assurance of safety should be performed with caution. Moreover, the body models typically used have a different geometry than the patient being imaged, therefore, geometrical inaccuracies associated with body models may yield inaccurate predictions of local SAR and temperature change (ΔT) distributions in the body. Plus, modeling of complex antenna-

load structures to match realistic physical conditions using EM field simulations is not straightforward and possible discrepancies between simulated and manufactured devices may reduce the accuracy of RF safety assessment [67]. It was also demonstrated by [74], then [51] that the relationship between SAR and temperature is not straightforward. Indeed, in areas of high perfusion, such as the brain, high SAR levels often lead to minimal temperature increase while in areas of lower perfusion rate, such as muscle or the eyes, the temperature may increase significantly even with relatively low SAR inputs.

While simulation and numerical modeling methods such as finite difference time domain may provide spatial temperature distribution, accurate computation of the fields near implants is a challenging task due to the presence of extremely high spatial gradients at these locations and the need for very fine computational structures.

Approaches based on MRI measurements

Methods to quantify induced currents into the device through **B_{1+} mapping**, using either magnitude [75] or phase images [76] were proposed. However, these methods require some assumptions (homogeneous or known B1 transmit and/or receive fields) to work efficiently. Moreover, they suffer from being simple surrogates of the relevant quantity of interest, which is tissue temperature.

Regarding RF safety assessment, the relevant parameter is the tissue temperature.

As an alternative to the above-mentioned methods, MRI was used for noninvasive measurement of temperature change. The merits and limitations of MR thermometry based upon these MR parameters are surveyed in the reviews of [77]–[79]. They provided rich and detailed support for drafting this section.

MR **T1-based** thermometry was used by Detti et al. [80] and Gensler et al. [81] to estimate the temperature elevation induced by the MR sequence in the neighborhood of metallic wire. One challenge with utilizing T1-based MRTI in biological tissues is that the change in T1 with temperature (measured in ms/°C or %/°C) is tissue type dependent due to the difference in macro-molecular content and microstructure for different soft tissue types. Therefore, this temperature dependence of T1 needs to be estimated for each tissue type of interest. Plus, the temperature sensitivity was shown to be on the order of 1-3%/°C, with slightly higher values reported for fat-based tissues than for water-based tissues, making

it thus challenging to detect small changes in temperature in the T1 maps. Another drawback of T1-based MRTI is that conventional pulses sequences that are used such as inversion- and saturation- recovery based methods are very slow.

MR thermometry methods based on PRFS [82], [83] have been proposed and used for temperature mapping, taking advantage of their high spatial and temporal resolution. In addition, a very important asset of this technique is its near-independence of tissue composition. This method rely on the phase variation (Figure 4-1), which is directly proportional to the temperature change as follows:

$$\Delta T = \frac{\Delta\varphi}{\gamma . \alpha . B_0 . TE} = \frac{\varphi_{TEMP} - \varphi_{REF}}{\gamma . \alpha . B_0 . TE} \qquad (4\text{-}7)$$

Where γ = 267.5 rad.s^{-1}.T^{-1} is the gyromagnetic ratio, α = -0.0094 ppm.°C^{-1} is the PRFS temperature coefficient, B_0 is the magnetic field strength and TE is the echo time of the MR-sequence.

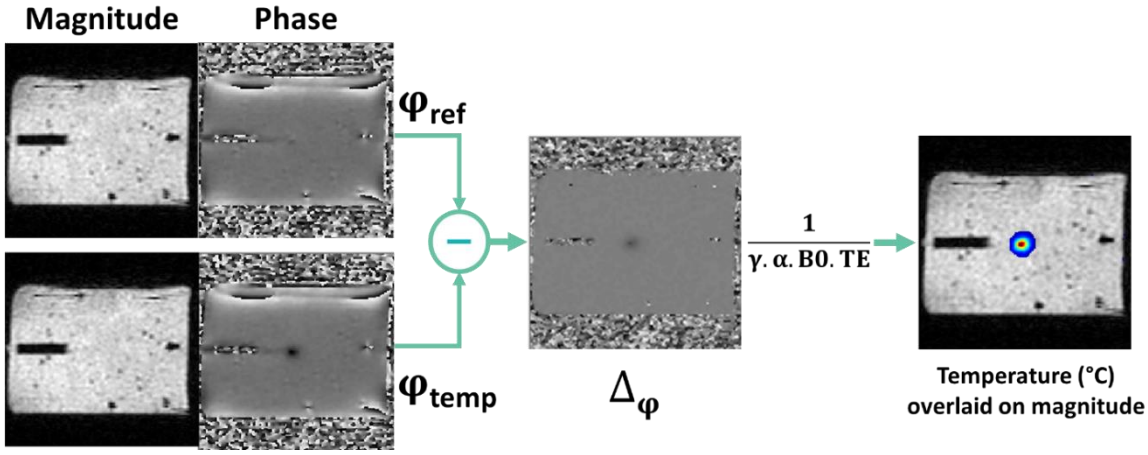

Figure 4-1: Principle of the PRF thermometry method on a static agar gel phantom. Magnitude and Phase images are acquired using the GRE-EPI sequence. During the heating, the incoming phase image is subtracted to a phase of reference acquired prior heating. The relative temperature is then derived from the subtracted phase using equation (4-7).

However, challenge with the PRF shift method include its lack of sensitivity in adipose tissues (this motivated the development of alternatives to measure temperature in adipose tissue such as T1-based or T2-based approaches). In voxels that contain a mixture of adipose and aqueous tissues, the measured change in the PRFS with temperature will be reduced, resulting in an underestimation of the measured temperature change. However, to avoid the problem of multiple species, either suppression of the fat signal or selective excitation of the water signal can be employed, especially at high field strengths (>1 T) where the frequency separation of the fat and water peaks is larger [79]. Other challenges associated with the PRFS technique are the severe susceptibility artifacts that can occur in the presence of metallic implants and the B_0 field drift. Thus, when field homogeneity is poor, e.g., due to an inserted needle or applicator, the PRF method may not be as accurate as diffusion or T1 relaxation, which can be acquired with spin echo methods. Temperature dependence of the magnetic susceptibility is often not considered (~0.0016 ppm/°C for aqueous tissues over a temperature range of 30-45°C, compared to 0.01ppm/°C for the PRF constant). Regarding the B_0 field drift, the PRFS method is sensitive to time-varying changes in the local magnetic field that result in phase drift. Although modern clinical scanners have relatively stable B_0 fields (field drifts in the range of 0.1 ppm/hour), additional drift can be caused by gradient system heating depending on the acquisition sequence. The drift is however slowly varying in space and time and can be corrected by image post-processing.

Absolute temperature measurements were proposed through MR-spectroscopy, but the methods are hardly compatible with high spatial resolution and rapid update time that are required in thermometry [79].

4.4.2. Objectives

Regarding the safety assessment of MRI for patients implanted with a medical device, there is a need for a method providing a **noninvasive**, **real-time** thermal map of tissues near the conductor. Hence, the choice of a method should be oriented given the following points:

- The method should be **rapid** (sub-second temporal resolution).
- It should provide sufficient **spatial coverage** with high spatial resolution (in the range of a few millimeters) and ideally volumetric thermometry,

- The method should provide **real time** temperature map with **accuracy below 1°C** to precisely monitor the temperature distribution within the targeted tissue and ensure patient safety with respect to the RF-related heating.

MRTI methods provide directly the temperature information and are non-invasive, however, current published methods do not fulfill all the aforementioned requirements. Detti et al. [80] proposed a T1-based thermometry with a temporal resolution of 0.5 s with 1 mm^2 spatial in-plane resolution and a 5 mm slice thickness with a temperature variation resolution of 0.2°C. Gensler et al [81] developed a T1-based method thermometry with a temporal resolution of 7.6s and a spatial in plane resolution of 2 mm. Standard deviation of calculated temperature values itself was determined to be 1.37°C. Dharmadhikari et al. [84]proposed a method based on paramagnetic lanthanide complex thulium not suited for in-vivo examination due to its possible toxicity in humans. Ehses et al.,2008 [85] combined a proton resonance frequency (PRF) shift MRI thermometry method with an MRI heating sequence for implant safety investigation. This technique allows for quantitative assessment of the temperature increase caused by the MRI sequence itself. Limitations of their method was spatial resolution with an in plane spatial resolution of 1.5 mm^2 and a slice thickness of 5 mm. Standard deviation was found to be 0.5°C. Moreover, the method proposed in Ehses et al [85] do not provide any flexibility in terms of energy deposition pattern since only one RF pulse is playing out between two consecutive imaging acquisitions and the sequence do not allow the visualization of the cooling down. Pfeil et al. 2012 [86] investigated a proton magnetic resonance spectroscopy thermometry on ex-vivo pig-heart. In contrast to phase-mapping methods, which are sensitive to motion, susceptibility, and variable tissue compositions with differing fat components, spectroscopic imaging is more robust but very time consuming. Echo-planar spectroscopic imaging sequences may help to overcome this problem. However, this technique is not efficient for visualizing possible hot spots along implants with a complex shape.

In this study, we propose a sub-second dynamic MRI-thermometry pipeline based on the PRFS technique with an adjustable module for energy deposition to quantify the potential RF-induced heating near implanted devices.

4.4.3. Prerequisites

4.4.3.1. Echo Planar Imaging

Single shot Gradient Echo Echo-Planar Imaging sequences (ssGE-EPI) is one of the fastest MR-acquisition available [87]. As compared to conventional MR-acquisitions, which acquire one line only after each radiofrequency excitation, ssGE-EPI acquires all the k-space lines after a single radiofrequency excitation (Figure 4-2). Major advantages of EPI over conventional MR imaging include reduced imaging time (< 100 ms), decreased motion artifact, and the ability to image rapid physiologic processes of the human body. Main drawbacks of this sequence is its intrinsic susceptibility to B0 field inhomogeneities, off-resonance effects and geometric distortions effects. .

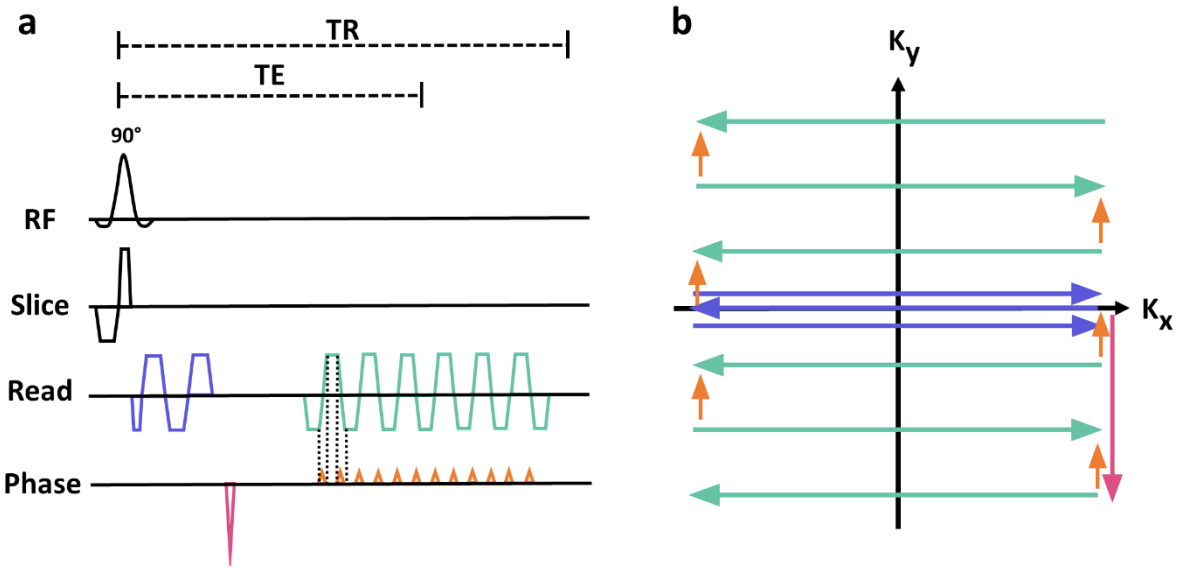

Figure 4-2: Single shot Gradient Echo Echo-Planar Imaging sequence. a) shows the chronogram of the sequence while b) gives the corresponding path in the k-space.

4.4.3.2. Reconstruction using the Gadgetron framework

Gadgtetron was introduced by Hansen et Sørensen [88] with the goal of providing a common source framework for medical image reconstruction. The framework implements a flexible system for creating streaming data processing pipelines where data pass through a series of modules or “Gadgets” from raw data to reconstructed images. Multiple Gadgets are connected to assemble a reconstruction process (a Gadget stream). GRAPPA EPI raw

data of the MR thermometry method implemented during the PhD were reconstructed using the following pipeline (Figure 4-3), described in [89]:

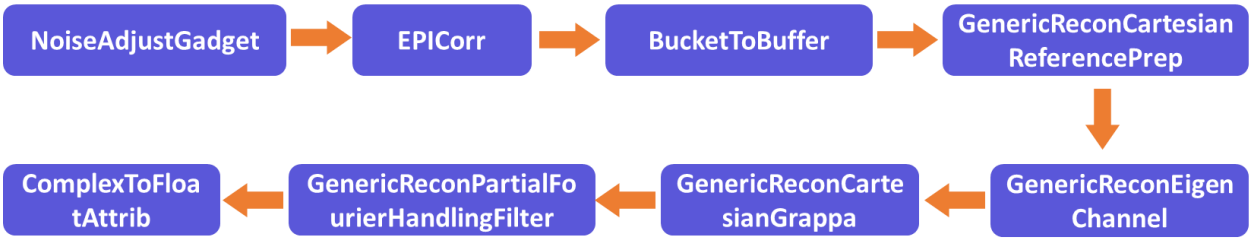

Figure 4-3: Pipeline of reconstruction. Schematic representation of the genric_EPI_grappa.xml. Ecah violet box represent a single Gadget.

- **Noise Adjustment Gadget** normalizes each individual coil based on the amount of coherence in the signal. For coils located close to the region to image, the coherence of the signal will be higher than a coil located far from the object. Doing so, we preserve coils with low signal to noise ratio (located far from the region to image or potentially broken coils), to propagate noise into the following gadgets and degrade nal image quality.
- **EPI cor** performs the B0 phase correction and odd-even readout phase correction. These corrections are based on the three lines acquired at the center of the k-space. This gadget deals with ghosting artifacts observed in the phase encoding direction. The acquired data are used to provide correction of distortions in the resulting image.

- **GenericReconEigenChannel** computes eigenvectors on acquired data for every dynamic acquisition. 1) Transform the receiver coils into virtual coils (using principal component analysis), ordered by their information content. 2) Reduce the number of coils to improve downstream performance and resulting image quality.
- **GenericReconCartesianGrappa** exports prepared calibration lines (**GenericRecon- CartesianReferencePrep**) and processes data for GRAPPA reconstruction. In addition, coil map sensitivity for multicoil reconstruction is performed using a coil map estimation proposed by [90].

- **GenericReconPartialFourierHandlingFilter** handles partial Fourier acquisitions using a projection onto convex set method.
- **ComplexToFloatAttrib** allows to retrieve from complex images, the magnitude and the phase image.

4.4.4. Materials and Methods

Set-up for ex vivo experiments

A Plexiglas box (11 x 8 x 6 cm^3) filled with agar (2% with 0.9% NaCl to match tissue electrical conductivity) was used for experiments. The container was designed to position a copper wire vertically and to hold a fluoroptic probe perpendicular to the wire (Figure 4-4).

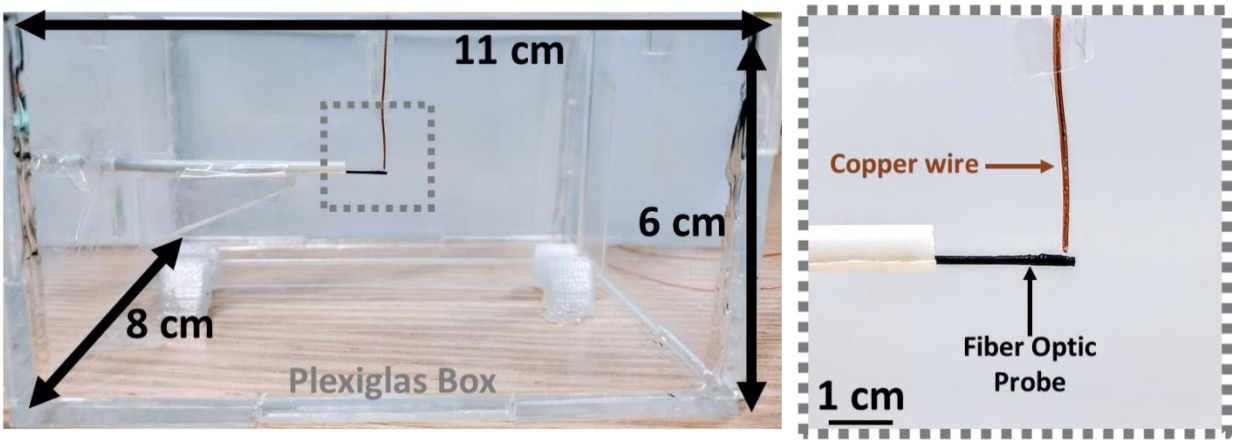

Figure 4-4: Setup used for MR-thermometry ground truth measurements. A zoom view (grey frame) focuses on the optical fiber and tip of the copper. Optical fiber (black arrow) is placed perpendicularly to the copper wire (brown arrow) into the agar gel.

MRI-thermometry sequence

All measurements were performed on a 1.5T clinical imaging system (MAGNETOM Avanto-fit, Siemens Healthcare Erlangen, Germany) equipped with a maximum gradient strength of 45 mT/m and a maximum slew rate of 200 T/m/s. A circular loop of 11 cm in diameter and two spine elements (4 elements each) were used for imaging (for a total of 9 receiver coils). The acquisition sequence (Figure 4-5) was a modified single-shot gradient echo planar imaging (EPI) sequence, with the following parameters: FOV = 120 mm,

TR/TE = 1000/18 ms, matrix size = 74x74 pixels (zero filled to 148x148 pixels), slice thickness = 2.4 mm, bandwidth = 1648 Hz/pixel, FA = 53°, GRAPPA 2, 7/8 Partial Fourier. Between each EPI acquisition (62 ms per slice, including fat saturation pulses), a train of RF-pulses (called “heating module” in the remaining text) was applied between dynamic acquisitions #10 and #90 with adjustable parameters: flip angle, inter-pulse delay and number of pulses. In the remaining text, the flip angle of the heating module RF pulses is called $FA_{HM.}$ Each RF pulse had a sinc shape of 1 ms duration (with an inter-pulse delay of 2 ms) and was emitted with a tunable frequency offset (typically 100 KHz) to avoid direct proton signal saturation [81], [85]. For 3 EPI slices and a repetition time (TR) of 1 s, 242 pulses were played between each stack of slices, resulting in a duty cycle of the heating

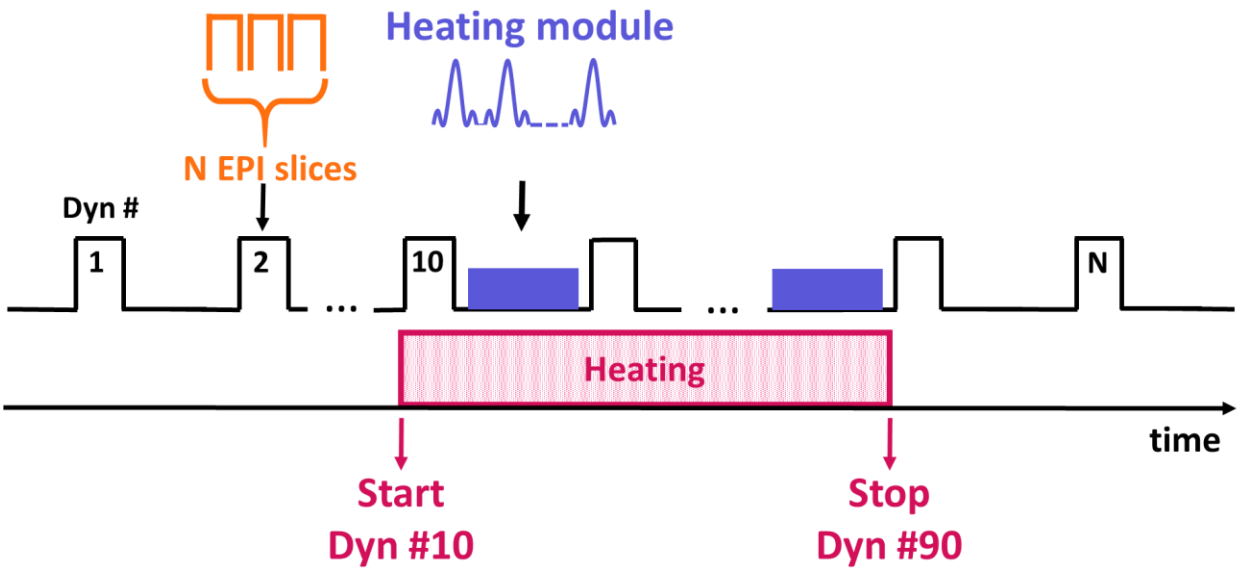

Figure 4-5: Schematic of the MRI-thermometry technique. Single shot gradient echo EPI acquisition interleaved with a train of RF pulses (heating module) with adjustable flip angle, inter-pulse delay and number of pulses.

module of 72% per TR.

Thermometry pipeline

Temperature evolution was computed and visualized in real time during experiments using an MRI-thermometry pipeline similar to one proposed for monitoring cardiac radiofrequency ablations [58], [59]. The MRI raw data were streamed through TCP/IP to the Gadgetron framework for online image reconstruction [88], including EPI ghost-correction followed by GRAPPA reconstruction [91]. Prior to Fourier transform of the data, zero filling was applied

resulting in a matrix size of 148x148 pixels and a reconstructed pixel size of 0.8x0.8mm². Temperature images were then computed from phase images using the PRFS method (with a constant of − 0.0094 ppm/ °C) [82], [83]. The first 10 acquired slice stacks in the time series were averaged together to create reference phase images for each slice. Potential spatio-temporal phase-drifts were corrected using the method proposed by Ozenne et al [58], using a temporal sliding window over the last 10 acquired stacks. Finally, a low pass temporal filter (first order Butterworth with 0.04 Hz cutoff frequency) was applied on a pixel-by-pixel basis on temperature curves to reduce uncertainty. Resulting temperature maps were sent online to a remote computer for display (Thermoguide, Image Guided Therapy, Pessac, France).

B_{1+rms} measurements

B_{1+rms} values were dynamically retrieved from the MRI scanner interface during acquisition at dynamic #90 (end of heating module). The total energy emitted by the sequence was computed and displayed in the user interface of the MRI console. A minimum delay of 6 minutes was observed between consecutive measurements with a different FA_{HM} to reset B_{1+rms} values by the MRI console. This delay also ensured proper cooling of the gel between consecutive experiments.

Validation of the MRI-thermometry method

For validation purposes, a test experiment was performed in a gel containing a copper wire (0.4 mm diameter, 1.2m length). One end of the wire was inserted into the Plexiglas tank filled with agar gel. The remaining part of the wire was positioned in contact with the tunnel bore to favor RF-induced heating (highest electric field emitted by the transmit coil [5]). A fluoroptic temperature fiber (Luxtron® Fiber Optic, STF probe, LumaSense Technologies, Santa Clara, CA, USA) was inserted in the gel perpendicularly to the copper wire. The distance between the wire tip and the optical sensor was approximately 1 mm (Figure 4-4). A 3D balanced-SSFP sequence was acquired to locate the fiber optic temperature probe within the gel, using the following acquisition parameters: bandwidth = 250 Hz/pixel, TR/TE = 666/2.43 ms, 0.8 mm isotropic resolution, FOV = 130 mm, Flip Angle = 90°. The position of the optical fiber tip was identified and the slice stacks of the thermometry sequence were positioned at this reference location.

Potential RF-induced heating near the implanted wire measurement

In a second batch of experiments, another gel of identical content was used and the optical fiber temperature sensor was not inserted to obtain temperature maps devoid of any signal drop close to the wire. The same imaging sequence was repeated while varying the FA_{HM} from 0° to 90° by steps of 10° in order to create a calibration dataset. For each acquisition, the temperature evolution in the same pixel was analyzed, selecting the pixel with the maximal temperature increase at the end of the energy deposition (acquisition #90) from the temperature data corresponding to the largest FA_{HM}. To verify absence of temperature drift during experiment, temperature evolution in a pixel located outside the heating zone was also plotted.

Potential RF-induced heating near a pacemaker lead

We evaluated our method on a commercial MR conditional pacemaker lead (CapSureFix Novus MRI Surescan, 65-cm length, Medtronic). The latter was inserted vertically (perpendicular to B_0) into a gel and not connected to its generator to simulate an abandoned lead scenario. The tip of the lead that is normally screwed into the myocardium was inserted into the gel while the other extremity was left in the air. A 3D gradient echo (TE/TR=3.9/8 ms, isotropic resolution of 0.8 mm) was acquired to locate the lead and position the central slice (stack of 3 slices) of the proposed sequence (with acquisition parameters identical to those mentioned above) at the lead tip

Statistical analyses

To assess the thermometry precision, a first acquisition with FA_{HM} = 0° of the heating module was performed in gel. The same scan parameters as described in section MRI-thermometry sequence were used. The temporal average of temperature (μ_T) and the temporal standard deviation of temperature (σ_T) were computed for each pixel in a region of interest around the wire over the 120 dynamic acquisitions. The same analysis was repeated after temporal filtering.

MRI-thermometry assessment in volunteer

A healthy volunteer was informed about the protocol and consented to be included in the study (the institution review board "Commité de protection des personnes îles de France IV" #IRB0003835 approved this study under the approval number 2017-A03313-50) in order to measure the mean temporal standard deviation of the temperature in the brain with the proposed method, without energy deposition (FA_{HM} = 0°). Image acquisition parameters were 40° FA, 149*149 mm FOV, 92x92 matrix (zero filled to 184x184), 1510 Hz/px bandwidth, 70 repetitions, 1s repetition time. Measurements were repeated with different TE values of 22, 30, 40, 50, 60 and 70 ms. The standard 16-elements head coil provided by the manufacturer was used. A ROI was manually drawn to cover most of the brain over the 3 slices. The temporal standard deviation (σ_T) was computed over the 3 slices and analyzed with a Box-and-Whisker plot (selected values: lower value, first quartile, median value, third quartile and 95% of the distribution) to characterize precision of the method.

Temperature dependence on Flip Angle, B_{1+rms} and energy emitted by the MRI sequence

For each experiment of the calibration dataset, a temporal window of 5 dynamic acquisitions was used to compute the mean temperature and the temporal standard deviation at the end of energy deposition (between acquisitions #86 and #90). The $\mu_T \pm \sigma_T$ temperature values were plotted as a function of the flip angle, B_{1+rms} and energy emitted (i.e. sum of the energies of each individual RF pulse, including pulses for imaging and pulses of the heating module). A quadratic fit was performed on the resulting first two curves and a linear fit on the last one. Coefficients (namely, β_1, β_2 and β_3) and R^2 of the fit were retrieved.

Prediction of temperature increase for other MRI sequences

In this section, we propose a semi-empirical approach to exploit temperature data obtained from a calibration dataset to predict the maximal temperature rise for any other MRI sequence. Considering that heating induced near an implanted wire is localized around its tip, we chose to approximate this heating source by a Gaussian function with isotropic dimensions. Under this assumption, temperature evolution at the hottest point resulting

from energy deposition at constant power (P_0) applied between t_0 and t_1 can be analytically described by the following equation [96]:

$$T(t) = \begin{cases} 0 & \text{for } t \leq t_0 \\ \alpha P_0 \tau \ln \dfrac{t - t_0 + \tau}{\tau} & \text{for } t_0 \leq t \leq t_1 \\ \alpha P_0 \tau \ln \dfrac{t - t_0 + \tau}{t - t_1 + \tau} & \text{for } t \geq t_1 \end{cases} \quad (4\text{-}8)$$

Where α is the absorption coefficient and τ is a time constant. Temperature evolution at the hottest point for each temperature curve of the calibration data set acquired at different powers P_i (i.e. for each flip angle of the SAR module) was fit using equation (4-8) to retrieve α and τ. Then, we plot α_i and τ_i as a function of P_i and fit these two curves with a second order polynomial function. The resulting functions allow then to compute α and τ values corresponding to the power of any other MRI sequence. Thus, temperature evolution for the selected sequence can then be simulated by taking its effective emitted power (total energy divided by acquisition duration) and its acquisition duration. In a third batch of experiments, we included the tip of the wire already described above together with the optical fiber into a gel (wire perpendicular to B_0 and identical gel preparation as described above). After the calibration data set was created, temperature curves for each flip angle were processed as indicated above. Then, three other acquisition sequences typically used in clinic were launched and temperature was recorded by the fiber optic probe:

- A 2D Turbo spin echo sequence, emitting 11.093 W power during 38 s
- A 3D gradient echo sequence, emitting 2.522 W during 2 min 15 s.
- A 2D cine true-fisp sequence, emitting 43.590 W during 9s

Temperature evolution simulated for these 3 sequences using equation [1] and parameters derived from the proposed method were compared to fiber optic readings.

4.4.5. Results

Precision of the MRI-thermometry method

Figure 4-6a shows the temporal average of temperature (μ_T) and the temporal standard deviation of temperature (σ_T) in the gel over the 120 dynamic acquisitions for the first slice, when no energy is deposited (FA_{HM}=0° for the heating module). μ_T and σ_T values were (mean ± std) 0.0±0.2 °C and 0.65±0.05 °C without filtering, and 0.0±0.2 °C and 0.21±0.04 °C after filtering, respectively. Figure 4-6b shows the three slices acquired on a volunteer with the proposed method (TE=30 ms) together with the map of temporal standard deviation in an ROI covering most of the brain. Box-and-whisker plots of σ_T show that median values decreased from 0.2 °C for a TE of 22 ms to 0.12 °C for a TE ranging 40-70 ms. Moreover, at least 75% of the pixels included in the ROI remained below 0.25 °C, irrespective of the echo time (90% or more for TE ranging 40-70 ms).

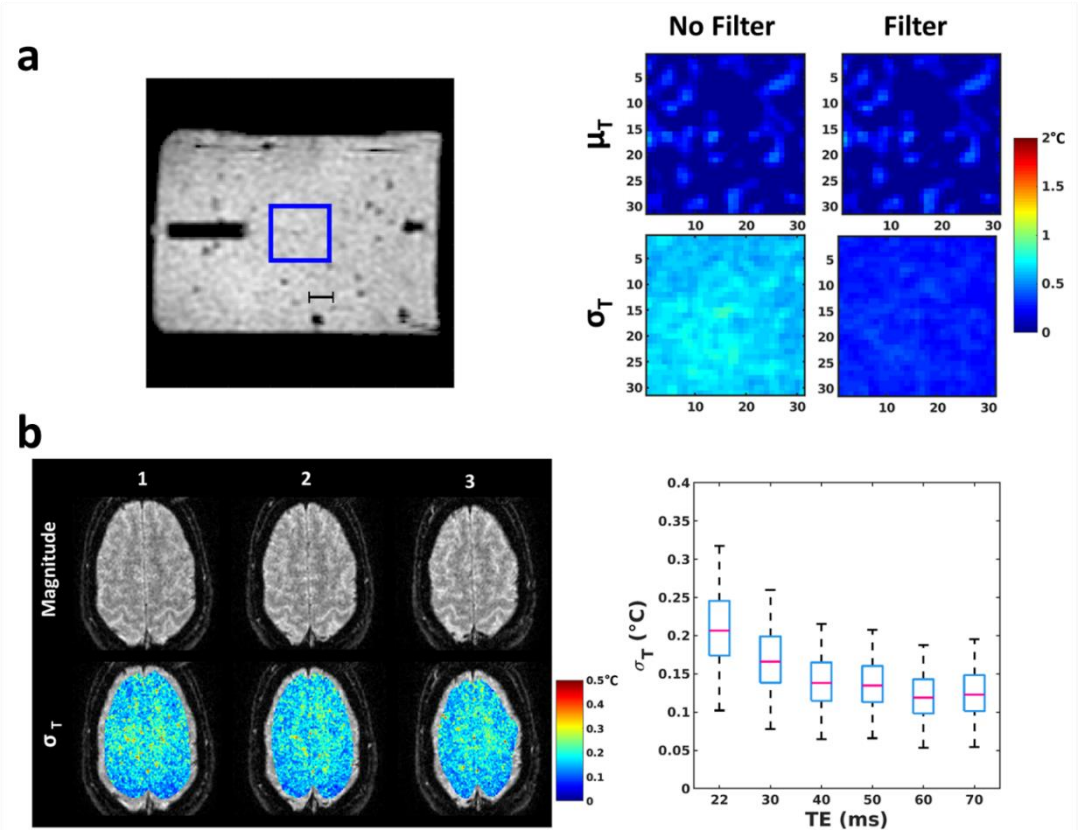

Figure 4-6 : Temperature precision in gel and in human brain. a) Left: Magnitude image of the thermometry sequence. The overlaid blue square delimits the region where the analysis of temperature data was performed. Horizontal bar represents 1 cm. Right: Maps of μ_T and σ_T computed over the complete time series before and after filtering with a Butterworth low-pass filter. Mean ± SD of μ_T and σ_T were 0.0±0.2 °C and 0.65±0.05 °C before filtering and 0.0±0.2 °C and 0.21±0.04 °C after filtering, respectively. b) Left: Measurement of the temperature standard deviation over the brain of a healthy volunteer. Images on the left show the magnitude images (top row) averaged over 10 consecutive acquisitions and temporal standard deviation of temperature (σ_T, bottom row) for a TE of 30 ms in a large ROI covering the brain. Right: Box and whiskers plots show the distribution of σ_T for different TE within the ROI. Median values are displayed in pink and box correspond to 25% (bottom of the blue box) and 75% (top of the blue box) of the distribution, while the upper limit of the whiskers corresponds to 95% of the pixels in the ROI.

Accuracy of the MRI-thermometry method during heating

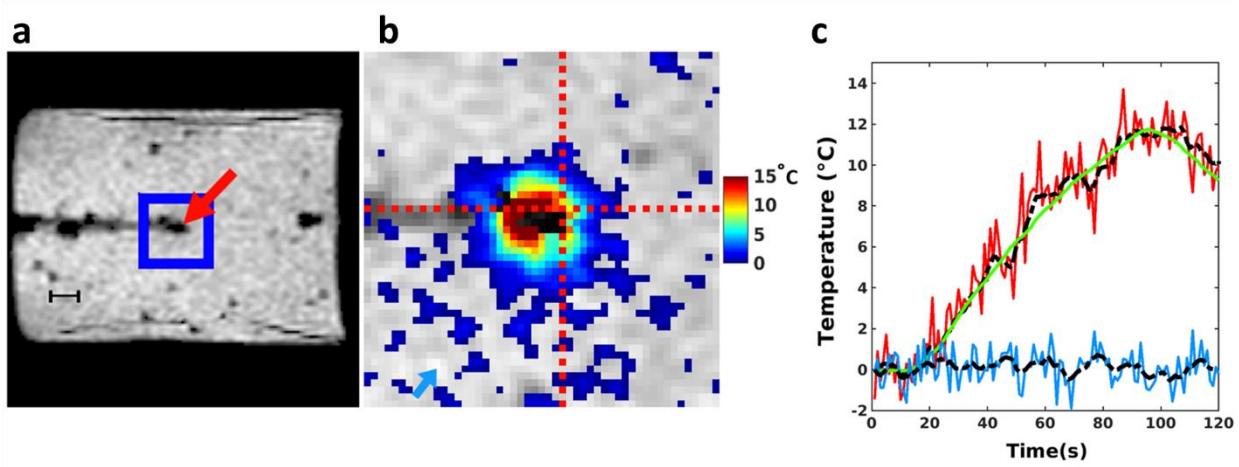

Figure 4-7: Comparison between temperature values given by the optical fiber and the proposed imaging method. a) Magnitude image where the fluoroptic sensor is visible. The blue square represents the region of interest and red arrow indicates the location of the fluoroptic tip. Horizontal bar represents 1 cm. b) Zoomed view of temperature map overlaid on magnitude image at the end of heating (dynamic acquisition #90). Intersection between the dashed red lines shows the pixel corresponding to the optical fiber tip location. The blue arrow indicates the selected pixel located outside the heated region. c) Temperature evolution (red and blue curves) plotted for the selected pixels in image b) with the temperature curve obtained from the optical fiber (green). Dashed lines are filtered curves

Figure 4-7a shows the magnitude image of the gel sample with the optical fiber inserted near the wire tip. Figure 4-7b displays the temperature distribution at the end of the energy deposition (dynamic acquisition #90) within the blue square shown in Figure 4-7a. Local heating can be observed around the tip of the copper wire. Evolution of the temperature over the 120 dynamic acquisitions is plotted in Figure 4-7c for a single pixel located near the fiber optic sensor, together with temperature evolution in another pixel located away from the heated region. Overlaid dashed lines correspond to the MRI-temperature data in the same pixels after low-pass filtering. A strong correspondence is observed between temperature evolution measured by the fiber optic sensor (green curve) and filtered MRI-temperature data (dashed black curve). The maximal temperature value computed over 5 dynamic acquisitions around #90 for filtered MRI-thermometry data and fluoroptic probe were 11.5 °C and 11.7 °C, respectively. To compensate the latency induced by the filter (delay of three repetition times) and compute correct root mean squared error (RMSE) values, the filtered curve was shifted left by three dynamic acquisitions in post processing

before subtraction to temperature readings from the optical thermometer. The resulting RMSE were 1.2 °C and 0.5 °C for unfiltered and filtered MR temperature values, respectively.

Phantom Experiments with varying flip angles

Figure 4-8a displays the MRI-temperature maps at the dynamic acquisition #90 for each flip angle of the heating module. A temperature increase was observed close to the tip of the wire, with an increasing maximal value with the flip angle. In the present configuration, the maximal temperature increase was 32.4 °C for a 90° flip angle. Temperature evolution is plotted in Figure 4-8b (red curves) for each flip angle in the same pixel (intersection of the dashed red lines) and in a pixel located outside the heated region (blue curves). Table 4-3 reports the measured B1+rms, total emitted energy and maximal temperature increases for flip angles of the heating module ranging from 0 to 90°. Maximal B_{1+rms} values were 4.1 µT for a 90° FA_{HM}. The maximal temperature as a function of the FA_{HM}, B_{1+rms} and energy is displayed in Figure 4-9, together with the fits. Coefficients resulting from the fits were $\beta_1=4.3 \pm 0.1.10^{-3}$ °C/°^{2}, $\beta_2=2.0 \pm 0.05$ °C/(µT)^2 and $\beta_3=2.3 \pm 0.1$ 10^{-3} °C/J, respectively. A strong correspondence was found between experimental data and fits (R^2=0.98 for each fit).

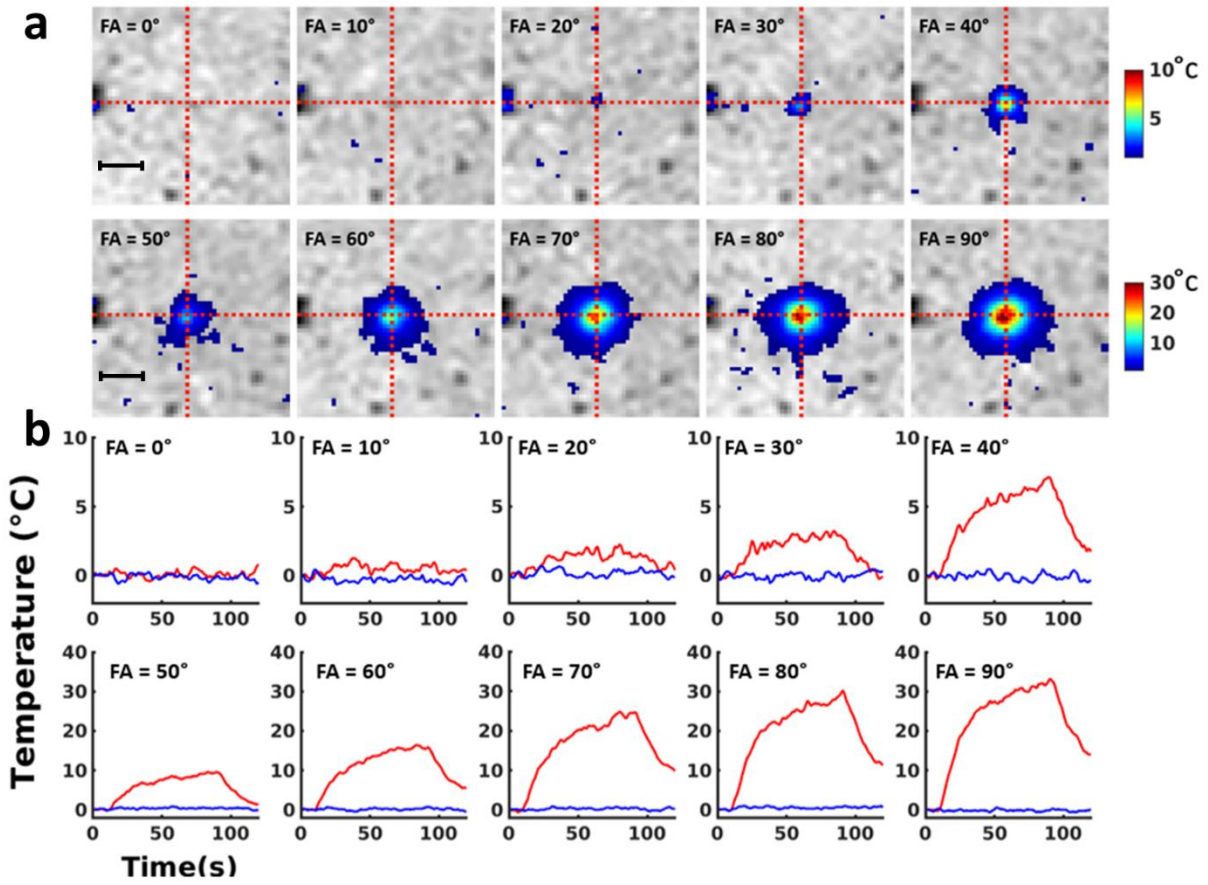

Figure 4-8: Evolution of temperature distribution with increasing flip angle: a) unfiltered temperature maps are overlaid on their corresponding cropped magnitude images at the end of heating (acquisition #90) and show the temperature spatial distribution for each flip angle. Intersection of red lines indicates the pixel of interest and the blue arrow indicates the pixel selected for background, respectively. This pixel is the same for every acquisition and is located in the region of maximum heating. Horizontal bar in the top left images represents 1 cm. (b) Temperature evolution versus time for the pixel of interest. Red and blue curves show the temperature evolution in the pixel of interest and in a pixel outside the region of interest respectively.

FA (°) (heating module)	B_{1+rms} (µT) (EPI + heating module)	Energy (J) (heating module)	Max temperature increase (°C)
0	0.6	0	0.2
10	0.8	150	0.7
20	1.1	602	1.4
30	1.4	1354	2.6
40	1.9	2407	6.7
50	2.3	3761	9
60	2.8	5415	15.7
70	3.2	7371	24
80	3.8	9627	29
90	4.1	12185	32.4

Table 4-3: Summary of experimental conditions and temperature increase as a function of the flip angle of the heating module. Measured B_{1+rms} are those provided by the scanner at the end of heating (dynamic acquisition #90). Energy values of the heating module are computed from the sequence. The last column reports the maximal temperature values measured by the proposed MRI thermometry method.

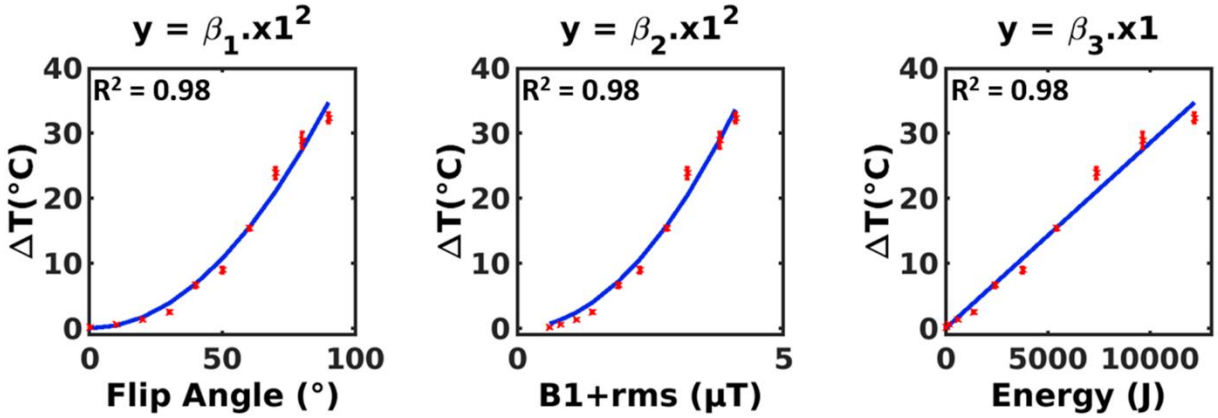

Figure 4-9: Dependence of temperature increase in a single pixel on Flip Angle, B1+rms and deposited energy by the MRI sequence. Each point corresponds to the mean of the temperature over 5 dynamic acquisitions at the end of the energy deposition (acquisition #90) obtained for FA_{HM} ranging from 0° to 90°. The same pixel was selected for each experiment. Error bars correspond to the σT over the same 5 dynamic acquisitions. A quadratic curve fit was performed for the two first curves and a linear fit for the last one. Coefficients resulting from the fits were β1=4.3 ± 0.1.10-3 °C/°2, β2=2.0 ± 0.05 °C/(µT)2 and β3=2.3 ± 0.1 10-3 °C/J, respectively.

Applicability of the method on a pacemaker lead

We evaluated our method on a commercial MR conditional pacemaker lead (CapSureFix Novus MRI Surescan, 65-cm length, Medtronic) inserted into a gel (see photograph of the setup in Fig 6a left) and not connected to its generator to simulate an abandoned lead scenario. The tip of the lead screwed into the myocardium (blue arrow) was inserted into the gel while the other extremity (orange arrow) was left in the air. A 3D gradient echo (TE/TR=3.9/8 ms, isotropic resolution of 0.8 mm) was acquired to locate the lead and position the central slice (stack of 3 slices) of the proposed sequence (with acquisition parameters identical to those mentioned above) at the lead tip. A local temperature rise up to 6.5 °C was observed near the tip of the device (Fig 6a right) for a 90° flip angle. Calibration curves are displayed in Fig 6b, with β_1, β_2 and β_3 values of $8.8\pm0.5.10^{-4}$ °C/°^{2} (R^2=0.96), 0.40±0.02 °C/µT^2 (R^2=0.97) and $5.8\pm0.3.10^{-4}$ °C/J (R^2=0.96) respectively.

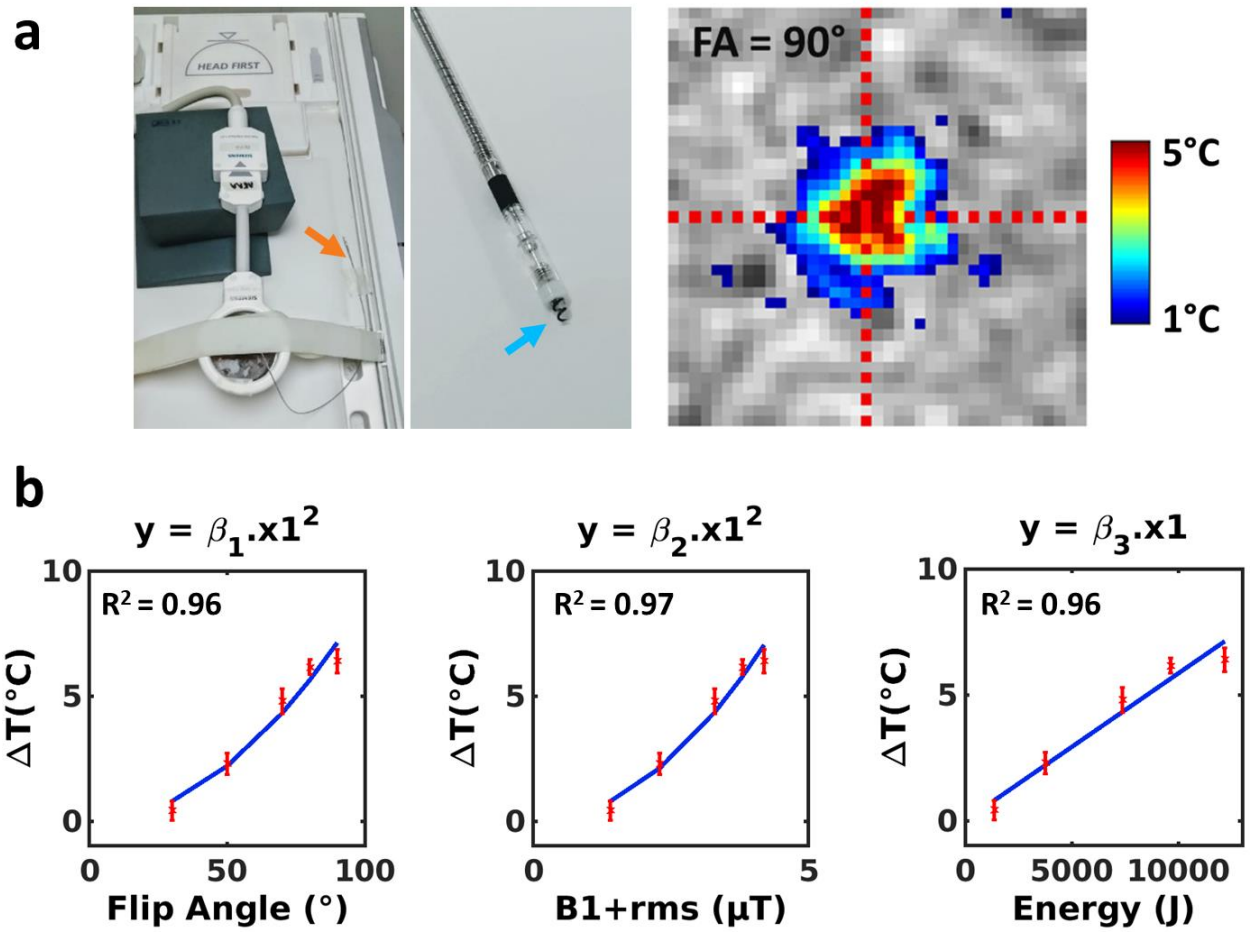

Figure 4-10: Application of the proposed method on a pacemaker lead. a) Experiments on a MR conditional pacemaker lead inserted into a gel. Left: photographs of the setup showing the position of the gel and lead on the MRI table (orange arrow indicates the position of the extremity of the lead, blue arrow indicated the tip screwed into the myocardium). Right: temperature image at dynamic acquisition #90 for a 90° flip angle of the heating module. b)Calibration curves obtained for a series of measurements with flip angles of 30°, 50°, 70°, 80° and 90°. Coefficients resulting from a quadratic fit were β1=8.8±0.5.10-4 °C/°$_2$, β2=0.4 ± 0.02 °C/(μT)^2 and coefficient resulting from a linearly fit was β3=5.8±0.3.10-4 °C/J.

Prediction of temperature rise for three MRI sequences

Figure 4-11 presents results from an additional experiment performed in a gel to evaluate the proposed model and processing technique. The temperature curves of the calibration data set (Figure 4-11a) were fit with Eq (4-8) for each flip angle of the FA_{HM}. The resulting α and τ values derived from these fits are plotted as a function of the corresponding powers in Figure 4-11b and Figure 4-11c, together with the results of the polynomial fits. Figure 8a displays the temperature values measured by the optic fiber during a 2D cine, a 2D turbo

spin-echo and a 3D gradient echo, emitting 43.59 W during 9 s, 11.09 W during 38 s and 2.52 W during 135 s, respectively. For each sequence, the temperature curves were simulated using Eq (4-8), after calculating α and τ from the polynomial fits shown in Fig 7b and 7c. A good correspondence can be observed between experimental and simulated curves, with maximal values of 11.19°C (Cine) 5.62°C (2D TSE) and 2.32°C (3D GRE) for experimental values and predicted values of 11.88°C, 5.85°C and 2.33°C, respectively. On the contrary, using the calibration curves (namely coefficient β_3) from Fig 5c to estimate the maximal temperature increase from the total energy of each sequence leads to 2.78°C, 2.96°C and 2.42°C, respectively. Such an approach is thus irrelevant for predicting maximal temperature rise in the context of an implanted wire.

Figure 8b shows contour plots of the predicted maximal temperature increases for a range of power and duration using the fitting method and for this experimental configuration. Isotherms can then be used to define acceptable exposure conditions for any sequence.

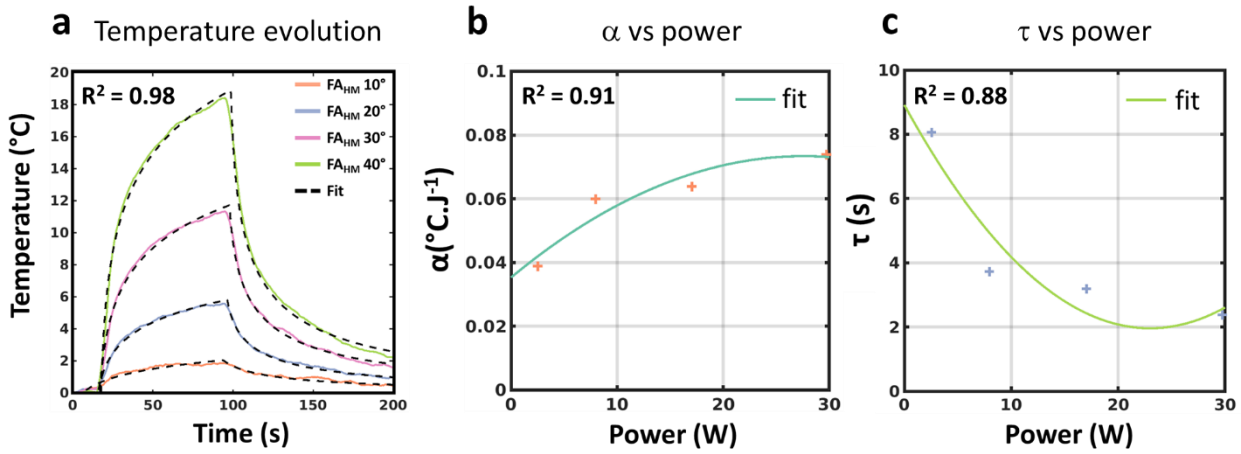

Figure 4-11: Temperature data for 4 different F_{AHM}. a) experimental and fitted curves for FA_{MH} of 10°, 20°, 30° and 40°. b) Plot of α as a function of power. c) Plot of τ as a function of power. In b) and c), solid lines represent the result of the polynomial fit with the resulting equations: $\alpha = -4.996P^2 + 2.758x10^{-2}\,P + 3.531x10^{-2}$ and $\tau = 1.316x10^{-2}\,P^2 - 6.049x10^{-1}\,P + 8.912$.

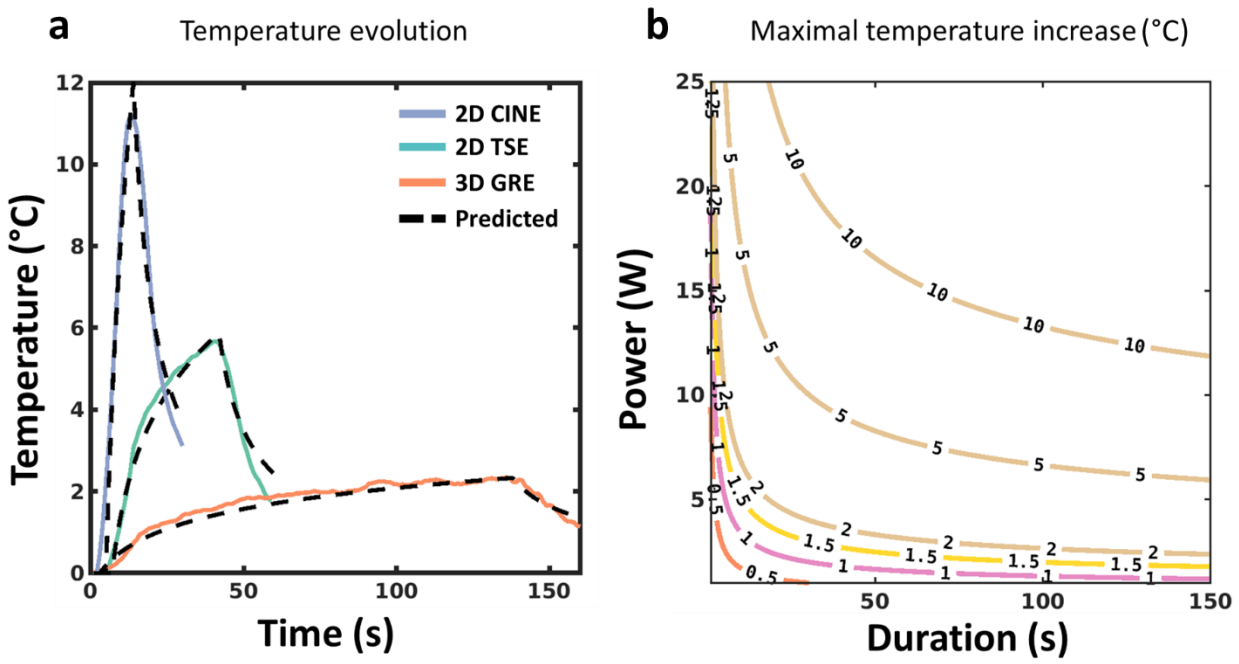

Figure 4-12: Prediction of maximal temperature rise for other acquisition sequences. a) Predicted (dashed lines) and measured temperature evolution by the optical fiber for the 2D cine (solid blue curve), the 2D TSE (solid green curve) and 3D GRE sequences (solid orange curve). b) Contour plot of isotherms showing the predicted maximal temperature increase as a function of the duration and power of a MRI acquisition sequence. Polynomial functions displayed in Figure 4-11 were used in the simulation.

4.5. Discussion

Sequence implementation

The hybrid sequence proposed in this study interleaves adjustable RF energy deposition with multi-slice EPI acquisitions to provide sufficient spatial (1.6 mm in-plane interpolated to 0.8 mm) and temporal resolution (1s refresh rate with a 3 s temporal footprint in our setting) for real-time visualization of the potential temperature increase in-situ. Similar approach was already proposed in Gensler et al, using T1 measurements to assess temperature evolution near a copper wire inserted into a gel. In plane spatial resolution was 2.3 mm with slice thickness of 5 mm, leading to an elementary voxel size of 26.5 mm^3, much larger (factor 4) than in the present study (6.1 mm^3, before interpolation). Ehses et al [85] proposed a PRF-based MR-thermometry method with similar in-plane spatial resolution (1.6 mm) but a slice thickness of 5 mm. Moreover, temporal resolution was 3.9 s per slice, making rapid and multi-slice monitoring of temperature evolution near the wire

more difficult than in the present study. Here, the achieved spatial resolution was considered sufficient for observing local temperature hot spots near the wire tip, since the heating region observed in Figure 4-8a had a dimension ranging from 2.4 to 5.6 mm (full width at half maximum of temperature profile for $FA_{HM} \geq 20°$). The proposed implementation provides flexibility between the number of slices to acquire volumetric temperature data and energy deposition duty cycle (72% in our experiment). The duty cycle can be adjusted by increasing repetition time of the sequence, since temperature evolution is relatively slow, as shown in Figure 4-7c. Alternatively, higher acceleration factors, partial Fourier sampling [92] and/or simultaneous multi-slice techniques [93] may be implemented to increase volume coverage at constant acquisition time.

Precision of the MRI-thermometry

In our implementation, a temperature uncertainty of ~0.2 °C was obtained on a clinical 1.5T MRI scanner (both on phantom and in vivo in the human brain). Such a precision was better than those previously reported (24,26) and was considered sufficient in the context of MR safety evaluation of devices, where maximum temperature should not exceed 39 °C for the brain (IEC-60601 and FDA regulation). Although optimal value for PRFS thermometry is achieved when TE equals T2*, the uncertainty in the human brain was found good enough for TE values ranging from 22 ms to 50 ms since they remained below 0.25 °C for at least 75% of the pixels located in the brain irrespective of echo time.

In a previous study, a similar thermometry technique without the heating module showed a good precision (around 1°C) in vivo in mobile organs such as the heart [58], [59] and the liver at 1.5T [60] including real time motion compensation and correction of the potential temporal drift of the magnet (also implemented in the present work). In the context of monitoring small temperature increases near implanted devices in mobile organs, more sophisticated filtering techniques could be used to further improve the precision of thermometry as proposed by Roujol et al [94] for example. Despite the proposed implementation creates a latency of 3 s, the risk of reaching a lethal thermal dose within this time scale (according to the CEM43 (40) model) which is unlikely to occur with optimized clinical devices.

Calibration technique

In the experiments with the copper wire, we observed an important temperature increase when the flip angle of the heating module was higher than 30°, although B_{1+rms} values provided by the scanner interface remained within regulatory limit (maximal B_{1+rms} of 3.2 µT, as indicated in the fixed-parameter option of IEC 60601 –2-33) for most of the experimental conditions (FA_{HM} up to 70 °, see Table 4-3). As expected from the theory [5], the maximal experimental temperature showed a quadratic variation (β_1 and β_2 coefficients) with the flip angle and B_{1+rms}, together with a linear dependence (β_3 coefficient) with the emitted energy. From these calibration curves, it is thus possible to estimate in situ on this sample the maximal temperature increase associated with any acquisitions sequence, based on the corresponding B_{1+rms} values provided by the scanner. In the experiment with the MR conditional pacemaker lead, we were able to perform identical experiments and obtain different calibration curves, with maximal temperature increase of 6.5 °C.

Prediction of temperature increase from the model

In the last experiment (Figure 4-11 and Figure 4-12), we illustrate that the proposed model can correctly fit the temperature curves of the calibration dataset. From these fits, we show that temperature evolution of other acquisition sequences can be reasonably estimated. An exponential fitting function was proposed in the literature to model temperature increase during the heating phase. However, experimental results reported in Ehses et al [85] and Gensler et al [81] did not perfectly fit the MR-temperature curves and diverged from fiber optic measurements using this model. Here, we chose a more physically-realistic model of temperature evolution (derived from a Gaussian-shaped heating source), although this shape is an approximation for RF-induced heating. This model fits both the heating and cooling phases of the temperature curve. Whatever the model, indeed, the two parameters resulting from the fit (here α and τ) are directly linked to tissue absorption and thermal diffusivity, and are thus not expected to vary with the emitted power, at least for moderate temperature increases (i.e. remaining below the lethal thermal dose). However, parameters α and τ (Figure 4-11b and Figure 4-11c) derived from the fit of temperature curves (Figure 4-11a) show a strong variation when varying FA_{HM} from 10° to 20° and lower changes for higher FA_{HM} (30° and 40°). For these reasons, we introduced a polynomial fitting function in Figure 4-11b and Figure 4-11c. Variation of α and τ as a function of the power was

attributed to the relative small dimensions of the heating spot for low FA_{MH} values, where partial volume effect of the thermometry sequence may play a role, although an effort was made to provide high resolution temperature images with the proposed sequence. This semi-empirical model allowed to predict the maximal temperature increase for three other MRI sequences. However, a key point of the calibration step is to avoid creating excessive temperature increase, since protein denaturation can occur when absolute temperature reaches 43°C (i.e. 6°C temperature rise above physiological body temperature). In our results, we reached much higher maximal temperature rises when wires were included in the gel. However, in our implementation, we chose a long duration of the heating module (80 s) to validate the acquisition method and the associated processing. Shorter duration of the heating module may be considered to reduce the temperature rise, taking advantage of the 1 s temporal resolution of our thermometry sequence to sample the temperature curve and thus derive α and τ, without inducing excessive temperature increase. Moreover, sampling the flip angles from 0 to 90° by 10° steps is probably not mandatory since risks are mainly associated with high power deposition, which correspond to large flip angles. This was observed on the pacemaker lead where significant heating was only observed for large flip angles (FA_{MH} of 70° and higher in see Figure 4-10b). Such an optimization of the calibration process was considered out of the scope of the present work, whose objective was to present the acquisition sequence and processing method and to evaluate them under well controlled experimental conditions, as a proof of concept.

The resulting temperature increases may differ in vivo since absorption, thermal diffusivity and perfusion (not present here) are tissue-specific, resulting in different calibration data sets. However, the method is expected to remain valid since perfusion acts as a scaling factor in temperature evolution. Thus, by generating calibration data set at the beginning of the MRI session, it should be possible to determine personalized RF exposure conditions for each patient with an implanted wire. In this objective, real-time MRI-thermometry as proposed here is of central interest to avoid creating excessive temperature rise during the calibration process.

Study limitations

This study has some limitations. First, PRFS technique is not applicable in fatty tissue. Second, our method may be dependent on size and magnetic susceptibility, limiting its applicability, since local image distortion and signal losses can be particularly severe with echo planar imaging. However, for tissue with long T2* such as in the brain, echo time can be reduced in the presence of an implanted device to balance the effect of local susceptibility artifacts, while keeping acceptable temperature accuracy (see Figure 4-9b). Moreover, shortening the echo train duration of the EPI by parallel imaging contributes to reducing susceptibility artifacts. Although EPI suffers from known limitations, this technique was preferred for the aforementioned advantages (rapid and multi slice imaging, high duty cycle), especially given that this technique is available on any scanner and that MRI compatibility of medical implants is under constant improvement by manufacturers [95]. In the present work however, no in vivo data with implanted devices could be produced to assess the method in real conditions, justifying further studies.

4.6. Conclusion

We propose here a practical MRI-based method to monitor the risk of heating during clinical MRI examination through direct measurement of local temperature increase. This method may be combined with other MR-based approaches [75], [76] that aim to measure effective current induced in the device. The proposed method could be used at preliminary stage of the design of new devices with implanted wires to quantify the risk of heating depending on the exposure conditions, using phantoms with tissue-mimicking absorption and thermal diffusivity for example. In patients having devices with implanted wires, this method might be used at the beginning of the MRI session to assess acceptable exposure conditions. This will however require optimization of the calibration process and further in vivo evaluation.

4.7. References

1] J.-N. Dacher et al., 'Joint Position Paper of the Working Group of Pacing and Electrophysiology of the French Society of Cardiology (SFC) and the Société française d'imagerie cardiaque et vasculaire diagnostique et interventionnelle (SFICV) on magnetic resonance imaging in patients with cardiac electronic implantable devices', Diagnostic and Interventional Imaging, p. S2211568420300358, Feb. 2020.

[2] L. Zrinzo et al., 'Clinical Safety of Brain Magnetic Resonance Imaging with Implanted Deep Brain Stimulation Hardware: Large Case Series and Review of the Literature', World Neurosurgery, vol. 76, no. 1–2, pp. 164–172, Jul. 2011.

[3] J. B. Erhardt et al., 'Should patients with brain implants undergo MRI?', J. Neural Eng., vol. 15, no. 4, p. 041002, Aug. 2018.

[4] 'Quick Safety 31: Strong MRI safety programs prevent safety events, FDA'. The Joint Commission, Mar. 2017, Accessed: Jan. 14, 2021. [Online]. Available: https://www.jointcommission.org/.

[5] W. R. Nitz, A. Oppelt, W. Renz, C. Manke, M. Lenhart, and J. Link, 'On the heating of linear conductive structures as guide wires and catheters in interventional MRI', Journal of Magnetic Resonance Imaging, vol. 13, no. 1, pp. 105–114, Jan. 2001.

[6] S.-M. Park, R. Kamondetdacha, and J. A. Nyenhuis, 'Calculation of MRI-induced heating of an implanted medical lead wire with an electric field transfer function', Journal of Magnetic Resonance Imaging, vol. 26, no. 5, pp. 1278–1285, Nov. 2007.

[7] S. Achenbach, W. Moshage, B. Diem, T. Bieberlea, V. Schibgilla, and K. Bachmann, 'Effects of magnetic resonance imaging on cardiac pacemakers and electrodes', American Heart Journal, vol. 134, no. 3, pp. 467–473, Sep. 1997.

[8] M. K. Konings, L. W. Bartels, H. F. M. Smits, and C. J. G. Bakker, 'Heating Around Intravascular Guidewires by Resonating RF Waves', Journal of Magnetic Resonance Imaging, vol. 12, no. 1, pp. 79–85, Jul. 2000.

[9] A. R. Rezai et al., 'Neurostimulation systems for deep brain stimulation: In vitro evaluation of magnetic resonance imaging-related heating at 1.5 tesla', Journal of Magnetic Resonance Imaging, vol. 15, no. 3, pp. 241–250, Mar. 2002.

[10] R. Luechinger et al., 'In vivo heating of pacemaker leads during magnetic resonance imaging', European Heart Journal, vol. 26, no. 4, pp. 376–383, Feb. 2005.

[11] E. Mattei et al., 'Complexity of MRI induced heating on metallic leads: Experimental measurements of 374 configurations', BioMedical Engineering Online, vol. 7, no. 1, p. 11, Mar. 2008.

[12] J. Spiegel et al., 'Transient dystonia following magnetic resonance imaging in a patient with deep brain stimulation electrodes for the treatment of Parkinson disease', Journal of Neurosurgery, vol. 99, no. 4, pp. 772–774, Oct. 2003.

[13] J. M. Henderson, J. Tkach, M. Phillips, K. Baker, F. G. Shellock, and A. R. Rezai, 'Permanent Neurological Deficit Related to Magnetic Resonance Imaging in a Patient with Implanted Deep Brain Stimulation Electrodes for Parkinson's Disease: Case Report', Neurosurgery, vol. 57, no. 5, pp. E1063–E1063, Nov. 2005.

[14] J. H. Indik et al., '2017 HRS expert consensus statement on magnetic resonance imaging and radiation exposure in patients with cardiovascular implantable electronic devices', Heart Rhythm, vol. 14, no. 7, pp. e97–e153, Jul. 2017.

[15] Y. Eryaman, E. A. Turk, C. Oto, O. Algin, and E. Atalar, 'Reduction of the radiofrequency heating of metallic devices using a dual-drive birdcage coil', Magnetic Resonance in Medicine, vol. 69, no. 3, pp. 845–852, Mar. 2013.

[16] L. Golestanirad et al., 'Construction and modeling of a reconfigurable MRI coil for lowering SAR in patients with deep brain stimulation implants', NeuroImage, vol. 147, pp. 577–588, Feb. 2017.

[17] Y. Zhu, L. Alon, C. M. Deniz, R. Brown, and D. K. Sodickson, 'System and SAR characterization in parallel RF transmission', Magnetic Resonance in Medicine, vol. 67, no. 5, pp. 1367–1378, May 2012.

[18] C. E. McElcheran, B. Yang, K. J. T. Anderson, L. Golestanirad, and S. J. Graham, 'Parallel radiofrequency transmission at 3 tesla to improve safety in bilateral implanted wires in a heterogeneous model: pTx at 3T to Improve Safety in Bilateral Implanted Wires', Magnetic Resonance in Medicine, vol. 78, no. 6, pp. 2406–2415, Dec. 2017.

[19] M. E. Ladd and H. H. Quick, 'Reduction of resonant RF heating in intravascular catheters using coaxial chokes', Magnetic Resonance in Medicine, pp. 79-85,, 2000.

[20] R. W. Gray, W. T. Bibens, and F. G. Shellock, 'Simple design changes to wires to substantially reduce MRI-induced heating at 1.5 T: implications for implanted leads', Magnetic Resonance Imaging, vol. 23, no. 8, pp. 887–891, Oct. 2005.

[21] L. Golestanirad et al., 'Reducing RF-induced Heating near Implanted Leads through High-Dielectric Capacitive Bleeding of Current (CBLOC)', Biophysics, preprint, Oct. 2018.

[22] Medtronic, Inc., 'MRI guidelines for Medtronic deep brain stimulation systems'. Dec. 2015.

[23] L. Winter, F. Seifert, L. Zilberti, M. Murbach, and B. Ittermann, 'MRI-Related Heating of Implants and Devices: A Review', Journal of Magnetic Resonance Imaging, p. jmri.27194, May 2020.

[24] G. Bashein and G. Syrovy, 'Burns associated with pulse oximetry during magnetic resonance imaging', [Letter], Anesthesiology, pp. 382–383, 1991.

[25] T. R. Brown, B. Goldstein, and J. little, 'Severe burns resulting from magnetic resonance imaging with cardiopulmonary monitoring. Risks and relevant safety precautions.' American Journal of Physical Medicine & Rehabilitation, pp. 166–167, 1993.

[26] S. J. Keens and A. S. Laurence, 'Burns caused by ECG monitoring during MRI imaging', Anaesthesia, Dec. 1996.

[27] M. F. Dempsey and B. Condon, 'Thermal Injuries Associated with MRI', Clinical Radiology, vol. 56, no. 6, pp. 457–465, Jun. 2001.

[28] M. Murbach, E. Zastrow, E. Neufeld, E. Cabot, W. Kainz, and N. Kuster, 'Heating and Safety Concerns of the Radio-Frequency Field in MRI', Curr Radiol Rep, vol. 3, no. 12, p. 45, Dec. 2015.

[29] E. Cabot et al., 'Evaluation of the RF heating of a generic deep brain stimulator exposed in 1.5 T magnetic resonance scanners', Bioelectromagnetics, vol. 34, no. 2, pp. 104–113, Feb. 2013.

[30] L. P. Panych and B. Madore, 'The physics of MRI safety: Physics of MRI Safety', Journal of Magnetic Resonance Imaging, vol. 47, no. 1, pp. 28–43, Jan. 2018.

[31] M. F. Dempsey, B. Condon, and D. M. Hadley, 'Investigation of the factors responsible for burns during MRI', Journal of Magnetic Resonance Imaging, vol. 13, no. 4, pp. 627–631, Apr. 2001.

[32] A. C. Özen, T. Lottner, and M. Bock, 'Safety of active catheters in MRI: Termination impedance versus RF-induced heating', Magnetic Resonance in Medicine, vol. 81, no. 2, pp. 1412–1423, Feb. 2019.

[33] M. C. Bennett et al., ‘Mechanisms and prevention of thermal injury from gamma radiosurgery headframes during 3T MR imaging’, Journal of Applied Clinical Medical Physics, vol. 13, no. 4, pp. 54–70, Jul. 2012.

[34] C. J. Yeung, R. C. Susil, and E. Atalar, ‘RF safety of wires in interventional MRI: Using a safety index’, Magnetic Resonance in Medicine, vol. 47, no. 1, pp. 187–193, Jan. 2002.

[35] H. Bassen, W. Kainz, G. Mendoza, and T. Kellom, ‘MRI-induced heating of selected thin wire metallic implants – laboratory and computational studies – findings and new questions raised’, Minimally Invasive Therapy & Allied Technologies, vol. 15, no. 2, pp. 76–84, Jan. 2006.

[36] The Foundation for Research on Information Technologies in Society (IT’IS), Jan. 2021. https://itis.swiss/virtual-population/tissue-properties/database/dielectric-properties/.

[37] R. Luechinger, V. A. Zeijlemaker, F. Duru, and P. Boesiger, ‘RF-Heating Effects on Coated Wires and Pacemaker Leads at 1.5T and 3.0T’, Proceedings of the 14th ISMRM Annual Meeting, Seattle, Washington, USA, 2006.

[38] D. A. Langman, I. B. Goldberg, J. P. Finn, and D. B. Ennis, ‘Pacemaker lead tip heating in abandoned and pacemaker-attached leads at 1.5 tesla MRI’, Journal of Magnetic Resonance Imaging, vol. 33, no. 2, pp. 426–431, Feb. 2011.

[39] M. Balasubramanian, W. M. Wells, J. R. Ives, P. Britz, R. V. Mulkern, and D. B. Orbach, ‘RF Heating of Gold Cup and Conductive Plastic Electrodes during Simultaneous EEG and MRI’, The Neurodiagnostic Journal, vol. 57, no. 1, pp. 69–83, Jan. 2017.

[40] C. Armenean, E. Perrin, M. Armenean, O. Beuf, F. Pilleul, and H. Saint-Jalmes, ‘RF-induced temperature elevation along metallic wires in clinical magnetic resonance imaging: Influence of diameter and length’, Magnetic Resonance in Medicine, vol. 52, no. 5, pp. 1200–1206, Nov. 2004.

[41] P. Nordbeck et al., ‘Measuring RF-induced currents inside implants: Impact of device configuration on MRI safety of cardiac pacemaker leads’, Magnetic Resonance in Medicine, vol. 61, no. 3, pp. 570–578, Mar. 2009.

[42] J. Kabil, ‘Étude des interactions par radiofréquence entre multiples dispositifs médicaux pour la compatibilité IRM’, Jan. 2018.

[43] T. M. Fiedler, M. E. Ladd, and A. K. Bitz, ‘SAR Simulations & Safety’, NeuroImage, vol. 168, pp. 33–58, Mar. 2018.

[44] Shellock R & D Services, ‘http://www.mrisafety.com/’. http://www.mrisafety.com/ (accessed Jan. 14, 2021).

[45] D. Formica and S. Silvestri, 'Biological effects of exposure to magnetic resonance imaging: an overview', BioMedical Engineering OnLine, p. 12, 2004.

[46] O. Bottauscio et al., 'Assessment of computational tools for MRI RF dosimetry by comparison with measurements on a laboratory phantom', Physics in Medicine and Biology., vol. 60, no. 14, pp. 5655–5680, Jul. 2015.

[47] L. Alon, C. M. Deniz, G. Carluccio, R. Brown, D. K. Sodickson, and C. M. Collins, 'Effects of anatomical differences on electromagnetic fields, SAR, and temperature change: RF SAFETY OF PATIENTS AT ULTRA HIGH MAGNETIC FIELD', Concepts in Magnetic Resonance Part B: Magnetic Resonance Engineering, vol. 46, no. 1, pp. 8–18, Feb. 2016.

[48] J. Nadobny, M. Szimtenings, D. Diehl, E. Stetter, G. Brinker, and P. Wust, 'Evaluation of MR-Induced Hot Spots for Different Temporal SAR Modes Using a Time-Dependent Finite Difference Method With Explicit Temperature Gradient Treatment', IEEE Transactions on Biomedical Engineering, vol. 54, no. 10, pp. 1837–1850, Oct. 2007.

[49] K. B. Baker et al., 'Evaluation of specific absorption rate as a dosimeter of MRI-related implant heating', Journal of Magnetic Resonance Imaging, vol. 20, no. 2, pp. 315–320, Aug. 2004.

[50] K. B. Baker, J. A. Tkach, M. D. Phillips, and A. R. Rezai, 'Variability in RF-induced heating of a deep brain stimulation implant across MR systems', Journal of Magnetic Resonance Imaging, vol. 24, no. 6, pp. 1236–1242, Dec. 2006.

[51] A. Massire et al., 'Thermal simulations in the human head for high field MRI using parallel transmission', Journal of Magnetic Resonance Imaging, vol. 35, no. 6, pp. 1312–1321, Jun. 2012.

[52] W. Faulkner, 'New MRI Safety Labels & Devices, Vol.5, Issue 1', Feb. 2016. https://www.ismrm.org/smrt/E-Signals/2016FEBRUARY/eSig_5_1_hot_2.htm.

[53] R. M. Shulman and B. Hunt, 'Cardiac implanted electronic devices and MRI safety in 2018—the state of play', Eur Radiol, vol. 28, no. 10, pp. 4062–4065, Oct. 2018.

[54] E. Kanal et al., 'ACR Guidance Document for Safe MR Practices: 2007', American Journal of Roentgenology, vol. 188, no. 6, pp. 1447–1474, Jun. 2007.

[55] Y. Cruypeninck et al., 'Pacemakers and MRI: A protocol in line with international guidelines and approved by the SFICV (French Society of Cardiovascular Imaging)', Diagnostic and Interventional Imaging, vol. 98, no. 3, pp. 203–215, Mar. 2017.

[56] P. Jabehdar Maralani et al., 'MRI safety and devices: An update and expert consensus', Journal of Magnetic Resonance Imaging, vol. 51, no. 3, pp. 657–674, Mar. 2020.

[57] B. D. de Senneville, S. Roujol, P. Jaïs, C. T. W. Moonen, G. Herigault, and B. Quesson, 'Feasibility of fast MR-thermometry during cardiac radiofrequency ablation', NMR in Biomedicine, vol. 25, no. 4, pp. 556–562, Apr. 2012.

[58] V. Ozenne et al., 'Improved cardiac magnetic resonance thermometry and dosimetry for monitoring lesion formation during catheter ablation', Magnetic Resonance in Medicine, vol. 77, no. 2, pp. 673–683, Feb. 2017.

[59] S. Toupin et al., 'Feasibility of real-time MR thermal dose mapping for predicting radiofrequency ablation outcome in the myocardium in vivo', Journal of Cardiovascular Magnetic Resonance, vol. 19, no. 1, Dec. 2017..

[60] P. Bour et al., 'Real-time monitoring of tissue displacement and temperature changes during MR-guided high intensity focused ultrasound: Monitoring of Changes During MRgHIFU', Magnetic Resonance in Medicine, vol. 78, no. 5, pp. 1911–1921, Nov. 2017.

[61] M.-B. Edwards, K. M. Taylor, and F. G. Shellock, 'Prosthetic heart valves: Evaluation of magnetic field interactions, heating, and artifacts at 1.5 T', Journal of Magnetic Resonance Imaging, vol. 12, no. 2, pp. 363–369, Aug. 2000.

[62] E. Mattei et al., 'Temperature and SAR measurement errors in the evaluation of metallic linear structures heating during MRI using fluoroptic® probes', Physics in Medicine and Biology, vol. 52, no. 6, pp. 1633–1646, Mar. 2007.

[63] T. Lottner, J. B. Erhardt, A. Reichert, A. C. Özen, L. Bielak, and M. Schuettler, 'Avoiding Systematic Errors of Fiber-optic Temperature Probes: MR Thermometry for Safety Assessment of Small Planar Metallic Structures', Proceedings of the 27th ISMRM Annual Meeting, Montreal, Canada 2019.

[64] H. C. Taylor, M. Burl, and J. W. Hand, 'Experimental verification of numerically predicted electric field distributions produced by a radiofrequency coil', Physics in Medicine and Biology., vol. 42, no. 7, pp. 1395–1402, Jul. 1997.

[65] A. Kangarlu, L. Tang, and T. S. Ibrahim, 'Electric field measurements and computational modeling at ultrahigh-field MRI', Magnetic Resonance Imaging, vol. 25, no. 8, pp. 1222–1226, Oct. 2007.

[66] I. Saniour et al., ‘Electro-optic probe for real-time assessments of RF electric field produced in an MRI scanner: Feasibility tests at 3 and 4.7 T’, NMR in Biomedicine, vol. 31, no. 1, p. e3849, Jan. 2018.

[67] L. Alon, G. Y. Cho, X. Yang, D. K. Sodickson, and C. M. Deniz, ‘A method for safety testing of radiofrequency/microwave-emitting devices using MRI: Safety Testing of RF/Microwave-Emitting Devices’, Magnetic Resonance in Medicine, vol. 74, no. 5, pp. 1397–1405, Nov. 2015.

[68] Xiaotong Zhang, S. Schmitter, P. Van de Moortele, Jiaen Liu, and Bin He, ‘From Complex B1 Mapping to Local SAR Estimation for Human Brain MR Imaging Using Multi-Channel Transceiver Coil at 7T’, IEEE Trans. Med. Imaging, vol. 32, no. 6, pp. 1058–1067, Jun. 2013.

[69] S. Oh, Y.-C. Ryu, G. Carluccio, C. T. Sica, and C. M. Collins, ‘Measurement of SAR-induced temperature increase in a phantom and in vivo with comparison to numerical simulation: SAR-Induced Temperature Rise’, Magnetic Resonance in Medicine, vol. 71, no. 5, pp. 1923–1931, May 2014.

[70] K. R. Gorny et al., ‘Measurements of RF heating during 3.0-T MRI of a pig implanted with deep brain stimulator’, Magnetic Resonance Imaging, vol. 31, no. 5, pp. 783–788, Jun. 2013.

[71] E. Mattei, E. Lucano, F. Censi, L. M. Angelone, and G. Calcagnini, ‘High dielectric material in MRI: Numerical assessment of the reduction of the induced local power on implanted cardiac leads’, in 2016 38th Annual International Conference of the IEEE Engineering in Medicine and Biology Society (EMBC), Orlando, FL, USA, pp. 2361–2364, Aug. 2016.

[72] B. Camps-Raga, W. Goertz, G. Schaefers, Y. Mezape, and A. Shalev, ‘A comparative study of numerical and experimental evaluation of RF-induced heating for an endovascular stent-graft at 1.5T and 3T’, Biomedical Engineering / Biomedizinische Technik, vol. 57, no. SI-1 Track-S, Jan. 2012.

[73] Y. Liu, J. Chen, F. G. Shellock, and W. Kainz, ‘Computational and experimental studies of an orthopedic implant: MRI-related heating at 1.5-T/64-MHz and 3-T/128-MHz’, Journal of Magnetic Resonance Imaging, vol. 37, no. 2, pp. 491–497, Feb. 2013.

[74] C. M. Collins et al., ‘Temperature and SAR calculations for a human head within volume and surface coils at 64 and 300 MHz’, Journal of Magnetic Resonance Imaging, vol. 19, no. 5, pp. 650–656, May 2004.

[75] M. Etezadi-Amoli, P. Stang, A. Kerr, J. Pauly, and G. Scott, ‘Controlling radiofrequency-induced currents in guidewires using parallel transmit: Controlling RF Current Using Parallel Transmit’, Magnetic Resonance in Medicine, vol. 74, no. 6, pp. 1790–1802, Dec. 2015.

[76] G. H. Griffin, K. J. T. Anderson, H. Celik, and G. A. Wright, 'Safely assessing radiofrequency heating potential of conductive devices using image-based current measurements: Images to Predict RF Heating Behavior', Magnetic Resonance in Medicine, vol. 73, no. 1, pp. 427–441, Jan. 2015.

[77] B. Quesson, J. A. de Zwart, and C. T. W. Moonen, 'Magnetic resonance temperature imaging for guidance of thermotherapy', Journal of Magnetic Resonance Imaging, vol. 12, pp. 525–533, Oct. 2000.

[78] V. Rieke and K. Butts Pauly, 'MR thermometry', Journal of Magnetic Resonance Imaging, vol. 27, no. 2, pp. 376–390, Feb. 2008.

[79] H. Odéen and D. L. Parker, 'Magnetic resonance thermometry and its biological applications – Physical principles and practical considerations', Progress in Nuclear Magnetic Resonance Spectroscopy, vol. 110, pp. 34–61, Feb. 2019.

[80] V. Detti, D. Grenier, E. Perrin, and O. Beuf, 'Assessment of radiofrequency self-heating around a metallic wire with MR T1-based thermometry', Magnetic Resonance in Medicine, vol. 66, no. 2, pp. 448–455, Aug. 2011.

[81] D. Gensler et al., 'MR safety: Fast T1 thermometry of the RF-induced heating of medical devices', Magnetic Resonance in Medicine, vol. 68, no. 5, pp. 1593–1599, Nov. 2012.

[82] Y. Ishihara et al., 'A precise and fast temperature mapping using water proton chemical shift', Magnetic Resonance in Medicine, vol. 34, no. 6, pp. 814–823, Dec. 1995.

[83] J. D. Poorter, 'Noninvasive MRI thermometry with the proton resonance frequency method: Study of susceptibility effects', Magnetic Resonance in Medicine, vol. 34, no. 3, pp. 359–367, Sep. 1995.

[84] S. Dharmadhikari, J. R. James, J. Nyenhuis, and N. Bansal, 'Evaluation of radiofrequency safety by high temperature resolution MR thermometry using a paramagnetic lanthanide complex: Evaluation of Specific Absorption Rate by MR Thermometry', Magnetic Resonance in Medicine, vol. 75, no. 5, pp. 2121–2129, May 2016.

[85] P. Ehses et al., 'MRI thermometry: Fast mapping of RF-induced heating along conductive wires', Magnetic Resonance in Medicine, vol. 60, no. 2, pp. 457–461, Aug. 2008..

[86] A. Pfeil et al., 'Compatibility of temporary pacemaker myocardial pacing leads with magnetic resonance imaging: an ex vivo tissue study', The International Journal of Cardiovascular Imaging, vol. 28, no. 2, pp. 317–326, Feb. 2012.

[87] M. Stehling, R. Turner, and P. Mansfield, ‘Echo-planar imaging: magnetic resonance imaging in a fraction of a second’, Science, vol. 254, no. 5028, pp. 43–50, Oct. 1991.

[88] M. S. Hansen and T. S. Sørensen, ‘Gadgetron: An open source framework for medical image reconstruction: Gadgetron’, Magnetic Resonance in Medicine, vol. 69, no. 6, pp. 1768–1776, Jun. 2013.

[89] P. Bour, ‘Non-invasive treatment of cardiac arrhythmias by high-intensity focussed ultrasound guided by magnetic resonance imaging’, Nov. 2017.

[90] S. J. Inati et al., ‘ISMRM Raw data format: A proposed standard for MRI raw datasets’, Magnetic Resonance in Medicine, vol. 77, no. 1, pp. 411–421, Jan. 2017.

[91] M. A. Griswold et al., ‘Generalized autocalibrating partially parallel acquisitions (GRAPPA)’, Magnetic Resonance in Medicine, vol. 47, no. 6, pp. 1202–1210, Jun. 2002.

[92] E. M. Haacke, E. D. Lindskogj, and W. Lin, ‘A fast, iterative, partial-fourier technique capable of local phase recovery’, Journal of Magnetic Resonance (1969), vol. 92, no. 1, pp. 126–145, Mar. 1991.

[93] P. T. S. Borman, C. Bos, T. de Boorder, B. W. Raaymakers, C. T. W. Moonen, and S. P. M. Crijns, ‘Towards real-time thermometry using simultaneous multislice MRI’, Physics in Medicine and Biology., vol. 61, no. 17, pp. N461–N477, Sep. 2016.

[94] S. Roujol, B. D. de Senneville, S. Hey, C. Moonen, and M. Ries, ‘Robust Adaptive Extended Kalman Filtering for Real Time MR-Thermometry Guided HIFU Interventions’, IEEE Trans. Med. Imaging, vol. 31, no. 3, pp. 533–542, Mar. 2012.

[95] K. Sethi and S. Chutani, ‘Magnetic resonance imaging-conditional devices: Where have we reached today?’, International Journal of Heart Rhythm, vol. 3, no. 1, p. 16, Jul. 2018.

[96] Quesson B, Vimeux F, Salomir R, de Zwart JA, Moonen CTW. Automatic Control of Hyperthermic Therapy Based on Real-Time Fourier Analysis of MR Temperature Maps. vol. 47, no 6, p. 1065-1072., Jun. 2002

Chapter 5

General Conclusion and Perspectives

High-resolution cardiac MRI at clinical field (1.5 T) represents a major technological challenge. Ultimately, it could increase the value of diagnostic MRI and guide or monitor therapeutic process in a more accurate way. In the present work, we tried to address:

- the need to increase signal to noise by developing and evaluating a local MRI coil,
- the need to provide a 3D motion descriptor with a sub millimeter certainty and combine them in order to obtain images with much higher spatial resolution than state-of-the-art clinical imaging ,
- the need to assess potential safety hazards associated with invasive devices operating into an electromagnetic environment with substantial energy deposition.

Several previous studies highlighted the tremendous potential of using an intravascular coil to enhance the spatial resolution in MR imaging of the blood vessels. Although some research groups have developed coils for intracardiac imaging, no study have shown images of a beating heart with a 300 µm in-plane spatial resolution.

In this thesis work, we demonstrated the feasibility of imaging a beating heart with a 200 µm in-plane spatial resolution on a clinical MRI scanner and therefore opened up new perspectives for high-resolution cardiac imaging. This preliminary work should be continued to develop a catheter with an imaging probe that can be deployed into the heart cavity. This obstacle seems accessible, in particular through the use of new innovative technologies in 3D printing of components and flexibility of materials. An important optimization work is also required to improve the iterative reconstruction methods combined with faster image acquisition. For example, the development of an antenna network with parallel imaging capabilities is expected to increase image quality when

combined with highly undersampled acquisition techniques and reconstruction algorithms based on iterative optimizations. In this work, however, we did not assess the possibility of obtaining images with different contrasts, since the primary goal was to evaluate the feasibility of obtaining highly resolved images of beating hearts.

At the beginning of this work, no instrumentation was available, nor 3D motion descriptors with submillimeter spatial precision. We also propose a method to assess device safety, which can be of particular concern in this context.

An important engineering work was necessary and required many iterative developments in pulse sequence programming, data processing and instrumentation, prior to image a beating heart.

The preliminary results resulting from this work allowed our team to obtain a research grant from the National Research Agency to further develop this technology, with the aim of going toward better image resolution for cardiac substrate characterization and potentially guide therapies in patients.

PUBLICATIONS

Accepted 2021

Abstract

Delcey M, Bour P, Saniour I, El Hamrani D, Ozenne V, Poirier-Quinot M, Quesson B, Feasibility of motion-resolved high resolution, cardiac MRI using a local receiver and MR-tracking micro-coils. SFRMBM, Lyon, France, Apr. 2021.

Under Revision

Papers

Delcey M, Bour P, Ozenne V, Benhassen W, Quesson B. A fast MRI-thermometry method for quantitative assessment of safety in the presence of an implanted wire. Plos One.

Felipe Godinez F, Tomi-Tricot R, **Delcey M**, Lykowsky G, Williams E S, Quesson B, Hajnal J V, S Malik S J. Interventional cardiac MRI using an add-on Parallel Transmit MR system: First in vivo experience in sheep. Magnetic Resonance in Medicine

Abstracts ISMRM

Delcey M, Bour P, Saniour I, El Hamrani D, Ozenne V, Poirier-Quinot M, Quesson B, Feasibility of motion-resolved high resolution, cardiac MRI using a local receiver and MR-tracking micro-coils. Proceedings of the 29th ISMRM Annual Meeting, Vancouver, Canada, May. 2021.

Ozenne V, Bour P, **Delcey M**, Cedilnik N, Sermesant M, Quesson B. Toward automatic lesion transmurality assessment using machine learning: a proof of concept in preclinical EP studies under MRI-guidance. Proceedings of the 29th ISMRM Annual Meeting, Vancouver, Canada, May. 2021.

Oral Presentations

Delcey M, Saniour I, Bour P, Vaillant F, Abell E, Benhassen W, Poirier-Quinot M, Quesson B. Initial technical developments of local RF coil for sub-millimeter cardiovascular MRI. Proceedings of the 28th ISMRM Annual Meeting, Sydney , Australia, May. 2020.

Delcey M, Bour P, Ozenne V, Benhassen W, Quesson B. Proof-of-concept of retrospective gating for interventional cardiac MRI using catheter microcoils readings, SFRMBM, Strasbourg, France, Mar. 2019

Posters

Godinez F, Tomi-Tricot R, **Delcey M**, Lykowsky G, Williams S E, Quesson B, Hajnal J V, and Malik S J · Dynamic control of RF currents in conductive guidewires with an auxiliary PTx system: First in vivo experience in sheep. Proceedings of the 28th ISMRM Annual Meeting, Sydney , Australia, May. 2020

Delcey M, Bour P, Ozenne V, Benhassen W, Quesson B. Proof-of-concept of retrospective gating for interventional cardiac MRI using catheter microcoils readings. Proceedings of the 27th ISMRM Annual Meeting, Montreal, Canada, May. 2019

Pierre Bour P, Ozenne V, **Delcey M**, Lloyd T, Schneider R, Pohl T , Benhassen W, Jais P, Quesson B. Real-time catheter tracking for cardiac MR-Thermometry during RF-ablation. Proceedings of the 27th ISMRM Annual Meeting, Montreal, Canada, May. 2019

Delcey M, Bour P, Ozenne V, Quesson B. Evaluation of RF-related heating of an MR-compatible catheter using MR-Thermometry. Proceedings of the 26th ISMRM Annual Meeting, Paris, France, 2018, Paris, France.

Quesson B, Ozenne V, Bour P, **Delcey M**, Schneider R, Pohl T, Benhassen W, Loyd T, Wedan S, Jais P. Cardiac radiofrequency ablation under real-time MRI thermometry and contact electrophysiology using actively tracked MR-compatible catheters, 12th interventional MRI symposium, Boston, Oct. 2018.

Ozenne V, Bour P, Denis de Senneville B, **Delcey M**, Benhassen W, Vaussy A, Schneider R, Quesson B. Evaluation of 2D simultaneous multi-slice EPI at 1.5T for MR-thermometry in presence of motion. Proceedings of the 26th ISMRM Annual Meeting, Paris, France, 2018, Paris, France.

Bour P, Ozenne V, **Delcey M**, Kitamura T, Gonthier D, Schmidt M, Forman C, Ben Hassen W, Cochet H, Jais P, Quesson B. Improvement of radiofrequency lesion visualization using 3D T1-weighted compressed sensing imaging. ISMRM Annual Meeting, Paris, France, 2018, Paris, France.

Bour P, Ozenne V, Rapacchi S, **Delcey M**, Schneider R, Ben Hassen W, Quesson B. Volumetric and rapid MR-acoustic radiation force imaging using simultaneous multi-slice imaging. ISMRM Annual Meeting, Paris, France, 2018, Paris, France.